Distribution Agreement

In presenting this thesis or dissertation as a partial fulfillment of the requirements for an advanced degree from Emory University, I hereby grant to Emory University and its agents the non-exclusive license to archive, make accessible, and display my thesis or dissertation in whole or in part in all forms of media, now or hereafter known, including display on the world wide web. I understand that I may select some access restrictions as part of the online submission of this thesis or dissertation. I retain all ownership rights to the copyright of the thesis or dissertation. I also retain the right to use in future works (such as articles or books) all or part of this thesis or dissertation.

Signature:

_____ _____

Jinhui Meng Date

Unveiling Electrochemical Surface Processes with *in situ* Vibrational Spectroscopy

By

Jinhui Meng
Doctor of Philosophy

Chemistry

_____
Tianquan Lian, Ph.D.
Advisor

_____
Brian Dyer, Ph.D.
Committee Member

_____
Craig L. Hill, Ph.D.
Committee Member

Accepted:

_____
Kimberly Jacob Arriola, Ph.D.
Dean of the James T. Laney School of Graduate Studies

_____
Date

Unveiling Electrochemical Surface Processes with *in situ* Vibrational Spectroscopy

By

Jinhui Meng

Advisor: Tianquan Lian, Ph.D.

An abstract of

A dissertation submitted to the faculty of the

James T. Laney School of Graduate Studies of Emory University

in partial fulfillment of the requirements for the degree of

Doctor of Philosophy

in Chemistry

2023

Abstract

Unveiling Electrochemical Surface Processes with *in situ* Vibrational Spectroscopy

By Jinhui Meng

This thesis is a comprehensive summary of the studies into the electrochemical interfaces on different processes with *in situ/operando* vibrational spectroscopies, such as Surface-enhanced Raman Spectroscopy (SERS), Shell-isolated nanoparticle enhanced Raman Spectroscopy (SHINERS) and Sum Frequency Generation Spectroscopy (SFGS).

First, the thesis focuses on characterizing the electric double layer at interfaces. Chapter 4 is the SERS investigation of the electric double layer structure in a model electrocatalysis system. The study focuses on utilizing the Stark probe of the adsorbed CO on Au, revealing the unique double layer structure of the system by its ionic strength dependency under the electric fields at the interfaces. Chapter 5 extends the investigation to assess how surface nanoparticles influence surface static electric fields, addressing a controversial question in the field. Utilizing a combination of SHINERS and SFGS, the study compares the effects of nanoparticle proximity on interfacial electric fields across different distances to the surface by various molecular probes. These findings in the two chapters offer a deeper molecular understanding of the electric double layer in electrochemical systems.

The thesis also pioneers a novel approach to control hydrogen bonding at electrochemical interfaces, as detailed in Chapter 6. Through potential-dependent SERS spectra, this research offers a detailed mechanistic study on electrochemical controlling hydrogen bonding between 4-mercaptobenzoic acid and aniline on Au electrode, providing insights into the application of the electro-induction effect and electrolyte interactions in forming and destabilizing hydrogen bond at electrochemical interfaces.

Lastly, in Chapters 7 and 8, the thesis provides more insights into the electrochemical CO_2 reduction reaction (CO_2RR). Chapter 7 highlights the competitive adsorption of carbonate ions on Cu surfaces during CO_2RR, using *in situ* SHINERS. This work sheds light on optimizing CO onset potentials by managing electrolyte composition and providing molecular understanding in this fine-tuning process. Chapter 8 explores the effects of light on electrochemical CO_2RR, revealing

significant findings about light-induced photoelectrochemical CO production and the interplay between surface morphology and reaction enhancement.

Overall, this thesis aims to study the electrochemical interfaces from the molecular aspects, trying to offer a deeper understanding of molecular interactions at electrochemical interfaces.

Unveiling Electrochemical Surface Processes with *in situ* Vibrational Spectroscopy

By

Jinhui Meng

Advisor: Tianquan Lian, Ph.D.

A dissertation submitted to the faculty of the
James T. Laney School of Graduate Studies of Emory University
in partial fulfillment of the requirements for the degree of
Doctor of Philosophy
in Chemistry
2023

Acknowledgment

My graduation research and this thesis would not be possible without the support of so many people whom I want to thank. Foremost, I would love to show my deepest gratitude to my advisor, Dr. Tianquan(Tim) Lian. In my 6-year-graduate life, he provided me the biggest freedom to study the fascinating scientific problems that I feel interested in, and continuously challenged me to think, conduct, and be an independent researcher; I truly appreciated his pursuit of rigorous studies which inspired and helped me polish better work.

Besides, I want to show my appreciation to my committee members, Dr. Brian Dyer, and Dr. Craig Hill, both of whom taught me advanced inorganic courses and provided me with remarkable and helpful feedback during each milestone presentation of mine.

I would like to thank the labmates who have worked in this lab with me. To Dr. Aimin Ge, I want to thank this easy-going senpai(senior labmate) who first trained me in the lab and taught me how to conduct experimental measurements and play with optics and lasers; to Dr. Wenxing Yang, I want to thank this lifetime friend for his sharing his insights and experience in doing research, accompanying me during my most difficult time and sharing so many most unforgettable memories with me; To Qiliang Liu, Dr. Jia Song, Dr. Zihao Xu, Dr. Yawei Liu, Dr. Tao Jin, Dr. Dhritiman Bhattacharyya, and Dr. Chaoyu Li, thank all of these previous labmates who helped me in my research and life.

I would also like to thank my current labmates, who have helped me so much in finishing the work in this thesis. Sara and Fengyi, my peer labmates, are both exceptional researchers and true friends, Sara's hard-working, and positive all the time, and Fengyi is such a good friend that we study, learn, and enjoy life together, I couldn't expected more sweet friends like them, I thank that I have the opportunity to have them as my colleagues in my life; Joey, his professionalism and optimism will always encourage me to follow; Nandan, who invited us for dinners for many times and is the most warm-hearted person I saw; Sheng, who is an excellent and honest colleague to work with; Isaac, who worked with me closely and also had many interesting conversations on various aspects; Sa, who is such a cheerful and careful labmate that makes the

lab comfortable to work in; Paul, who is a lovely friend who makes me happy all the time; and Zhicheng, who always offered help when I'm in need.

I'm grateful to my family. My wife Chan Gao has had a long-distance worldwide relationship with me for over 4 years and always accompanied me whatever happens, and thanks to Dr. Lian who granted me leave to get back to get married, we have the chance to re-unite in Atlanta. My mother Hongyun Lian and my father Jianjun Meng, their priceless support and love with nothing expected in return throughout my whole life made me a better person to do whatever I felt passionate about. It was a difficult time for us when my father had a stroke one year before I graduated, but I felt extremely lucky and blessed to see him gradually recover now. Lastly, I want to say thank you to my two grandparents on my father's and mother's side, Xiuyun Cheng and Peijiang Lian, who passed away during my graduate life, their love will always be with me.

Table of Contents

Abbreviations and Symbols

ACN	acetonitrile
ATR	attenuated total reflectance
CO_2RR	carbon dioxide reduction reaction
CT	chare transfer
CV	cyclic voltammetry
DC	Dielectric constant
DCM	Dichloromethane
DEMS	Differential electrochemical mass spectrometry
DFT	density functional theory
EDL	Electric double layer
FT-IR	Fourier transform infrared spectroscopy
FWHM	full-width at half-maximum
GC	gas chromatography
HB	Hydrogen bonding/bonded
HER	hydrogen evolution reaction
HOMO	highest occupied molecular orbitals
IEF	interfacial electric field
HOMO	highest occupied molecular orbitals
IEF	interfacial electric field
IPCE	incident photo-to-current efficiency
IHP	inner Helmholtz plane
ITO	indium tin oxide
LSV	linear sweep voltammetry
MC	Monte Carlo
NP	nanoparticle
NPoM	Nanoparticle-on-Mirror
OHP	outer Helmholtz plane
pc	polycrystalline

PIC	phenyl isocyanide
RHE	reversible hydrogen electrode
SAM	self-assembled monolayers
SEM	scanning electron microscope
SERS	surface enhanced Raman spectroscopy
SEIRAS	Surface enhanced Infra-red absorption spectroscopy
SHINERS	Shell isolated nanoparticle enhanced Raman spectroscopy
SFG	Sum frequency generation
PEEC	photo-enhanced electrochemical/electrochemistry
pMBA	*para*-mercaptobenzoic acid
pMPAA	*para*-mercaptophenylacetic acid
SPR	surface plasma resonance
TA	transient absorption
TBA	tetrabutylammonium
TEM	transmission electron microscope
UV-Vis	ultraviolet-visible spectroscopy
VSFGS	Vibrational sum frequency generation spectroscopy
4-MBA	4-mercaptobenzonic acid
4-MBN	4-mercaptobenzonitrile
4-MPAA	4-mercaptophenylacetic acid

1. Chapter 1 Introduction

1.1. Motivation

Electrochemistry is everywhere, from rusty nails to batteries inside of electric vehicles, it happens at any interface between the electron-conductive materials (metals, carbon, semiconductors, etc.) and ion-conductive medium (water, organic solvents, etc.). Particularly in the multiple fields of cutting-edge technologies and industries, such as bioelectronics and sensor industries, energy harvesting, conversion, and storage, the study of electrochemical interfaces supports the development of modern society. To advance these technologies and industries, it becomes imperative to gain deeper fundamental scientific insights into the electrochemical interfaces of various processes with suitable techniques. It took a significant amount of time for modern electrochemistry to develop electrochemical techniques, such as voltammetry, to meet the demands of providing the key information on the thermodynamics/kinetics of the electron transfer across the interfaces. However, pure electrochemical techniques alone only provide little molecular information at the interfaces, which greatly hinders the understanding of the electrochemical processes. With this limitation, additional characterization techniques are highly necessary for a more complete comprehensive picture at the interfaces. One such technique is in vibrational spectroscopy, with abundant fingerprint information on unknown molecular species and sensitive insights into the properties of the adsorbate molecules, such as binding structure(mode), bond type, strength, configuration, and orientation at the solid-liquid phase interface. The *in situ/operando* coupled vibrational spectroscopies at the electrochemical interfaces, make more powerful tools, allowing the real-time monitoring of the molecular changes and structure evolutions at the interfaces during the controlled electrochemical processes. This technique can further enable a deeper molecular understanding of the dynamic electrochemical interfaces, with the speciation of the electrode surface changes, the adsorption/desorption, and the identification of certain intermediates, as well as the investigation of electric double layers at the interfaces controlled by electric fields.

The development of vibrational spectroscopy at electrochemical interfaces undergoes a long history of over 50 years[1,2]. The discovery of Surface-enhanced Raman Spectroscopy

(SERS)[3,4] in the 1970s by Martin Fleischmann and Richard Van Duyne first opened a new scope of studying electrochemical interfaces, enabling the researchers to detect the signals of sub-monolayer coverage of adsorbates with a weak spectral cross-section on a roughened metal electrode. The concept of surface-enhancement signal by a "roughened metal" was then adopted into infrared absorption spectroscopy in the early 1980s to discover Surface-enhanced Infrared Absorption Spectroscopy (SEIRAS)[5]. After several years, in the late 1980s, Yuen-Ron Shen et al. [6,7] developed a nonlinear laser spectroscopy intrinsically probing the interfaces, Sum Frequency Generation Spectroscopy (SFGS) and obtained the molecular composition, orientation, and structural information at the gas/solid, gas/liquid and liquid/solid interfaces with the further capability to provide ultrafast time resolution. After these developments, a growing number of in situ electrochemical spectroscopic studies have been applied to reveal more insights into the physical and chemical phenomena at the electrochemical interfaces.

From fundamental principles and the possible applications of *in situ* vibrational spectroscopy, researchers may have tried to bring up many important questions and diligently pursue the answers. In this thesis, I have tried to study some other questions upon the scopes of the great. These questions include:

1) In terms of understanding properties of electric double layer in electrochemical catalysis systems, what should be a good description of adsorbates in the electric double layer(such as adsorbates on metals) and how do these adsorbates respond to the electrolyte changes at different potential region?

2) For different *in situ* vibrational spectroscopic tools, are there any differences in probing and reporting the same species at the interfaces? To be more specific, are there noticeable influences on specific parameters of the local environments, such as electric fields when the additional nanoparticles used in some SERS studies?

3) Despite that the charge transfer related chemical reactions occur at the interfaces, is that possible to initiate possible non-covalent interactions, such as surface hydrogen bonding, by an electrochemical way? 4) as for energy conversion reactions, how does the local surface environment affect the surface adsorbates population to tune the reaction?

5) With the different intensity and wavelength of light flux on the electrochemical surface, how the probe light affects the interfacial reactions?

Although these questions remain investigated and may not be fully answered in a few years, this thesis aims to study some of these topics and discuss the relevant questions to provide meaningful results, and I hope the results and discussions in this thesis can help to reveal a part of the puzzles to some extent.

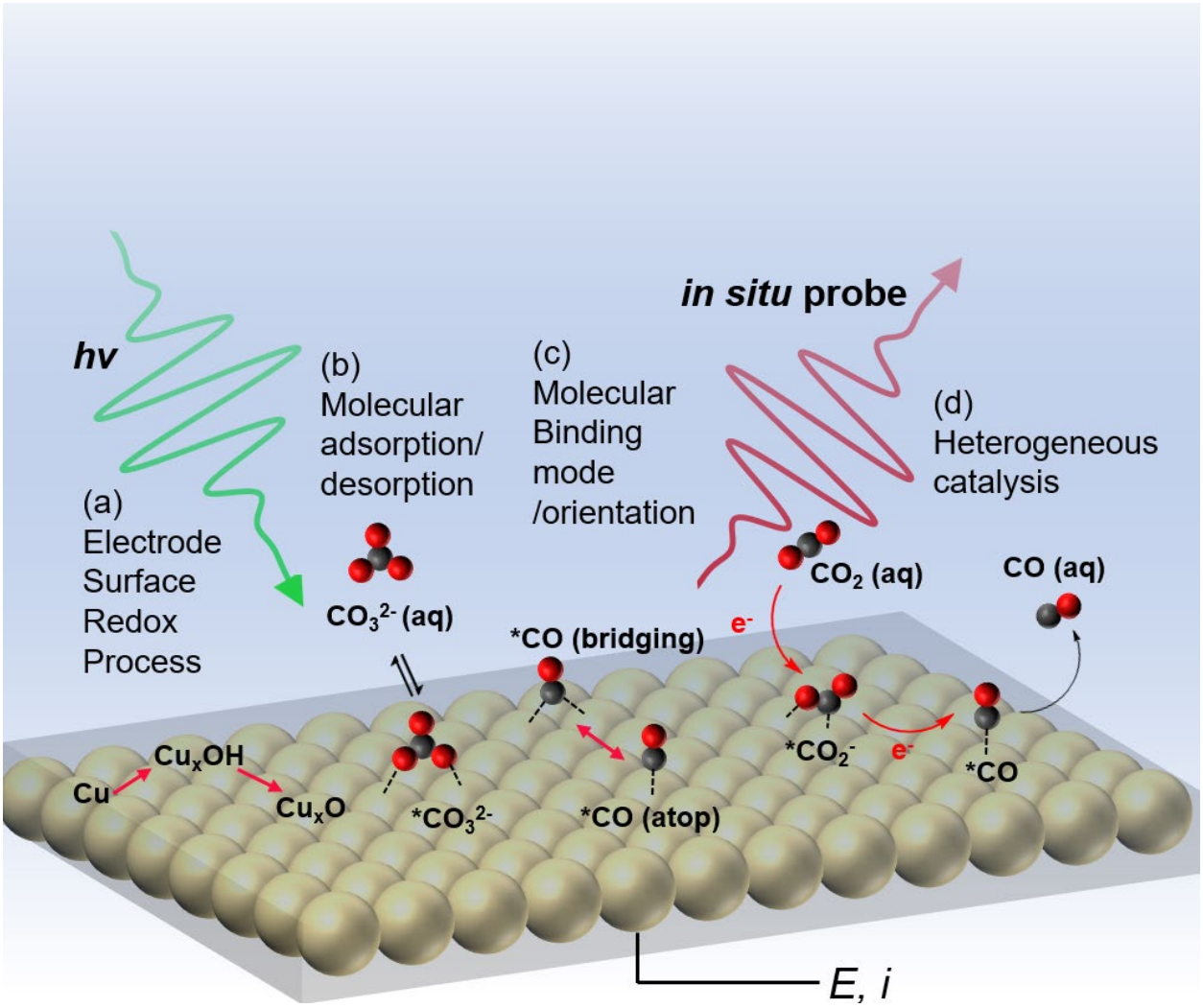

Figure 1.1. Electrochemical processes at interfaces that are accessible by the *in situ* vibrational spectroscopy.

1.2. Outline

Chapter 2 introduces the background and the theoretical knowledge of previous studies in the relevant fields.

Chapter 3 summarizes all the key methods that have been used in the studies. The spectroscopic techniques include *in-situ* surface enhanced Raman spectroscopy (SERS), Shell-isolated nanoparticle-enhanced Raman spectroscopy (SHINERS), and vibrational sum frequency generation (SFG) spectroscopy (VSFGS). The chapter introduces the optical setups used for these measurements, the corresponding spectra fitting, the designs of the Spectro-electrochemical cells, and the additional materials and sample preparation.

Chapter 4 is targeted to the first question, trying to reveal the properties of the electric double layer of an adsorbate on the metal. The chapter covers the core findings from a quite simple but important system in the electrochemical field—adsorbed CO on Au, mainly on the exploring of interfacial static electric fields on metal electrodes. Through the utilization of the *in-situ* SERS, we investigate the ionic strength-dependent Stark tuning rates of the adsorbed CO. Interestingly, we observe adsorbed CO assigned as bridging and atop modes at two potential ranges with different responses to the ionic strength changes. At more positive potential, the adsorbed atop and bridging CO both show an ionic strength dependence, while at the negative potential range, bridging CO is missing and the atop CO shows independence. With the understanding on how different double layer (DL) structures respond to the ionic strength change, we analyzed the observed difference in the dependence on the ionic strength of adsorbed CO at different potentials. The ionic strength dependent CO indicates its existence in diffuse layer and the independent CO indicates that within OHP. This chapter provides a new scope on the properties of DL of the CO on the Au system, shedding light on the molecular understanding of molecular adsorption, ionic strength effects, and electric field effects in electrocatalysis.

Chapter 5 broadens the application of the tool used in Chapter 4, the Stark tuning rate of the molecules, into a different field for trying to answer the second question— "How the nanoparticles near the surface can affect the surface static electric fields". The motivation is to answer the long-standing question in the "gap mode" SERS field how much drop-cast

nanoparticles (NPs) on the surface affect the interfacial electric fields (IEF)? These NPs refer to the plasmonic NPs widely used in *in-situ* vibrational spectroscopic techniques, i.e., “gap mode” SHINERS and SERS with nanoparticles on the mirror (NPoM) scheme. These tools have emerged as valuable tools for probing electrochemical interfaces and providing information on the intensity and spatial profile of interfacial electric fields (IEF); however, debates have arisen and existed for a long time on whether the purposely drop-cast NPs affect the IEF. In this chapter, by experimentally investigating the same electrochemical Au surface with two different *in-situ* techniques, SHINERS with NPs and VSFGS without NPs, we explore the influence of nanoparticle proximity on IEFs by comparing the absolute frequencies and Stark tuning rates of vibrational modes in a series of vibrational probes with spatial variations. These probes consist of 3 groups: 1) the probe moiety close to the NPs within outer Helmholtz plane (OHP): adsorbed CO, phenyl isocyanide SAM, 2) the probe moiety close to NPs and in the diffuse layer of electrode DL: 4-mercaptobenzonitrile and 3) the multiple probe moieties in different position of DL: tungsten-pentacarbonyl(1,4-phenelenediisocyanide). These probes provide a spatial picture of how the NPs affect the IEF ranging from around 0.1 to 1 nm off the electrode surface. Our results indicate that the perturbation of the IEF due to NPs is relatively small near the electrode surface within the OHP, while the influence of the NPs on the IEF is much more substantial in the diffuse layer at the region directly adjacent to the NPs.

With the previous two chapters' understanding of the interfacial EFs, in Chapter 6, we move forward to partially respond to the third question, to study one of the most widely discussed non-covalent interactions at the electrochemical interfacial process—hydrogen bonding (HB). This chapter introduces a novel electrochemical approach for directly controlling H-bonding between 4-mercaptobenzoic acid (4-MBA) and aniline at the interface. Through comprehensive *in-situ* SERS measurements, we identify the HB by distinct frequency shifts on 4-MBA and aniline peaks, and through the potential dependent Raman spectra, we estimate the relative quantity of the HB near the surface under different potentials and find the most favorable condition for forming the HB is at -0.4 V. We further provide evidence on the molecular mechanism, revealing the key roles of electro-induction effect rather than electric field effect in forming the HB from 0.2 to -0.4 V and electrolyte interactions in destabilizing the HB from -0.4 to -0.6 V. These results provide a complete molecular picture on understanding and controlling the HB at electrochemical interfaces, opening new a scope for harnessing and manipulating these

interactions in designing advanced methods and materials for surface assembly, electro-catalysis, and surface analytical chemistry.

Chapter 7 includes the study to the fourth question on the detailed assignments and investigations on the intermediate during energy conversion reaction—electrochemical CO_2 reduction reaction (CO_2RR). In this chapter, we study the hindering effects of the carbonate anion's adsorption into CO_2RR on Cu utilizing electrochemical *in situ* SHINERS. Our results on spectral assignments—derived from density functional theory (DFT) – reveal the strong preference for carbonate ions at the interface during key intermediate steps in the CO_2 reduction reaction. Based on this observation, we assert that carbonate hinders CO_2 reduction via competitive adsorption with the surface-bound intermediate COO^-. In support of this assertion, we demonstrate that fewer adsorbed carbonates lead to a more anodic onset of CO production. To explore the consequences of this competitive adsorption, we present a simple lattice adsorption model parameterized by DFT binding energies and the analysis of SHINERS data. Our work highlights the importance of considering the competitive binding of electrolyte anions carbonate in CO_2RR mechanistic analysis at low overpotentials. These results firstly reveal the negative effects of the carbonate anions during CO_2RR and shed light on the fine-tuning of the CO_2RR by changing the composition of the electrolyte.

Chapter 8 is another project related with electrochemical CO_2RR, we explore the effects of light on metals (Au) under the electrochemical conditions to elucidate how much the probe light can affect the interfaces. This chapter focuses on studying the light-induced photoelectrochemical CO production at the gold (Au)/aqueous solution interface, utilizing vibrational SFG spectroscopy and other electrochemical measurements. Our findings reveal two significant observations that show the complexities of interfacial electrochemical reactions involved with light. Firstly, we observe that the electrochemical onset potential for CO production on gold is markedly higher (0.4 to 0.9 V) than the actual electrochemical onset (0.2 V vs RHE), indicating an unusually substantial CO production stimulated by 800 nm, 35 fs pulses of light. Secondly, we found that with increasing surface roughness, the CO signal per unit time notably increased, revealing the noticeable surface morphology effects in the CO production enhancement. These observations were further validated through a photo-current experiment conducted on an Au NP electrode with around 520 nm plasmonic absorption. Continuous wave

(CW) light at 532 nm and pulsed light at 800 nm both initiated a noticeable photocurrent under CO_2RR conditions in an aqueous solution. The observation of the process may involve multiple possible mechanisms, the plasmonic heating, plasmonic electron transfer, solvated electrons direct laser-induced plasma reaction, etc. With some attempts made to elucidate a "possible solvated electron mechanism" with transient absorption spectroscopy, we conclude that the CO production and the light-induced CO_2RR on the Au system are quite complicated to be well understood and still require further detailed investigation.

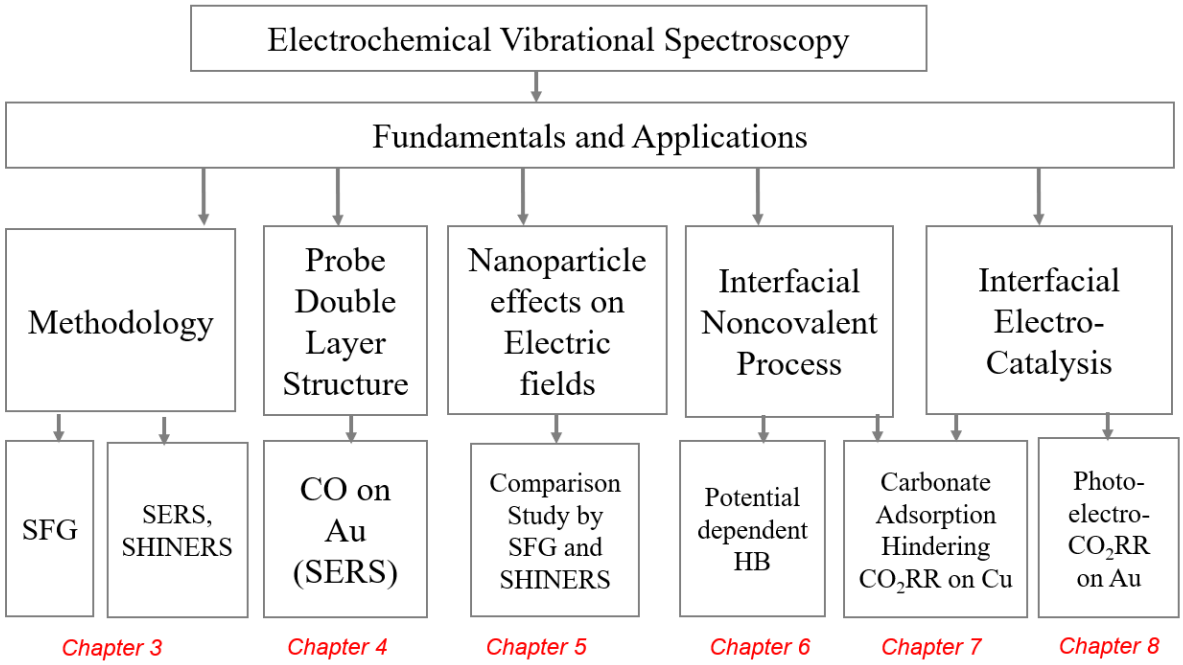

Figure 1.2. An overview graph of the content of all chapters.

1.3. References

(1) Hansen, W. N.; Osteryoung, R. A.; Kuwana, T. Internal Reflection Spectroscopic Observation of Electrode-Solution Interface. *J. Am. Chem. Soc.* **1966**, *88* (5), 1062–1063. https://doi.org/10.1021/ja00957a040.
(2) Mark, H. B.; Pons, B. S. An *in Situ* Spectrophotometric Method for Observing the Infrared Spectra of Species at the Electrode Surface During Electrolysis. *Anal. Chem.* **1966**, *38* (1), 119–121. https://doi.org/10.1021/ac60233a002.
(3) FLEISCHMANN, M.; HENDRA, P. J.; McQUILLAN, A. J. RAMAN SPECTRA OF PYRIDZNE ADSORBED AT A SILVER ELECTRODE. Chem. Phys. Lett. 26 (2), 4.
(4) Jeanmaire, D. L.; Duyne, R. P. V. SURFACE RAMAN SPECTROELECTROCHEMISTRY.
(5) Hartstein, A.; Kirtley, J. R.; Tsang, J. C. Enhancement of the Infrared Absorption from Molecular Monolayers with Thin Metal Overlayers. *Phys. Rev. Lett.* **1980**, *45* (3), 201–204. https://doi.org/10.1103/PhysRevLett.45.201.
(6) Hunt, J. H.; Guyot-Sionnest, P.; Shen, Y. R. Observation of C-H Stretch Vibrations of Monolayers of Molecules Optical Sum-Frequency Generation. *Chem. Phys. Lett.* **1987**, *133* (3), 189–192. https://doi.org/10.1016/0009-2614(87)87049-5.
(7) Guyot-Sionnest, P.; Dumas, P.; Chabal, Y. J.; Higashi, G. S. Lifetime of an Adsorbate-Substrate Vibration: H on Si(111). *Phys. Rev. Lett.* **1990**, *64* (18), 2156–2159. https://doi.org/10.1103/PhysRevLett.64.2156.

2. Chapter 2 Basic Theoretical Background

2.1. Electrochemical Interfaces and electrochemical reactions

2.1.1. Overview of the electrochemical interfaces

The electrochemical interface consists of two phases and is controlled under electrochemical conditions, in most common cases, the solid phase—electrolyte and the liquid phase-electrolyte. This uniquely charged interface thus can serve as an environment for various processes to occur at the same time. 1) Under a certain potential change, the electrode surface (such as metal or metal oxide) can experience a structural change or oxidation-reduction(redox) process to regenerate the surface; 2) when the different potential is applied, the fermi level of the electrode is changed, driven by the electric field changes, different molecules and ions can transport and induce a charging current, under this condition, the ones with good affinity to the surface can experience a surface specific adsorption/desorption; 3) under different electrode potentials or different surface conditions, the molecular configuration, binding mode and/or the orientation may change; 4) when the charge transfer occurs from the metal electrodes to the adsorbed molecules, the possible intermediate is produced at the time, a whole electrochemical reaction may include multiple charge transfer steps.

2.1.2. Background of the electric double layer at electrochemical interfaces

The understanding and characterization of electric fields play a crucial role in various scientific disciplines[1–3], including chemistry[4], physics, and biology.

The picture of the electric double layer (EDL) was revealed with different models and verified by a series of experiments. For spectroscopists, the development of *in-situ* vibrational spectroscopic techniques has enabled researchers to study static electric fields based on the molecular-level information at the interfaces based on the Stark effect. With the help of these advances and information, these concepts provide valuable insights into the fundamental principles governing the behavior of charged species in different environments.

A comprehensive introduction and review of different models of the electric double layers at electrochemical interfaces can be found in Bard et al.'s book[5]. The electric double layer refers to the interface between a charged surface and an electrolyte solution. It consists of two distinct regions: the inner Helmholtz plane (IHP) and the outer Helmholtz plane (OHP). The IHP is a narrow region in immediate proximity to the charged surface, where ions are strongly attracted due to electrostatic interactions. The OHP, on the other hand, extends further into the solution and is characterized by a lower concentration of ions. Various models have been proposed to describe the electric double layer and its properties. One such model is the Gouy-Chapman model, which assumes that the ions are distributed in a diffuse layer near the charged surface. This model considers the electrostatic repulsion between ions and the role of thermal energy in determining the distribution of ions in the double layer. Another model, known as the Stern model, takes into account the specific adsorption of ions at the charged surface, leading to the formation of an inner compact layer along with the diffuse layer.

The Stark effect is a phenomenon observed in the presence of an external electric field, where the energy levels of an atom or molecule shift due to the interaction with the field. This effect arises from the electric dipole moment of the molecule and its interaction with the electric field. The magnitude and direction of the field directly influence the energy levels and can lead to the splitting or shifting of spectral lines. The Stark effect has found wide-ranging applications

in studying the electronic structure and properties of molecules. By examining the energy shifts induced by an external electric field, valuable information about molecular polarizability, charge distribution, and electric field strength can be obtained. This makes the Stark effect a powerful tool for investigating molecular dynamics, intermolecular interactions, and chemical reactions in a variety of systems. The electric field-dependent vibrational frequency shift, named as the vibrational Stark effect[6], has been widely used as a probe for the local electric field and to describe the profile of the EDL at a molecular level.

Based on the vibrational Stark effect, researchers developed electrochemical *in-situ* vibrational spectroscopic techniques to investigate the local electric fields at the interfaces[7–9], these techniques either selectively enhance the signal from interfaces (i.e. SERS) or are intrinsically generated from the surface[10] (i.e. VSFGS[11]), providing an experimental profile of EDL with the a direct measurement of the frequency of certain vibrational mode affected by different electric field strength with different bias applied. These results at the molecular level facilitate a good supplement for verifying the theoretical models of EDL such as the Gouy-Chapman model, Gouy-Chapman-Stern model, etc[5,8].

In a vibrational Stark probe measurement, to correlate with the calculations, the experimental data is usually interpreted in the context of the conventional Stark equation[7–9]:

$$h\nu = -\Delta\vec{\mu} \cdot \vec{F}$$

where h is Planck's constant, ν is the vibrational frequency of the nitrile group, $\Delta\vec{\mu}$ is the Stark tuning rate, and $\vec{F}$ is the electric field.

From this equation, we can also derive the expression of the absolute electric field strength as a function of potential[8] (applied voltage):

$$F(\varphi) = \frac{d\omega(\varphi)}{d\varphi} \cdot \frac{1}{\Delta\mu} \cdot (\varphi - \varphi_{PZC})$$

where $\frac{d\omega(\varphi)}{d\varphi}$ is measured in experiments, and $\Delta\mu$ is from calculations, φ_{PZC} is the potential of zero of charge in the system.

The experimental measured Stark tuning rate of the certain mode and its position in the EDL can thus provide a complete picture of how much field strength the mode at the position feels and how largely the potential drops at the certain position.

The understanding of electric fields at the molecular level is of great importance in many scientific disciplines. The conventional electric double-layer models provide insights into the behavior of charged species at interfaces. To experimentally verify and modify these models, the vibrational Stark probe can be a good tool, allowing for the investigation of molecular properties and actual electric field profiles at the electrochemical interfaces.

2.1.3. Background of energy conversions at interfaces—CO_2RR

There are many key electrochemical reactions at the interfaces, water oxidation reaction, hydrogen evolution reaction, alcohol oxidation reaction, nitrogen reduction reaction CO_2 reduction reaction, etc. The elucidation of the molecular mechanisms for these multiple electrons involved steps at the electrochemical interfaces remains a heated topic. In the last two chapters, we covered the content on the CO_2RR at the electrochemical interfaces as our group has put great emphasis and effort into studying this reaction at the metal (especially at Cu) surfaces. Herein, to help the readers have better background knowledge of this specific electrochemical reaction, an additional introduction on the CO_2RR is also provided.

CO_2 electrochemical reduction reaction (CO_2RR) has gained great attention as it provides a feasible and efficient means of reducing the atmospheric CO_2 level and producing value-added chemicals and fuels[12,13]. However, overcoming the energy barrier to produce high-order carbon products(C2+) remains challenging, because the product distribution of CO_2RR is dependent on many complicated factors, such as the chemical nature of the metals. For instance, Hori, et al.[14–16] conducted a series of electrolysis experimental studies on different metals while quantifying both liquid and gas phase products, and further classified these metals into 4 groups based on their product distribution: metals like Au, Ag, Zn, and Pd mostly generate carbon monoxide (CO) as a product under the mild conditions; Pb, Hg, Tl, and Sn can move a step further, as they

primarily produce formic acid or formate (HCOOH or $HCOO^-$); Pt, Ni, and Fe can barely produce useful CO_2RR products into bulk phase; Cu shows a unique property among them, as it is the only known solo metal to produce higher order hydrocarbon products such as hydrocarbons, aldehydes and alcohols at noticeable and continuous Faradaic efficiency. Following theoreticians[17] have tried to explain the CO_2RR selectivity of the metals and the unique property of Cu based on their affinities or binding energies to different intermediates during hydrogen evolution reaction (HER) or CO_2RR, where Cu is the only case showing a relatively bigger negative adsorption energy of *CO (weakly binds on Cu) but a relatively smaller positive adsorption energy of *H.

The progress of understanding the reaction pathways and mechanism of electrochemical CO_2RR on Cu still heavily rely on theoretical predictions rather than experimental observations, as only a limited number of theoretical, electro-kinetic and electrochemical spectroscopic studies provided clear and verifiable analysis and assignments of key intermediates other than oxide or *CO species[13,18]. Efforts from these studies have been focusing on identifying the intermediates and revealing the roles of other chemical components for two key steps of electrochemical CO_2RR on Cu, the CO_2 activation step[19–22], and further *CO (the 2 e^- reduction product) reduction step (including C-C coupling step) to form high order products[20,23–31].

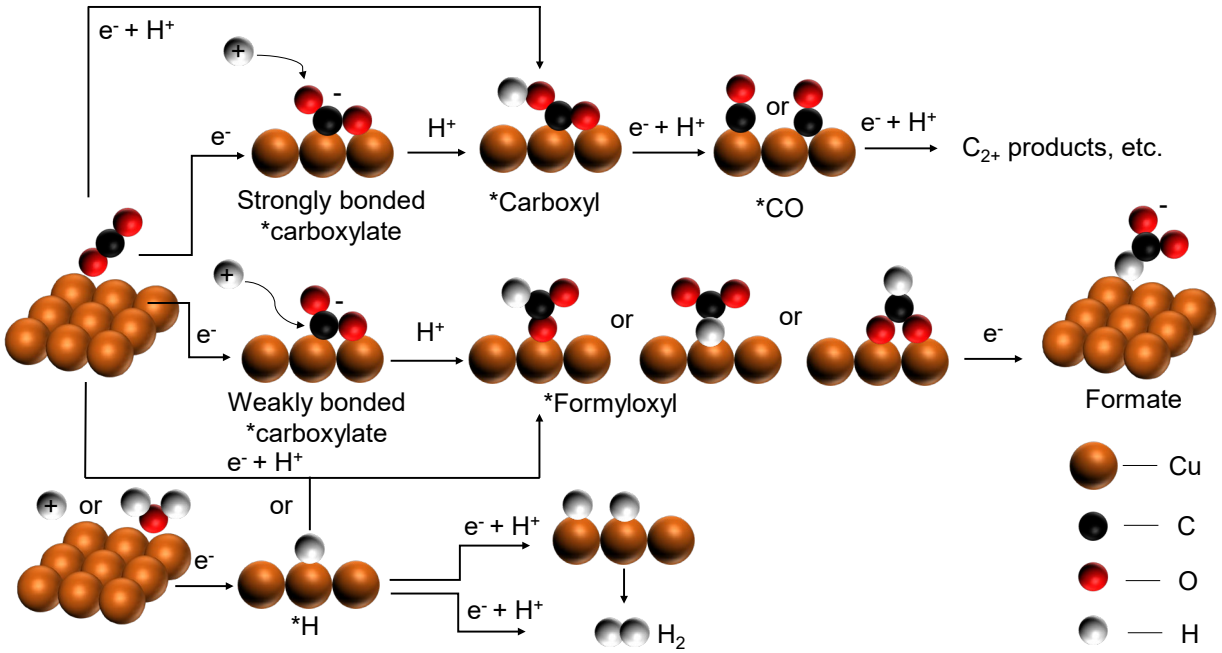

Figure 2.1. Overview of electrochemical CO_2RR pathways on Cu(poly) towards CO or formate as products.

Different color spheres represent different atoms: black-carbon, red-oxygen, white-hydrogen, and brown-copper.

The CO_2 activation step involves physical adsorption and is followed by chemical adsorption (1 e^- reduction) of CO_2 at a relatively mild potential region, further leading to the formation of CO or formate as the next step product[16]. This process is the very first step and directly determine the pathways of the later steps (to be formate or CO) of CO_2RR, thus, it is important to find out which specific chemical identity of CO_2 activation intermediate can respectively lead to formate or CO pathway, and how to further tune the CO_2 activation activity by changing other parameters, such as electrolyte ions or surface species.

It has been proposed[14,16] by Hori et al. that COOH is difficult to be the activation intermediates on Cu-like metal surfaces due to insufficient M-H formation during CO_2 activation from relatively higher overpotential of HER, the activation process should go through the pathway with carboxylate $*COO^-$ (C-down or C,O-down structure)as the first intermediate. In this pathway, the way the carboxylate binds on the surface may determine the further products of activation: a strongly adsorbed carboxylate can be later protonated to a carboxyl *COOH and further reduced to CO via the PCET process; a weakly bonded C-down and C,O-down carboxylate or a O,O-down carboxylate will go through a hydronated C rather O intermediate, formyloxyl *OCHO, directly leading to formate production.

Despite that there are still debates on how carboxyl and formyloxyl are formed[19,32–34], the validation of the existence of carboxylate$*COO^-$, has been conducted by electrochemical spectroscopic studies[21,35,36]. Under rigorously controlled conditions, the Surface-enhanced Raman spectroscopic(SERS) study[21] excluded the possibility of possible carbonate assignment on the vibrational mode at ~1520-1570 cm^{-1} in other previous studies[37–39] with carbonate-free and isotopic labeling control measurements, the authors concluded that it should be the asymmetric C-O stretching mode of weakly bonded C,O-down carboxylate $*COO^-$, which may directly lead to the formation of formate on Cu. However, a valid molecular understanding of the specific intermediate-oriented pathway is still missing, as either $*COO^-$ to CO or formate cannot be fully verified in these studies: the missing (sensitive) spectroscopic detection of surface adsorbed formate-related species at the relevant potential window makes formate pathway not fully convincing; the carboxylate to CO pathway is not conclusive either, as it has been shown[21,35,36] that there is a 0.1 to 0.2 V potential gap between the disappearance of $*COO^-$ and

the onset of *CO, which makes the reaction process of carboxylate to CO seemingly impossible in a discontinuous conversion. Therefore, a more sensitive spectroscopic study with consideration of more surface species is highly needed to provide information on the full picture of the activation process and, further, to rule out the possibility of carboxylate to either formate or CO pathway.

To distinguish the actual pathway and better describe the activation process, many possible co-existing species should be considered. These species may include adsorbed cations or anions, adsorbed side products or intermediates (produced by other reduction reactions, such as HER), and undiminished Cu oxides and hydroxyls. Some electrochemical surface spectroscopic studies may have offered answers to the roles of the species in a broader CO_2RR and CORR process. Cations show abilities to affect CO reduction activity and selectivity by tuning the interfacial water structure[27] or changing the thickness of electric double layer by different hydrated cations[28,40], and they are also indicated to be the key to stabilize the structure of carboxylate $*COO^-$[21]; commonly used anions like bicarbonates/carbonates not only work as a buffer to support surface pH[41] and indirect reactant to support certain concentration of surface localized CO_2[37,42], but can be a specific nerd surface binder to displace the CO reduction adsorption[43]; Cu related oxides and hydroxyls, with their theoretically improvement to lower activation energy on a mixed oxides/Cu surface[19,20], have succeeded in tuning C2+ products selectivity and activity by purposely preparing Cu surfaces with different amounts of oxides/hydroxyls or oxidation states[26,31], with some spectroscopic evidences to show high frequency CO OH interaction[31] and lower frequency hydroxyls during Cu electro-oxidation or under oxidative species[22,44].

2.2. Background of SERS and SHINERS

2.2.1. Background of Raman scattering and Raman spectroscopy

Indian physicist Sir Chandrasekhara Venkata Raman unveiled the phenomenon of Raman scattering phenomena in 1928[45]: by Employing a mercury lamp as the light source, he obtained the light scattering of pure liquid benzene, discovering that, upon dispersion through a prism, scattering light exhibited not only spectral lines with frequencies identical to the incident light (Rayleigh scattering), but also faint spectral lines with frequencies different from the incident light (either increased or decreased), denoted as Raman scattering. Subsequently, scholars from

the former Soviet Union and France independently observed this phenomenon experimentally[46]. Due to its profound advantages in investigating molecular vibrational and rotational structures, Sir Raman was awarded the Nobel Prize in Physics in 1930.

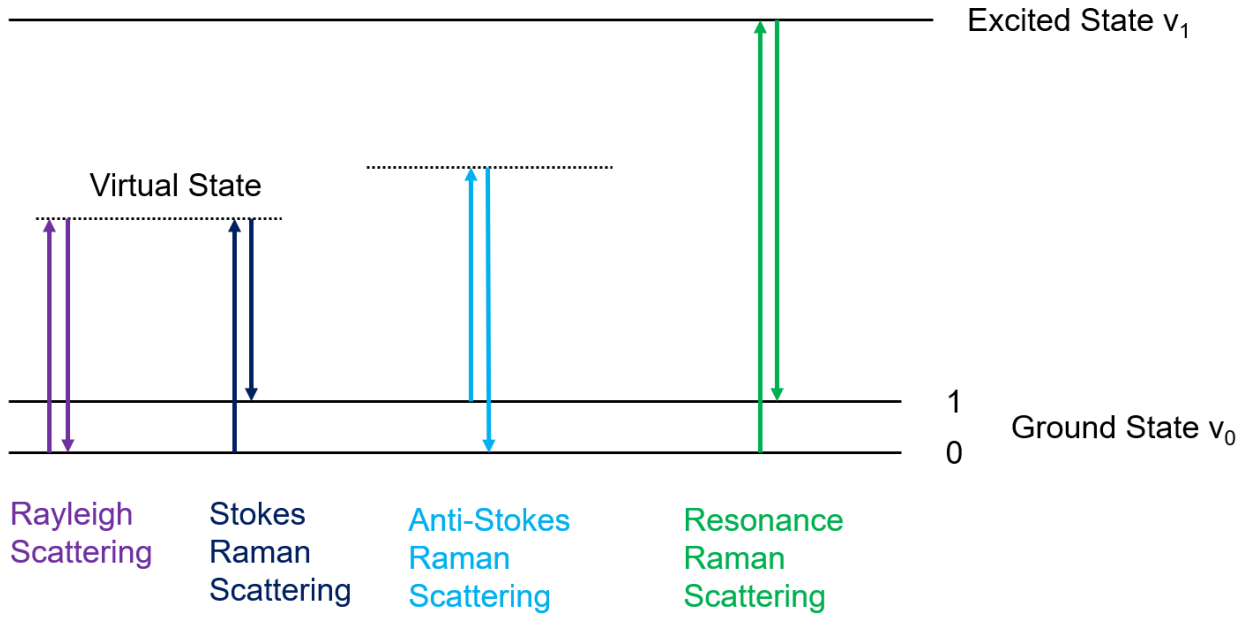

Figure 2.2. Illustration of Rayleigh and Raman scattering

As *Figure 2.3* illustrates, the scattering spectral description results from the interaction of excitation photons with the molecules. The monochromatic light with a frequency of ν_0 possesses photon energy $h\nu_0$ (where h is the Planck constant). Upon interaction, two types of collisions arise: elastic and inelastic. In the elastic collision process, no energy exchange transpires between photons and molecules; the photons merely alter their direction while conserving frequency, resulting in what is termed Rayleigh scattering. On the other hand, the inelastic collision process exchanges energies, resulting in alterations in both photon direction and frequency. For instance, when a molecule in the virtual state transitions to $E_v = 1$, it corresponds to an inelastic collision. In this case, a portion of energy $h\nu$ is transferred from the photon to the molecule, resulting in a scattered photon energy of $h(\nu_0 - \nu)$, commonly referred to as the Stokes line. Analogous processes can occur when a molecule in $E_v = 1$ transitions to the excited virtual state following photon $h\nu_0$ excitation, then returns to the $E_v = 0$ ground state, where photons relinquish some energy to the molecule, altering the scattered photon energy to $h(\nu 0 + \nu)$, termed the anti-Stokes line. Thus, the frequency of Raman scattering photons varies in relation to the incident photon

frequency, resulting in what is termed the Raman shift, and both Stokes and anti-Stokes lines in the Raman spectrum are symmetrically distributed on either side of the Rayleigh line.

It is noteworthy that Raman scattering is a second-order photon process, and the differential Raman scattering cross-section of molecules typically remains exceedingly low, even lower than that of infrared and fluorescence, typically around (or even less than) 10^{-29} $cm^{-2}sr^{-1}$. This intrinsically leads to the weak signal intensity of Raman scattering, generally around 10^{-3} to 10^{-6} times that of Rayleigh scattering.

On the other hand, the early use of mercury lamps as excitation light sources had limited energy, poor monochromaticity, directionality, and coherence, and was mostly unpolarized. This resulted in spectroscopic acquisition times spanning several hours or even days. These practical experimental difficulties impeded the rapid development of Raman spectroscopy over the subsequent three decades. The invention of laser technology in the 1960s made new life into Raman spectroscopy as a new excitation light source. When compared to the earlier employed mercury lamps, lasers show advantages such as high output power and energy concentration, superior monochromaticity, coherence, and near polarization purity. The improvements in optical components and detection devices further expedited the rapid development of Raman spectroscopy. In particular, the integration of Raman spectrometers with computers streamlined data recording and analysis.

Nevertheless, even with these advancements, the application of Raman spectroscopy for studying surface or interfacial molecular structures and properties remains challenging, primarily due to the involvement of species participating in surface processes or reactions that often comprise only monolayers or sub-monolayers of molecules. For instance, if conventional laser Raman spectrometers are employed to detect species in surface monolayers, the scattered Raman signal intensity from each molecule, when illuminated by 1 W of laser light within a 1 mm^2 area, amounts to less than a photon count per hour (far below the detection limit of conventional spectrometers), severely constraining the utility of Raman spectroscopy. As a result, it is primarily employed as a supplementary technique to infrared spectroscopy for identifying functional groups, structures, and configurations of partial organic compounds.

In 1974, Fleischmann and colleagues[47] achieved high-quality Raman spectra of pyridine adsorbed on roughened Ag electrodes after electrochemical oxidation-reduction roughening

treatment, a phenomenon initially attributed to an increase in the electrode surface area following electrochemical roughening, thereby allowing for enhanced signal detection of adsorbed molecules. However, subsequent investigations by Van Duyne[48] and Creighton[49] revealed, through meticulous experiments and theoretical calculations, that the 10^6-fold enhancement of pyridine molecule signals generated on the roughened Ag electrode surface far surpassed the signal enhancement caused by the increased rough electrode surface area. With this, they proposed that a certain effect must exist on the roughened electrode surface, which was later termed Surface-Enhanced Raman Scattering (SERS). Based on this effect, the spectroscopic technique was coined Surface-Enhanced Raman Spectroscopy (SERS).

2.2.2. The feature of SERS effects

Since the discovery of SERS, it has drawn close attention from physicists and chemists, driving extensive experimental and theoretical investigations that have greatly advanced its application in surface science. Over five decades, several distinct characteristics of the SERS effect have been discovered[50–52]:

Remarkable SERS enhancement is observed only for a select group of metals such as Au, Ag, and Cu, typically yielding enhancements surpassing 10^6. In some cases, particularly at the junctions of aggregated Ag or Au nanoparticles, enhancements exceeding ten orders of magnitude have been reported[53], enabling detection limits at the level of individual molecules. This establishes SERS as a vibrational spectroscopic technique distinguished by exceedingly high surface detection sensitivity. The SERS effects on transition metals' surfaces, including Pt, Pd, Rh, Ru, Fe, Co, and Ni, are considerably weaker.

The SERS effect is highly associated with nanoscale structures on the substrates, wherein its intensity not only depends on the metal itself but also the size, shape, and spacing of the nanostructures. Generally, the prerequisites for generating SERS involve substrates with nano-scale roughness or substrates modified with particles featuring sizes on the order of tens to hundreds of nanometers to induce physical or chemical enhancement. Under the same conditions (laser wavelength, adsorbates, etc.), the SERS enhancement effects generated by different nanostructures vary significantly, even exhibiting differences for several orders of magnitude.

SERS exhibits an extraordinarily high surface detection sensitivity, with the maximum enhancement obtained for molecules adsorbed on the first layer near the metal surface. Concurrently, SERS also displays a long-range enhancement effect, remaining effective within several nanometers, or even tens of nanometers, away from the metal surface. However, these enhancement effects exponentially diminish with increasing distance.

The selection rules for SERS are quite different than that of normal Raman, with more modes being evident in SERS spectra[54–56]. In conventional normal Raman spectroscopy, the appearance of spectral peaks adheres strictly to the selection rules governing Raman transitions. However, for SERS, the selection rules are less strict, allowing the detection of many Raman-inactive vibrational modes in the SERS spectra. This is mainly related to the charge transfer enhancement mechanism introduced later.

SERS spectral peak intensities and frequencies deviate from the normal Raman spectra of molecules. Particularly in electrochemical interface systems, the intensity and frequency of SERS peaks are highly dependent on the electrode potential applied. The influence of potential on different vibrational modes of the same molecule can also differ. As a consequence, the SERS intensity is not strictly linearly proportional to the number of molecules under different potentials, whereas in conventional normal Raman spectra, Raman signal intensity correlates proportionally with molecular quantity or concentration. This characteristic is also displayed in the chapters in this thesis (in chapter 6, the unusual peaks enhancement of SAM/Au in SERS).

With these unique features, SERS has found extensive applications across various fields, including electrochemical adsorption, catalysis, corrosion, biomedicine, environmental science, materials science, and beyond. In the field of electrochemical adsorption, SERS has emerged as a prominent technique[57,58], enabling the determination of adsorption configurations, adsorption capacities, co-adsorption behaviors, and real-time monitoring of chemical reactions on substrate surfaces. In the realm of catalysis, SERS serves to investigate the adsorption and reaction of surface molecules on catalysts, such as the adsorption and electrocatalytic oxidation of methanol on platinum in fuel cells[59–61].

2.2.3. Mechanism of SERS effects

SERS has been explored for over four decades, with wide applications across diverse domains. Nevertheless, the interpretation of the mechanisms driving SERS enhancement remains a topic of ongoing debate. Currently, the most widely accepted enhancement mechanisms are electromagnetic (EM) field enhancement and charge transfer (CT) enhancement. The former attributes enhancement to amplified local electromagnetic fields around metal surfaces by the excitation, while the latter emphasizes polarization changes arising from chemical interactions or charge transfer between molecules and metals. Experimental and theoretical studies predominantly focus on the EM field enhancement mechanism, rendering it more extensively developed and applied.

The electromagnetic field enhancement mechanism (EM)[62,63] constitutes a physical model asserting that under irradiation by incident laser light, the surface of a metal substrate exhibiting certain nanoscale roughness experiences intensified local electromagnetic fields. Given that Raman scattering intensity is proportional to the square of the electric field strength experienced by molecules, the enhanced local electromagnetic fields significantly raise the probability of molecules adsorbed on the surface undergoing Raman scattering. Ultimately, this greatly augments the Raman signal intensity of surface-adsorbed molecules[64]. Currently, the Surface Plasmon Resonance (SPR) is the primary widely accepted theory to explain the enhancement: on metal surfaces with specific nanostructures, electrons collectively oscillate when subjected to incident laser radiation, giving rise to surface plasmon resonance (SPR) at certain frequencies. The excitation energy of SPR substantially augments the local optical field on the metal surface, significantly enhancing the Raman signals of probe molecules residing within. Thus, the presence of nanoscale roughness on metal surfaces is a prerequisite for SERS enhancement. However, the electric field intensity generated by SPR diminishes exponentially as the distance from the surface increases, operating within a range of a few nanometers, thus constituting a long-range effect. Nevertheless, not all metals can generate surface plasmon resonance under visible laser excitation. Metals like noble metals (Au, Ag, and Cu) and alkali metals with free electrons are prominent examples of those capable of exhibiting surface plasmon resonance.

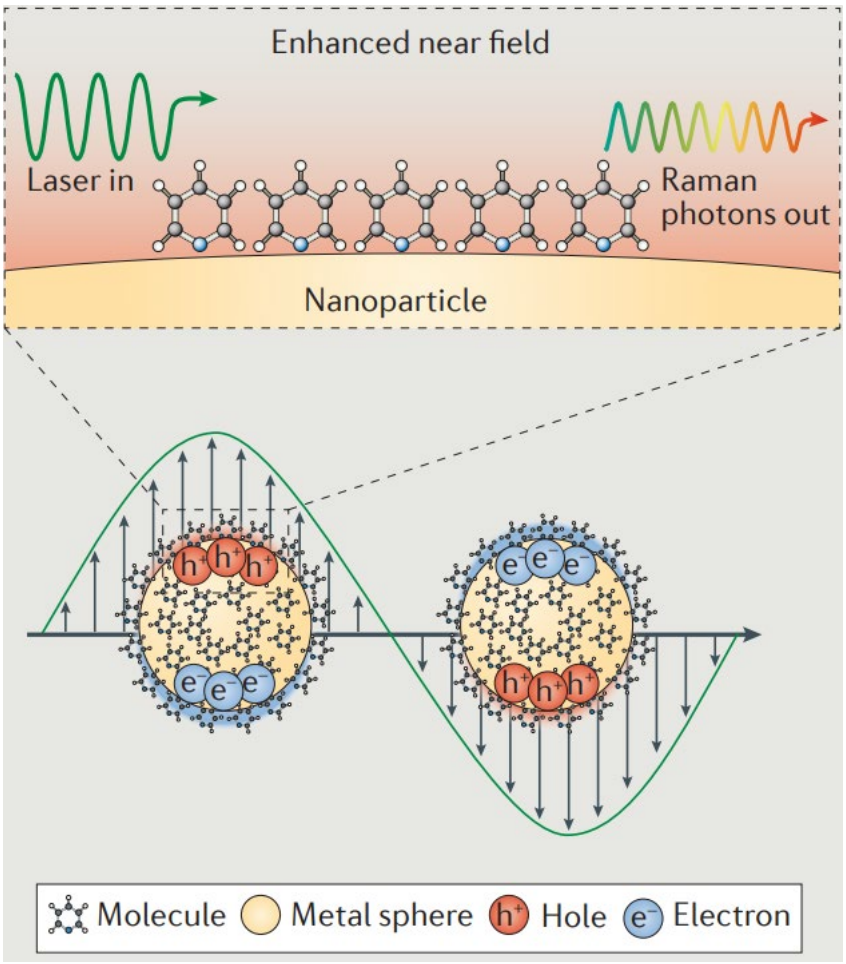

Figure 2.3. The illustration of Surface Plasmon Resonance enhanced near-field process Adapted with permission by Springer Nature from "Nanostructure-based plasmon-enhanced Raman spectroscopy for surface analysis of materials"[63]

On the other hand, while EM has gained wide consensus and has been employed in the analysis of SERS spectra, there remain numerous experimental phenomena that require additional explanation other than EM, leading to the emergence of the charge transfer (CT) enhancement mechanism[65–67]. The charge transfer enhancement mechanism can be understood as a type of resonance-enhanced process[55]. In response to incident light, charge transfer between metals and molecules can occur when the photon's energy matches the energy required for charge transfer. Under these conditions, charge transfer resonance emerges, resulting in substantial enhancement of the molecules' polarizability and, consequently, signal intensity. This process requires the presence of strong chemical interactions between adsorbed molecules and metal surfaces, leading to the formation of surface compounds. Charge transfer enhances only on molecules directly interacting with metals, making it a short-range effect that lacks the long-

range characteristic of electromagnetic field enhancement[68]. Charge transfer is generally classified as either metal-to-molecule charge transfer or molecule-to-metal charge transfer.

2.2.4. The development of “borrowing” method and SHINERS

Due to the fact that only a few metals, such as Au, Ag, and Cu, possess highly effective SERS activity on their rough surfaces, efforts have been directed towards extending SERS to surfaces of other materials by proposing a concept of "borrowing” SERS activity through Au or Ag nanostructures" (termed "borrowing"). This approach aims to enhance the universality of SERS substrates.

Specific nanostructures, under the influence of excitation light at appropriate wavelengths, can generate localized surface plasmon resonance (LSPR), which effectively amplifies the optical field at certain specific regions within the nanostructure. Given the long-range nature of the optical field, its strength exponentially attenuates with increasing distance from the surface. Consequently, even molecules not in direct contact with the nanostructure surface can experience the influence of the optical field, thereby resulting in enhanced Raman signals. The "borrowing" concept was first introduced by Van Duyne et al. in 1983. They successfully obtained SERS signals from molecules adsorbed on the surface of non-SERS active semiconductor n-GaAs by electrochemically depositing silver nanoscale islands[69–71]. This method capitalizes on the far-reaching effects of the intense electromagnetic field generated by high SERS-active Ag islands to enhance SERS signals from species adsorbed on the semiconductor surface nearby. However, the success of this method is under a crucial condition: during the study of surface species adsorption, it is imperative for these species to selectively adsorb only on non-SERS active substrates, avoiding adsorption onto highly SERS active Ag islands. Otherwise, the SERS signals from species adsorbed on Ag islands would greatly surpass those from the semiconductor, leading to erroneous results. In practice, most molecules tend to adsorb on highly SERS-active Ag islands.

Starting from 1987, Fleischmann and Weaver's groups independently deposited ultra-thin layers of weak or non-SERS active materials onto highly SERS-active Ag[72,73], and Au[74–76] substrates, respectively. Leveraging the substantial electromagnetic field enhancement generated

by the underlying high SERS-active Ag or Au, this technique even influences molecules not directly in contact with the SERS-active substrate, resulting in enhanced Raman signals. However, it's noteworthy that electromagnetic field intensity significantly diminishes as the distance from the Ag or Au surface increases, necessitating ultra-thin transition metal films, usually a few atomic layers thick, to be deposited onto Ag or Au surfaces. The challenge, at the time, lay in depositing complete ultra-thin metal layers on irregular substrates, avoiding the occurrence of "pinholes." Furthermore, this approach inherently entails material-specific deposition conditions, rendering its success limited to only a few metal surfaces, which hinders the SERS applications in other fields.

In recent years, bicomponent core-shell nanoparticles have gained increasing popularity in SERS applications. Notably, the most widespread application involves core-shell nanoparticles with highly SERS-active Au nanoparticles as cores. These nanoparticles can be divided into two categories based on the shell materials used for encapsulation: one class involves chemically active shell materials such as Pt, Pd, Rh, Ru, and other transition metals; the other class includes chemically inert shell materials such as SiO_2, Al_2O_3, etc.

For core-shell nanoparticles with chemically inert shell materials, while thick shells typically range from 20 to 50 nm and are commonly used as carriers for SERS labels in biological studies[77–79]., ultra-thin shells range from 1-2 nm to 3-5 nm were firstly systematically studied by Jianfeng Li et al. in 2010, named as SHINERS[80], and gradually they are widely used in electrochemical interfaces and due to its wide applicability. There are several advantages of utilizing the ultrathin shell of core-shell nanoparticles. First, the ultrathin shells without pinholes separate the cores from the material surface (and the environment), thus ensuring that no molecular contact between the core and the environment. Second, the chemically inert SiO_2 or Al_2O_3 shell effectively avoids interparticle and particle–metal substrate fusion under laser excitation or other sample treatments, which significantly improves the stability of the nanoparticles and the probe structures. Third, the shell thickness controlled by the synthesis can be used to control the spacing nanogap between the core particles and the substrates and consequently enables different degrees of the particle–substrate electromagnetic coupling[80,81].

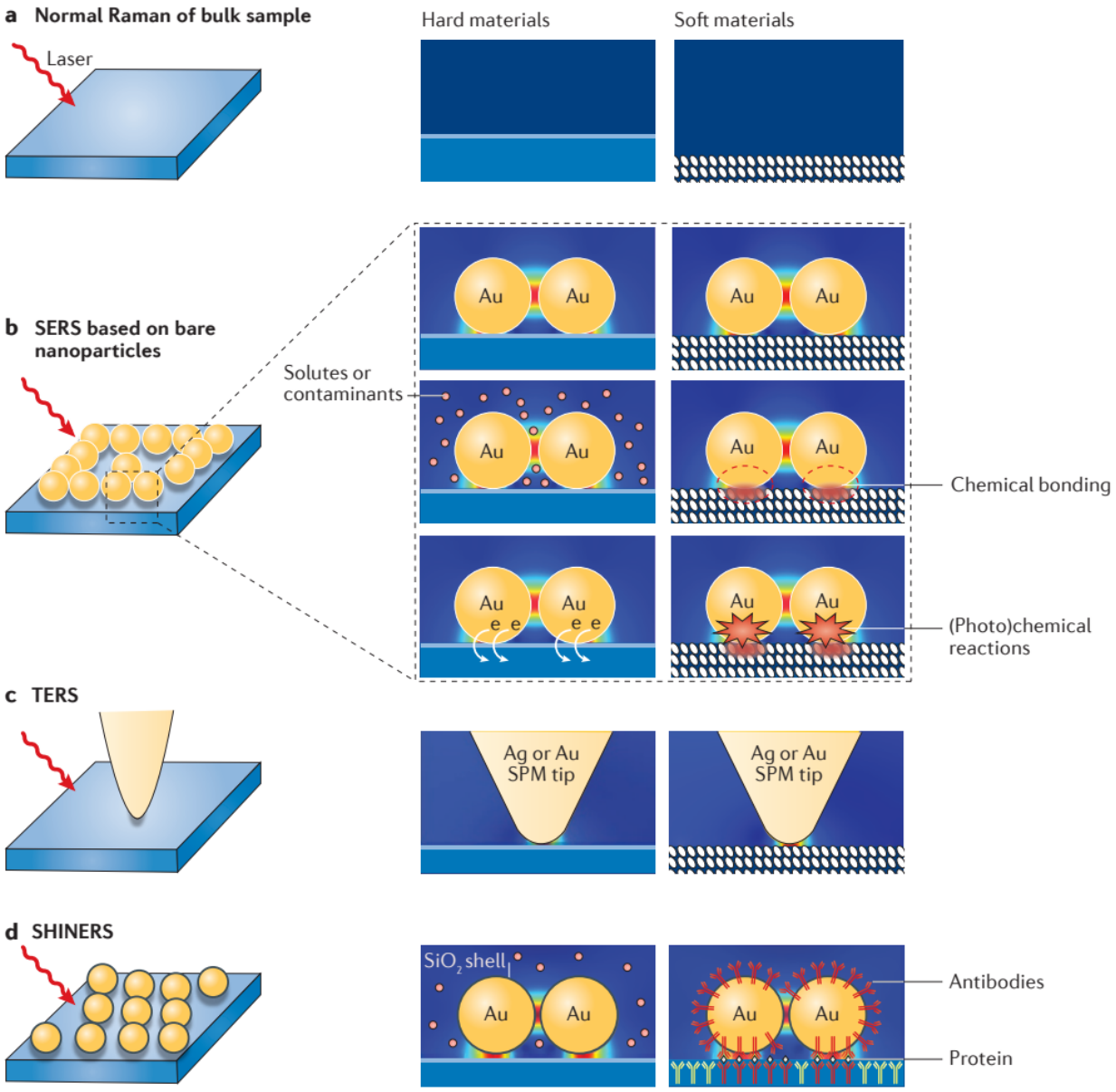

Figure 2.4. Different measurement modes of Raman and PERS on hard and soft materials. (a) Raman measurements on bulk samples comprise signals mainly from the bulk. (b)Surface-enhanced Raman spectroscopy (SERS) measurements. (c)Tip-enhanced Raman spectroscopy (TERS) measurements of hard and soft materials. (d) Shell-isolated nanoparticle-enhanced Raman spectroscopy (SHINERS) measurements of solid/liquid interfaces.
Adapted with permission by Springer Nature from "Nanostructure-based plasmon-enhanced Raman spectroscopy for surface analysis of materials"[63]

SHINERS show great advantages over conventional SERS in many electrochemical fundamental mechanistic studies, especially on the single crystals systems[44,82–84], which require

the atomic level smooth surface which is against the concept of the roughening surface by conventional SERS. Besides, it is also widely applied to studies on various reactions we mentioned, including HER[80,85], ORR[84,86], CO/CO2 reduction[87–90], CO oxidation[91,92], OER[93], and NRR[94]. In the thesis, we choose methods of SERS or SHINERS in measurements for different purposes. For systems conducted on non-Au and smooth surfaces, we tend to use SHINERS to gain enhancement; for the system requires simplicity and without further perturbations, we prefer conventional SERS. The preparation of the SERS or SHINERS substrates is discussed in Chapter 3.

2.3. Basics of VSFGS

In this thesis, besides the SERS and SHINERS, the VSFGS is also utilized as a supplementary experimental spectroscopic tool to investigate the interfacial processes. Thus, the background on VSFGS is also introduced.

Vibrational sum frequency generation (VSFG) spectroscopy is built upon the foundation of non-linear optical processes, offering a unique approach to probing molecular structures and behaviors at interfaces[95]. Unlike linear spectroscopic methods that involve the absorption or emission of photons, non-linear optical processes occur when two or more photons interact simultaneously with a material, resulting in the generation of new frequencies that are the sum or difference of the original photons[96]. $\omega_{SFG} = \omega_{IR} + \omega_{VIS}$

The advantage of this higher frequency detection is that it allows background-free detection with even single photons to be detected in principle. This can be understood through its two-step process: resonant vibrational excitation followed by Raman scattering. The process begins with the absorption of an infrared (IR) photon, which excites a vibrational transition within a molecule absorbed at the interface. This transition imparts vibrational coherence to the molecule, setting it into motion. Subsequently, a visible or near-infrared (NIR) photon interacts with the molecule, inducing Raman scattering. The two photons' energies combine to generate a sum-frequency photon, which is detected as the VSFG signal. In practice, a tunable IR beam with different frequencies can be applied and the visible beam is usually fixed to overlap spatially and temporally to generate the SFG signal.

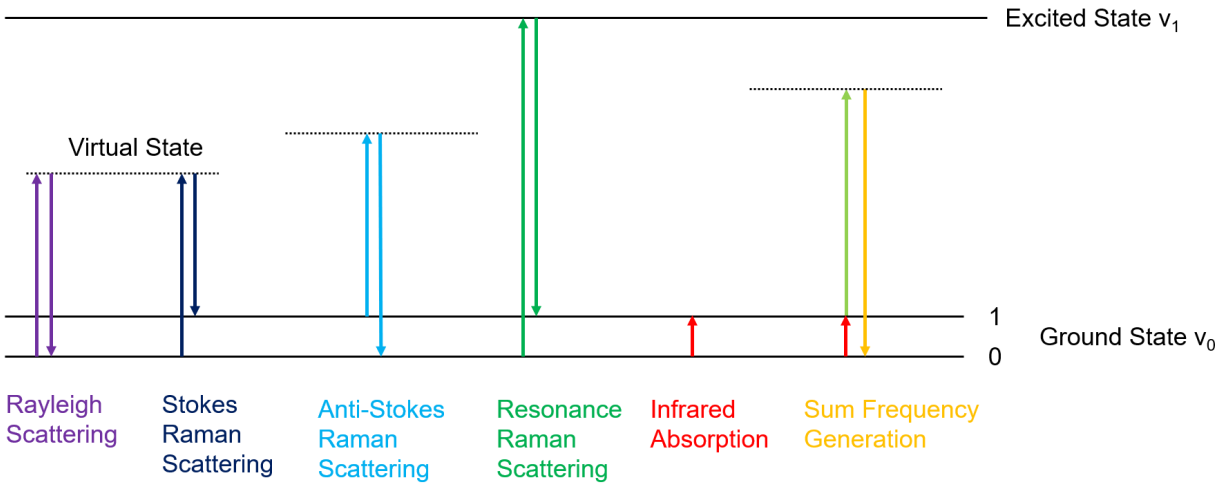

Figure 2.5. Comparison between the techniques of vibrational spectroscopy

Raman scattering (Stokes-dark blue, anti-Stokes- light blue, resonance Raman-green), infrared absorption (red), and vibrational sum-frequency generation (orange).

Importantly, the SFG process requires that the vibrational transition is both IR and Raman active and is particularly powerful for investigating interfacial phenomena due to its inherent surface specificity. SFG is a second-order nonlinear process, which lies in the concept of inversion symmetry breaking at the interface between centrosymmetric materials. In centrosymmetric media, the inversion symmetry ensures that even-order non-linear processes, such as second harmonic generation (SHG), are forbidden. However, when two such media are brought into contact, as is the case at an interface, the symmetry is disrupted, and the non-linear process becomes allowed. In summary, the SFG photons can be only generated at the interfaces between two centrosymmetric media. This is the attribute of the surface specificity of VSFG spectroscopy.

The VSFG analysis involves resonant and non-resonant contributions in the total signal. The intensity of the resonant contribution is directly related to the resonant polarization of the probed molecules at the interface and from the oscillating electric dipole of the vibrational modes. A non-resonant (NR) signal also emerges, often from the collective response of surface electrons to the intense laser fields. This NR signal can mask or interfere with the resonant signal, leading to complex spectra that require deconvolution for accurate interpretation. Since

SFG is a second-order process, its intensity can be expressed as a relationship to the cond-order nonlinear susceptibility of the sample, which can be modeled by a Lorentzian model for an adsorbate[97]:

$$ISFG \propto \left|\chi^{(2)}\right|^2 = \left|A_{NR}e^{i\phi} + \sum_n \frac{A_n}{\omega_{IR} - \omega_n + i\Gamma_n}\right|^2$$

In the previous equation, A_n, ω_n, and Γ_n represent the amplitude, frequency, and line width (half-width at half maximum, HWHM) of the resonant nth vibrational mode of the adsorbate, whereas A_{NR} and ϕ represent the amplitude and phase of any non-resonant susceptibility. Furthermore, the amplitude of the resonant nth vibrational mode A_n is related to the hyperpolarizability tensor of the molecule, which in turn also depends on the orientation of the molecule at the interface, thus the comparison of the SFG intensities with different polarization combinations of the IR, visible, and SFG beams enable to obtain orientational information.

In practice, under the proper experimental design, the VSFGS can obtain the sub-monolayer molecular information at the interfaces. Moreover, the advantage of the VSFGS is that it avoids surface roughening or putting additional nanoparticles on the surface used in the surface-enhanced spectroscopies. Thus, it can be applied to a wider range of electrode materials.

2.4. References

(1) Ge, A.; Rudshteyn, B.; Videla, P. E.; Miller, C. J.; Kubiak, C. P.; Batista, V. S.; Lian, T. Heterogenized Molecular Catalysts: Vibrational Sum-Frequency Spectroscopic, Electrochemical, and Theoretical Investigations. *Acc. Chem. Res.* **2019**, *52* (5), 1289–1300. https://doi.org/10.1021/acs.accounts.9b00001.

(2) Ardo, S.; Sun, Y.; Staniszewski, A.; Castellano, F. N.; Meyer, G. J. Stark Effects after Excited-State Interfacial Electron Transfer at Sensitized TiO_2 Nanocrystallites. *J. Am. Chem. Soc.* **2010**, *132* (19), 6696–6709. https://doi.org/10.1021/ja909781g.

(3) Murgida, D. H.; Hildebrandt, P. Electron-Transfer Processes of Cytochrome *c* at Interfaces. New Insights by Surface-Enhanced Resonance Raman Spectroscopy. *Acc. Chem. Res.* **2004**, *37* (11), 854–861. https://doi.org/10.1021/ar0400443.

(4) Yu, J.; Yin, J.; Li, R.; Ma, Y.; Fan, Z. Interfacial Electric Field Effect on Electrochemical Carbon Dioxide Reduction Reaction. *Chem Catal.* **2022**, *2* (9), 2229–2252. https://doi.org/10.1016/j.checat.2022.07.024.

(5) *Electrochemical Methods: Fundamentals and Applications, 2nd Edition | Wiley*. https://www.wiley.com/en-us/Electrochemical+Methods:+Fundamentals+and+Applications,+2nd+Edition-p-9780471043720 (accessed 2023-06-19).

(6) Bishop, D. M. The Vibrational Stark Effect. *J. Chem. Phys.* **1993**, *98* (4), 3179–3184. https://doi.org/10.1063/1.464090.

(7) Sarkar, S.; Patrow, J. G.; Voegtle, M. J.; Pennathur, A. K.; Dawlaty, J. M. Electrodes as Polarizing Functional Groups: Correlation between Hammett Parameters and Electrochemical Polarization. *J. Phys. Chem. C* **2019**, *123* (8), 4926–4937. https://doi.org/10.1021/acs.jpcc.8b12058.

(8) Bhattacharyya, D.; Videla, P. E.; Palasz, J. M.; Tangen, I.; Meng, J.; Kubiak, C. P.; Batista, V. S.; Lian, T. Sub-Nanometer Mapping of the Interfacial Electric Field Profile Using a Vibrational Stark Shift Ruler. *J. Am. Chem. Soc.* **2022**, *144* (31), 14330–14338. https://doi.org/10.1021/jacs.2c05563.

(9) Wright, D.; Sangtarash, S.; Mueller, N. S.; Lin, Q.; Sadeghi, H.; Baumberg, J. J. Vibrational Stark Effects: Ionic Influence on Local Fields. *J. Phys. Chem. Lett.* **2022**, *13* (22), 4905–4911. https://doi.org/10.1021/acs.jpclett.2c01048.

(10) Lambert, A. G.; Davies, P. B.; Neivandt, D. J. Implementing the Theory of Sum Frequency Generation Vibrational Spectroscopy: A Tutorial Review. *Appl. Spectrosc. Rev.* **2005**, *40* (2), 103–145. https://doi.org/10.1081/ASR-200038326.

(11) Shen, Y. R. Surface Properties Probed by Second-Harmonic and Sum-Frequency Generation. *Nature* **1989**, *337* (6207), 519–525. https://doi.org/10.1038/337519a0.

(12) Birdja, Y. Y.; Pérez-Gallent, E.; Figueiredo, M. C.; Göttle, A. J.; Calle-Vallejo, F.; Koper, M. T. M. Advances and Challenges in Understanding the Electrocatalytic Conversion of Carbon Dioxide to Fuels. *Nat. Energy* **2019**, *4* (9), 732–745. https://doi.org/10.1038/s41560-019-0450-y.

(13) Nitopi, S.; Bertheussen, E.; Scott, S. B.; Liu, X.; Engstfeld, A. K.; Horch, S.; Seger, B.; Stephens, I. E. L.; Chan, K.; Hahn, C.; Nørskov, J. K.; Jaramillo, T. F.; Chorkendorff, I. Progress and Perspectives of Electrochemical CO_2 Reduction on Copper in Aqueous Electrolyte. *Chem. Rev.* **2019**, *119* (12), 7610–7672. https://doi.org/10.1021/acs.chemrev.8b00705.

(14) Hori, Y.; Kikuchi, K.; Suzuki, S. PRODUCTION OF CO AND CH_4 IN ELECTROCHEMICAL REDUCTION OF CO_2 AT METAL ELECTRODES IN AQUEOUS HYDROGENCARBONATE SOLUTION. *Chem. Lett.* **1985**, *14* (11), 1695–1698. https://doi.org/10.1246/cl.1985.1695.
(15) Hori, Y.; Wakebe, H.; Tsukamoto, T.; Koga, O. Electrocatalytic Process of CO Selectivity in Electrochemical Reduction of CO2 at Metal Electrodes in Aqueous Media. *Electrochimica Acta* **1994**, *39* (11–12), 1833–1839. https://doi.org/10.1016/0013-4686(94)85172-7.
(16) Hori, Y. Electrochemical CO2 Reduction on Metal Electrodes. In *Modern Aspects of Electrochemistry*; Vayenas, C. G., White, R. E., Gamboa-Aldeco, M. E., Eds.; Modern Aspects of Electrochemistry; Springer New York: New York, NY, 2008; Vol. 42, pp 89–189. https://doi.org/10.1007/978-0-387-49489-0_3.
(17) Bagger, A.; Ju, W.; Varela, A. S.; Strasser, P.; Rossmeisl, J. Electrochemical CO_2 Reduction: A Classification Problem. *ChemPhysChem* **2017**, *18* (22), 3266–3273. https://doi.org/10.1002/cphc.201700736.
(18) Heidary, N.; Ly, K. H.; Kornienko, N. Probing CO_2 Conversion Chemistry on Nanostructured Surfaces with Operando Vibrational Spectroscopy. *Nano Lett.* **2019**, *19* (8), 4817–4826. https://doi.org/10.1021/acs.nanolett.9b01582.
(19) Favaro, M.; Xiao, H.; Cheng, T.; Goddard, W. A.; Yano, J.; Crumlin, E. J. Subsurface Oxide Plays a Critical Role in CO_2 Activation by Cu(111) Surfaces to Form Chemisorbed CO_2, the First Step in Reduction of CO_2. *Proc. Natl. Acad. Sci.* **2017**, 201701405. https://doi.org/10.1073/pnas.1701405114.
(20) Xiao, H.; Goddard, W. A.; Cheng, T.; Liu, Y. Cu Metal Embedded in Oxidized Matrix Catalyst to Promote CO_2 Activation and CO Dimerization for Electrochemical Reduction of CO_2. *Proc. Natl. Acad. Sci.* **2017**, 201702405. https://doi.org/10.1073/pnas.1702405114.
(21) Chernyshova, I. V.; Somasundaran, P.; Ponnurangam, S. On the Origin of the Elusive First Intermediate of CO_2 Electroreduction. *Proc. Natl. Acad. Sci.* **2018**, 201802256. https://doi.org/10.1073/pnas.1802256115.
(22) He, M.; Li, C.; Zhang, H.; Chang, X.; Chen, J. G.; Goddard, W. A.; Cheng, M.; Xu, B.; Lu, Q. Oxygen Induced Promotion of Electrochemical Reduction of CO2 via Co-Electrolysis. *Nat. Commun.* **2020**, *11* (1). https://doi.org/10.1038/s41467-020-17690-8.
(23) Pérez-Gallent, E.; Figueiredo, M. C.; Calle-Vallejo, F.; Koper, M. T. M. Spectroscopic Observation of a Hydrogenated CO Dimer Intermediate During CO Reduction on Cu(100) Electrodes. *Angew. Chem.* **2017**, *129* (13), 3675–3678. https://doi.org/10.1002/ange.201700580.
(24) Pérez-Gallent, E.; Marcandalli, G.; Figueiredo, M. C.; Calle-Vallejo, F.; Koper, M. T. M. Structure- and Potential-Dependent Cation Effects on CO Reduction at Copper Single-Crystal Electrodes. *J. Am. Chem. Soc.* **2017**, *139* (45), 16412–16419. https://doi.org/10.1021/jacs.7b10142.
(25) Li, J.; Chang, X.; Zhang, H.; Malkani, A. S.; Cheng, M.; Xu, B.; Lu, Q. Electrokinetic and in Situ Spectroscopic Investigations of CO Electrochemical Reduction on Copper. *Nat. Commun.* **2021**, *12* (1), 3264. https://doi.org/10.1038/s41467-021-23582-2.
(26) Zhao, Y.; Chang, X.; Malkani, A. S.; Yang, X.; Thompson, L.; Jiao, F.; Xu, B. Speciation of Cu Surfaces During the Electrochemical CO Reduction Reaction. *J. Am. Chem. Soc.* **2020**. https://doi.org/10.1021/jacs.0c02354.
(27) Li, J.; Li, X.; Gunathunge, C. M.; Waegele, M. M. Hydrogen Bonding Steers the Product Selectivity of Electrocatalytic CO Reduction. *Proc. Natl. Acad. Sci.* **2019**, *116* (19), 9220–9229. https://doi.org/10.1073/pnas.1900761116.

(28) Malkani, A. S.; Li, J.; Oliveira, N. J.; He, M.; Chang, X.; Xu, B.; Lu, Q. Understanding the Electric and Nonelectric Field Components of the Cation Effect on the Electrochemical CO Reduction Reaction. *Sci. Adv.* **2020**, *6* (45), eabd2569. https://doi.org/10.1126/sciadv.abd2569.
(29) Chang, X.; Zhao, Y.; Xu, B. pH Dependence of Cu Surface Speciation in the Electrochemical CO Reduction Reaction. *ACS Catal.* **2020**, *10* (23), 13737–13747. https://doi.org/10.1021/acscatal.0c03108.
(30) Gunathunge, C. M.; Ovalle, V. J.; li, yawei; Janik, M. J.; Waegele, M. M. Existence of an Electrochemically Inert CO Population on Cu Electrodes in Alkaline pH. *ACS Catal.* **2018**. https://doi.org/10.1021/acscatal.8b01552.
(31) Iijima, G.; Inomata, T.; Yamaguchi, H.; Ito, M.; Masuda, H. Role of a Hydroxide Layer on Cu Electrodes in Electrochemical CO $_2$ Reduction. *ACS Catal.* **2019**, *9* (7), 6305–6319. https://doi.org/10.1021/acscatal.9b00896.
(32) Feaster, J. T.; Shi, C.; Cave, E. R.; Hatsukade, T.; Abram, D. N.; Kuhl, K. P.; Hahn, C.; Nørskov, J. K.; Jaramillo, T. F. Understanding Selectivity for the Electrochemical Reduction of Carbon Dioxide to Formic Acid and Carbon Monoxide on Metal Electrodes. *ACS Catal.* **2017**, *7* (7), 4822–4827. https://doi.org/10.1021/acscatal.7b00687.
(33) Durand, W. J.; Peterson, A. A.; Studt, F.; Abild-Pedersen, F.; Nørskov, J. K. Structure Effects on the Energetics of the Electrochemical Reduction of CO2 by Copper Surfaces. *Surf. Sci.* **2011**, *605* (15–16), 1354–1359. https://doi.org/10.1016/j.susc.2011.04.028.
(34) Cheng, T.; Xiao, H.; Goddard, W. A. Reaction Mechanisms for the Electrochemical Reduction of CO $_2$ to CO and Formate on the Cu(100) Surface at 298 K from Quantum Mechanics Free Energy Calculations with Explicit Water. *J. Am. Chem. Soc.* **2016**, *138* (42), 13802–13805. https://doi.org/10.1021/jacs.6b08534.
(35) Jiang, S.; Klingan, K.; Pasquini, C.; Dau, H. New Aspects of Operando Raman Spectroscopy Applied to Electrochemical CO $_2$ Reduction on Cu Foams. *J. Chem. Phys.* **2019**, *150* (4), 041718. https://doi.org/10.1063/1.5054109.
(36) Katayama, Y.; Nattino, F.; Giordano, L.; Hwang, J.; Rao, R. R.; Andreussi, O.; Marzari, N.; Shao-Horn, Y. An *In Situ* Surface-Enhanced Infrared Absorption Spectroscopy Study of Electrochemical CO $_2$ Reduction: Selectivity Dependence on Surface C-Bound and O-Bound Reaction Intermediates. *J. Phys. Chem. C* **2019**. https://doi.org/10.1021/acs.jpcc.8b09598.
(37) Zhu, S.; Jiang, B.; Cai, W.-B.; Shao, M. Direct Observation on Reaction Intermediates and the Role of Bicarbonate Anions in CO $_2$ Electrochemical Reduction Reaction on Cu Surfaces. *J. Am. Chem. Soc.* **2017**, *139* (44), 15664–15667. https://doi.org/10.1021/jacs.7b10462.
(38) Heyes, J.; Dunwell, M.; Xu, B. CO $_2$ Reduction on Cu at Low Overpotentials with Surface-Enhanced in Situ Spectroscopy. *J. Phys. Chem. C* **2016**, *120* (31), 17334–17341. https://doi.org/10.1021/acs.jpcc.6b03065.
(39) Moradzaman, M.; Mul, G. In Situ Raman Study of Potential-Dependent Surface Adsorbed Carbonate, CO, OH, and C Species on Cu Electrodes During Electrochemical Reduction of CO2. *ChemElectroChem* **2021**, *8* (8), 1478–1485. https://doi.org/10.1002/celc.202001598.
(40) Li, J.; Wu, D.; Malkani, A. S.; Chang, X.; Cheng, M.; Xu, B.; Lu, Q. Hydroxide Is Not a Promoter of C $_{2+}$ Product Formation in the Electrochemical Reduction of CO on Copper. *Angew. Chem. Int. Ed.* **2020**, *59* (11), 4464–4469. https://doi.org/10.1002/anie.201912412.
(41) Dunwell, M.; Yang, X.; Setzler, B. P.; Anibal, J.; Yan, Y.; Xu, B. Examination of Near-Electrode Concentration Gradients and Kinetic Impacts on the Electrochemical Reduction of CO

$_2$ Using Surface-Enhanced Infrared Spectroscopy. *ACS Catal.* **2018**, 3999–4008. https://doi.org/10.1021/acscatal.8b01032.
(42) Dunwell, M.; Lu, Q.; Heyes, J. M.; Rosen, J.; Chen, J. G.; Yan, Y.; Jiao, F.; Xu, B. The Central Role of Bicarbonate in the Electrochemical Reduction of Carbon Dioxide on Gold. *J. Am. Chem. Soc.* **2017**, *139* (10), 3774–3783. https://doi.org/10.1021/jacs.6b13287.
(43) Wuttig, A.; Ryu, J.; Surendranath, Y. Electrolyte Competition Controls Surface Binding of CO Intermediates to CO $_2$ Reduction Catalysts. *J. Phys. Chem. C* **2021**, *125* (31), 17042–17050. https://doi.org/10.1021/acs.jpcc.1c04337.
(44) Bodappa, N.; Su, M.; Zhao, Y.; Le, J.-B.; Yang, W.-M.; Radjenovic, P.; Dong, J.-C.; Cheng, J.; Tian, Z.-Q.; Li, J.-F. Early Stages of Electrochemical Oxidation of Cu(111) and Polycrystalline Cu Surfaces Revealed by *in Situ* Raman Spectroscopy. *J. Am. Chem. Soc.* **2019**, *141* (31), 12192–12196. https://doi.org/10.1021/jacs.9b04638.
(45) Raman, C. V.; Krishnan, K. S. A New Type of Secondary Radiation. *Nature* **1928**, *121* (3048), 501–502. https://doi.org/10.1038/121501c0.
(46) *The discovery of combinational scattering of light (the Raman effect) - IOPscience*. https://iopscience-iop-org.proxy.library.emory.edu/article/10.1070/PU1978v021n09ABEH005682 (accessed 2023-08-25).
(47) FLEISCHMANN, M.; HENDRA, P. J.; McQUILLAN, A. J. RAMAN SPECTRA OF PYRIDZNE ADSORBED AT A SILVER ELECTRODE. *Chem. Phys. Lett. 26* (2), 4.
(48) Jeanmaire, D. L.; Van Duyne, R. P. Surface Raman Spectroelectrochemistry: Part I. Heterocyclic, Aromatic, and Aliphatic Amines Adsorbed on the Anodized Silver Electrode. *J. Electroanal. Chem. Interfacial Electrochem.* **1977**, *84* (1), 1–20. https://doi.org/10.1016/S0022-0728(77)80224-6.
(49) Albrecht, M. G.; Creighton, J. A. Anomalously Intense Raman Spectra of Pyridine at a Silver Electrode. *J. Am. Chem. Soc.* **1977**, *99* (15), 5215–5217. https://doi.org/10.1021/ja00457a071.
(50) Tian, Z.-Q.; Ren, B.; Wu, D.-Y. Surface-Enhanced Raman Scattering: From Noble to Transition Metals and from Rough Surfaces to Ordered Nanostructures. *J. Phys. Chem. B* **2002**, *106* (37), 9463–9483. https://doi.org/10.1021/jp0257449.
(51) Campion, A.; Kambhampati, P. Surface-Enhanced Raman Scattering. *Chem. Soc. Rev.* **1998**, *27* (4), 241–250. https://doi.org/10.1039/A827241Z.
(52) Otto, A. Surface Enhanced Raman Scattering. *Vacuum* **1983**, *33* (10), 797–802. https://doi.org/10.1016/0042-207X(83)90613-9.
(53) Kneipp, K.; Wang, Y.; Kneipp, H.; Perelman, L. T.; Itzkan, I.; Dasari, R. R.; Feld, M. S. Single Molecule Detection Using Surface-Enhanced Raman Scattering (SERS). *Phys. Rev. Lett.* **1997**, *78* (9), 1667–1670. https://doi.org/10.1103/PhysRevLett.78.1667.
(54) Qian, Y.; Li, X.; Harutyunyan, A. R.; Chen, G.; Rao, Y.; Chen, H. Herzberg–Teller Effect on the Vibrationally Resolved Absorption Spectra of Single-Crystalline Pentacene at Finite Temperatures. *J. Phys. Chem. A* **2020**, *124* (44), 9156–9165. https://doi.org/10.1021/acs.jpca.0c07896.
(55) Lombardi, J. R.; Birke, R. L. A Unified Approach to Surface-Enhanced Raman Spectroscopy. *J. Phys. Chem. C* **2008**, *112* (14), 5605–5617. https://doi.org/10.1021/jp800167v.
(56) Kundu, S.; Roy, P. P.; Fleming, G. R.; Makri, N. Franck–Condon and Herzberg–Teller Signatures in Molecular Absorption and Emission Spectra. *J. Phys. Chem. B* **2022**, *126* (15), 2899–2911. https://doi.org/10.1021/acs.jpcb.2c00846.

(57) Lipkowski, J.; Stolberg, L.; Yang, D.-F.; Pettinger, B.; Mirwald, S.; Henglein, F.; Kolb, D. M. Molecular Adsorption at Metal Electrodes. *Electrochimica Acta* **1994**, *39* (8), 1045–1056. https://doi.org/10.1016/0013-4686(94)E0019-V.
(58) Tian, Z.-Q.; Ren, B.; Chen, Y.-X.; Zou, S.-Z.; Mao, B.-W. Probing Electrode/Electrolyte Interfacial Structure in the Potential Region of Hydrogen Evolution by Raman Spectroscopy. *J. Chem. Soc. Faraday Trans.* **1996**, *92* (20), 3829–3838. https://doi.org/10.1039/FT9969203829.
(59) Yang, H.; Yang, Y.; Zou, S. Surface-Enhanced Raman Spectroscopic Evidence of Methanol Oxidation on Ruthenium Electrodes. *J. Phys. Chem. B* **2006**, *110* (35), 17296–17301. https://doi.org/10.1021/jp063694s.
(60) Mrozek, M. F.; Luo, H.; Weaver, M. J. Formic Acid Electrooxidation on Platinum-Group Metals: Is Adsorbed Carbon Monoxide Solely a Catalytic Poison? *Langmuir* **2000**, *16* (22), 8463–8469. https://doi.org/10.1021/la000760n.
(61) Williams, C. T.; Takoudis, C. G.; Weaver, M. J. Raman Spectral Evidence of Reactive Oxide Formation during Methanol Oxidation on Polycrystalline Rhodium at High Gas Pressures. *J. Catal.* **1997**, *170* (1), 207–210. https://doi.org/10.1006/jcat.1997.1748.
(62) Wang, X.; Huang, S.-C.; Hu, S.; Yan, S.; Ren, B. Fundamental Understanding and Applications of Plasmon-Enhanced Raman Spectroscopy. *Nat. Rev. Phys.* **2020**, *2* (5), 253–271. https://doi.org/10.1038/s42254-020-0171-y.
(63) Ding, S.-Y.; Yi, J.; Li, J.-F.; Ren, B.; Wu, D.-Y.; Panneerselvam, R.; Tian, Z.-Q. Nanostructure-Based Plasmon-Enhanced Raman Spectroscopy for Surface Analysis of Materials. *Nat. Rev. Mater.* **2016**, *1* (6), 16021. https://doi.org/10.1038/natrevmats.2016.21.
(64) Moskovits, M. Surface-Enhanced Spectroscopy. *Rev. Mod. Phys.* **1985**, *57* (3), 783–826. https://doi.org/10.1103/RevModPhys.57.783.
(65) Burstein, E.; Chen, Y. J.; Chen, C. Y.; Lundquist, S.; Tosatti, E. "Giant" Raman Scattering by Adsorbed Molecules on Metal Surfaces. *Solid State Commun.* **1979**, *29* (8), 567–570. https://doi.org/10.1016/0038-1098(79)90665-3.
(66) Gersten, J. I.; Birke, R. L.; Lombardi, J. R. Theory of Enhance I Light Scattering from Molecules Adsorbed at the Metal-Solution Interface. *Phys. Rev. Lett.* **1979**, *43* (2), 147–150. https://doi.org/10.1103/PhysRevLett.43.147.
(67) Demuth, J. E.; Sanda, P. N. Observation of Charge-Transfer States for Pyridine Chemisorbed on Ag(111). *Phys. Rev. Lett.* **1981**, *47* (1), 57–60. https://doi.org/10.1103/PhysRevLett.47.57.
(68) *Modern Raman Spectroscopy: A Practical Approach, 2nd Edition | Wiley*. Wiley.com. https://www.wiley.com/en-us/Modern+Raman+Spectroscopy%3A+A+Practical+Approach%2C+2nd+Edition-p-9781119440550 (accessed 2023-08-25).
(69) Van Duyne, R. P.; Haushalter, J. P. Surface-Enhanced Raman Spectroscopy of Adsorbates on Semiconductor Electrode Surfaces: Tris(Bipyridine)Ruthenium(II) Adsorbed on Silver-Modified n-Gallium Arsenide(100). *J. Phys. Chem.* **1983**, *87* (16), 2999–3003. https://doi.org/10.1021/j100239a004.
(70) Rubim, J. C.; Kannen, G.; Schumacher, D.; Dünnwald, J.; Otto, A. Raman Spectra of Silver Coated Graphite and Glassy Carbon Electrodes. *Appl. Surf. Sci.* **1989**, *37* (2), 233–243. https://doi.org/10.1016/0169-4332(89)90485-6.
(71) Van Duyne, R. P.; Haushalter, J. P.; Janik-Czachor, M.; Levinger, N. Surface-Enhanced Resonance Raman Spectroscopy of Adsorbates on Semiconductor Electrode Surfaces. 2. In Situ

Studies of Transition Metal (Iron and Ruthenium) Complexes on Silver/Gallium Arsenide and Silver/Silicon. *J. Phys. Chem.* **1985**, *89* (19), 4055–4061. https://doi.org/10.1021/j100265a026.
(72) Fleischmann, M.; Tian, Z. Q.; Li, L. J. Raman Spectroscopy of Adsorbates on Thin Film Electrodes Deposited on Silver Substrates. *J. Electroanal. Chem. Interfacial Electrochem.* **1987**, *217* (2), 397–410. https://doi.org/10.1016/0022-0728(87)80231-0.
(73) Mengoli, G.; Musiani, M. M.; Fleischman, M.; Mao, B.; Tian, Z. Q. Enhanced Raman Scattering from Iron Electrodes. *Electrochimica Acta* **1987**, *32* (8), 1239–1245. https://doi.org/10.1016/0013-4686(87)80042-7.
(74) Tadayyoni, M. A.; Farquharson, S.; Li, T. T. T.; Weaver, M. J. Surface-Enhanced Raman Spectroscopy of Electrochemically Characterized Interfaces. Transition-Metal Isothiocyanate Adsorbates at Silver Electrodes. *J. Phys. Chem.* **1984**, *88* (20), 4701–4706. https://doi.org/10.1021/j150664a052.
(75) Leung, L. W. H.; Weaver, M. J. Extending Surface-Enhanced Raman Spectroscopy to Transition-Metal Surfaces: Carbon Monoxide Adsorption and Electrooxidation on Platinum- and Palladium-Coated Gold Electrodes. *J. Am. Chem. Soc.* **1987**, *109* (17), 5113–5119. https://doi.org/10.1021/ja00251a011.
(76) Leung, L. W. H.; Weaver, M. J. Adsorption and Electrooxidation of Carbon Monoxide on Rhodium- and Ruthenium-Coated Gold Electrodes as Probed by Surface-Enhanced Raman Spectroscopy. *Langmuir* **1988**, *4* (5), 1076–1083. https://doi.org/10.1021/la00083a002.
(77) Mulvaney, S. P.; Musick, M. D.; Keating, C. D.; Natan, M. J. Glass-Coated, Analyte-Tagged Nanoparticles: A New Tagging System Based on Detection with Surface-Enhanced Raman Scattering. *Langmuir* **2003**, *19* (11), 4784–4790. https://doi.org/10.1021/la026706j.
(78) Smith, W. E. Practical Understanding and Use of Surface Enhanced Raman Scattering/Surface Enhanced Resonance Raman Scattering in Chemical and Biological Analysis. *Chem. Soc. Rev.* **2008**, *37* (5), 955–964. https://doi.org/10.1039/B708841H.
(79) Doering, W. E.; Nie, S. Spectroscopic Tags Using Dye-Embedded Nanoparticles and Surface-Enhanced Raman Scattering. *Anal. Chem.* **2003**, *75* (22), 6171–6176. https://doi.org/10.1021/ac034672u.
(80) Li, J. F.; Huang, Y. F.; Ding, Y.; Yang, Z. L.; Li, S. B.; Zhou, X. S.; Fan, F. R.; Zhang, W.; Zhou, Z. Y.; Wu, D. Y.; Ren, B.; Wang, Z. L.; Tian, Z. Q. Shell-Isolated Nanoparticle-Enhanced Raman Spectroscopy. *Nature* **2010**, *464* (7287), 392–395. https://doi.org/10.1038/nature08907.
(81) Graham, D. The Next Generation of Advanced Spectroscopy: Surface Enhanced Raman Scattering from Metal Nanoparticles. *Angew. Chem. Int. Ed.* **2010**, *49* (49), 9325–9327. https://doi.org/10.1002/anie.201002838.
(82) Li, C.-Y.; Dong, J.-C.; Jin, X.; Chen, S.; Panneerselvam, R.; Rudnev, A. V.; Yang, Z.-L.; Li, J.-F.; Wandlowski, T.; Tian, Z.-Q. In Situ Monitoring of Electrooxidation Processes at Gold Single Crystal Surfaces Using Shell-Isolated Nanoparticle-Enhanced Raman Spectroscopy. *J. Am. Chem. Soc.* **2015**, *137* (24), 7648–7651. https://doi.org/10.1021/jacs.5b04670.
(83) Li, C.-Y.; Yu, Y.; Wang, C.; Zhang, Y.; Zheng, S.-Y.; Li, J.-F.; Maglia, F.; Jung, R.; Tian, Z.-Q.; Shao-Horn, Y. Surface Changes of $LiNi_x Mn_y Co_{1-x-y} O_2$ in Li-Ion Batteries Using in Situ Surface-Enhanced Raman Spectroscopy. *J. Phys. Chem. C* **2020**, *124* (7), 4024–4031. https://doi.org/10.1021/acs.jpcc.9b11677.
(84) Dong, J.-C.; Zhang, X.-G.; Briega-Martos, V.; Jin, X.; Yang, J.; Chen, S.; Yang, Z.-L.; Wu, D.-Y.; Feliu, J. M.; Williams, C. T.; Tian, Z.-Q.; Li, J.-F. In Situ Raman Spectroscopic Evidence for Oxygen Reduction Reaction Intermediates at Platinum Single-Crystal Surfaces. *Nat. Energy* **2018**, *4* (1), 60–67. https://doi.org/10.1038/s41560-018-0292-z.

(85) Li, J.-F.; Anema, J. R.; Yu, Y.-C.; Yang, Z.-L.; Huang, Y.-F.; Zhou, X.-S.; Ren, B.; Tian, Z.-Q. Core–Shell Nanoparticle Based SERS from Hydrogen Adsorbed on a Rhodium(111) Electrode. *Chem. Commun.* **2011**, *47* (7), 2023–2025. https://doi.org/10.1039/C0CC04049E.
(86) Galloway, T. A.; Hardwick, L. J. Utilizing in Situ Electrochemical SHINERS for Oxygen Reduction Reaction Studies in Aprotic Electrolytes. *J. Phys. Chem. Lett.* **2016**, *7* (11), 2119–2124. https://doi.org/10.1021/acs.jpclett.6b00730.
(87) Zhao, Y.; Chang, X.; Malkani, A. S.; Yang, X.; Thompson, L.; Jiao, F.; Xu, B. Speciation of Cu Surfaces During the Electrochemical CO Reduction Reaction. *J. Am. Chem. Soc.* **2020**. https://doi.org/10.1021/jacs.0c02354.
(88) Li, J.; Chang, X.; Zhang, H.; Malkani, A. S.; Cheng, M.; Xu, B.; Lu, Q. Electrokinetic and in Situ Spectroscopic Investigations of CO Electrochemical Reduction on Copper. *Nat. Commun.* **2021**, *12* (1), 3264. https://doi.org/10.1038/s41467-021-23582-2.
(89) Zhao, Y.; Zhang, X.-G.; Bodappa, N.; Yang, W.-M.; Liang, Q.; Radjenovica, P. M.; Wang, Y.-H.; Zhang, Y.-J.; Dong, J.-C.; Tian, Z.-Q.; Li, J.-F. Elucidating Electrochemical CO_2 Reduction Reaction Processes on Cu(*Hkl*) Single-Crystal Surfaces by *in Situ* Raman Spectroscopy. *Energy Environ. Sci.* **2022**, *15* (9), 3968–3977. https://doi.org/10.1039/D2EE01334G.
(90) Shao, F.; Wong, J. K.; Low, Q. H.; Iannuzzi, M.; Li, J.; Lan, J. In Situ Spectroelectrochemical Probing of CO Redox Landscape on Copper Single-Crystal Surfaces. *Proc. Natl. Acad. Sci.* **2022**, *119* (29), e2118166119. https://doi.org/10.1073/pnas.2118166119.
(91) Liang, M.-M.; Wang, Y.-H.; Shao, R.; Yang, W.-M.; Zhang, H.; Zhang, H.; Yang, Z.-L.; Li, J.-F.; Tian, Z.-Q. In Situ Electrochemical Surface-Enhanced Raman Spectroscopy Study of CO Electrooxidation on PtFe Nanocatalysts. *Electrochem. Commun.* **2017**, *81*, 38–42. https://doi.org/10.1016/j.elecom.2017.05.022.
(92) Su, M.; Dong, J.-C.; Le, J.-B.; Zhao, Y.; Yang, W.-M.; Yang, Z.-L.; Attard, G.; Liu, G.-K.; Cheng, J.; Wei, Y.-M.; Tian, Z.-Q.; Li, J.-F. In Situ Raman Study of CO Electrooxidation on Pt(Hkl) Single-Crystal Surfaces in Acidic Solution. *Angew. Chem. Int. Ed.* **2020**, *59* (52), 23554–23558. https://doi.org/10.1002/anie.202010431.
(93) Saeed, K. H.; Forster, M.; Li, J.-F.; Hardwick, L. J.; Cowan, A. J. Water Oxidation Intermediates on Iridium Oxide Electrodes Probed by in Situ Electrochemical SHINERS. *Chem. Commun.* **2020**, *56* (7), 1129–1132. https://doi.org/10.1039/C9CC08284K.
(94) Butcher, D. P.; Gewirth, A. A. Nitrate Reduction Pathways on Cu Single Crystal Surfaces: Effect of Oxide and Cl−. *Nano Energy* **2016**, *29*, 457–465. https://doi.org/10.1016/j.nanoen.2016.06.024.
(95) Arnolds, H.; Bonn, M. Ultrafast Surface Vibrational Dynamics. *Surf. Sci. Rep.* **2010**, *65* (2), 45–66. https://doi.org/10.1016/j.surfrep.2009.12.001.
(96) Nihonyanagi, S.; Mondal, J. A.; Yamaguchi, S.; Tahara, T. Structure and Dynamics of Interfacial Water Studied by Heterodyne-Detected Vibrational Sum-Frequency Generation. *Annu. Rev. Phys. Chem.* **2013**, *64* (1), 579–603. https://doi.org/10.1146/annurev-physchem-040412-110138.
(97) Zhuang, X.; Miranda, P. B.; Kim, D.; Shen, Y. R. Mapping Molecular Orientation and Conformation at Interfaces by Surface Nonlinear Optics. *Phys. Rev. B* **1999**, *59* (19), 12632–12640. https://doi.org/10.1103/PhysRevB.59.12632.

3. Chapter 3 Methodology

3.1. Spectroscopic setups

3.1.1. Raman setup and signal processing

A home-built Raman system (shown in ***Figure 3.1***) is utilized for all Raman measurements. The system includes a polarized 632.8 nm He-Ne laser source, corresponding needed optics, and Raman signal was collected by a spectrograph (Shamrock, Andor) and further detected by an electron-multiplied charge coupled device (Newton EMCCD, Andor). The HeNe laser source was from Thorlabs (HNL210LB); a 10X microscope objective (10X Olympus Plan Achromat Objective, 0.25 NA, 10.6 mm WD, from Thorlabs, RMS10X) and a 50X objective (50X Objective, 0.55 NA, 13 mm WD, from Newport, MLWD-50X) were separately used during spectra acquisition. Xe light was used for calibration from 100 to 4000 cm^{-1} spectral window before experimental measurements.

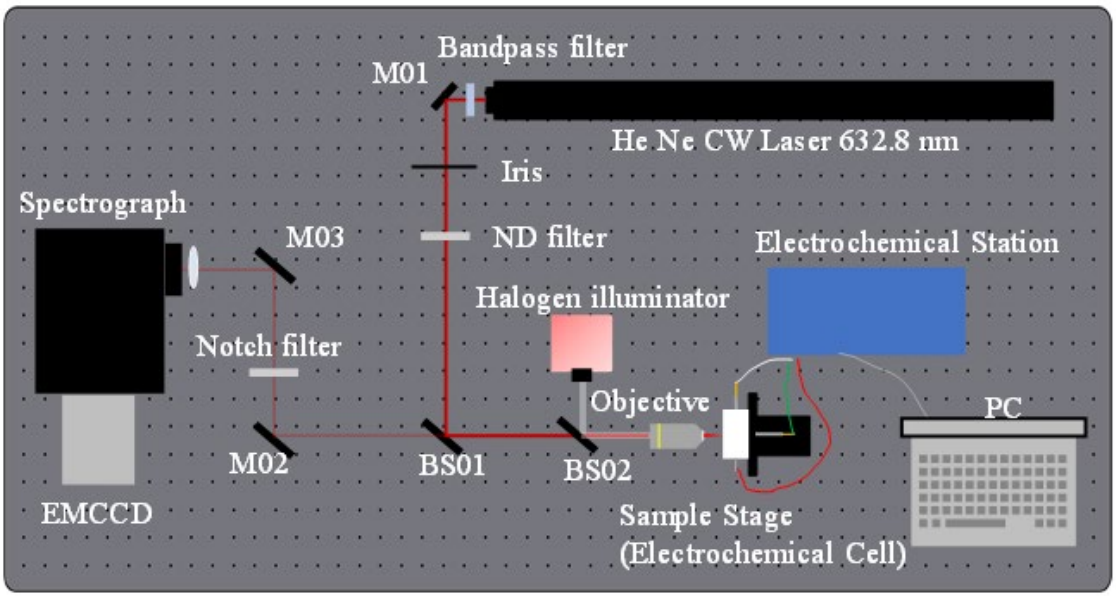

Figure 3.1. Schematic diagram of the home-built Raman system.

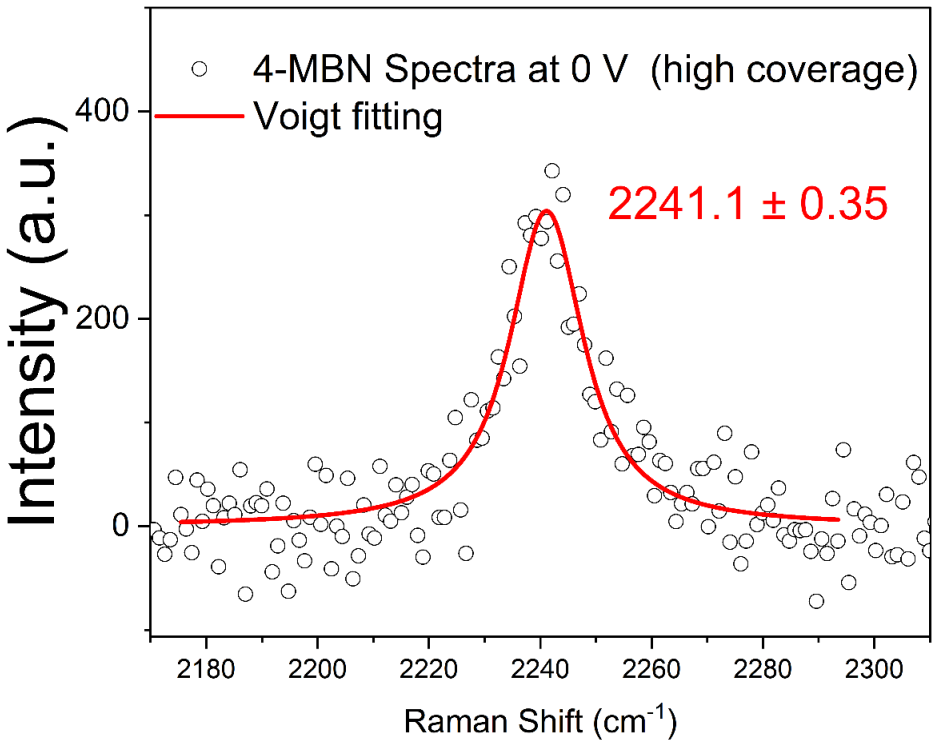

Figure 3.2. Example of Raman spectra fitting
Representative spectrum of 4-MBN at 0 V on Au (black circles) and fitting results (red line). The obtained spectra were fitted with a Voigt function to obtain the frequency.

As shown in ***Figure 3.2***, the obtained Raman spectra are fitted with a Voigt function to obtain the exact frequency, intensity and FWHM information.

3.1.2. SFG setup and signal processing

Sum frequency generation (SFG) spectroscopy combined with electrochemistry can be used to probe the vibrational information strictly from intrinsic solid/liquid electrode/electrolyte surfaces while measuring the charges (voltage and current density) transferred between the surfaces. Thus, this method provides much strictly surface-confined but still abundant real-time vibrational spectroscopic and electrochemical information together. A typical combination of in-situ VSFG-electrochemical system consists of three key components: a steady sum-frequency generation spectrometer, an SFG spectro-electrochemical cell, and an electrochemical potentiostat. The SFG spectrometer and the SFG electrochemical cell components are briefly

introduced as follows. All the experiments in this report were done with three different home-built sum-frequency generation spectrometers. As ***Figure 3.3*** shows, an SFG spectrometer typically includes a visible pulse and an IR pulse from the same light source, a delay line to control the passing length of the two beams to make their phases perfectly match, several wave plates or/and polarizers to tune the polarization of the beam and focusing lenses to tune the beam sizes.

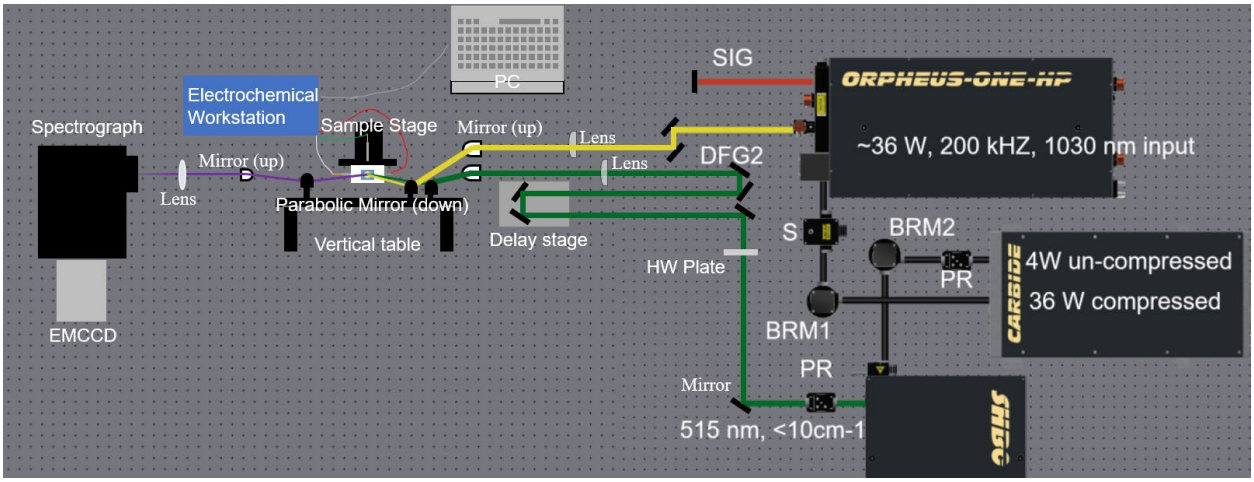

Figure 3.3. Schematic Picture of an SFG spectrometer

For experiments requiring probing the bands at the wavelength in this region which water will considerably interfere, water moisture in the air has to be purged by dry air; thus, a well-sealed box for the IR pulse paths is needed to be built up and often supposed to be equipped for dry air. The data in this report are collected by 3 different home-built SFG spectrometers with different laser sources (Mai Tai, Astrella and Carbide).

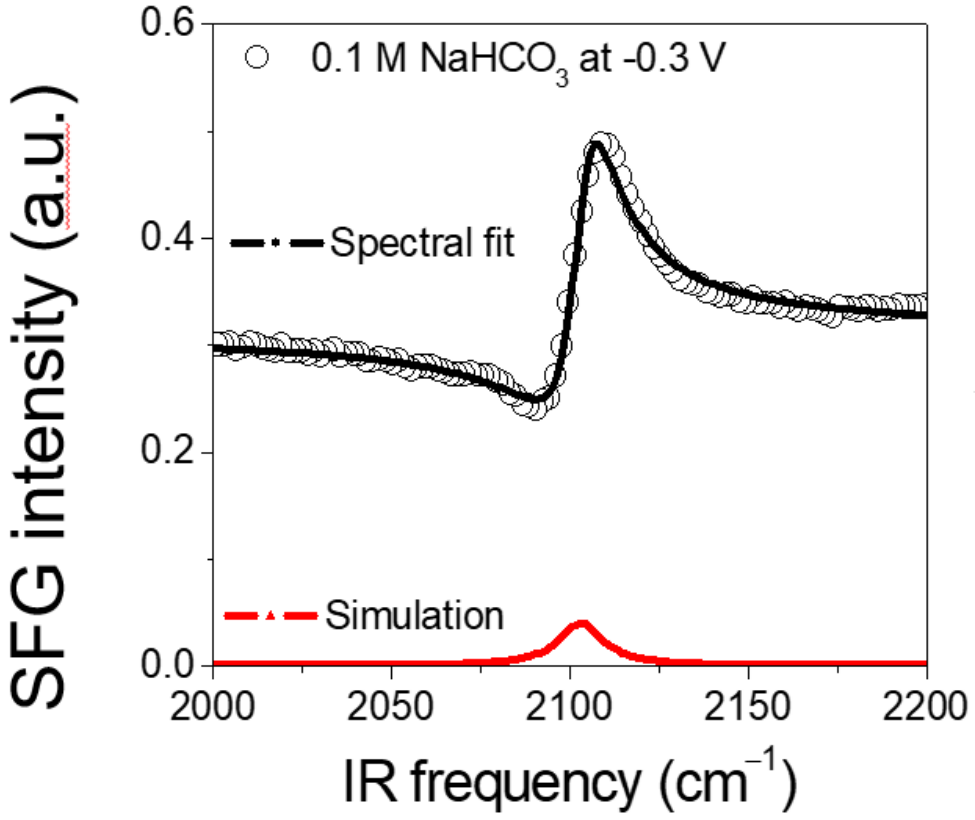

Figure 3.4. Example of SFG spectra fitting

Representative spectrum of CO on Au at -0.3 V (black circles) and fitting results (black line and red line). The obtained spectra were fitted with a Voigt function to obtain the frequency.

The intensity of the SFG signal can be given by[1]:

$$I(\omega_{SF}) \propto \left|\chi^{(2)}_{eff}\right|^2 I_{vis}(\omega_{vis}) I_{IR}(\omega_{IR})$$

Where $I_{vis}(\omega_{vis})$ and $I_{IR}(\omega_{IR})$ are the intensities of the input visible and IR beam fields, and $\chi^{(2)}_{eff}$ is the effective second-order nonlinear susceptibility of the surface, here it is written as:

$$\chi^{(2)}_{eff} = [\hat{\boldsymbol{e}}(\omega_{SF}) \cdot \boldsymbol{L}(\omega)] \cdot \chi^{(2)} : [\boldsymbol{L}(\omega_{vis}) \cdot \hat{\boldsymbol{e}}(\omega_{vis})][\boldsymbol{L}(\omega_{IR}) \cdot \hat{\boldsymbol{e}}(\omega_{IR})]$$

Where $\hat{\boldsymbol{e}}(\omega)$ is the polarization vector of the frequency ω , $\boldsymbol{L}(\omega)$ is the Fresnel factor at the frequency ω. In SFG with a different combination of the selective polarization, different components of $\chi^{(2)}$ can be acquired. Here, z is along the surface normal, thus in this experiment, considering all adsorbed CO at interfaces are along the normal direction, all measurements are tuned with ppp polarization. $\chi^{(2)}$can be taken as a sum of non-resonant component $\chi^{(2)}_{NR}$ and resonant contribution component $\chi^{(2)}_{R}$. In practical, the non-resonant signal is firstly acquired to

determine the conditions are suitable for SFG measurements, and normalization is usually taken bare non-resonant signal at a certain bias. The analysis of SFG spectra also requires the surface is smooth. Thus, the pre-treatment for electrode smoothness is crucial.With these information, the actual SFG spectra can be fitted by the equation ***Equation 1***, in practical, the normalized spectra are often used (the spectra of sample with resonant signal is normalized by the bare substrate without resonant signal), so that the spectra can be fitted with the other parameters only related with the resonant signal.

$$I_{SFG} \propto \left|\chi_{NR}^{(2)} + \chi_{R}^{(2)}\right|^2 = \left|A_{NR}e^{i\delta} + \sum\nolimits_n \frac{A_n}{\omega_{IR} - \omega_n + i\Gamma_n}\right|^2$$

Equation 1. The fitting equation for SFG spectra

Based on the fitting results, we then can obtain the resonant frequency (the frequency related with molecular information) and the amplitude (related with the surface molecule population and the orientation).

3.2. Electrochemical setups and materials

3.2.1. Electrochemical workstations and electrochemical cells

Raman Electrochemical cells. A home-built 3-electrode Teflon electrochemical cell is used for measurements with the disk electrodes (***Figure 3.5***). A potentiostat (CH Instruments) was used to control the potentials. The electrochemical cell body was cleaned in boiling mixed concentrated acids (H_2SO_4/HNO_3, 1:1) for one hour followed by sonication and thorough rinse with ultrapure water prior to use. An Ag/AgCl electrode (1 M KCl, CH Instruments) was used as reference electrode. The potentials were converted to the reversible hydrogen electrode (RHE) scale using E(RHE) = E(Ag/AgCl) + 0.0591×pH + 0.236. A graphite rod was used as counter electrodes respectively, to eliminate possible contamination from Pt counter electrode, all spectroscopic electrochemical measurements were reproduced with the graphite rod counter electrode. The distance between the electrode surface and the cell window is estimated to be ~ 250 μm. Another quartz cell (from Gauss Union INC.) is used for measurements with the film electrodes, as shown in ***Figure 3.6***. It equips with a electrode holder to tightly connect the film working electrode, a Pt net counter electrode and a reference electrode. The advantage of this cell is that we can do other visible light related measurements, such as photo current measurements and transient reflectance measurements.

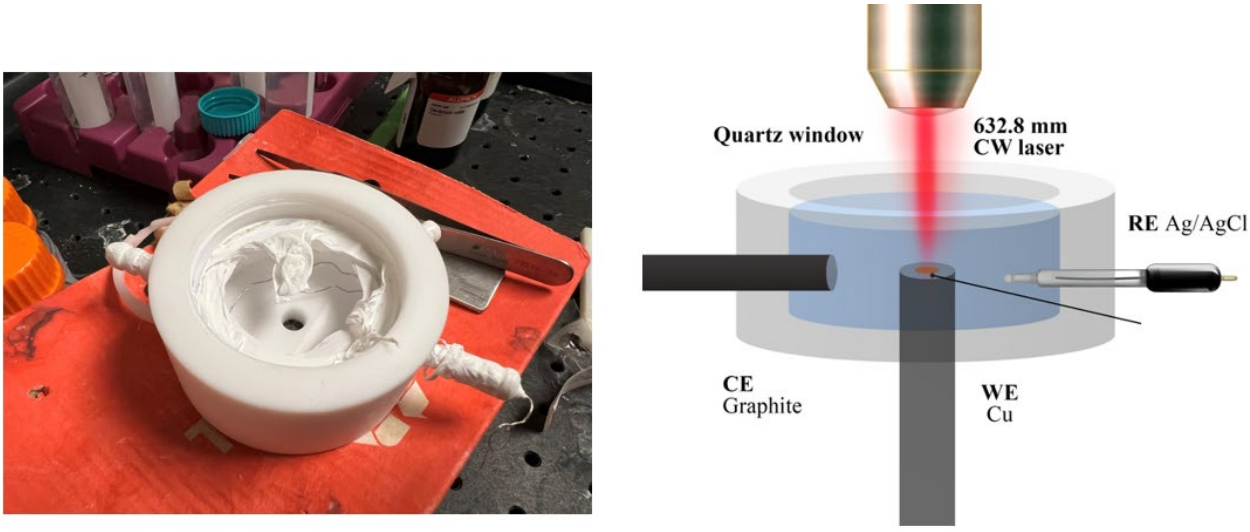

Figure 3.5. Raman spectro-electrochemical cell-01

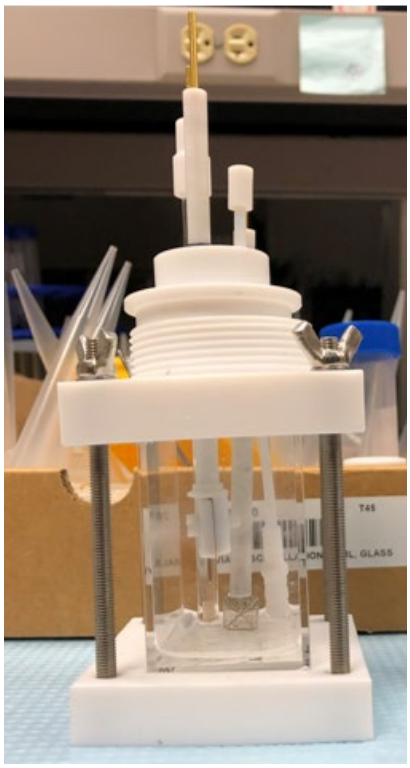

Figure 3.6. Raman spectro-electrochemical cell-02

SFG spectro-electrochemical cells. These cells for SFG are quite unique with more considerations to be designed compared to Raman or ATR-IR spectro-electrochemical cells. When Raman cells have a thicker layer electrolyte and ATR-IR cells do not need to take thickness of electrolyte in account due to the refection from the working electrode film side, the SFG electrochemical cells need to be designed with enough space left for an ultrathin layer of electrolyte. 3 criteria should be noted: the layer should be ideal neither too thick to decrease IR pulse energy reached at the surface (in water solution), nor too thin to distort the real-time electrochemical mass transport responses, an usual way to realize it is to put a steady spacer between the window and the electrode, and test it in electrochemical scan ; second, the orientation of the electrode should be close parallel to the calcium fluoride window and the electrolyte layer, so that the reflection is easier and more efficient to be tuned for SFG signals; the electrolyte chamber should be isolated and sealed to get rid of the interference from the air. The cell with this concept is home-made in **Figure 3.7**.

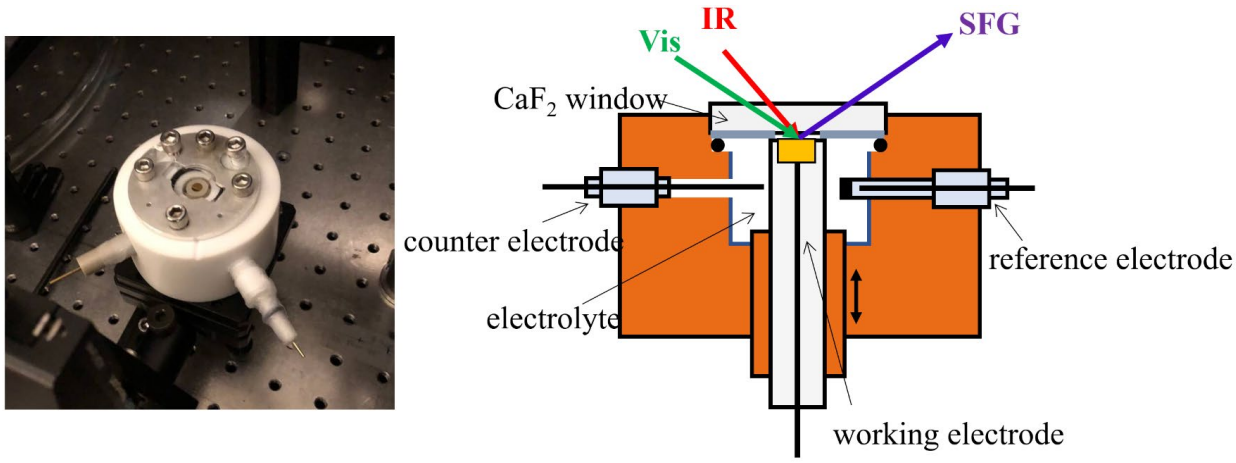

Figure 3.7. SFG spectro-electrochemical cell-01

To enhance the air tightness and reproducibility of the cell locations, a new cell shown in **Figure 3.8** is designed and made with several adjustments shown in . Round shape has changed to square to be better suited at the sample stage and fixed by screws; a rectangular cut at the bottom of the cell to help connect the electrode more efficiently and stably; two screws sealed top can functionalize as an inlet and outlet for electrolyte when the experiments are still ongoing.

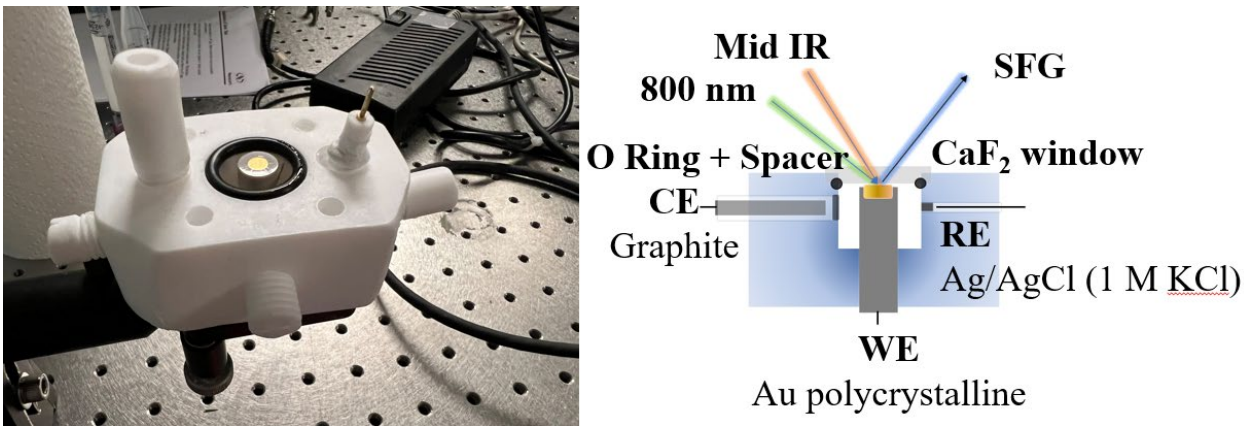

Figure 3.8. SFG spectro-electrochemical cell-02

3.2.2. Chemicals and other materials

Electrochemical measurements in aqueous solutions. Na_2CO_3 (99.999%) and $NaH^{13}CO_3$ (99%) were purchased from Acros Organics and Cambridge Isotope Laboratories, respectively. All electrolytes were prepared by using ultrapure water (Milli-Q, 18.2 MΩ□cm). Deuterium labelling experiments were prepared with D_2O (99.9 atom% D) from Sigma-Aldrich. Potassium carbonate (99.995% trace metals basis), $NaClO_4$ (hydrate, 99.99%) was purchased from Sigma-Aldrich. To prepare CO_2-saturated $NaHCO_3$ solutions, the Na_2CO_3 solutions were purged with high purity CO_2 gas (99.99%, nexAir) overnight. Ar and N_2-saturated solutions (Na_2CO_3, $NaClO_4$) were prepared by purging the prepared solutions for 2 h with ultrahigh purity Ar (99.999%, nexAir) or N_2 gas (99.999%, nexAir). CO purged solutions were purged under ultrahigh purity CO (99.999%, PRAXAIR) for 2 h, A pH meter (Accumet basic AB15) was used to measure the pH of all electrolytes prior to use.

Electrochemical measurements in organic solvents. Tetrabutylammonium hexafluorophosphate (99%, $TBAPF_6$), Acetonitrile (anhydrous, 99.8%), Aniline (ACS Reagent Grade, Liquid, ≥99.5%) are from Sigma Aldrich.

Electrodes. Indium tin oxide coated glass slide (square,surface resistivity 8-12 Omega/sq), Platinum wire (diam. 0.5 mm, 99.99% trace metals basi), Gold wire (diam. 0.5 mm, 99.999% trace metals basis), are from Sigma Aldrich; Gold electrode (OD:6mm, ID:3mm),

Nanoparticles synthesis. L-Ascorbic acid (≥99.0%), Sodium citrate tribasic dihydrate (ACS reagent, ≥99.0%), Sodium silicate solution (Na2O(SiO2)x·xH2O, 12.0-13.0% Si) are from Sigma Aldrich; (3-Aminopropyl) trimethoxysilane (97%) is from Alfa Aesar.

SAM organic molecules related. 4-Mercaptophenylacetic acid (97%), 4-(Mercaptomethyl) benzonitrile, 3-Mercaptopropanenitrile, Terephthalic acid, Benzanilide (98%), 4-Nitrothiophenol (technical grade, 80%), 4-Mercaptobiphenylcarbonitrile, are from Sigma Aldrich; 2-(4-Mercaptophenyl)acetonitrile is from Aurum Pharmatech; 4-Mercaptobenzonitrile is from Carbosynth.

Water. Resistivity >18MW·cm. Millipore Sigma Direct Q-5 ultrapure water system.

3.3. Preparation for electrochemical electrodes

3.3.1. Electrochemical polishing of the electrodes

Cu electrode. The polycrystalline Cu disk electrodes (OD 6 mm, ALS, Co., Ltd) are firstly polished by 0.05 μm Al_2O_3 with polishing pads, then rinsed by ultrapure water and electrochemically cleaned in 85% H_3PO_4 at 1.5 V vs. Ag/AgCl (1 M KCl) for 30 seconds until showing mirror-like surfaces.

Au electrode. The polycrystalline Au disk electrodes (OD 6 mm and 10 mm, ALS, Co., Ltd) are also polished by 0.05 μm Al_2O_3 with polishing pads, then rinsed by ultrapure water firstly, but then electrochemically polished in a different way: they are cleaned in a 50 mM H_2SO_4 solution from -0.2 V to 1.3 V vs. Ag/AgCl (1 M KCl) at 50 mV/s scan rate for 20 -30 min until the oxidation peak of Au oxide to Au at around 0.8 V can be reproduce between two different scans.

3.3.2. Electrochemical roughening electrodes for SERS measurements

Electrochemical roughening Au surface. The SERS substrates, electrochemical-roughened Au electrodes, were prepared by placing the smooth polycrystalline Au electrodes in KCl electrolyte and applying voltametric cycles of oxidation and reduction. The procedure of roughening Au smooth film into SERS Au electrode followed the procedure reported by Liu et al.[2] The polycrystalline Au coated film (Angstrom Engineering, 99.999% purity) working electrodes was immersed in 0.1 M KCl solution, and a graphite counter electrode and Ag/AgCl reference electrode were used during the roughening process. Around 15 oxidation-reduction cycles were performed for the roughening.

3.3.3. Electrochemical deposition

Au on ITO. Electro-deposition of Au on the ITO electrode (***Figure 3.9***) is followed by the procedure in previous report[3]. Firstly, ITO-coated glass plates were meticulously cleaned using a sonication process for 30 minutes. The cleaning procedure included sequential immersion in different solvents: soapy water, water, pure acetone, and 1M NaOH. Subsequently, a gold film, approximately 50nm thick as estimated by AFM, was

deposited onto the cleaned ITO glass plate. Electrodeposition was employed to create three types of gold nanostructures: pyramidal, rod-like, and spherical. This was achieved by immersing the glass plate in separate aqueous solutions containing 0.1M HClO4 and varying concentrations of HAuCl4 (40mM, 4mM, and 40mM, respectively). The electrodeposition process occurred at different voltages: -0.08V for the pyramidal structures, -0.08V for the rod-like structures, and -0.2V for the spherical structures. The electrodeposition was conducted for a duration of 2 minutes for each structure, with reference to Ag/AgCl electrode.

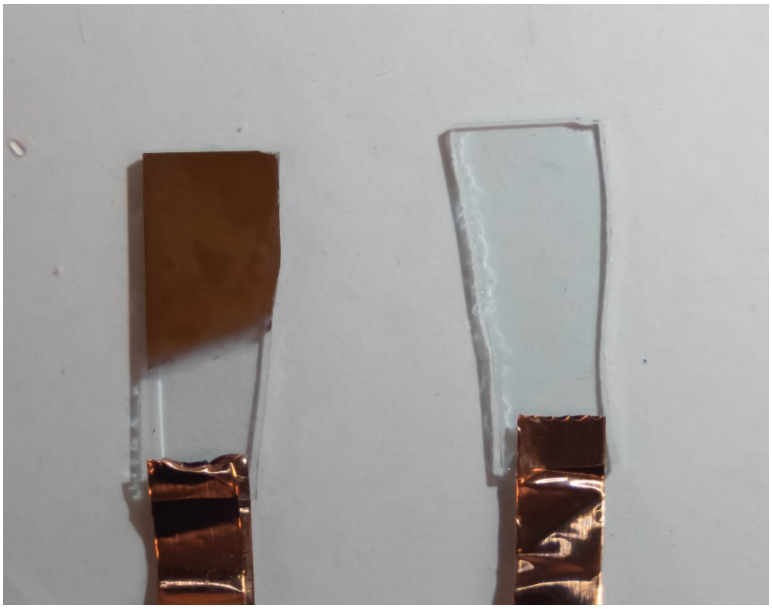

Figure 3.9. Electrodeposited Au on ITO disc electrode
Before deposition(right), after deposition (left)

Cu on Au. Electrodeposition of Cu on Au (**Figure 3.10**) procedures are quite similar as the ones on Au films[4], taking a $CuSO_4$ and sulfuric acid solution as a growth base, electrodeposit a certain thickness Cu on the Au. Before electrodeposition, cyclic voltammetry measurement should be taken to identify the surface conditions for Au disc electrode. After this measurement, an electric charge of around 0.002 C should be reached when around 10 nm thickness of Cu electrodeposits at the 6 mm diameter Au electrode. (Details in the **Figure *3.11***)

Figure 3.10. Electrodeposited Cu on Au disc electrode
Before deposition(left), after deposition (right)

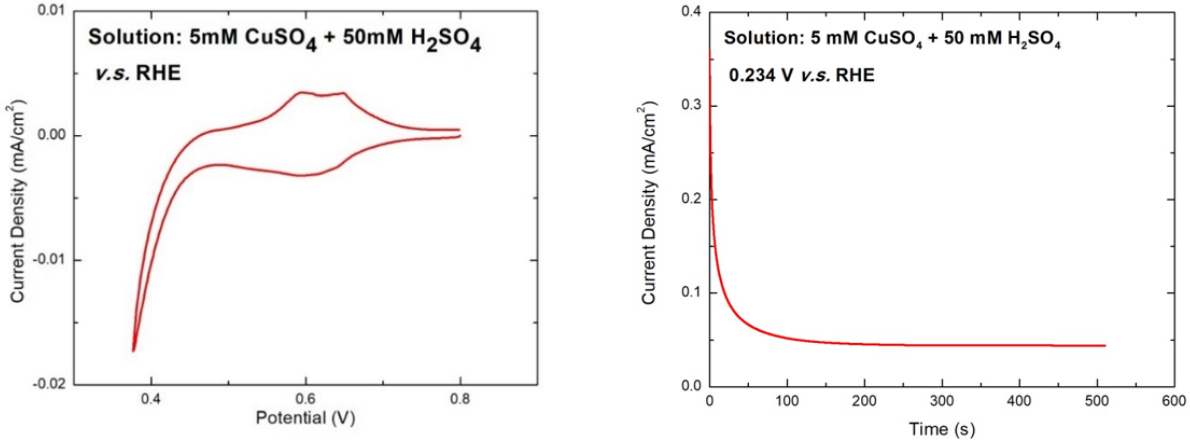

Figure 3.11. Measurement of electrodeposited Cu on Au disc electrode
Cyclic voltammetry of Au electrode in Ar-saturated 5mM $CuSO_4$ + 50 mM H_2SO_4(left),
i-t Curve of Au electrode in Ar-saturated 5mM $CuSO_4$ + 50 mM H_2SO_4(right)

3.4. Preparation for materials and characterizations

3.4.1. Au nanoparticles synthesis for SERS

A 200 ml aqueous solution of $HAuCl_4$ with a mass fraction of 0.01% is heated to boiling. Then, 1.4 ml of a sodium citrate solution with a mass fraction of 1% is quickly added. After about 1 minute, the solution changes color from pale yellow to black, and after 2 to 3 minutes, it turns reddish-brown. The solution is maintained at a gentle boil for 40 minutes and then the reaction is stopped, followed by cooling in a water bath. This process results in the formation of reddish-brown gold nanoparticles with an approximate diameter of 55 nm (***Figure 3.12***).

To synthesize gold nanoparticles of different sizes, the amount of sodium citrate added needs to be adjusted. For instance, to synthesize 12 nm gold nanoparticles, 6 ml of sodium citrate solution should be added. For 45 nm gold nanoparticles, 2 ml of sodium citrate solution should be added.

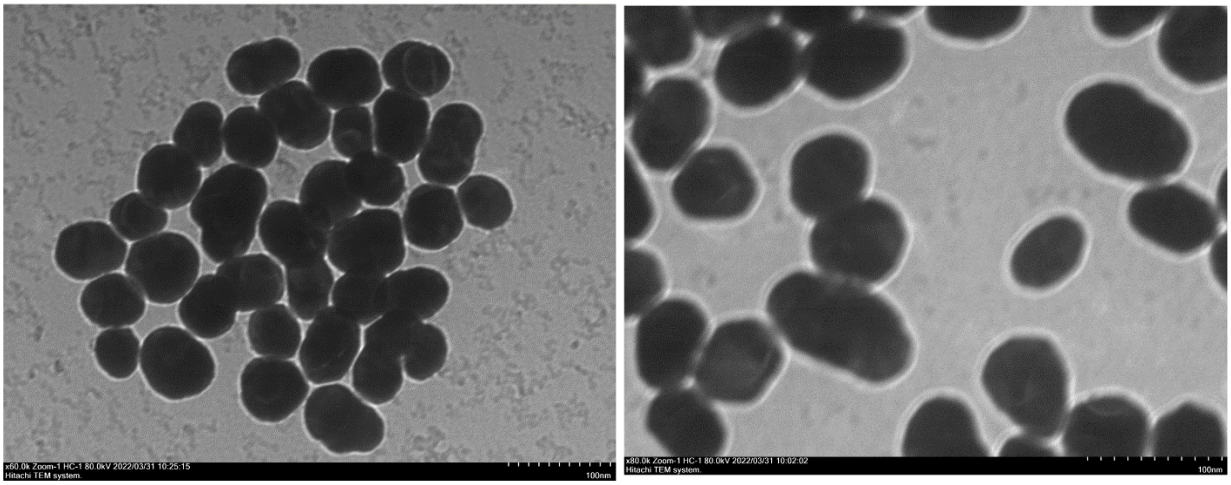

Figure 3.12. TEM image of synthesized Au nanoparticles
Diameter ~55 nm. Zoom out image (left) and zoom in image (right).

3.4.2. Au@SiO_2 nanoparticles synthesis for SHINERS

Au@SiO_2 nanoparticles were prepared based on the methods developed by Li, et al[5]. The obtained shell-isolated nanoparticles were characterized by TEM and electrochemical methods to verify the SiO_2 shell fully covered the Au core (**Figure 3.13**).

Take 30 ml of a colloidal solution containing 55 nm gold nanoparticles and add 0.4 ml of a 1 mM solution of 3-aminopropyltrimethoxysilane in water. Stir the mixture for 15 minutes and then add 3.2 ml of a 0.54% solution of sodium silicate. Continue stirring for an additional 3

minutes. Next, place the reaction container in a water bath heated to 95°C to initiate the reaction. To stop the reaction, simply remove the colloidal solution from the bath and place it in an ice-water bath. By controlling the reaction time, nanoparticles with different silica shell thicknesses can be obtained. For nanoparticles with a shell thickness of approximately 2 nm, the reaction should be carried out for 20 minutes. The shell of 3 nm needs around 30 minutes. For a shell thickness of 4-5 nm, the reaction time should be 60 minutes.

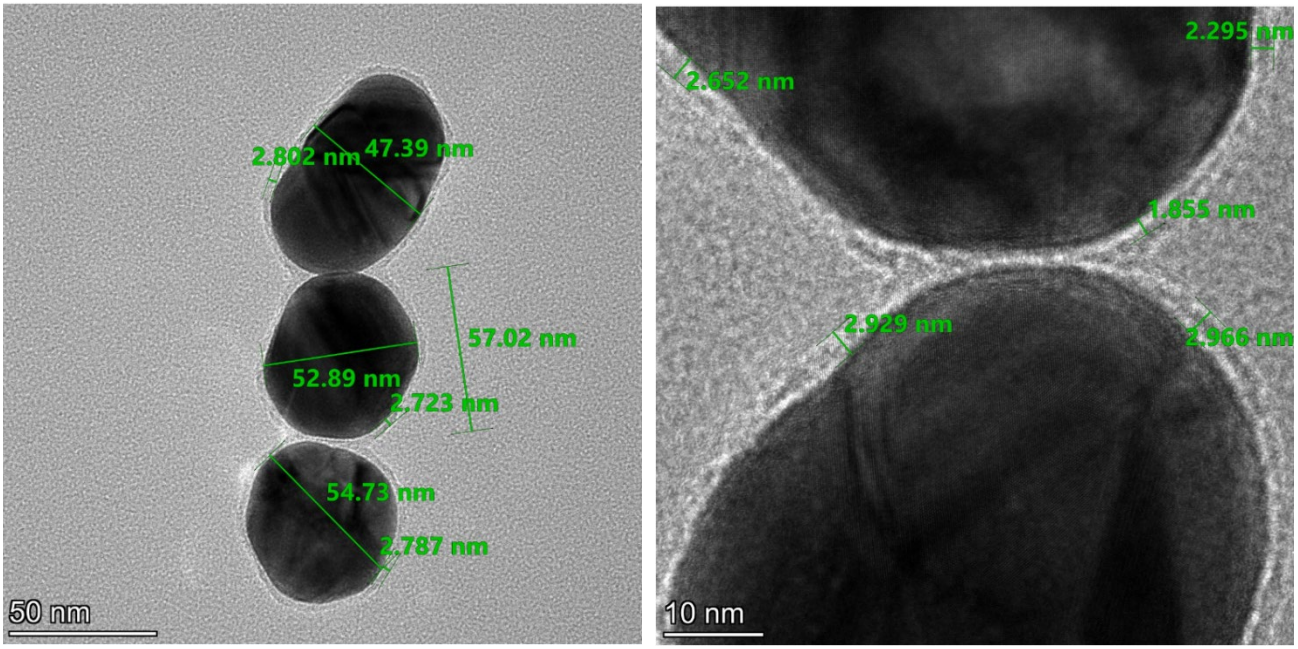

Figure 3.13. High resolution TEM image of synthesized Au@SiO_2 nanoparticles Diameter ~55 nm, thickness of Si_2O shell ~ 2-3 nm. Zoom out image (left) and zoom in image (right).

3.4.3. SAM on electrode preparation

The coverage dependent SAM formation method followed the procedure reported by Hu et al.[6] The pre-made roughened Au films were soaked in a concentration of 0.01 mM SAM molecules ethanol solution for different times to obtain the samples with different coverage (from 20 s to overnight, over 48 hours).

3.5. References

(1) Chen, Z.; Shen, Y. R.; Somorjai, G. A. S TUDIES OF P OLYMER S URFACES BY S UM F REQUENCY G ENERATION V IBRATIONAL S PECTROSCOPY. *Annu. Rev. Phys. Chem.* **2002**, *53* (1), 437–465. https://doi.org/10.1146/annurev.physchem.53.091801.115126.
(2) Liu, Y.-C.; Hwang, B.-J.; Jian, W.-J. Effect of Preparation Conditions for Roughening Gold Substrate by Oxidation–Reduction Cycle on the Surface-Enhanced Raman Spectroscopy of Polypyrrole. *Mater. Chem. Phys.* **2002**, *73* (2–3), 129–134. https://doi.org/10.1016/S0254-0584(01)00354-6.
(3) Tian, Y.; Liu, H.; Zhao, G.; Tatsuma, T. Shape-Controlled Electrodeposition of Gold Nanostructures. *J. Phys. Chem. B* **2006**, *110* (46), 23478–23481. https://doi.org/10.1021/jp065292q.
(4) Zhu, S.; Jiang, B.; Cai, W.-B.; Shao, M. Direct Observation on Reaction Intermediates and the Role of Bicarbonate Anions in CO_2 Electrochemical Reduction Reaction on Cu Surfaces. *J. Am. Chem. Soc.* **2017**, *139* (44), 15664–15667. https://doi.org/10.1021/jacs.7b10462.
(5) Li, J. F.; Huang, Y. F.; Ding, Y.; Yang, Z. L.; Li, S. B.; Zhou, X. S.; Fan, F. R.; Zhang, W.; Zhou, Z. Y.; Wu, D. Y.; Ren, B.; Wang, Z. L.; Tian, Z. Q. Shell-Isolated Nanoparticle-Enhanced Raman Spectroscopy. *Nature* **2010**, *464* (7287), 392–395. https://doi.org/10.1038/nature08907.
(6) Hu, S.; Liu, B.-J.; Feng, J.-M.; Zong, C.; Lin, K.-Q.; Wang, X.; Wu, D.-Y.; Ren, B. Quantifying Surface Temperature of Thermoplasmonic Nanostructures. *J. Am. Chem. Soc.* **2018**, *140* (42), 13680–13686. https://doi.org/10.1021/jacs.8b06083.

4. Chapter 4 Vibrational Spectroscopic Stark probe of the interfacial electric double layer of CO on Au

4.1. Introduction and background

Understanding and characterizing the local environment and the properties of interfacial electric double layer (EDL) holds significance not only within the fields of electrochemical ineterfaces[1–3] but also across various domains in electro-catalysis, photo-catalysis, and biology[2,4,5]. The utilization of *in-situ* vibrational spectroscopic techniques has opened new possibilities for investigating the EDL structure through molecular-level insights from multiple vibrational spectroscopic techniques at the interfaces. The vibrational Stark effect, denoting the electric field-dependent shift in vibrational frequency, has gained as a crucial indicator of the local electric field's attributes and the EDL's molecular-level architecture[6].

In a vibrational Stark probe measurement, to correlate with the calculations, the experimental data is usually interpreted in the context of the conventional Stark equation[7–

[9]: $h\nu = -\Delta\vec{\mu} \cdot \vec{F}$, where h is Planck's constant, ν is the vibrational frequency of the probed group, $\Delta\vec{\mu}$ is the Stark tuning rate, and $\vec{F}$ is the electric field. From the previous equation, we can also derive the expression of the absolute electric field strength as a function of potential[7] (applied voltage): $F(\varphi) = \frac{d\omega(\varphi)}{d\varphi} \cdot \frac{1}{\Delta\mu} \cdot (\varphi - \varphi_{PZC})$, where $\frac{d\omega(\varphi)}{d\varphi}$ is measured in experiments, and $\Delta\mu$ is from calculations, φ_{PZC} is the potential of zero of charge in the system.

Measuring the Stark tuning rate of specific vibrational modes and their positions within the EDL affords a comprehensive view of the field strength and potential variations at those specific locations. The development of electrochemical *in-situ* vibrational spectroscopic methods has enabled the possibilities for measuring local electric fields at interfaces[7–9]. Techniques such as Surface Enhanced Raman Spectroscopy (SERS)[10], Surface-enhanced Infrared absorption Spectroscopy[11–13], and Vibrational Sum Frequency Generation Spectroscopy (VSFGS)[7,14,15] have been employed to capture EDL profiles by directly measuring the frequency shifts of vibrational modes affected by varying electric field strengths induced by applied biases. These experimental results, operating at the molecular level, offer valuable validation for theoretical EDL models such as the Gouy-Chapman model and the Gouy-Chapman-Stern model[7,16].

Notably, among these molecular probes, the presence of adsorbed *CO emerges as a useful tool. Its significance is not only being an intermediate or product in many vital electrochemical reactions such as CO_2 reduction, and methanol/ethanol oxidation but also due to its distinct vibrational spectral features and potential-dependent vibrational Stark effect. In prior investigations[17–19], the *CO on Pt system served as a testing ground for delving into double-layer effects in both aqueous and organic electrolytes. In both systems, Stark tuning slopes of the CO/Pt showed an independent relationship to the ionic strength or other changes in the diffuse layer, indicating a unique double structure with the CO inside of the OHP. However, the double-layer structure for other metals, such as CO/Au, remains unclear.

Herein, we present an investigation of the properties of the electric double layer in *CO on the Au system by *in situ* Raman technique. By studying how the changes of the diffuse layer (ionic strength) affect the responses of the *CO on Au in terms of the Stark tuning rates on CO stretching frequency, we illustrate the position of the adsorbed *CO on Au metal. By in situ Raman measurements, we observe two binding modes of *CO on Au, (bridging mode and atop

mode) at different potential ranges. Unlike CO Pt has been proposed to be strongly adsorbed as an adlayer of metal with no observable response to the diffuse layer changes (ionic strength), or different lengths of SAM into the diffuse layers with noticeable responses with ionic strength, we found a unique response of the two types of *CO to the electrolyte ionic strength of *CO on Au. We detailed the study of how the Stark tuning rate of the *CO at different potential ranges behaves under the different ionic strengths and revealed a more detailed understanding of the double layer of *CO in the Au system.

4.2. Experimental design of CO on Au and spectra fitting

To obtain a surface-enhanced Raman signal and avoid possible contamination from direct interaction between the molecules and the Au nanostructures, the Shell-isolated Nanoparticle enhanced Raman Spectroscopy is utilized in this study. The SiO_2 shell-coated Au core nanoparticles were drop-cast on the Au electrode surface and then equipped in the electrochemical Raman cell for measurements. Additional results with SFG prove that the adjacent NPs in SHINERS measurements do not affect the absolute frequencies or the interfacial electric field near the surface.

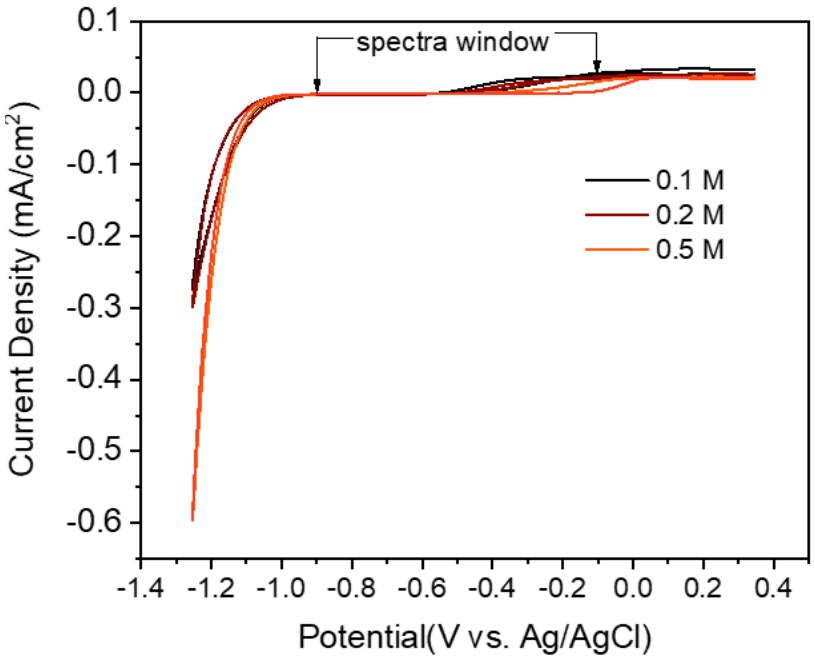

Figure 4.1. Electrochemical cyclic voltammetry of CO on Au in $NaClO_4$.

Whether the reaction occurring simultaneously (with a large Faradaic current) on the electrode surface affects the Stark tuning rate measurement is still under debate. Therefore, to ensure the accuracy of the spectroscopic measurement on the Stark tuning rate of CO, the region with noticeable currents or the electrochemical reactions should be avoided. The cyclic voltammetry measurements are conducted to identify the suitable electrochemical window for

the spectroscopic measurements. As shown in ***Figure 4.1***, the potential region negative than –1.0 V shows an obvious current increase from the hydrogen evolution reaction. In this study, the region from – 0.1 to –0.8 V is chosen for spectroscopic measurements of CO Stark tuning rates to avoid either CO oxidation at a more positive potential region or the hydrogen evolution reaction region with a large Faradaic current.

After the Raman spectra were obtained, the peaks were fitted with the Voigt function with multiple peaks, as shown in ***Figure 4.2***. We obtain two modes in the measurement, and we label the mode at the lower frequency ~2080 cm^{-1} as A1 mode and the mode at the higher frequency ~2120 cm^{-1} as A2 mode. According to the previous studies by IR and Raman, these two modes should both belong to the 2-fold bridging mode and atop mode of *CO on Au, repectively[20–22].

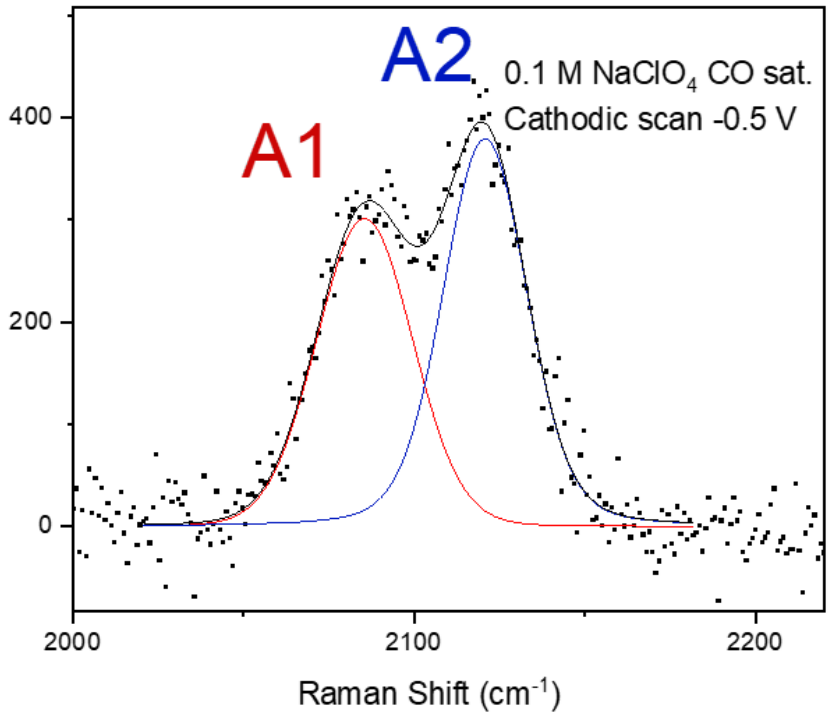

Figure 4.2. Example of the fitting Raman spectrum with two peaks.

4.3. Raman result analysis— CO on Au as a Stark probe

In the case of CO on Pt, the CO is typically considered an adlayer of the metal or positioned within the Stern layer (inner OHP). Consequently, it remains unaffected by changes in the diffuse layer resulting from alterations in ionic strength or pH[17]. To precisely determine the location of CO within the electrochemical double layer (EDL) on Au, specifically whether it resides in the Stern layer or the diffuse layer, we conducted experiments to investigate the dependence of the Stark tuning rate of CO by tuning the concentration of the electrolyte (ionic strength). We selected $NaClO_4$ as the electrolyte, with concentrations ranging from 0.01 to 0.5 M, while ensuring the pH was maintained around 7 to 7.6. As the ClO_4^- anion does not strongly bind to the surface, it avoids inducing competitive binding with CO, which could significantly alter the surface coverage of CO and thereby affect the Stark tuning rate measurements.

The initial measurement was carried out in 0.5 M NaClO4 electrolyte with saturated CO. The obtained spectra are depicted in ***Figure 4.3***, revealing two modes in the range from -0.9 V to -0.1 V. The higher frequency mode, A2, at approximately 2120 cm^{-1}, is present across the entire range, while the lower frequency mode, A1, at around 2080 cm^{-1}, is observed only from -0.35 to -0.1 V. As anticipated, the vibrational frequency of CO undergoes a shift towards higher wavenumbers as the potential increases. This is primarily attributed to the reduction of electronic back donation between the Au d states and the 2p* orbital of the chemisorbed CO at more positive potentials. Consequently, the C-O bond shortens, causing an increase in the internal stretching frequency and resulting in higher wavenumbers. Through spectra fitting, we obtained the frequencies of these modes as a function of potential, as shown in ***Figure 4.3*** B and C. In this condition with $NaClO_4$ electrolyte, the A1 mode exhibits a Stark tuning rate of approximately ~57.3 cm^{-1}/V, while the A2 mode displays a nonlinear behavior with a Stark tuning rate of ~27.9 cm^{-1}/V from -0.9 V to -0.4 V and a different rate of ~23.4 cm^{-1}/V from -0.35 to -0.1 V, where the A1 mode coexists in the region. According to the previous detailed study of CO on Au[20–22], the A1 mode should be assigned with the 2-fold bridging mode of CO, and the A2 mode should be assigned with the atop mode of CO.

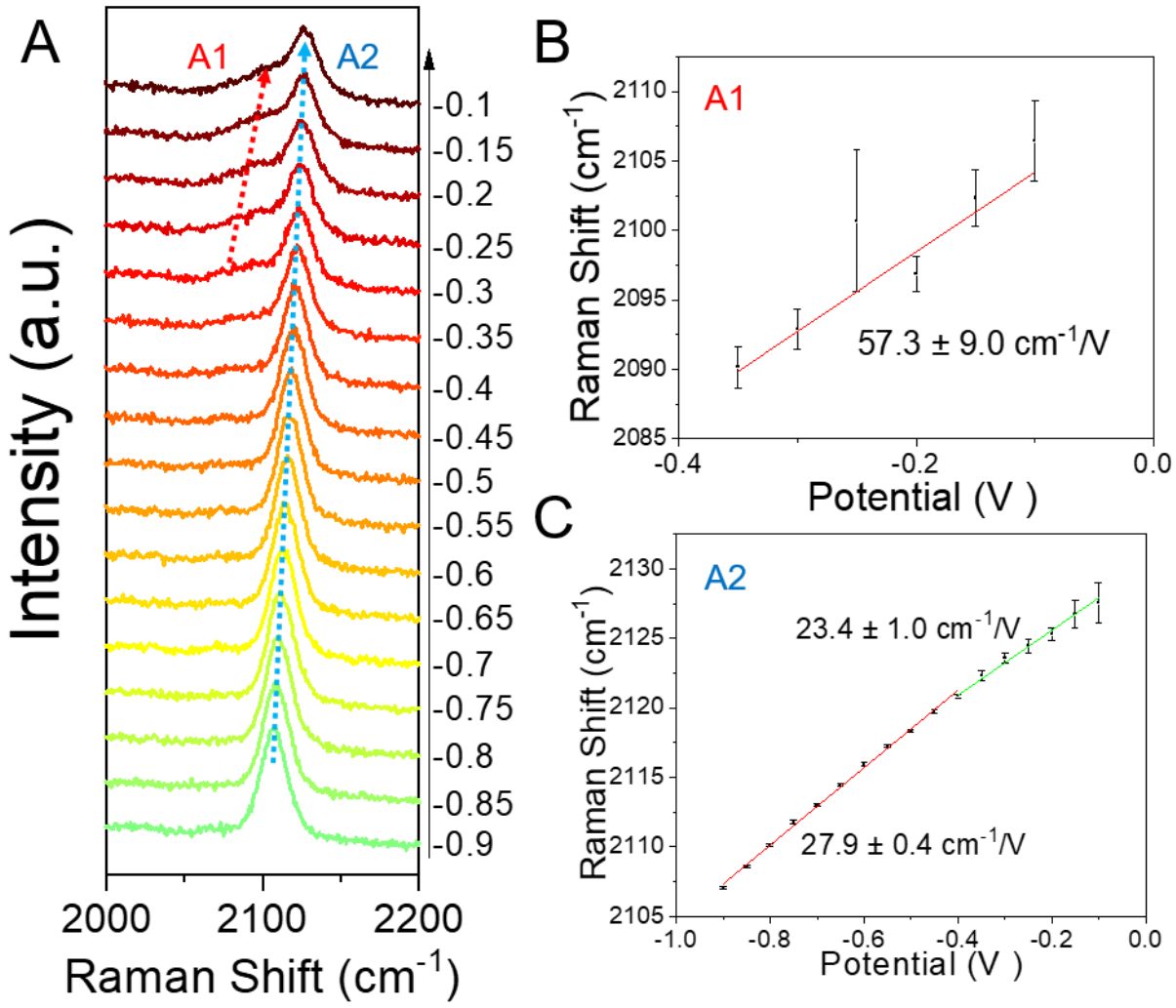

Figure 4.3. Raman spectra of CO on Au in 0.5 M $NaClO_4$.
(A) the potential dependent Raman spectra from -0.9 V to -0.1 V. (B) Fitting frequency of A1 mode as a function of potential. (C) Fitting frequency of A2 mode as a function of potential.

The nonlinear potential-dependent frequency shift slope feature seen in the A2 mode was also reported in CO on Pd and CO on Pt systems[23,24], and this phenomenon is likely associated with the co-adsorption of water or hydrogen adatoms on the surface within the same electrochemical window, which leads to the displacement of adsorbed CO to different sites. In our study, we hypothesize that a similar process occurs at the surface. Previous results indicate that the frequency shift slope of the higher frequency (atop) mode is smaller when two modes coexist, compared to that when the A1 mode is absent[23,24]. Additionally, the cyclic voltammetry

(CV) data shown in ***Figure 4.1*** provide further evidence supporting the correlation between the reduction peak at -0.35 V and water dissociation. The hypothesis is illustrated in ***Figure 4.4***: at more positive potentials where the water adsorption and reduction have not occurred (-0.1 to -0.35 V in a 0.5 M $NaClO_4$ solution), the CO adsorbed on two different sites with 2-fold bridging mode (~2080 cm^{-1}) and atop mode (~2120 cm^{-1}), respectively, and at more negative potentials, co-adsorbed H atoms or water molecules displace the bridging CO molecules, transforming them into atop CO (at ~2120 cm^{-1}); and due to the different surface environment with different adsorbates and CO coverages, the dipole-dipole interactions among *CO should be affected from positive potential to negative potential range (positive potential: bridging CO and atop CO; negative potential: only atop CO), the potential dependent frequency shift slopes of A2 (atop) mode is affected as a result.

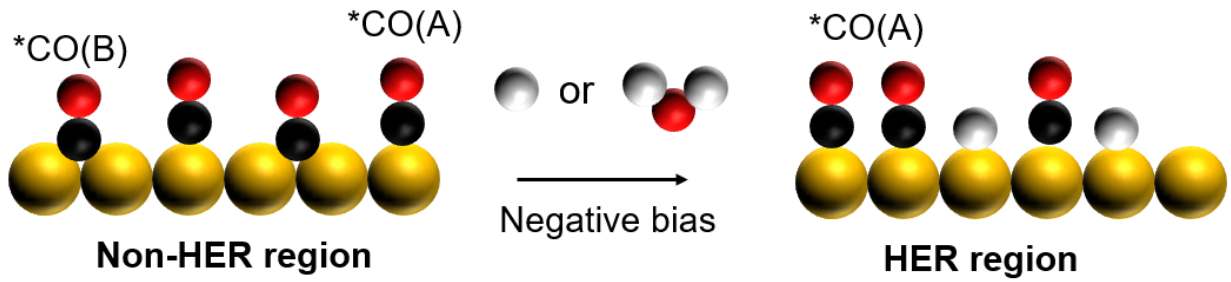

Figure 4.4. Hypothesized scheme of H adsorption induced exchange of CO adsorption sites. Balls of different colors represent different atoms: yellow-gold, black-carbon, red-oxygen, and white-hydrogen. *CO(B) represents the adsorbed CO in bridging sites, *CO(A) represents the adsorbed CO in atop sites. NER region means the potential at more positive than the water reduction onset, and the HER region means the potential region within the water reduction.

Besides, we also comment on the "Stark tuning rate" term. With the understanding of the literature report[17], we think that the Stark tuning rate is mainly influenced by two factors. Firstly, it is determined by the exchange of electrons between the orbitals of the electrode and the CO adsorbate. Specifically, when the potential becomes more negative, there is an increased back donation from the electronic d states of the metal to the 2p* adsorbate state. Secondly, it is affected by changes in the molecular polarizability caused by the electric field. This involves the interaction of the interfacial electric field with the dipole moment of the adsorbate. Thus, the vibrational spectroscopic changes as a result of the tuning electrochemical potential can be

differentiated from the conventional Stark effect (only induced by the electric field), it will includes 2 factors in the "electrochemical Stark effect"[17]: the changes originated from the chemical bonding changing, the changes due to the pure electric field changing.

4.4. Raman result analysis— Ionic strength effect on CO Stark tuning rate

To verify the hypothesis on the H adsorption-induced transformation and to assess the impact of the diffuse layer thickness on the vibrational properties of the adsorbed CO, the electrochemical Stark tuning rate was determined for various concentrations of the supporting electrolyte in addition to 0.5 M, 0.2 M, 0.1 M, 0.01 M $NaClO_4$.

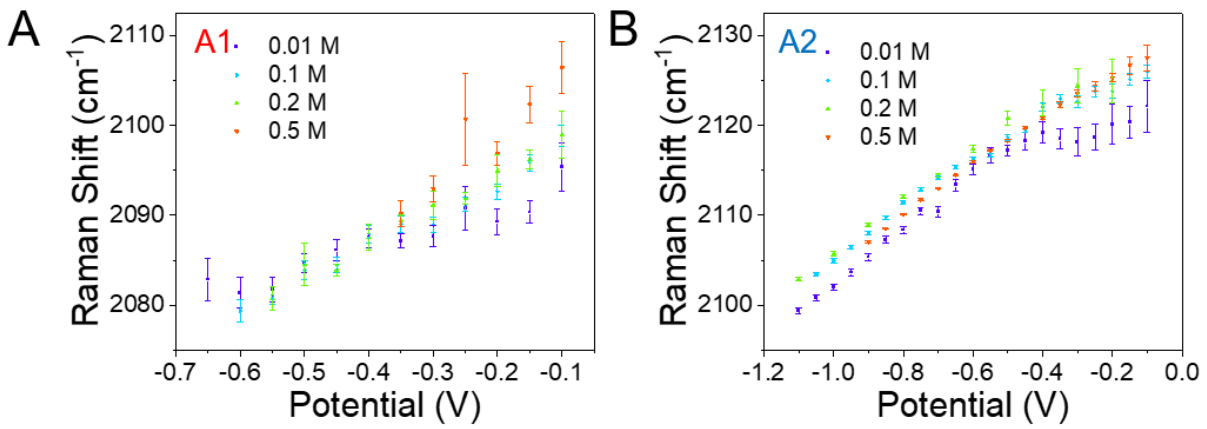

Figure 4.5. Ionic strength-dependent vibrational frequencies of A1 and A2 modes. (A) the frequency of A1 mode obtained from Raman measurement. (B) the frequency of A2 mode obtained from Raman measurement. All the measurements were conducted in supporting electrolytes with 0.5 M 0.2 M, 0.1 M, 0.01 M $NaClO_4$ saturated with CO.

Figure 4.5 A and B show the potential dependent vibrational frequency of adsorbed CO on Au in different binding sites, 2-fold bridging mode (A1, in A) and atop mode (A2, in B). Each data point represents the fitted frequency from the Raman spectra of the specific system. The original Raman spectra are shown below.

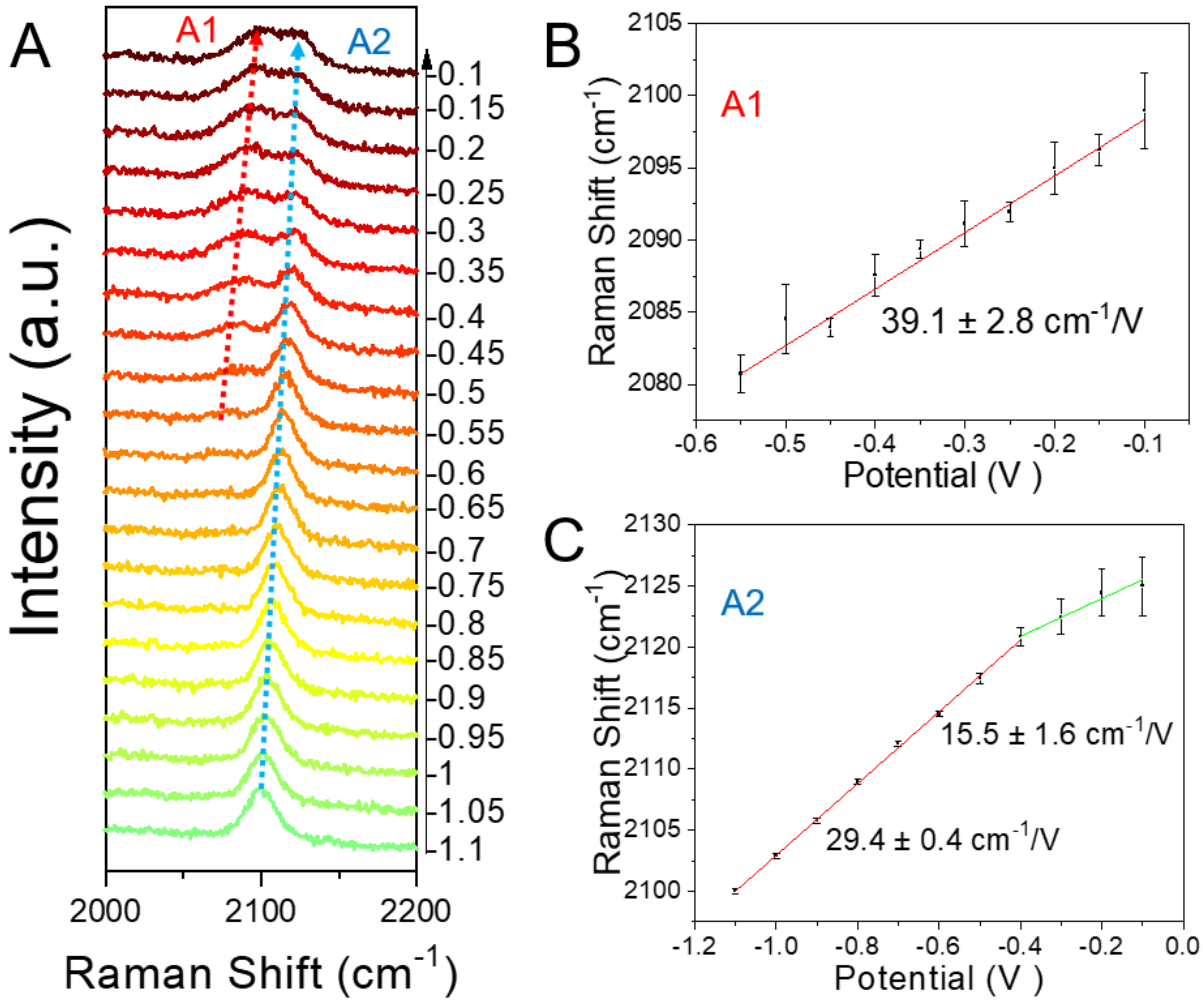

Figure 4.6. Raman spectra of CO on Au in 0.2 M $NaClO_4$.
(A) the potential dependent Raman spectra from -0.9 V to -0.1 V. (B) Fitting frequency of A1 mode as a function of potential. (C) Fitting frequency of A2 mode as a function of potential.

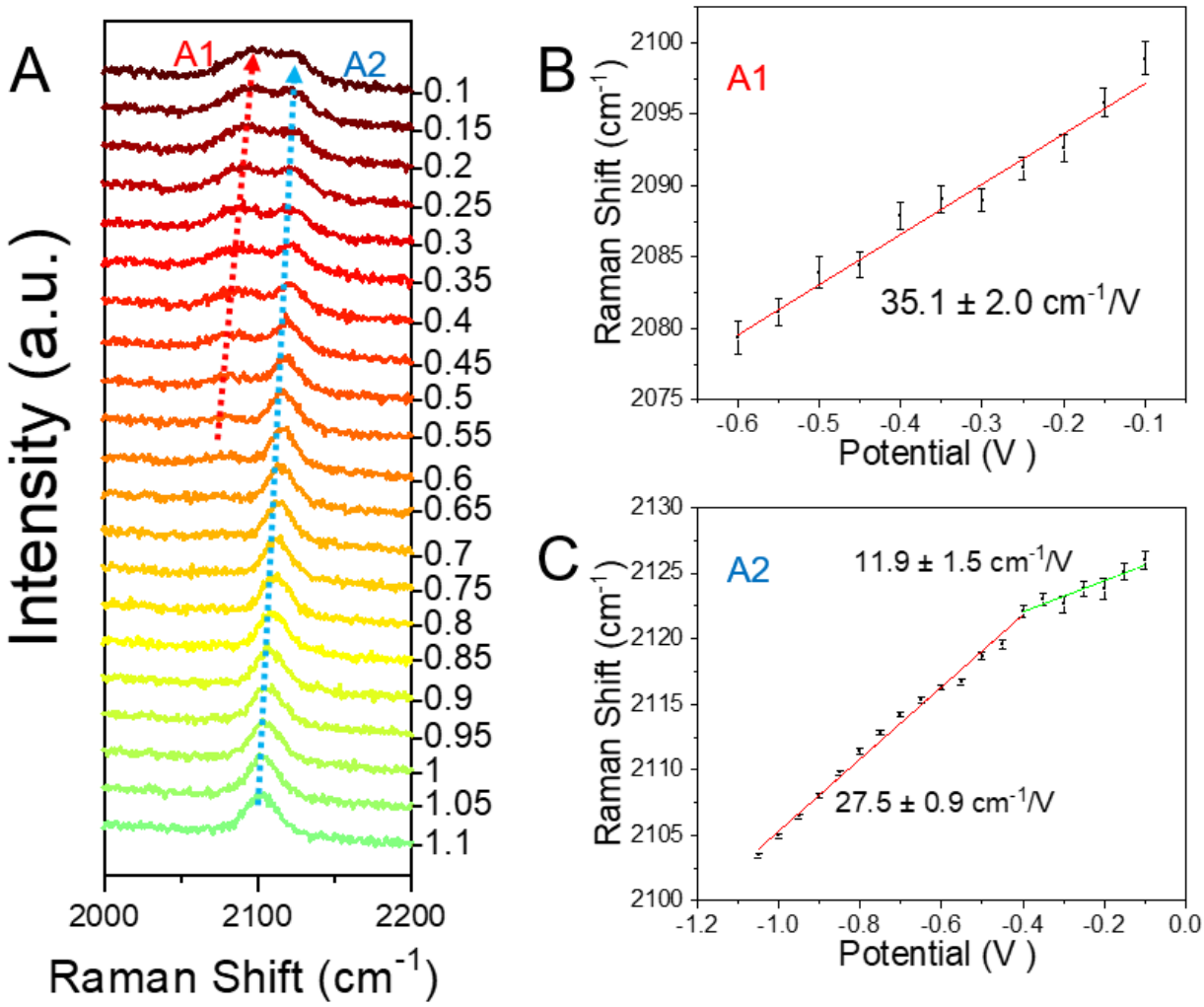

Figure 4.7. Raman spectra of CO on Au in 0.1 M $NaClO_4$.
(A) the potential dependent Raman spectra from -0.9 V to -0.1 V. (B) Fitting frequency of A1 mode as a function of potential. (C) Fitting frequency of A2 mode as a function of potential.

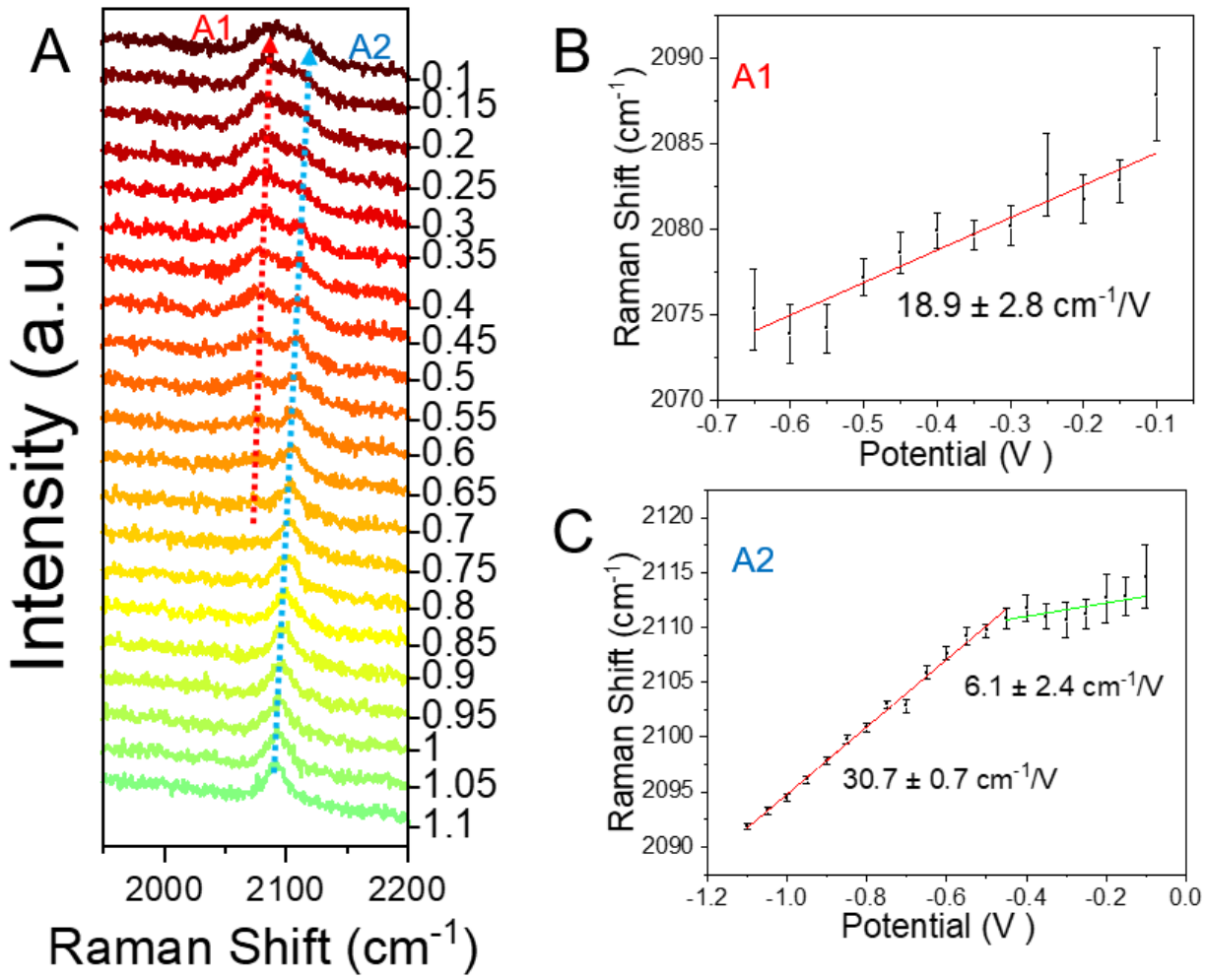

Figure 4.8. Raman spectra of CO on Au in 0.01 M $NaClO_4$.
(A) the potential dependent Raman spectra from -0.9 V to -0.1 V. (B) Fitting frequency of A1 mode as a function of potential. (C) Fitting frequency of A2 mode as a function of potential.

The corresponding Raman spectra and the fitting results on the potential dependent frequency shift slopes of the A1 and A2 modes can be found in Figure 4.6 (0.2 M), Figure 4.7 (0.1 M), and Figure 4.8 (0.01 M). From the information, we fitted the potential dependent frequency and summarized the ionic strength-dependent Stark slopes of 2 modes in the tables.

Table 1 and ***Table 2*** summarize the fitted Stark tuning slopes of the A1 and A2 modes as a function of potential. Firstly, in the A1 mode, it is clear that the data in the whole potential region can be separated into 2 parts with different Stark tuning slopes. One part is roughly from -1.1 V to -0.6 V, where the slope shows independence of concentration and stays constant at

around 27.5~ 30.7 cm^{-1}/V. The other part is from -0.6 V to -0.1 V, where the Stark slope appears to be dependent on ionic strength.

Table 1. Ionic strength-dependent results for *CO —A1 mode.

The potential dependent frequency shift slopes of *CO frequencies (A1 mode) from 0 to -0.4 V.

Condition	pH	R (cm^{-1}/V)
0.50 M	7.6	57.3 ± 9.0
0.20 M	7.4	39.1 ± 2.8
0.10 M	7.5	35.1 ± 2.0
0.01 M	7.7	18.9 ± 2.8

Table 2. Ionic strength-dependent results for *CO —A2 mode.
The potential dependent frequency shift slopes of *CO frequencies (A2 mode), R1 refers to the slopes independent of ionic strength (from ~ -0.4 V to -1.1 V), R2 refers to the slopes dependent on ionic strength (from 0.1 V to ~ -0.4 V).

Condition	pH	R1 (cm^{-1}/V)	R2 (cm^{-1}/V)
0.50 M	7.6	27.9 ± 0.4	23.4 ± 1.0
0.20 M	7.4	29.4 ± 0.4	15.5 ± 1.6
0.10 M	7.5	27.5 ± 0.9	11.9 ± 1.5
0.01 M	7.7	30.7 ± 1.6	6.1 ± 2.4

From the results in ***Table 1*** and ***Table 2***, it is seen that from 0.1 to -0.4 V, when the atop mode (R2) and bridging mode coexist on the Au surface, A1 and A2 both experience a dependence on the ionic strength of the electrolyte, and the Stark tuning rate decreases as a function of the concentration; from -0.4 V to -1.1 V, where only atop mode exists, the CO stretching mode is no longer dependent on the ionic strength.

4.5. The theoretical model of the electric double layer of CO on Au and the discussion

The electrical double layer (EDL) describes how ionic charges are distributed near the interface of a charged surface in contact with a liquid electrolyte[25]. Traditionally, the EDL is separated into two distinct regions: the Helmholtz layer and the outer diffuse or Gouy-Chapman layer. The Helmholtz layer represents the lowest point where ions approach the electrode surface. When specific adsorption occurs, the Helmholtz layer is divided into two parts: the Inner Helmholtz Plane (IHP), which consists of specifically adsorbed ions, and the Outer Helmholtz Plane (OHP), which consists of non-specifically adsorbed ions approaching the surface. Non-specifically adsorbed ions at the OHP are surrounded by solvent and interact with the charged surface through electrostatic forces. The outermost portion of the EDL region is known as the diffuse layer, where fully solvated ions are distributed in a manner resembling the Debye-Hückel theory, interacting through electrostatic forces with the charged surface. The charge on the electrode surface is effectively shielded by the opposite charge within the EDL, meaning that the potential difference between the (metal) electrode and the electrolyte primarily occurs within this EDL. Exploring the configuration of the electrochemical double layer (EDL) and its impact on electrochemical reactions has been one of the important topics in the field of physical electrochemistry.

double-layerudies[17,26,27] demonstrate the sensitivity of the molecular Stark effect probes to the changes in the diffuse double-layer by examining the Stark slopes of the nitrile/CO probes changes with the ionic strength (Debye length). The nitrile-terminated SAMs on Au and Ag[26,27] enable the probe of how the vibrational mode at different positions relative to the boundary between the Stern layer and diffuse layer responds to the ionic strength change in the diffuse layer. And the discussion of CO on Pt[17], which falls within the Stern layer, shows that the tuning rate of CO is independent of the ionic strength. These results[17,26,27] provide a comprehensive picture of how the probe moiety responds to the ionic strength, which can be divided into 3 distinct cases shown below, according to the Gouy-Chapman theory.

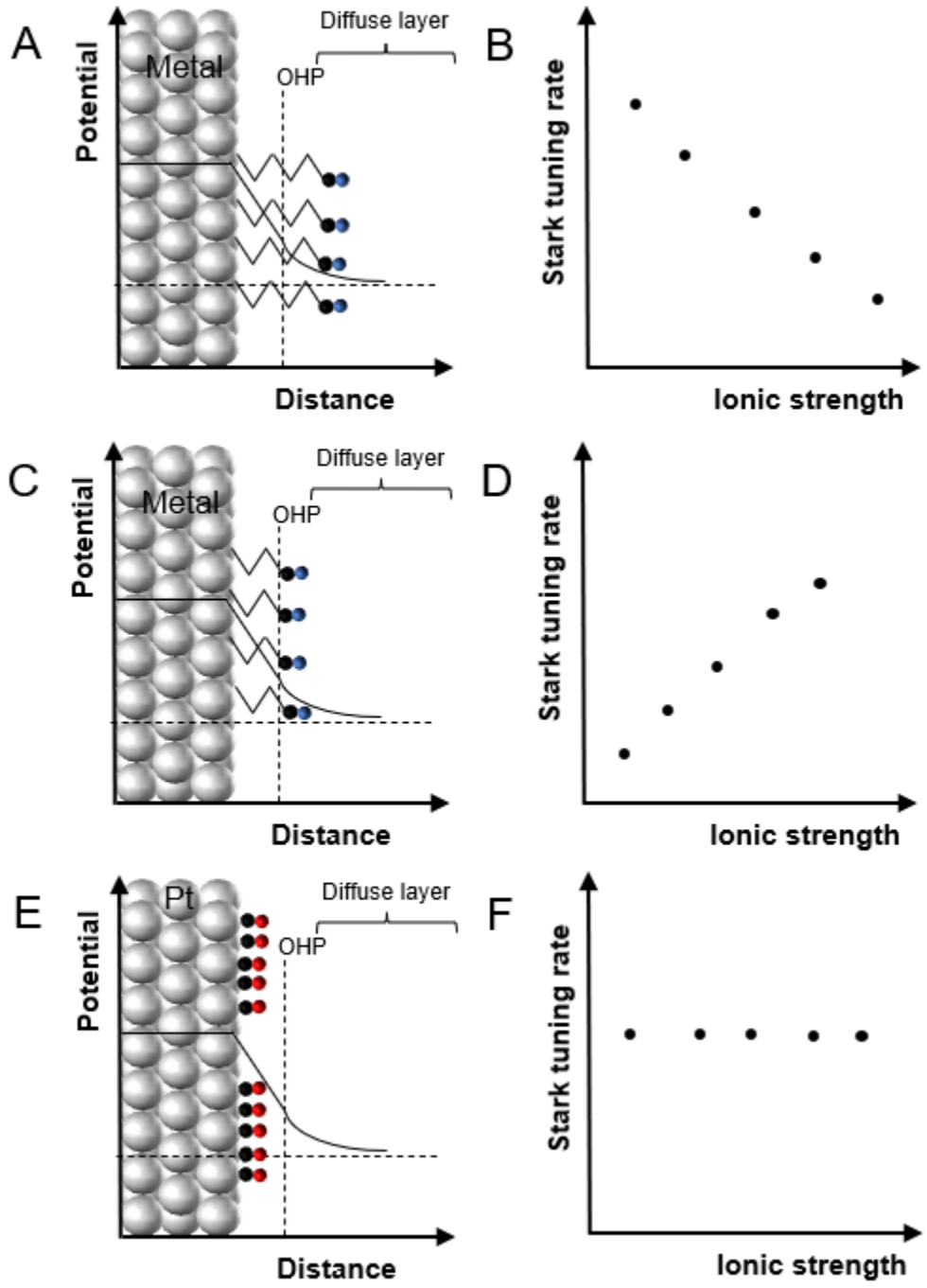

Figure 4.9. The 3 models of Stark tuning rates of molecular probes in the double layer under different ionic strengths.

In the first scenario, the probed mode resides within the diffuse layer, as exemplified by the Au/Ag-attached SAM molecule illustrated in **Figure 4.9**A. In this case, as the ionic strength is gradually increased, the Stark tuning rate is expected to diminish progressively until it

becomes practically unmeasurable, as shown in **Figure 4.9**B. This negative response between the ionic strength and the Stark tuning rates behavior can be explained as 1) when the ionic strength is small (the large Debye length), the double-layer arrangement generates electric fields at the interface that extend over tens of angstroms into the neighboring solution; consequently, a noticeable Stark tuning effect manifest on the nitrile probe molecules even though it is far from the interface; 2) when the ionic strength increases (short Debye lengths), compression of the double layer happens, and the probed moiety falls outside the region where the potential drop mainly occurs, thus, Stark tuning rates are predicted to be smaller; 3) this compression leads to a faster decay of the electric field in a shorter range before reaching the nitrile molecule. As the ionic strength increases (resulting in a decrease in Debye length), the double layer experiences more pronounced compression, consequently leading to a further reduction in the electrochemical potential gradient at the position of the nitrile group and even unmeasurable Stark tuning rates.

The second scenario refers to the situations where the probed moiety is positioned in a closer region within the diffuse layer (**Figure 4.9**C), yet still not within the OHP. As the ionic strength increases, the probe is also expected to experience an increasing interfacial electric field (**Figure 4.9**D). This phenomenon also can be explained by the predictions outlined by the Gouy-Chapman theory. According to the theory and discussions in the previous case, a more compact Debye length should give rise to a more substantial potential gradient (EFs). Notably, the EFs are concentrated within a limited spatial range, positioned only at a few angstroms from the interfacial boundary. As the ionic strength increases and the Debye length shortens, the confined space of the diffuse layer facilitates the generation of bigger potential gradients. These gradients effectively influence the probed moieties, contributing to a positive tuning response.

To elaborate on the two scenarios listed above, we used a numerical solver (COMSOL Multiphysics 6.1) to simulate the coupling between electrostatics and the transport of ions, the two physical chemistry process that dictates the electric field ($\vec{F}$) profile in an electrochemical cell as a function of applied potential ϕ_M and ionic strength (ions concentration). The position dependent Stark tuning slope $\frac{d\omega}{d\phi_M}$ is then related to $\frac{d\vec{F}}{d\phi_M}$, the response of electric field to applied potential, through $\frac{d\omega}{d\phi_M} = \frac{d\omega}{d\vec{F}}\frac{d\vec{F}}{d\phi_M} = -\Delta\vec{\mu}\cdot\frac{d\vec{F}}{d\phi_M}$. It should be noted that both $\vec{F}$ and $\frac{d\vec{F}}{d\phi_M}$ is the e distance

(measured from the surface of electrode) the dependent, one needs to specify a position when reporting their values.

To capture the position dependent $\vec{F}$ and $\frac{d\vec{F}}{d\phi_M}$ profile, we restricted our model as a one-dimensional system as depicted in **Figure 4.10**A. And without loss of generality, we assume the thickness of the Stern layer, or equivalently, the distance between the electrode surface and OHP, is 0.5 nm and the concentration of $NaClO_4$ is tuned from 0.1 M to 0.5 M. To mimic the two scenarios in Figure 4.9A, C, we select two points: point *a* resides in the diffuse layer (scenario 1) and point *b* is positioned in a closer region within the diffuse layer (scenario 2). The position dependent potential ϕ (the results returned from the numerical solver) and electric field $\vec{F} = -\nabla\phi$ are plotted in **Figure 4.10**b and **Figure 4.10**C for 0.1 M $NaClO_4$. The linear relationship between ϕ and *x*, and most importantly, the constant $\vec{F}$ within the Stern layer (insets) confirm the robustness of the simulation. The same analysis is then extended to other ionic strengths and applied potential, and the simulated electric field (blue circle) and corresponding linear fit (red line) at point *a* and *b* are displayed in **Figure 4.10**D. The linear fit yields the slope $\frac{d\vec{F}}{d\phi_M}$ for each curve which dictates the Stark tuning slope and is depicted in **Figure 4.10**E. As mentioned above that $\frac{d\vec{F}}{d\phi_M}$ determines the trend of Stark tuning slope, our simulated results collaborated well with the two scenarios in Figure 4.9. It should be noted that the though the value of $\frac{d\vec{F}}{d\phi_M}$ seems small, the multiplication with $-\Delta\vec{\mu}$ is the one that is comparable with experimental measured $\frac{d\omega}{d\phi_M}$.

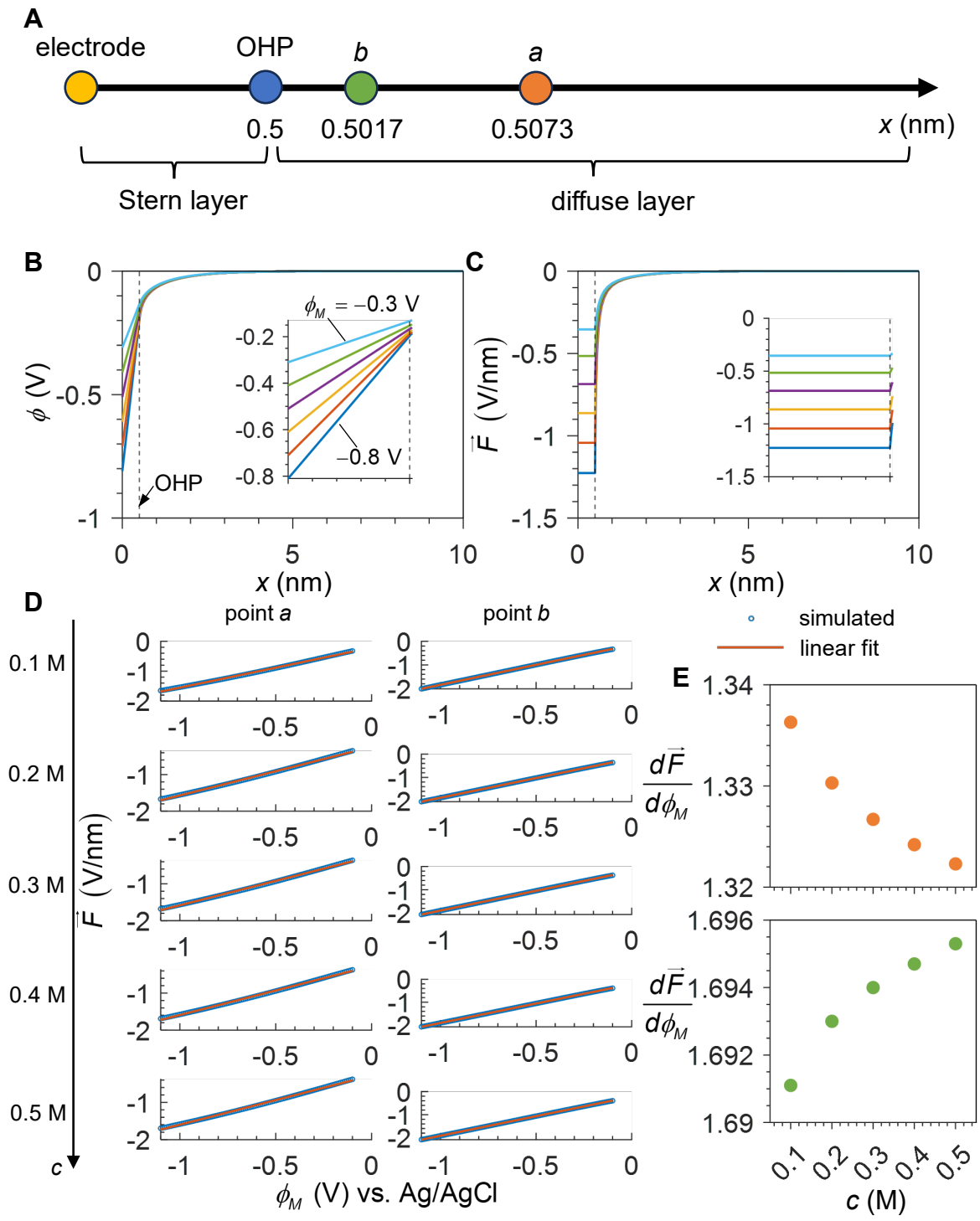

Figure 4.10. Simulated results of position-dependent Stark tuning slope. (A) One-dimensional model represents diffusion of ions away from gold electrode with double-layer structure defined. (B) Simulated potential and (C) electric field at each position evaluated at

different applied potential. (D) Ion concentration dependent $\vec{F}$-ϕ_M curve evaluated at point *a* and *b*. (E) Fitted slope $\frac{d\vec{F}}{d\phi_M}$ for point *a* (top) and *b* (bottom).

In the third scenario, we consider cases in which the probed modes of the molecules are densely packed close to the interface shown as **Figure 4.9**E. In this configuration, these modes are entirely contained within the OHP. As a result of this compact arrangement, the potential drop across these modes remains relatively modest, and the dominance of the potential drop occurs between the end of the molecule and the OHP. Consequently, the anticipated change in response is independent of the ionic strength (**Figure 4.9**F). This absence of an ionic strength-dependence origins from the fact that modifications in the ionic strength primarily happens in the diffuse layer.

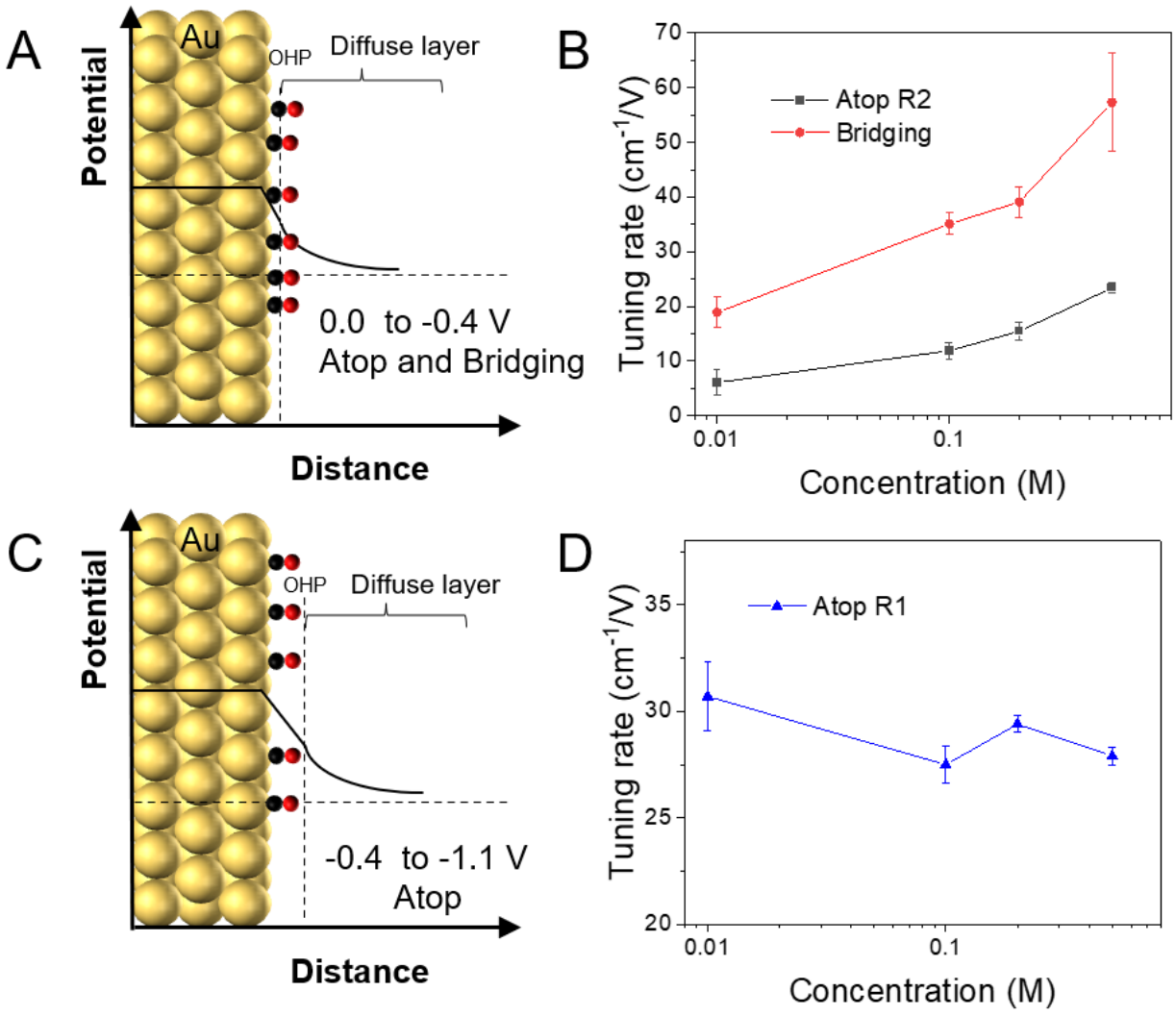

Figure 4.11. The models of different structures of CO in the double layer on Au

(A) From 0.0 V to -0.4 V, the atop mode and bridging mode coexist within diffuse layer. (B) Stark tuning rates of CO on Au: bridging (A1) atop (A2, R2) as a function of ionic strength in solutions with different ionic strength: 0.01 M, 0.1 M, 0.2 M, 0.5 M $NaClO_4$
(C) From -0.4 to -1.1 V, only the atop mode exists (within OHP), (B) Stark tuning rates of CO on Au: atop (A1, R1) The solutions are: 0.01 M, 0.1 M, 0.2 M, 0.5 M $NaClO_4$.

Returning to the analysis of the adsorbed CO on the Au system, we have observed two distinct ionic strength dependencies within different potential regions. From 0 V to -0.4 V, we observe two binding modes of *CO: the atop mode and the bridging mode. Both of these modes exhibit a dependence on changes in ionic strength. Notably, as the ionic strength increases, resulting in a smaller Debye length, the Stark slopes exhibit a corresponding increase. We infer that within this potential range, both forms of CO likely show relatively loose packing configurations on the Au surface. Consequently, this behavior is consistent with the second scenario discussed previously. The potential drops across the CO layer, and their response serves as a reflection of the properties of the surrounding diffuse layer during this phase.

From -0.4 V to -1.1 V, the bridging mode of CO disappears, and all CO converts into the atop configuration. Remarkably, the frequency of atop CO within this range shows negligible dependence on the ionic strength. This phenomenon indicates a strong interaction with the Au metal substrate such as CO on Pt[17]. CO can be also taken as forming an adlayer on the metal surface. Here, the potential drop predominantly occurs at the juncture of the CO and the Overlapping Helmholtz Plane (OHP). The behavior of *CO in this range remains is consistent with the third scenario discussed previously.

4.6. Conclusion

In conclusion, we investigate the structure and properties of the interfacial electric double layers (EDLs) of the adsorbed CO on Au system through vibrational Stark tuning slopes of the CO. Through the application of in-situ SERS technique, we observe two distinct peaks of adsorbed CO on Au, atop mode of CO at higher frequency region and bridging mode at lower frequency region. By changing the ionic strength of the electrolyte, our investigation reveals the effects of the diffuse layer thickness on the Stark effect of adsorbed CO on Au. Our results reveal that these 2 modes exhibit different appearance electrochemical windows and show different ionic strength dependence. In the potential range spanning from 0 V to -0.4 V, the coexistence of atop and bridging *CO modes is observed, both exhibiting a positive ionic strength dependence (with increasing ionic strength, the Stark slopes increases). This positive relationship between ionic strength and Stark slopes suggests that within this range, both forms of *CO likely assume loose packing configurations on the Au surface so that they feel the changes in the diffuse layer. From -0.4 V to -1.1 V, we only observe atop configuration without bridging mode. And within the range, the atop *CO exhibits independence from ionic strength variations, signifying a robust interaction with the Au metal substrate. This observation indicates the *CO as an adlayer on the Au metal surface, with potential drop primarily localized at the CO-OHP juncture, thus almost no potential drop can be felt across CO within this range. In summary, our observation and investigation reveal the double layer properties of adsorbed CO on Au, providing deeper insights into electrocatalysis.

4.7. Reference

(1) Yu, J.; Yin, J.; Li, R.; Ma, Y.; Fan, Z. Interfacial Electric Field Effect on Electrochemical Carbon Dioxide Reduction Reaction. *Chem Catal.* **2022**, *2* (9), 2229–2252. https://doi.org/10.1016/j.checat.2022.07.024.
(2) Ge, A.; Rudshteyn, B.; Videla, P. E.; Miller, C. J.; Kubiak, C. P.; Batista, V. S.; Lian, T. Heterogenized Molecular Catalysts: Vibrational Sum-Frequency Spectroscopic, Electrochemical, and Theoretical Investigations. *Acc. Chem. Res.* **2019**, *52* (5), 1289–1300. https://doi.org/10.1021/acs.accounts.9b00001.
(3) Bhattacharyya, D.; Videla, P. E.; Cattaneo, M.; Batista, V. S.; Lian, T.; Kubiak, C. P. Vibrational Stark Shift Spectroscopy of Catalysts under the Influence of Electric Fields at Electrode–Solution Interfaces. *Chem. Sci.* **2021**, *12* (30), 10131–10149. https://doi.org/10.1039/D1SC01876K.
(4) Ardo, S.; Sun, Y.; Staniszewski, A.; Castellano, F. N.; Meyer, G. J. Stark Effects after Excited-State Interfacial Electron Transfer at Sensitized TiO_2 Nanocrystallites. *J. Am. Chem. Soc.* **2010**, *132* (19), 6696–6709. https://doi.org/10.1021/ja909781g.
(5) Murgida, D. H.; Hildebrandt, P. Electron-Transfer Processes of Cytochrome *c* at Interfaces. New Insights by Surface-Enhanced Resonance Raman Spectroscopy. *Acc. Chem. Res.* **2004**, *37* (11), 854–861. https://doi.org/10.1021/ar0400443.
(6) Bishop, D. M. The Vibrational Stark Effect. *J. Chem. Phys.* **1993**, *98* (4), 3179–3184. https://doi.org/10.1063/1.464090.
(7) Bhattacharyya, D.; Videla, P. E.; Palasz, J. M.; Tangen, I.; Meng, J.; Kubiak, C. P.; Batista, V. S.; Lian, T. Sub-Nanometer Mapping of the Interfacial Electric Field Profile Using a Vibrational Stark Shift Ruler. *J. Am. Chem. Soc.* **2022**, *144* (31), 14330–14338. https://doi.org/10.1021/jacs.2c05563.
(8) Sarkar, S.; Patrow, J. G.; Voegtle, M. J.; Pennathur, A. K.; Dawlaty, J. M. Electrodes as Polarizing Functional Groups: Correlation between Hammett Parameters and Electrochemical Polarization. *J. Phys. Chem. C* **2019**, *123* (8), 4926–4937. https://doi.org/10.1021/acs.jpcc.8b12058.
(9) Wright, D.; Sangtarash, S.; Mueller, N. S.; Lin, Q.; Sadeghi, H.; Baumberg, J. J. Vibrational Stark Effects: Ionic Influence on Local Fields. *J. Phys. Chem. Lett.* **2022**, *13* (22), 4905–4911. https://doi.org/10.1021/acs.jpclett.2c01048.
(10) Lambert, A. G.; Davies, P. B.; Neivandt, D. J. Implementing the Theory of Sum Frequency Generation Vibrational Spectroscopy: A Tutorial Review. *Appl. Spectrosc. Rev.* **2005**, *40* (2), 103–145. https://doi.org/10.1081/ASR-200038326.
(11) Staffa, J. K.; Lorenz, L.; Stolarski, M.; Murgida, D. H.; Zebger, I.; Utesch, T.; Kozuch, J.; Hildebrandt, P. Determination of the Local Electric Field at Au/SAM Interfaces Using the Vibrational Stark Effect. *J. Phys. Chem. C* **2017**, *121* (40), 22274–22285. https://doi.org/10.1021/acs.jpcc.7b08434.
(12) Sarkar, S.; Patrow, J. G.; Voegtle, M. J.; Pennathur, A. K.; Dawlaty, J. M. Electrodes as Polarizing Functional Groups: Correlation between Hammett Parameters and Electrochemical Polarization. *J. Phys. Chem. C* **2019**, *123* (8), 4926–4937. https://doi.org/10.1021/acs.jpcc.8b12058.

(13) Delley, M. F.; Nichols, E. M.; Mayer, J. M. Interfacial Acid–Base Equilibria and Electric Fields Concurrently Probed by *In Situ* Surface-Enhanced Infrared Spectroscopy. *J. Am. Chem. Soc.* **2021**, *143* (28), 10778–10792. https://doi.org/10.1021/jacs.1c05419.
(14) Clark, M. L.; Ge, A.; Videla, P. E.; Rudshteyn, B.; Miller, C. J.; Song, J.; Batista, V. S.; Lian, T.; Kubiak, C. P. CO_2 Reduction Catalysts on Gold Electrode Surfaces Influenced by Large Electric Fields. *J. Am. Chem. Soc.* **2018**, *140* (50), 17643–17655. https://doi.org/10.1021/jacs.8b09852.
(15) Ge, A.; Videla, P. E.; Lee, G. L.; Rudshteyn, B.; Song, J.; Kubiak, C. P.; Batista, V. S.; Lian, T. Interfacial Structure and Electric Field Probed by *in Situ* Electrochemical Vibrational Stark Effect Spectroscopy and Computational Modeling. *J. Phys. Chem. C* **2017**, *121* (34), 18674–18682. https://doi.org/10.1021/acs.jpcc.7b05563.
(16) *Electrochemical Methods: Fundamentals and Applications, 2nd Edition | Wiley*. https://www.wiley.com/en-us/Electrochemical+Methods:+Fundamentals+and+Applications,+2nd+Edition-p-9780471043720 (accessed 2023-06-19).
(17) Figueiredo, M. C.; Hiltrop, D.; Sundararaman, R.; Schwarz, K. A.; Koper, M. T. M. Absence of Diffuse Double Layer Effect on the Vibrational Properties and Oxidation of Chemisorbed Carbon Monoxide on a Pt(111) Electrode. *Electrochimica Acta* **2018**, *281*, 127–132. https://doi.org/10.1016/j.electacta.2018.05.152.
(18) Wasileski, S. A.; Koper, M. T. M.; Weaver, M. J. Field-Dependent Electrode−Chemisorbate Bonding: Sensitivity of Vibrational Stark Effect and Binding Energetics to Nature of Surface Coordination. *J. Am. Chem. Soc.* **2002**, *124* (11), 2796–2805. https://doi.org/10.1021/ja012200w.
(19) Roth, J. D.; Weaver, M. J. Role of Double-Layer Cation on the Potential-Dependent Stretching Frequencies and Binding Geometries of Carbon Monoxide at Platinum-Nonaqueous Interfaces. *Langmuir* **1992**, *8* (5), 1451–1458. https://doi.org/10.1021/la00041a034.
(20) Blizanac, B. B.; Arenz, M.; Ross, P. N.; Marković, N. M. Surface Electrochemistry of CO on Reconstructed Gold Single Crystal Surfaces Studied by Infrared Reflection Absorption Spectroscopy and Rotating Disk Electrode. *J. Am. Chem. Soc.* **2004**, *126* (32), 10130–10141. https://doi.org/10.1021/ja049038s.
(21) Beltramo, G. L.; Shubina, T. E.; Koper, M. T. M. Oxidation of Formic Acid and Carbon Monoxide on Gold Electrodes Studied by Surface-Enhanced Raman Spectroscopy and DFT. *ChemPhysChem* **2005**, *6* (12), 2597–2606. https://doi.org/10.1002/cphc.200500198.
(22) Oberst, J. L.; Jhong, H.-R. "Molly"; Kenis, P. J. A.; Gewirth, A. A. Insight into the Electrochemical Reduction of CO2 on Gold via Surface-Enhanced Raman Spectroscopy and N-Containing Additives. *J. Solid State Electrochem.* **2016**, *20* (4), 1149–1154. https://doi.org/10.1007/s10008-015-2874-z.
(23) Zhang, P.; Wei, Y.; Cai, J.; Chen, Y.-X.; Tian, Z.-Q. Nonlinear Stark Effect Observed for Carbon Monoxide Chemisorbed on Gold Core/Palladium Shell Nanoparticle Film Electrodes, Using in Situ Surface-Enhanced Raman Spectroscopy. *Chin. J. Catal.* **2016**, *37* (7), 1156–1165. https://doi.org/10.1016/S1872-2067(15)61106-8.
(24) Zhang, P.; Cai, J.; Chen, Y.-X.; Tang, Z.-Q.; Chen, D.; Yang, J.; Wu, D.-Y.; Ren, B.; Tian, Z.-Q. Potential-Dependent Chemisorption of Carbon Monoxide at a Gold Core−Platinum Shell Nanoparticle Electrode: A Combined Study by Electrochemical in Situ Surface-Enhanced Raman Spectroscopy and Density Functional Theory. *J. Phys. Chem. C* **2010**, *114* (1), 403–411. https://doi.org/10.1021/jp908478m.

(25) Parsons, R. The Electrical Double Layer: Recent Experimental and Theoretical Developments. *Chem. Rev.* **1990**, *90* (5), 813–826. https://doi.org/10.1021/cr00103a008.
(26) Oklejas, V.; Sjostrom, C.; Harris, J. M. SERS Detection of the Vibrational Stark Effect from Nitrile-Terminated SAMs to Probe Electric Fields in the Diffuse Double-Layer. *J. Am. Chem. Soc.* **2002**, *124* (11), 2408–2409. https://doi.org/10.1021/ja017656s.
(27) Oklejas, V.; Sjostrom, C.; Harris, J. M. Surface-Enhanced Raman Scattering Based Vibrational Stark Effect as a Spatial Probe of Interfacial Electric Fields in the Diffuse Double Layer. *J. Phys. Chem. B* **2003**, *107* (31), 7788–7794. https://doi.org/10.1021/jp0344693.

5. Chapter 5 Vibrational Spectroscopic Probing the impact of Nanoparticle Proximity on Interfacial Electric Fields

5.1. Introduction and background

Probing and understanding the interfacial electric field within electric double layers (EDLs) is of great importance in electro/photo-catalysis on metal/semiconductor surfaces[1–3], which plays a vital role in tuning electrochemical performances[4–7]. The development of electrochemical *in-situ* vibrational spectroscopic techniques has enabled researchers to study static electric fields based on the molecular-level information at the interfaces[8–13]. The spectroscopic tools, either selectively enhance the signal from interfaces (i.e. Surface Enhanced Raman Spectroscopy, SERS) or are intrinsically generated from the surface[14] (i.e. Vibrational Sum Frequency Generation Spectroscopy, VSFGS[15,16]), and can report the frequency of certain vibrational modes and their dependence on the ruling factors, such as electric field[13,17,18], temperature[19], coverage[20], etc. The electric field-dependent vibrational frequency shift, known as the Stark effect[21,22], can be used as a probe for the local electric field experienced by the vibrational modes of interest[8,10,17,18,23,24]. These measurements provide an experimental picture of the EDL with the profile of the electric field strength at the molecular level and facilitate the investigation of interfacial electric fields, which can be compared with classic theoretical models of the EDL such as Gouy-Chapman model, Gouy-Chapman-Stern model, etc[25].

Among the various surface-sensitive spectroscopic techniques, surface-enhancement-based techniques, such as Surface-enhanced Raman and surface-enhanced Infrared absorption, require plasmonic nanostructures or nanoparticles (NPs) near the surface to enhance the intensity of the interfacial optical phenomena[26–28]. The extent to which the addition of these NPs perturbs the EDL and further affects the characterization results remains debated. For instance, *in situ* Shell Isolated Nanoparticle Enhanced Raman Spectroscopy (SHINERS)[29], employing shell-isolated plasmonic nanoparticles, has been widely utilized in probing electrochemical electrode/electrolyte interfaces[30,31] and identifying key intermediates in energy conversion systems[32–35], but it is recently reported[36] that the absolute frequency of certain modes of

molecules are also affected and show a NP-distance dependence when the Raman signal is enhanced via the electromagnetic field enhancement mechanism in a SHINERS system, which indicates the additional NPs' influence on the surface static electric field. When utilizing a scanning-tip-enhanced Raman experiment, previous studies[37,38] also reported substantial perturbation of the EDL in the presence of the STM tip, highlighting the potential sensitivity of the interfacial environment to physical and chemical modifications. SERS with Nanoparticle-on-Mirror(NPoM) scheme[13,39–44] presents a similar controversial question on whether the probed IEF is affected. It has been reported[13,40] that the molecules inside the "sandwich" structure show a Stark tuning slope similar to that measured by conventional SERS without sandwich structures, indicating the unaffected static IEF in the EDL; conversely, other studies[45–47] claimed that the vibrational molecular probes are affected by the local electric field environment in a gap mode SERS, which can be modulated by the gap size and affected by the polarized NPs from the electron tunneling across the junction.

In this section, shown in ***Figure 5.1***, we aim to investigate the influence of nanoparticle proximity on interfacial static interfacial electric fields (IEF) by comparing the absolute frequencies and the Stark tuning slopes (the potential dependent frequency shift) of several vibrational modes on the same electrode with nanoparticles on the surface probed by SHINERS and without nanoparticles probed by VSFGS (shown in Figure 1.). The pronounced vibrational modes of molecules are intentionally selected with a longitudinal distance-dependent difference, specifically νCO in CO, νNC in phenyl isocyanide, νCN in 4-mercaptobenzonitrile, and νCO and νNC in tungsten-pentacarbonyl(1,4-phenelenediisocyanide) (molecular ruler used by previous work[18]). By examining the Stark tuning rates of these modes and comparing the results obtained using both SHINERS and VSFGS on the same "smooth" Au(polycrystalline) electrode surface, we seek to answer whether and how the NPs on the surface affect the static IEF at an electrochemical interface. Furthermore, we intend to provide valuable insights into the spatial variance of the impact of nanoparticles on IEF and the applicability of SHINERS and SFG for studying such phenomena.

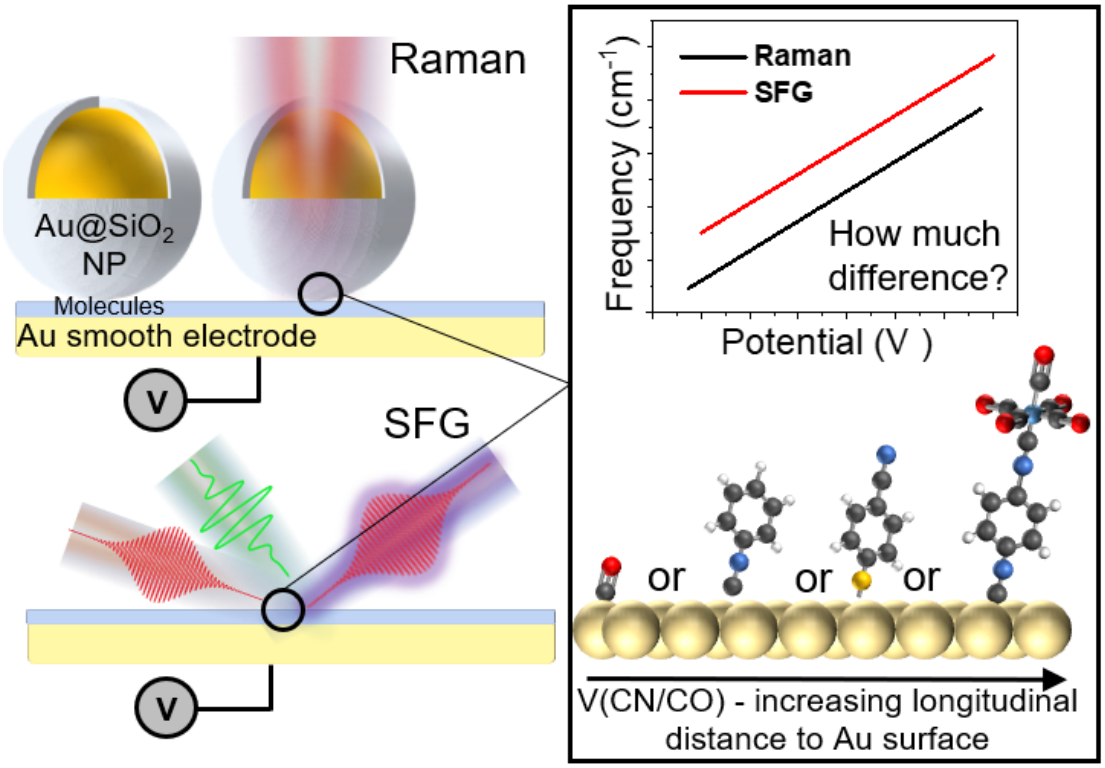

Figure 5.1. Scheme of Stark probe comparison of SFG and SHINERS
Schematic of *in situ* electrochemical SHINERS/VSFGS measurements in probing interfacial electric fields by Stark tuning slopes of the molecules on Au(poly) electrodes. Different color spheres represent different atoms: black-carbon, red-oxygen, white-hydrogen, and blue-nitrogen.

5.2. Impacts of NPs on EF probed by the comparison of SFG/SHINERS

5.2.1. Considerations for SHINERS/VSFGS comparison

The different vibrational spectroscopic techniques should have identical frequencies for the same probed modes of the species in theoretical principle if they are both IR and Raman active. This is because the transition between energy levels is uniquely determined and is irrelevant to the techniques. In practical experiments, the spectra obtained using different measurement techniques may not be identical due to many reasons. For example, the full-width at half-maximum (FWHM) of a vibrational mode may differ due to different selection rules or surface inhomogeneity[33], as well as the convolution of the probe FWHM with the spectral width of the vibrational mode itself. Differing enhancement mechanisms often show very different spectra, as not every mode will benefit from equal enhancement[49]. Besides, if the surface enhancement by different surface treatments is involved, more factors may perturb the actual surface environment, leading to discrepancies in the observed absolute frequencies among different techniques, i.e. different surface adsorption sites/geometries under different probing techniques[32,34,35], the surface roughness of substrates[33], surface selection rules[48], and different local temperatures[19]/coverage[20]/orientation, etc.

In our measurements, such mentioned surface environmental differences may cause a difference in spectra measured with VSFGS versus SHINERS, as while VFSGS intrinsically probes the behavior of the majority of molecules at the interfaces, surface-enhanced spectroscopies only probe the subpopulation of the molecules at the "hot spot" where the electromagnetic electric fields are enhanced. Thus, to control the focus of the study on the effect of NPs and exclude the effects of others, we use the same Au electrode with the same treatment process (mechanical polishing and electrochemical cleaning), except for NP drop-casting in the case of SHINERS measurements, and the same molecular samples. Furthermore, to validate the applicability of the measurements with two different techniques to elucidate possible light effects by different light sources, a model system of weakly bonded CO on Au which is sensitive to light perturbation in spectroscopic measurements is chosen first for benchmarking.

5.2.2. Feasibility test on spectroscopic comparison — CO_{ad} on Au

CO adsorbed on Au is a model system for vibrational spectroscopic studies — CO is comprised of only two atoms and the stretching mode ν(CO) shows a pronounced peak in many surface-sensitive spectroscopic tools, e.g., SEIRAS, SERS, and SFG. Due to the weak binding energy of CO_{ad} on Au, this system can be easily perturbed by external electromagnetic fields, thus techniques with varied wavelengths (e.g. IR vs. Raman)[50] and/or different optical powers (e.g., pulsed vs. continuous illumination)[19] may lead to large differences in absolute frequencies and Stark tuning rates[50], and even induce some desorption of CO[19].

With the weakly bonded CO on Au, we can first investigate how different external electromagnetic fields from two techniques influence Stark tuning slopes in our measurements. It is worth noting that the laser characteristics in Raman measurements (continuous wave, 633 nm) differ from those in SFG measurements (1 kHz pulsed, featuring narrowband 800 nm and broadband IR centered around 4700 nm). Thus, we hypothesize that if the results measured by SFG and SHINERS are quite similar in binding onset potentials, absolute frequencies, and Stark tuning slopes within the weakly bound CO-Au system, then these similarities can rule out the interference of external electromagnetic fields in the comparison study, or other words, the different conditions/environment at the surfaces by two techniques should not introduce observable differences. Under this hypothesis, we further believe that these effects from external illumination should not impact more strongly bonded systems, such as self-assembled monolayers (SAM).

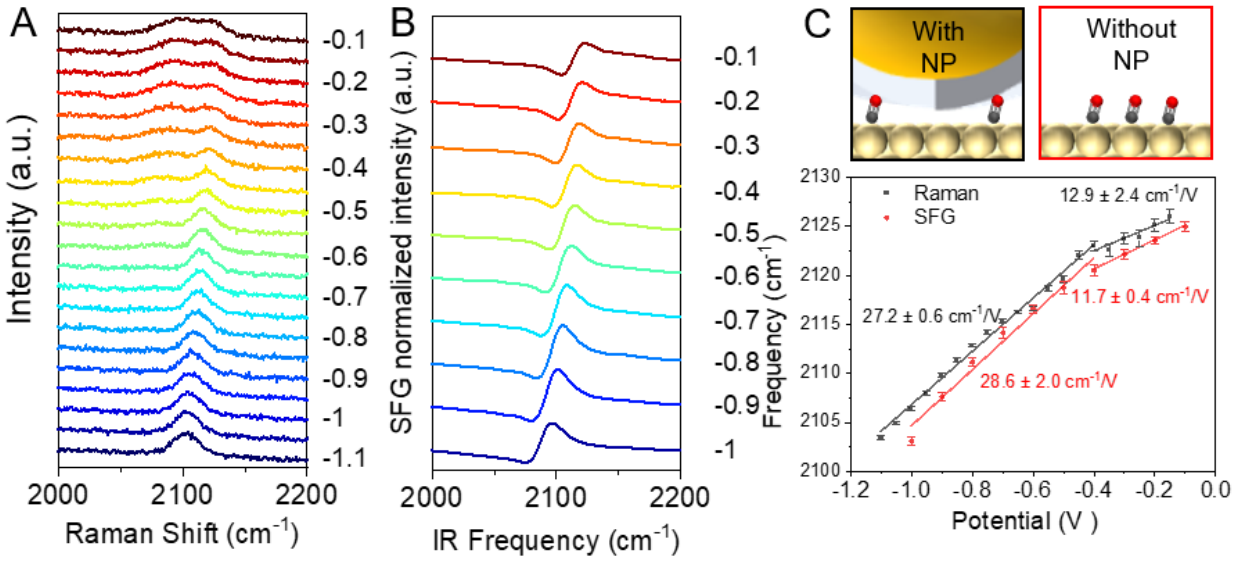

Figure 5.2. Comparison results of *CO on Au
(A) Potential dependent *in situ* Raman spectra of CO_{ad} on Au(poly) in CO-saturated 0.1 M $NaClO_4$ solution. (B) Potential dependent *in situ* vibrational SFG spectra of CO_{ad} on Au(poly) with the same sample in CO saturated 0.1 M $NaClO_4$ solution. (C) The CO stretching frequencies at around 2100 cm^{-1} (obtained from fitting) in Raman and SFG measurements as a function of potential. The squares and circles represent the measured data points, and the lines represent the linear fitting of the data, the Stark tuning slopes are obtained by the intercepts from the fitting lines, and all data are labeled in black (Raman) and red (SFG).

As illustrated in ***Figure 5.2***, the Raman and SFG peak frequencies were obtained by fitting the spectra (seen in Chapter 3). two pronounced peaks at around 2080 cm^{-1} and 2120 cm^{-1} were observed in Raman, where the lower frequency peak shows from -0.1 V to -0.5 V, and the higher frequency peak is prominent in all potential regions. In SFG spectra, the 2080 cm^{-1} peak is not as obvious as in Raman, but the weaker feature is still observable from -0.1 V to -0.5 V, the other higher frequency peak is more obvious through all potential windows at 2120 cm^{-1}. Based on the previous study[50], we assign the two peaks at different frequencies to different binding environments (i.e. terrace sites vs. step sites) and the peak at around 2080 cm^{-1} may have originated from competitive water or H_{ad} on metal co-adsorption[50,51]. To have a better comparison, we chose the more pronounced peak at 2120 cm^{-1} for detailed potential dependent frequency analysis. From the results in Figure 2C, we found that both Raman and SFG showed two separate Stark slopes from the single 2120 cm^{-1} peak, the first region is from -0.1 to around -0.5 V, the slopes are 12.9 and 11.7 cm^{-1}/V respectively, the second region is from -0.5 to -1.0 V, the slopes are 27.2 and 28.6 cm^{-1}/V respectively. The two-segment slope pattern and the

appearance of the lower Stark tuning slopes in the first region may be related to the CO_{ad} surface coverage difference originating from competitive co-adsorption of water or H_{ad} on metal, as the lower frequency CO_{ad} also appears in the first region. Similar observations on the double-slope of Stark tuning rates have also been reported for CO_{ad} on Pd[51], in which it is presumably initiated by the co-adsorption or H_{ad}.

Nevertheless, the Stark tuning slopes of CO_{ad} on Au by Raman and SFG showed quite similar results, both in the absolute frequencies and the Stark tuning slopes, this indicates that the comparison between the two techniques with different laser properties is plausible. Furthermore, it shows that for the weakly bonded molecules as the CO_{ad} on Au, the presence of nanoparticles places little effect on the static electric field within the double layer, or more specifically, the static IEF within the outer Helmholtz plane(OHP) region where CO_{ad} exists is not noticeably affected.

5.2.3. The impacts of NPs within OHP — PIC on Au

With the previous validation of the concept of comparison by different techniques, we further did similar measurements with PIC SAM on Au to test the impacts of NPs on EDL within OHP. The main difference between the SAM and the CO_{ad} is that SAM forms a relatively stronger bond with the Au surface through the Au-C or Au-S bond, which makes a more stable surface coverage without changing the population of adsorbates during an electrochemical potential change. Thus, the results of SAM can provide a more rigorous comparison by ruling out the adsorbate population changes. PIC binds on the Au surface through the Au-C bond, where the -NC group is directly attached to the Au surface and can be a probe of EF change within OHP in EDL.

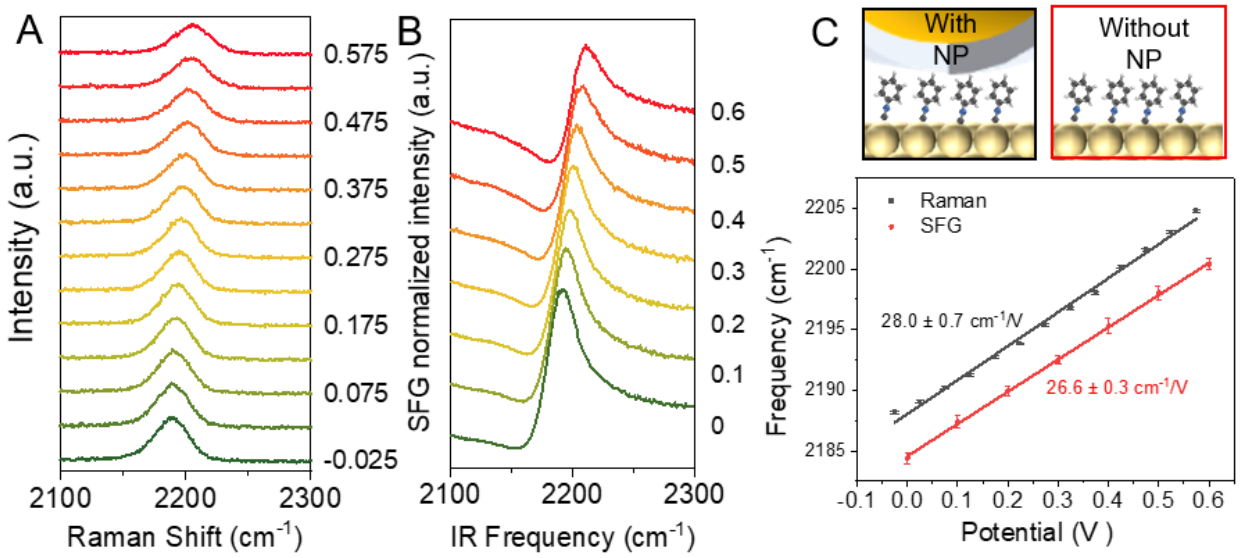

Figure 5.3. Comparison results of PIC on Au
(A) Potential dependent *in situ* Raman spectra of SAM (phenyl isocyanide) on Au(poly) in Ar saturated 0.1 M $NaClO_4$ solution. (B) Potential dependent *in situ* vibrational SFG spectra of SAM (phenyl isocyanide) on Au(poly) with the same sample in Ar saturated 0.1 M $NaClO_4$ solution. (C) The -NC stretching mode frequencies in Raman and SFG measurements as a function of potential. The squares and circles represent the measured data points, and the lines represent the linear fitting of the data, the Stark tuning slopes are obtained by the intercepts from the fitting lines, and all data are labeled in black (Raman) and red (SFG).

As ***Figure 5.3***A and B show, Raman and SFG spectra were collected from 0 V to 0.6 V in Ar Ar-saturated 0.1 M $NaClO_4$ solution. The PIC SAM was firstly prepared on Au electrode surface and the NPs were then drop-cast later to form the "sandwich" structure. The -NC stretching band appears in both cases with one noticeable peak at around 2190 cm^{-1} region. By detailed fitting of the spectra, the potential dependent frequency was obtained in Figure 3-C. The Stark tuning slopes of PIC on Au are also quite similar for the two techniques, 28.1 cm^{-1}/V for Raman and 27.7 cm^{-1}/V for SFG. Similar to the previous scenario, the similarity on the Stark tuning slopes indicates that the nanoparticles place little effect on the static electric field within the double layer within the inner Helmholtz plane. However, the absolute frequencies of the two techniques show a roughly ~5 cm^{-1} difference, this difference indicates that the existence of nanoparticles on the surface may change the surface coverage of the PIC SAM, leading to the frequency shifts from different degrees of intermolecular interaction (dipole-dipole interaction[20]). Besides, we also noticed that the Stark slope of the -NC group in PIC is slightly different from what was reported in 1,4-pheylene diisocyanide (PDI) on Au (~16-20 cm^{-1}/V)[16], we believe this

discrepancy is due to the para-substituted group on the other end of the benzene ring – as it may modify the electron density of the benzene ring and -NC, which induced different response to the change of electric field.

5.2.4. The impacts of NPs within diffuse layer— 4-MBN on Au

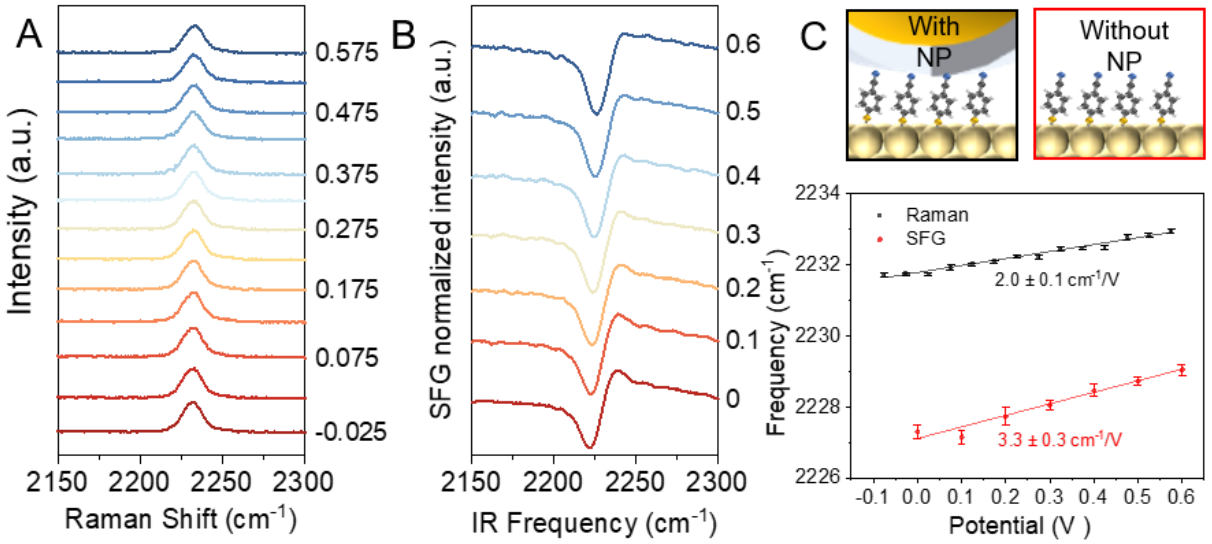

Figure 5.4. Comparison results of 4-MBN on Au

(A) Potential dependent *in situ* Raman spectra of SAM(4-mercaptobenzonitrile) on Au(poly) in Ar saturated 0.1 M $NaClO_4$ solution. (B) Potential dependent *in situ* vibrational SFG spectra of SAM(4-mercaptobenzonitrile) on Au(poly) with the same sample in Ar saturated 0.1 M $NaClO_4$ solution. (C) The -CN stretching mode frequencies in Raman and SFG measurements as a function of potential. The squares and circles represent the measured data points, and the lines represent the linear fitting of the data, the Stark tuning slopes are obtained by the intercepts from the fitting lines, and all data are labeled in black (Raman) and red (SFG).

We then move on to analyze another extreme, in which the molecular probe is adjacent to NPs and is relatively far away from the electrode surface and within the diffuse layer. In this scenario, we anticipate that the NPs should have a nonnegligible effect on the static electric field around it and thus the Stark tuning slopes should have quite different features for Raman (w/ NPs) and SFG (w/o NPs). To test this hypothesis, we utilized the 4-MBN SAM, in which the nitrile group -CN is far away from the electrode surface (compared with PIC or CO) and pointing

towards the NPs. Many previous reports[10,52,53] have successfully shown that 4-MBN can be applied on metal surfaces as a molecular probe for the surface electric field strength, and the Stark slopes can vary based on certain conditions (solvents, ionic strength, potential region, etc.). In our case, we compared the spectra in Ar-saturated 0.1 M NaClO4 solution from 0 V to 0.6 V to avoid any possible reactions that may interfere with the measurements. As Figure 4A and B shows, one pronounced -CN stretching mode at ~2220 to 2230 cm^{-1} was observed in both Raman and SFG. With the spectra fitting, the detailed potential dependent frequency can be obtained (in Figure 4C). In contrast to PIC on Au, the Stark tuning slopes of 4 -MBN measured by SFG and Raman are quite different (SFG is ~65% larger than Raman), with 2.0 cm^{-1}/V for Raman and 3.3 cm^{-1}/V for SFG, with the absolute frequencies also showing 4~5 cm^{-1} difference. This dramatic difference indeed bolstered the initial hypothesis, that is, the existence of NPs poses a noticeable effect on the static electric field near the NP surface.

5.2.5. The whole profile of the EF affected by the NPs —molecular Ruler on Au

To quantify the length of the affected region due to NPs, we further conducted an SFG/Raman comparison study using the ruler molecule: tungsten-pentacarbonyl(1,4-phenelenediisocyanide) since it contains multiple vibrational active groups located at different positions.

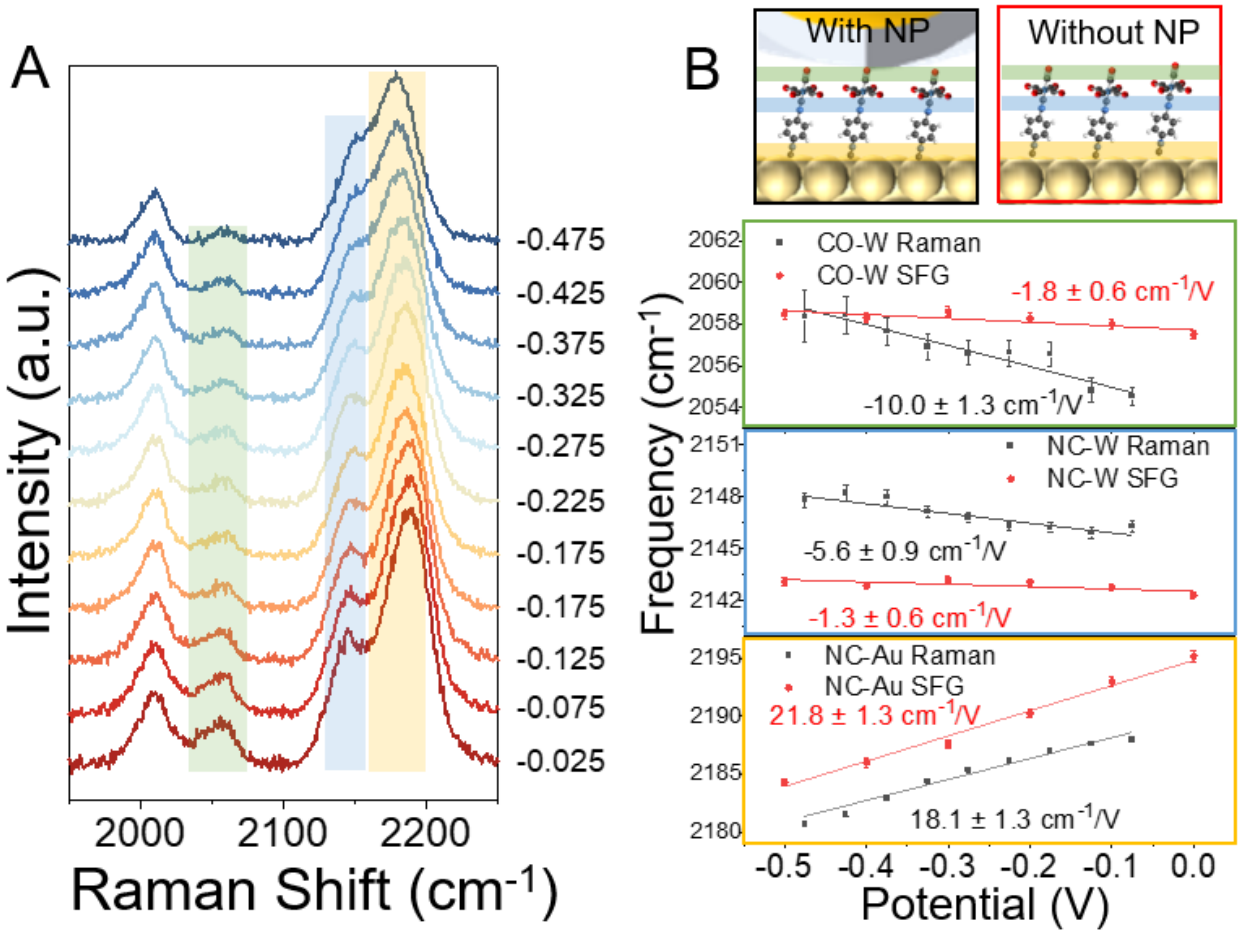

Figure 5.5. Comparison results of the molecular ruler on Au

(A) Potential dependent *in situ* Raman spectra of SAM (tungsten-pentacarbonyl(1,4-phenelenediisocyanide)) on Au(poly) in Ar saturated 0.2 M $TBAPF_6$ acetonitrile solution. (B) The -NC-Au (yellow label), -NC-W (blue label), and W-CO (green label) frequencies in Raman and SFG measurements as a function of potential. Results of SFG data are taken from previous publication[18]. The squares and circles represent the measured data points, and the lines represent the linear fitting of the data, the Stark tuning slopes are obtained by the intercepts from the fitting lines, and all data are labeled in black (Raman) and red (SFG).

Our previous SFG study[18] has shown the success of describing the static electric field profile based on the measurements of the multiple -NC and -CO modes in the ruler molecule. Thus, we took advantage of the multiple modes in the study and placed the same SAM under the same condition with NPs for the comparison.

As ***Figure 5.5***A shows, the Raman spectra of ruler molecules showed 4 peaks at different frequencies, ~2000 cm^{-1} for Fermi resonance, ~2060 cm^{-1} for the -CO attached with W, ~2140

cm^{-1} for -NC attached with W, ~2190 cm^{-1} for -NC attached with Au. We obtained the SFG results at a similar potential region from the study[18] in our group and compared them with Raman results in ***Figure 5.5***A. For the mode closer to the Au electrode surface, NC-Au (yellow labeled), shows a similar Stark tuning slope by Raman and SFG, with 21.8 cm^{-1}/V and 18.1 cm^{-1}/V respectively; while a larger difference on the Stark tuning slope can be observed by Raman -5.6 cm^{-1}/V and SFG -1.3 cm^{-1}/V for the mode further to the surface, NC-W (blue labeled); as for the mode close to the NPs, CO-W, a noticeable difference on the tuning slope is shown, -10 cm^{-1}/V for Raman and -1.8 cm^{-1}/V for SFG. The observation on the ruler molecule system confirms that the different vibrational modes in one molecule on the electrode surface can experience different influences on the local static electric field (EF) by the NPs assembled on the electrode, the closer the modes are from the NPs, the bigger changes on the EF they can feel.

5.2.6. The model of the electric double layer with NPs

The physical picture of the EDL is usually described and interpreted by theoretical models. In the conventional Gouy-Chapman-Stern model54, the electric double layer consists of a Stern layer where the electric potential drops linearly as a function of distance to the surface and a diffuse layer where the electric potential drops exponentially. This model considers the specific adsorption of ions at the charged surface. The position where the nearest solvated ions from the electrolyte can penetrate the surface adsorbates by diffusion is the Outer Helmholtz Plane (OHP), which divides the Stern layer and the diffuse layer. In the case of 4-MBN, PIC like SAM adsorbates electrolyte such as around 0.1 M NaClO4, the OHP should be near the end of the benzene ring of the molecules[13,18].

The Stark tuning rate of certain mode reflects how electric potential drops(EF) at the exact position; therefore, the differences in the measured tuning rates of the mode with and without NPs describes how the EF is affected by the NPs, and analyzing the differences with the modes at different positions can provide a quantitative description of the degree of the EF being influenced by NPs and their relative positions of the NPs-effect. We label the probed modes in different molecules as 2 categories based on their relative positions in the EDL of the Au electrode: within the Stern layer (close to the electrode and far from the NPs) and within the

diffuse layer (close to the NPs and far from the electrode). The measured modes within the Stern layer region show a relatively smaller difference in Stark tuning rate, i.e., the vCO on Au shows ~ -5 % difference with Raman vs. SFG comparison, the vNC mode in PIC also shows ~ 5 % difference, and the vNC mode in molecular ruler shows ~ -17 % difference. This experimental observation indicates the assembled NPs on Au electrode surface only pose a limited effect on the electric potential gradient (electric field) within Stern layer. As for the modes within the diffuse layer of the electrode surface, they show much bigger difference, i.e., the vCN in 4-MBN show ~40 % difference, vCN of W-CN and vCO of W-CO in the ruler molecular system show ~ 330 % and ~ 455 % differences, respectively. The bigger difference reveals that the electric field in the diffuse layer is quite different from that with the addition of the NPs.

To validate this conclusion from the experimental observation, we have other simulation in progress. The results are summarized into a qualitative model (seen in **Figure 5.6**) to describe the impacts of NPs near the electrode in the molecular ruler system. In this model, the adjacent NP is next to the SAM molecule on the surface, the OHP divides the Stern layer and the diffuse layer, the red and black lines represent the profile of the electric potential as a function of distance to the surface with NPs and without NPs, respectively; within the Stern layer, the difference on the profile of electric potential between the two conditions is not noticeable, and within the diffuse layer, the electric potential with NPs is affected by the existence of the adjacent NPs, and thus shows a significant variance compared with that under no NPs condition. This different electric potential profile with NPs should be mainly attributed to the superposition of the electric field from the Au electrode surface and the additional electric field generated from Au NPs. Other possible reasons are discussed in the following section. And it should be noted that what is presented in the figure is that the electric potential drops faster without the NP, but the exact effects may vary based on different conditions (i.e., the potential of zero charge on the surface, the SAM molecular structure with different function groups, the ions in the electrolyte, etc.). This model may help to understand why previous studies of the vibrational mode close to the electrode with NP showed little difference in the Stark tuning rate compared to that without NP[40], and the mode far from the surface showed a distinct difference[45].

The origins of the differences in Stark tuning rates. In the above model, we observe a Stark tuning difference in the diffuse layer with and without NPs and conclude that the NPs also

generate a certain electric field near its surface within a relatively short range, and thus the IEF in the diffuse layer can be changed. Besides this explanation, we think there should be other effects that the NPs can lead to and affect the IEF in the diffuse layer. The first possible effect may be from the interaction between the electrolytes and the surface NP. In specific, the NP near the surface should also interact with the electrolyte ions (Coulombic interaction or/and chemical interaction) and thus preferentially repel or attract certain ions from the electrolyte, making the screening charges different for the electrodes with NPs. It should be mentioned that in most measurements with small loading/assembling of NPs in spectroscopic studies, the NP-affected surface compared to the whole active surface of the electrodes is quite small, thus it is not easy to directly detect the difference in charging/discharging by electrochemical methods. Another possible effect may be due to the existence of the overlay IEF from both the Au electrode surface and NPs in the positions near the NP's surface. The IEF contributions from the NPs can also be fine-tuned by the polarization of the NPs through the electron tunneling effect[13,45] from the gap. While the electrode is being polarized, the NP near the surface can also be polarized by electron tunneling, so that another double layer and related electrochemical potential gradient can be formed near the NP/electrolyte interface. The molecules inside of the gap may feel the overlay of the two static electric fields, and the vibrational probes then respond differently.

The absolute frequency difference. Besides the different EF in the diffuse layer, which we interpreted from the observation based on the Stark tuning rates, we also noticed that in all molecule systems, the absolute frequencies probed by SFG and SHINERS present some variations. The variation by different techniques in CO_{ad} on the Au system is around 2~3 cm^{-1} (Raman bluer, SFG redder), 5~6 cm^{-1} in PIC or 4-MBN (Raman bluer, SFG redder), and 2~6 cm^{-1} in molecular ruler system. We first rule out the possibility of systematic errors in the observation, this is verified by the careful calibration of spectrometers before each measurement used in Raman and SFG spectroscopy (seen in SI). We then comment on the possible origins of the frequencies measured by different techniques, as mentioned earlier, the selection rules for Raman or SFG should present the same frequency, therefore, we believe this difference should be related to the surface environment difference: with or without NP. With NP standing on the surface and the molecules inside the “sandwich” structure, 1) the different dipole-dipole intermolecular interaction induced frequency shift[20] induced by different surface coverages w/ and w/o NPs; 2) frequency shift lead by the different orientation condition w/ and w/o NPs[55].

This cause also helps to explain why the absolute frequencies of the SAM systems are more influenced by NPs compared to that of CO, where the end of SAM is directly contacted with NP and the orientation is easier to be affected while a more rigid CO molecule may not.

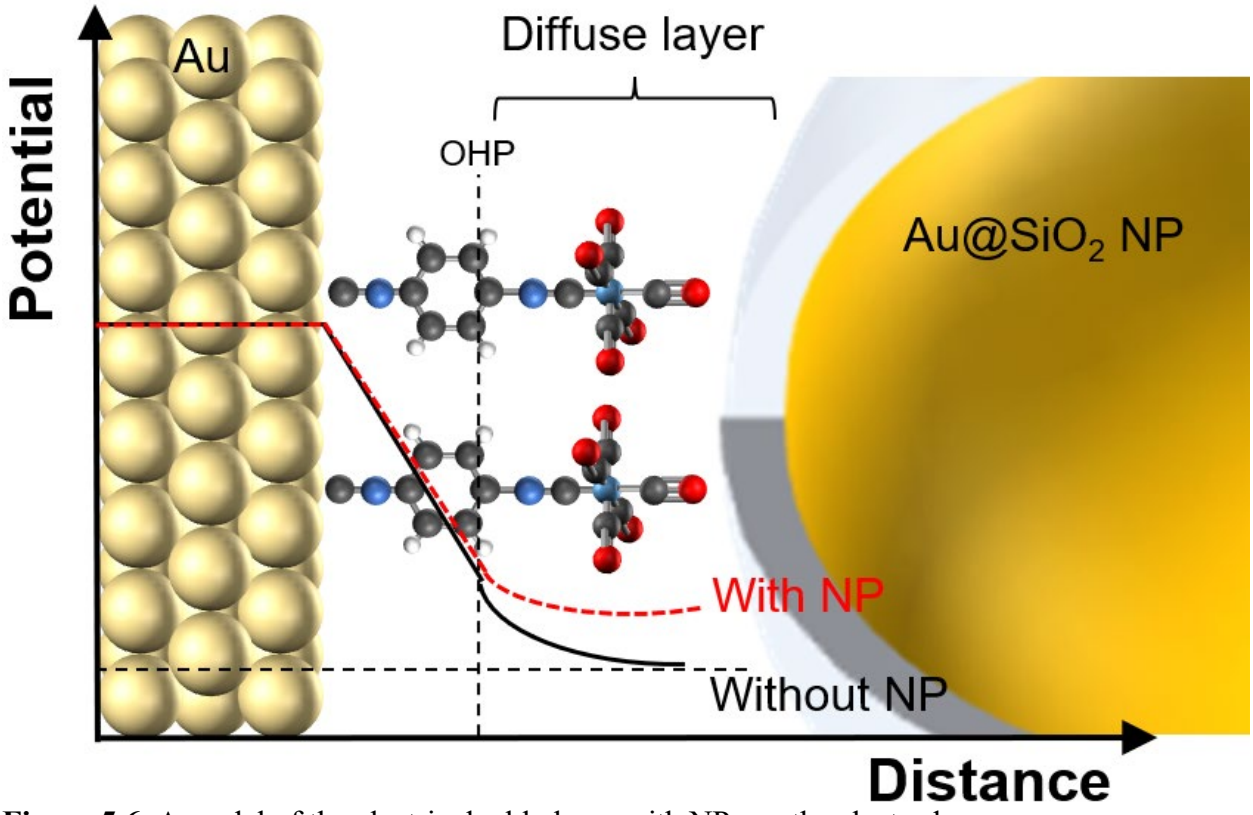

Figure 5.6. A model of the electric double layer with NPs on the electrode.
The black solid line represents the electrochemical potential profile without NPs, red dashed line represents the electrochemical potential profile with the NPs near the surface. The balls with colors represent different atoms (yellow-Au, black-C, dark blue-N, light blue-W, red-O).

5.3. Conclusions

To summarize, we conducted an *in situ* electrochemical SHINERS and VSFGS comparison study on 4 types of different molecular Stark reporters to study the impact of NP proximity on local static interfacial electric fields (IEF). The results of weakly bonded CO_{ad} on Au, as a benchmark showing similar Stark tuning slopes of CO with the two techniques, indicates the comparison by two techniques with different illumination conditions is feasible to represent the comparison by those with and without NPs adjacent to the surface; the results of other longitudinal length dependent SAM systems, phenyl isocyanide(close to electrode), 4-mercaptobenzonitrile(close to NP) and tungsten-pentacarbonyl(1,4-phenelenediisocyanide), representing the results of the probed moieties at different relative position in the electric double layers, present the following results: within OHP in the EDL, similar Stark tuning slopes of the molecular probes can be observed in PIC (~ 5% difference) and -NC in the ruler molecules(~ 17% difference); in the diffuse layer of the electrode, or closer to the NPs, the probed modes present quite different slopes, with the -CN in 4-MBN (~40 % difference), W-CN (~ 330 % difference), and W-CO (~ 455 % difference) in ruler molecular systems. These observations indicate that the NP near the electrode surface can greatly affect the EF in the diffuse layer but impacts little within OHP. We speculate that the differences should originate from the co-polarized NPs when the electrode is scanned at different potentials. The results with 4 different types of molecules on the Au surface provide a complete picture of how the static electric field is affected by the assembled NPs, where the closer to the NPs, the difference is. Our findings contribute to a deeper understanding of the interferences of the additional nanoparticles at electrochemical interfaces on the aspect of static interfacial electric fields, guiding researchers in selecting the most suitable techniques for their specific research goals and challenges in electrochemical spectroscopic studies, suggesting that applying NPs on the electrode for the analysis of vibrational spectroscopy requires the detailed consideration of the regions of interest and the methods of utilization.

5.4. References

(1) Ge, A.; Rudshteyn, B.; Videla, P. E.; Miller, C. J.; Kubiak, C. P.; Batista, V. S.; Lian, T. Heterogenized Molecular Catalysts: Vibrational Sum-Frequency Spectroscopic, Electrochemical, and Theoretical Investigations. *Acc. Chem. Res.* **2019**, *52* (5), 1289–1300. https://doi.org/10.1021/acs.accounts.9b00001.
(2) Ardo, S.; Sun, Y.; Staniszewski, A.; Castellano, F. N.; Meyer, G. J. Stark Effects after Excited-State Interfacial Electron Transfer at Sensitized TiO_2 Nanocrystallites. *J. Am. Chem. Soc.* **2010**, *132* (19), 6696–6709. https://doi.org/10.1021/ja909781g.
(3) Murgida, D. H.; Hildebrandt, P. Electron-Transfer Processes of Cytochrome *c* at Interfaces. New Insights by Surface-Enhanced Resonance Raman Spectroscopy. *Acc. Chem. Res.* **2004**, *37* (11), 854–861. https://doi.org/10.1021/ar0400443.
(4) Yu, J.; Yin, J.; Li, R.; Ma, Y.; Fan, Z. Interfacial Electric Field Effect on Electrochemical Carbon Dioxide Reduction Reaction. *Chem Catal.* **2022**, *2* (9), 2229–2252. https://doi.org/10.1016/j.checat.2022.07.024.
(5) Zhu, Q.; Wallentine, S. K.; Deng, G.-H.; Rebstock, J. A.; Baker, L. R. The Solvation-Induced Onsager Reaction Field Rather than the Double-Layer Field Controls CO_2 Reduction on Gold. *JACS Au* **2022**, *2* (2), 472–482. https://doi.org/10.1021/jacsau.1c00512.
(6) Warburton, R. E.; Hutchison, P.; Jackson, M. N.; Pegis, M. L.; Surendranath, Y.; Hammes-Schiffer, S. Interfacial Field-Driven Proton-Coupled Electron Transfer at Graphite-Conjugated Organic Acids. *J. Am. Chem. Soc.* **2020**, *142* (49), 20855–20864. https://doi.org/10.1021/jacs.0c10632.
(7) Shaik, S.; Ramanan, R.; Danovich, D.; Mandal, D. Structure and Reactivity/Selectivity Control by Oriented-External Electric Fields. *Chem. Soc. Rev.* **2018**, *47* (14), 5125–5145. https://doi.org/10.1039/C8CS00354H.
(8) Schkolnik, G.; Salewski, J.; Millo, D.; Zebger, I.; Franzen, S.; Hildebrandt, P. Vibrational Stark Effect of the Electric-Field Reporter 4-Mercaptobenzonitrile as a Tool for Investigating Electrostatics at Electrode/SAM/Solution Interfaces. *Int. J. Mol. Sci.* **2012**, *13* (6), 7466–7482. https://doi.org/10.3390/ijms13067466.
(9) Sarkar, S.; Tseng, C.; Maitra, A.; Voegtle, M. J.; Dawlaty, J. M. Advances in Vibrational Stark Shift Spectroscopy for Measuring Interfacial Electric Fields. In *ACS Symposium Series*; Berman, M. R., Young, L., Dai, H.-L., Eds.; American Chemical Society: Washington, DC, 2021; Vol. 1398, pp 199–224. https://doi.org/10.1021/bk-2021-1398.ch010.
(10) Sarkar, S.; Maitra, A.; Banerjee, S.; Thoi, V. S.; Dawlaty, J. M. Electric Fields at Metal–Surfactant Interfaces: A Combined Vibrational Spectroscopy and Capacitance Study. *J. Phys. Chem. B* **2020**, *124* (7), 1311–1321. https://doi.org/10.1021/acs.jpcb.0c00560.
(11) Oklejas, V.; Sjostrom, C.; Harris, J. M. SERS Detection of the Vibrational Stark Effect from Nitrile-Terminated SAMs to Probe Electric Fields in the Diffuse Double-Layer. *J. Am. Chem. Soc.* **2002**, *124* (11), 2408–2409. https://doi.org/10.1021/ja017656s.
(12) Oklejas, V.; Sjostrom, C.; Harris, J. M. Surface-Enhanced Raman Scattering Based Vibrational Stark Effect as a Spatial Probe of Interfacial Electric Fields in the Diffuse Double Layer. *J. Phys. Chem. B* **2003**, *107* (31), 7788–7794. https://doi.org/10.1021/jp0344693.

(13) Wright, D.; Sangtarash, S.; Mueller, N. S.; Lin, Q.; Sadeghi, H.; Baumberg, J. J. Vibrational Stark Effects: Ionic Influence on Local Fields. *J. Phys. Chem. Lett.* **2022**, *13* (22), 4905–4911. https://doi.org/10.1021/acs.jpclett.2c01048.
(14) Lambert, A. G.; Davies, P. B.; Neivandt, D. J. Implementing the Theory of Sum Frequency Generation Vibrational Spectroscopy: A Tutorial Review. *Appl. Spectrosc. Rev.* **2005**, *40* (2), 103–145. https://doi.org/10.1081/ASR-200038326.
(15) Shen, Y. R. Surface Properties Probed by Second-Harmonic and Sum-Frequency Generation. *Nature* **1989**, *337* (6207), 519–525. https://doi.org/10.1038/337519a0.
(16) Ge, A.; Videla, P. E.; Lee, G. L.; Rudshteyn, B.; Song, J.; Kubiak, C. P.; Batista, V. S.; Lian, T. Interfacial Structure and Electric Field Probed by *in Situ* Electrochemical Vibrational Stark Effect Spectroscopy and Computational Modeling. *J. Phys. Chem. C* **2017**, *121* (34), 18674–18682. https://doi.org/10.1021/acs.jpcc.7b05563.
(17) Sarkar, S.; Patrow, J. G.; Voegtle, M. J.; Pennathur, A. K.; Dawlaty, J. M. Electrodes as Polarizing Functional Groups: Correlation between Hammett Parameters and Electrochemical Polarization. *J. Phys. Chem. C* **2019**, *123* (8), 4926–4937. https://doi.org/10.1021/acs.jpcc.8b12058.
(18) Bhattacharyya, D.; Videla, P. E.; Palasz, J. M.; Tangen, I.; Meng, J.; Kubiak, C. P.; Batista, V. S.; Lian, T. Sub-Nanometer Mapping of the Interfacial Electric Field Profile Using a Vibrational Stark Shift Ruler. *J. Am. Chem. Soc.* **2022**, *144* (31), 14330–14338. https://doi.org/10.1021/jacs.2c05563.
(19) Hu, S.; Liu, B.-J.; Feng, J.-M.; Zong, C.; Lin, K.-Q.; Wang, X.; Wu, D.-Y.; Ren, B. Quantifying Surface Temperature of Thermoplasmonic Nanostructures. *J. Am. Chem. Soc.* **2018**, *140* (42), 13680–13686. https://doi.org/10.1021/jacs.8b06083.
(20) Pfisterer, J. H. K.; Zhumaev, U. E.; Cheuquepan, W.; Feliu, J. M.; Domke, K. F. Stark Effect or Coverage Dependence? Disentangling the EC-SEIRAS Vibrational Shift of Sulfate on Au(111). *J. Chem. Phys.* **2019**, *150* (4), 041709. https://doi.org/10.1063/1.5047941.
(21) Bishop, D. M. The Vibrational Stark Effect. *J. Chem. Phys.* **1993**, *98* (4), 3179–3184. https://doi.org/10.1063/1.464090.
(22) Lambert, D. K. Vibrational Stark Effect of Adsorbates at Electrochemical Interfaces. *Electrochimica Acta* **1996**, *41* (5), 623–630. https://doi.org/10.1016/0013-4686(95)00349-5.
(23) Patrow, J. G.; Sorenson, S. A.; Dawlaty, J. M. Direct Spectroscopic Measurement of Interfacial Electric Fields near an Electrode under Polarizing or Current-Carrying Conditions. *J. Phys. Chem. C* **2017**, *121* (21), 11585–11592. https://doi.org/10.1021/acs.jpcc.7b03134.
(24) Delley, M. F.; Nichols, E. M.; Mayer, J. M. Electrolyte Cation Effects on Interfacial Acidity and Electric Fields. *J. Phys. Chem. C* **2022**, *126* (19), 8477–8488. https://doi.org/10.1021/acs.jpcc.2c01134.
(25) *Electrochemical Methods: Fundamentals and Applications, 2nd Edition | Wiley*. https://www.wiley.com/en-us/Electrochemical+Methods:+Fundamentals+and+Applications,+2nd+Edition-p-9780471043720 (accessed 2023-06-19).
(26) Wang, X.; Huang, S.-C.; Hu, S.; Yan, S.; Ren, B. Fundamental Understanding and Applications of Plasmon-Enhanced Raman Spectroscopy. *Nat. Rev. Phys.* **2020**, *2* (5), 253–271. https://doi.org/10.1038/s42254-020-0171-y.
(27) Hartstein, A.; Kirtley, J. R.; Tsang, J. C. Enhancement of the Infrared Absorption from Molecular Monolayers with Thin Metal Overlayers. *Phys. Rev. Lett.* **1980**, *45* (3), 201–204. https://doi.org/10.1103/PhysRevLett.45.201.

(28) Ding, S.-Y.; Yi, J.; Li, J.-F.; Ren, B.; Wu, D.-Y.; Panneerselvam, R.; Tian, Z.-Q. Nanostructure-Based Plasmon-Enhanced Raman Spectroscopy for Surface Analysis of Materials. *Nat. Rev. Mater.* **2016**, *1* (6), 16021. https://doi.org/10.1038/natrevmats.2016.21.
(29) Li, J. F.; Huang, Y. F.; Ding, Y.; Yang, Z. L.; Li, S. B.; Zhou, X. S.; Fan, F. R.; Zhang, W.; Zhou, Z. Y.; Wu, D. Y.; Ren, B.; Wang, Z. L.; Tian, Z. Q. Shell-Isolated Nanoparticle-Enhanced Raman Spectroscopy. *Nature* **2010**, *464* (7287), 392–395. https://doi.org/10.1038/nature08907.
(30) Li, J.-F.; Zhang, Y.-J.; Rudnev, A. V.; Anema, J. R.; Li, S.-B.; Hong, W.-J.; Rajapandiyan, P.; Lipkowski, J.; Wandlowski, T.; Tian, Z.-Q. Electrochemical Shell-Isolated Nanoparticle-Enhanced Raman Spectroscopy: Correlating Structural Information and Adsorption Processes of Pyridine at the Au(Hkl) Single Crystal/Solution Interface. *J. Am. Chem. Soc.* **2015**, *137* (6), 2400–2408. https://doi.org/10.1021/ja513263j.
(31) Bodappa, N.; Su, M.; Zhao, Y.; Le, J.-B.; Yang, W.-M.; Radjenovic, P.; Dong, J.-C.; Cheng, J.; Tian, Z.-Q.; Li, J.-F. Early Stages of Electrochemical Oxidation of Cu(111) and Polycrystalline Cu Surfaces Revealed by *in Situ* Raman Spectroscopy. *J. Am. Chem. Soc.* **2019**, *141* (31), 12192–12196. https://doi.org/10.1021/jacs.9b04638.
(32) Shao, F.; Wong, J. K.; Low, Q. H.; Iannuzzi, M.; Li, J.; Lan, J. In Situ Spectroelectrochemical Probing of CO Redox Landscape on Copper Single-Crystal Surfaces. *Proc. Natl. Acad. Sci.* **2022**, *119* (29), e2118166119. https://doi.org/10.1073/pnas.2118166119.
(33) Zhao, Y.; Zhang, X.-G.; Bodappa, N.; Yang, W.-M.; Liang, Q.; Radjenovica, P. M.; Wang, Y.-H.; Zhang, Y.-J.; Dong, J.-C.; Tian, Z.-Q.; Li, J.-F. Elucidating Electrochemical CO_2 Reduction Reaction Processes on Cu(*Hkl*) Single-Crystal Surfaces by *in Situ* Raman Spectroscopy. *Energy Environ. Sci.* **2022**, *15* (9), 3968–3977. https://doi.org/10.1039/D2EE01334G.
(34) Li, C.-Y.; Chen, M.; Liu, S.; Lu, X.; Meng, J.; Yan, J.; Abruña, H. D.; Feng, G.; Lian, T. Unconventional Interfacial Water Structure of Highly Concentrated Aqueous Electrolytes at Negative Electrode Polarizations. *Nat. Commun.* **2022**, *13* (1), 5330. https://doi.org/10.1038/s41467-022-33129-8.
(35) Li, C.-Y.; Dong, J.-C.; Jin, X.; Chen, S.; Panneerselvam, R.; Rudnev, A. V.; Yang, Z.-L.; Li, J.-F.; Wandlowski, T.; Tian, Z.-Q. In Situ, Monitoring of Electrooxidation Processes at Gold Single Crystal Surfaces Using Shell-Isolated Nanoparticle-Enhanced Raman Spectroscopy. *J. Am. Chem. Soc.* **2015**, *137* (24), 7648–7651. https://doi.org/10.1021/jacs.5b04670.
(36) Chen, S.; Xiao, Y.-H.; Qin, M.; Zhou, G.; Dong, R.; Devasenathipathy, R.; Wu, D.-Y.; Yang, L. Quantification of the Real Plasmonic Field Transverse Distribution in a Nanocavity Using the Vibrational Stark Effect. *J. Phys. Chem. Lett.* **2023**, *14* (7), 1708–1713. https://doi.org/10.1021/acs.jpclett.2c03818.
(37) Kurouski, D.; Mattei, M.; Van Duyne, R. P. Probing Redox Reactions at the Nanoscale with Electrochemical Tip-Enhanced Raman Spectroscopy. *Nano Lett.* **2015**, *15* (12), 7956–7962. https://doi.org/10.1021/acs.nanolett.5b04177.
(38) Marr, J. M.; Schultz, Z. D. Imaging Electric Fields in SERS and TERS Using the Vibrational Stark Effect. *J. Phys. Chem. Lett.* **2013**, *4* (19), 3268–3272. https://doi.org/10.1021/jz401551u.
(39) Benz, F.; Schmidt, M. K.; Dreismann, A.; Chikkaraddy, R.; Zhang, Y.; Demetriadou, A.; Carnegie, C.; Ohadi, H.; de Nijs, B.; Esteban, R.; Aizpurua, J.; Baumberg, J. J. Single-Molecule Optomechanics in "Picocavities." *Science* **2016**, *354* (6313), 726–729. https://doi.org/10.1126/science.aah5243.

(40) Wright, D.; Lin, Q.; Berta, D.; Földes, T.; Wagner, A.; Griffiths, J.; Readman, C.; Rosta, E.; Reisner, E.; Baumberg, J. J. Mechanistic Study of an Immobilized Molecular Electrocatalyst by in Situ Gap-Plasmon-Assisted Spectro-Electrochemistry. *Nat. Catal.* **2021**, *4* (2), 157–163. https://doi.org/10.1038/s41929-020-00566-x.
(41) Benz, F.; Schmidt, M. K.; Dreismann, A.; Chikkaraddy, R.; Zhang, Y.; Demetriadou, A.; Carnegie, C.; Ohadi, H.; de Nijs, B.; Esteban, R.; Aizpurua, J.; Baumberg, J. J. Single-Molecule Optomechanics in "Picocavities." *Science* **2016**, *354* (6313), 726–729. https://doi.org/10.1126/science.aah5243.
(42) Li, L.; Hutter, T.; Steiner, U.; Mahajan, S. Single Molecule SERS and Detection of Biomolecules with a Single Gold Nanoparticle on a Mirror Junction. *The Analyst* **2013**, *138* (16), 4574. https://doi.org/10.1039/c3an00447c.
(43) Benz, F.; Chikkaraddy, R.; Salmon, A.; Ohadi, H.; De Nijs, B.; Mertens, J.; Carnegie, C.; Bowman, R. W.; Baumberg, J. J. SERS of Individual Nanoparticles on a Mirror: Size Does Matter, but so Does Shape. *J. Phys. Chem. Lett.* **2016**, *7* (12), 2264–2269. https://doi.org/10.1021/acs.jpclett.6b00986.
(44) Hu, J.; Tanabe, M.; Sato, J.; Uosaki, K.; Ikeda, K. Effects of Atomic Geometry and Electronic Structure of Platinum Surfaces on Molecular Adsorbates Studied by Gap-Mode SERS. *J. Am. Chem. Soc.* **2014**, *136* (29), 10299–10307. https://doi.org/10.1021/ja502008t.
(45) Wang, H.; Yao, K.; Parkhill, J. A.; Schultz, Z. D. Detection of Electron Tunneling across Plasmonic Nanoparticle–Film Junctions Using Nitrile Vibrations. *Phys. Chem. Chem. Phys.* **2017**, *19* (8), 5786–5796. https://doi.org/10.1039/C6CP08168A.
(46) Banik, M.; El-Khoury, P. Z.; Nag, A.; Rodriguez-Perez, A.; Guarrottxena, N.; Bazan, G. C.; Apkarian, V. A. Surface-Enhanced Raman Trajectories on a Nano-Dumbbell: Transition from Field to Charge Transfer Plasmons as the Spheres Fuse. *ACS Nano* **2012**, *6* (11), 10343–10354. https://doi.org/10.1021/nn304277n.
(47) Kwasnieski, D. T.; Wang, H.; Schultz, Z. D. Alkyl-Nitrile Adlayers as Probes of Plasmonically Induced Electric Fields. *Chem. Sci.* **2015**, *6* (8), 4484–4494. https://doi.org/10.1039/C5SC01265A.
(48) Corrigan, D. S.; Gao, P.; Leung, L. W. H.; Weaver, M. J. Comparisons between Surface Infrared and Surface-Enhanced Raman Spectroscopies: Band Frequencies, Bandwidths, and Selection Rules for Pseudohalide and Related Adsorbates at Gold and Silver Electrodes. *Langmuir* **1986**, *2* (6), 744–752. https://doi.org/10.1021/la00072a012.
(49) Santos, J. J.; Toma, S. H.; Monezi, N. M.; Ando, R. A.; Corio, P.; Araki, K. Selecting the Mechanism of Surface-Enhanced Raman Scattering Effect Using Shell Isolated Nanoparticles and an Oxo–Triruthenium Acetate Cluster Complex. *Inorg. Chem.* **2019**, *58* (15), 10399–10407. https://doi.org/10.1021/acs.inorgchem.9b01618.
(50) Chang, X.; Vijay, S.; Zhao, Y.; Oliveira, N. J.; Chan, K.; Xu, B. Understanding the Complementarities of Surface-Enhanced Infrared and Raman Spectroscopies in CO Adsorption and Electrochemical Reduction. *Nat. Commun.* **2022**, *13* (1), 2656. https://doi.org/10.1038/s41467-022-30262-2.
(51) Zhang, P.; Wei, Y.; Cai, J.; Chen, Y.-X.; Tian, Z.-Q. Nonlinear Stark Effect Observed for Carbon Monoxide Chemisorbed on Gold Core/Palladium Shell Nanoparticle Film Electrodes, Using in Situ Surface-Enhanced Raman Spectroscopy. *Chin. J. Catal.* **2016**, *37* (7), 1156–1165. https://doi.org/10.1016/S1872-2067(15)61106-8.
(52) Voegtle, M. J.; Pal, T.; Pennathur, A. K.; Menachekanian, S.; Patrow, J. G.; Sarkar, S.; Cui, Q.; Dawlaty, J. M. Interfacial Polarization and Ionic Structure at the Ionic Liquid–Metal

Interface Studied by Vibrational Spectroscopy and Molecular Dynamics Simulations. *J. Phys. Chem. B* **2021**, *125* (10), 2741–2753. https://doi.org/10.1021/acs.jpcb.0c11232.
(53) Sorenson, S. A.; Patrow, J. G.; Dawlaty, J. M. Solvation Reaction Field at the Interface Measured by Vibrational Sum Frequency Generation Spectroscopy. *J. Am. Chem. Soc.* **2017**, *139* (6), 2369–2378. https://doi.org/10.1021/jacs.6b11940.
(54) *Electrochemical Methods: Fundamentals and Applications, 2nd Edition | Wiley*. Wiley.com. https://www.wiley.com/en-us/Electrochemical+Methods%3A+Fundamentals+and+Applications%2C+2nd+Edition-p-9780471043720 (accessed 2023-07-18).
(55) Li, Y.; Lu, D.; Swanson, S. A.; Scott, J. C.; Galli, G. Microscopic Characterization of the Interface between Aromatic Isocyanides and Au(111): A First-Principles Investigation. *J. Phys. Chem. C* **2008**, *112* (16), 6413–6421. https://doi.org/10.1021/jp7111044.

6. Chapter 6 Harness reversible interfacial hydrogen bonding at the interface with electro-induction effect

6.1. Introduction and background

Hydrogen bonding (H-bonding) stands as one of the most fundamental and essential intermolecular interactions in nature, playing a crucial role in shaping the properties and behavior of various chemical systems: from molecular self-assembly/recognition to the stability of biomolecular structures (such as DNA, proteins) and the solvation phenomena in solvent environments[1–3]. The study of H-bonding has attracted considerable attention from researchers across various scientific disciplines, in chemistry, materials science, biochemistry, etc.

The H-bonding is usually initiated by the electron-deficient hydrogen atoms to form specific directional bonds with electronegative atoms with rich electron density, such as oxygen, nitrogen, and fluorine[4]. In most cases, H-bonding can be expressed as X-H···Y, where X and Y are the electronegative atoms and Y usually exhibits one or more lone pairs of electrons[5]. This interaction differs from neither electrostatic attraction (ion-ion interaction, ~100-200 kcal/mol binding energy) or covalent-like interaction (~50-150 kcal/mol binding energy), with distinct features on specific directionality and much lower binding energy (usually lower 10 kcal/mol)[6]. The strength of H-bonds significantly influences molecular structures, solubilities, properties, and even the reaction rates[5,7], making them a heated topic to be probed.

Due to the weak binding energy of H-bonding, it is difficult to probe the H-bonded complexes spectroscopically. Current literature reports provided two direct strategies to achieve a direct probe on the vibrational features of H-bonded complexes: 1) initiate a big population of H-bonding in bulk phase[8,9], or 2) the utilization of the surface-specific techniques at the interfaces, such as Sum-Frequency generation spectroscopy[10–12]. These studies enriched the molecular understanding of H-bonding, but in systems with weak vibrational features of X-H or Y-H changes, direct probes may not be plausible. Thus, an indirect approach has also been proposed to probe the H-bonding—it focuses on probing the vibrational features of the secondary structures stabilized by the H-bonding and then evaluating the strength of the H-bonding[13,14].

Besides studies on H-bonding in bulk phases and non-electrochemical interfaces, these strategies have been proven to be successful in probing the electrochemical solid/liquid interfaces, revealing a rich mechanistic understanding of the roles of H-bonding in catalytic systems, including hydrogen oxidation/evolution reactions[15], oxygen reduction reaction[16], CO/CO_2 reductions[17], molecular recognition[18], and energy storage systems[19], etc. However, as a key parameter at the electrochemical interface, how the electrochemical potential affects the formation of interfacial intermolecular H-bonding remains unclear. Many relevant factors led by the tuning electrochemical potential can be expected. For instance, the static electric field at the interface can attract or repel species[20] such as electron-deficient hydrogen of the H-bonding donors, or the electrolyte ions as a competitor on H-bonding; at the same time, the electro-induction effect[21] to the surface bonded species can also stabilize or destabilize the H-bonding via changing electron-density of the adsorbates.

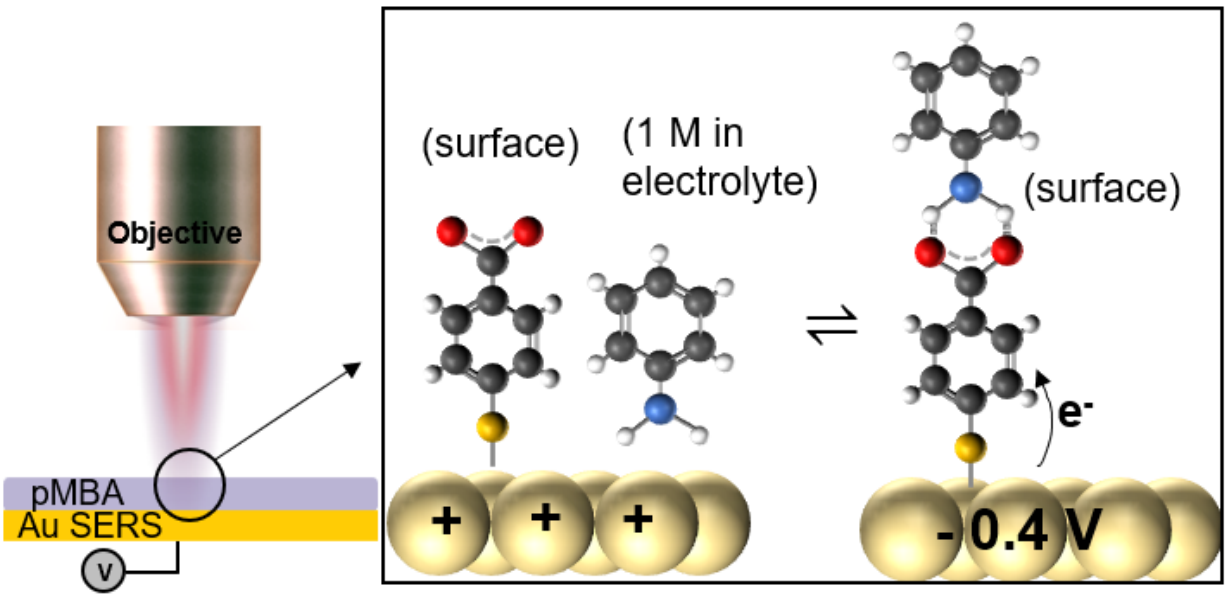

Figure 6.1 A scheme of SERS study on the electrochemical interfacial hydrogen bonding. Hydrogen bonding formation (-0.4 V vs. Ag/AgCl) and dissociation (at positive potentials) between surface-assembled 4-MBA and aniline in the electrolyte bulk phase on the roughened Au surface. The balls in the cartoon represent different atoms of the molecules: light yellow- Au, dark yellow- S, black- C, red- O, blue- N, and white- H.

Herein, to better understand the interfacial intermolecular H-bonding under electrochemical polarization, we present an observation of electrochemical controlling reversible interfacial H-bonding and an in-depth mechanistic study on the nature of the electrochemical interfacial H-bonding. We modify the widely studied and understood system— 4-mercapto benzoic acid (4-MBA or *para*-mercaptobenzoic acid, pMBA)[22–24] self-assembled monolayers (SAM) on a SERS-active Au electrode (seen in Figure 1.), by adding the hydrogen bond donors (aniline) in the organic electrolyte (0.1 M $TBAPF_6$ in acetonitrile, ACN). The 4-MBA/Au exhibits strong vibrational features related to C-C, C-H, and carboxylate groups can be affected by the interaction with electrolyte bulk species, if hydrogen bonding forms or dissociates during a potential change.

We present an *in situ* electrochemical SERS spectroscopic study that demonstrates the reversible forming and dissociation of the hydrogen bonding between the 4-MBA SAM on the surface and solution phase anilines at different potentials (left panel in Figure 1). Specifically, we present four key findings: 1) it shows noticeable vibrational spectral frequency shifts for both 4-MBA and aniline before and after the intermolecular hydrogen binding, as easy and direct evidence to support hydrogen bonding formation or dissociation; 2) unlike most of conventional hydrogen bonding in bulk phases, the electrochemical polarized surface achieves a reversible control of the hydrogen bonding (the population of hydrogen bonded complex on the surface) by applying the different bias, in our case at -0.4 V, the hydrogen bonded complex reaches the maximum and destabilize at more positive or negative potentials; 3) further control measurements are conducted to understand the mechanisms of H-bonding formation: electric field effect and the electro-induction effect are elucidated by the comparison results on conjugated and non-conjugated acids, electrolyte ions effects in destabilizing H-bonding and the exact (acid or base form)species to form the H-bonding are also investigated; 4) the kinetic study shows the hydrogen bonding can be quickly established in seconds in a potential jump from unfavorable potentials to one favorable. By integrating all the experimental studies, we provide valuable insights into the formation, strength, and specificity of the interfacial H-bonds driven by electrochemical potentials.

6.2. Results and discussion

6.2.1. The vibrational spectroscopic confirmation for hydrogen bonding formation

We first conduct a series of control measurements to confirm the formation of the hydrogen-bonded complex. As *Figure 6.2* shows, the electrochemical SERS spectra at -0.4 V in the same electrolyte of o4-MBA only (violet-blue), aniline only (light green), and 4-MBA with aniline (dark green) are shown in different colors respectively. In the spectra of 4-MBA at -0.4 V, two distinct Raman features at ~1168 cm^{-1} and ~1585 cm^{-1} can be observed and assigned with 4-MBA δ(C-H)[25] and ν (C-C, ring) [22,23,26,27] respectively; in the spectra of aniline at -0.4 V, the signature modes from 1340 to 1450 cm^{-1} are most noticeable, according to the previous reports, they can be assigned with ν(C-C)[28,29] / ν(C-N)[30–33] and δ(C-H)[34] / ν(C-C) [35] from aniline. Then, the evaluation of the spectra of 4-MBA with aniline shows interesting observations, both signature features of 4-MBA at ~1168 cm^{-1} and ~1585 cm^{-1} and those of aniline from 1340 to 1450 cm^{-1} are obtained, and the modes of the 4-MBA in dark green show red-shifts by ~4.4 cm^{-1} and ~2.2 cm^{-1} compared with original peaks in violet blue, while those modes of the aniline in dark green show blue-shift by ~33.3 cm^{-1} compared with those of light green.

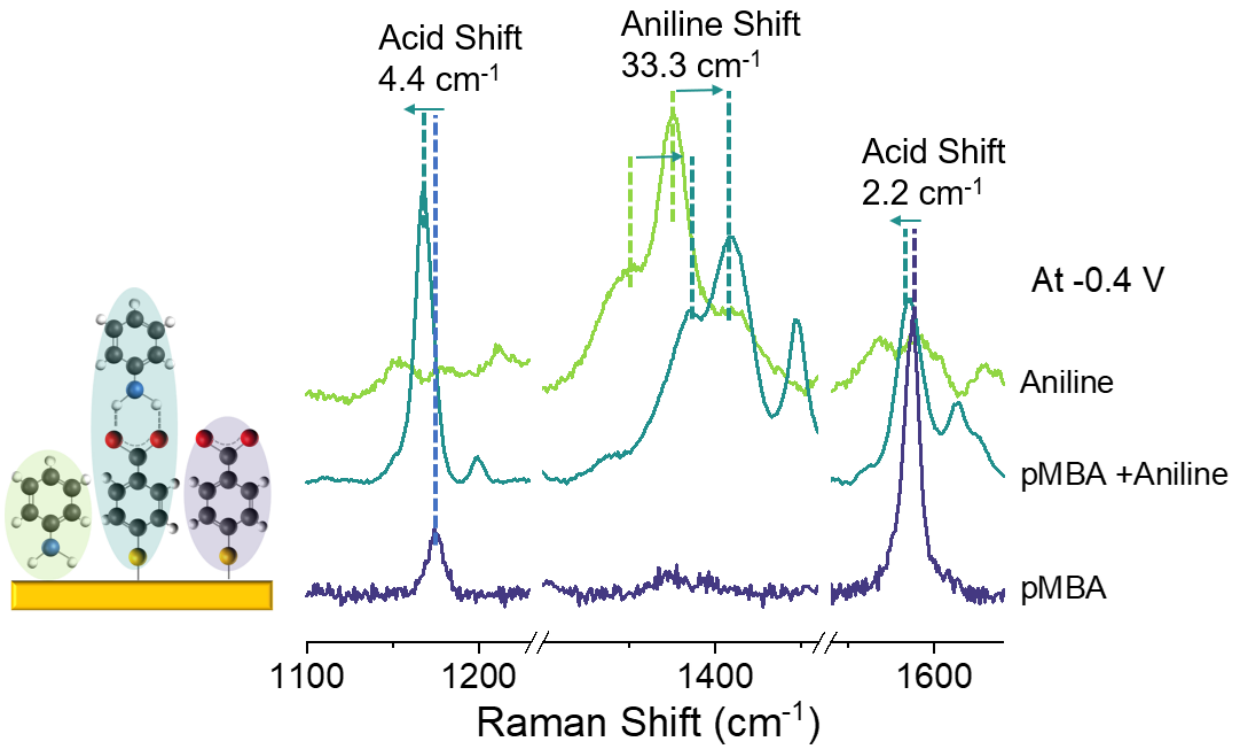

Figure 6.2. Validation of the existence of H bonding.
SERS spectra of 4-MBA SAM on Au at -0.4 V (violet-blue) with the electrolyte (0.1 M $TBAPF_6$ in ACN), pure aniline on Au at -0.4 V (light green) with the same electrolyte and H-bonded complex between 4-MBA and aniline (1 M in electrolyte) on Au surface at -0.4 V (dark green) with the electrolyte. Vibrational modes belong to 4-MBA C-C and C-H redshift after H bonding, and the modes belong to aniline blue shift after H bonding.

To further validate these noticeable frequency shifts are believed to be directly induced by the formation of hydrogen bonding by putting aniline near a 4-MBA functionalized surface, we also conducted additional control on the aniline concentration dependence experiments (seen in *Figure 6.3*) with gradual frequency shift on 4-MBA modes.

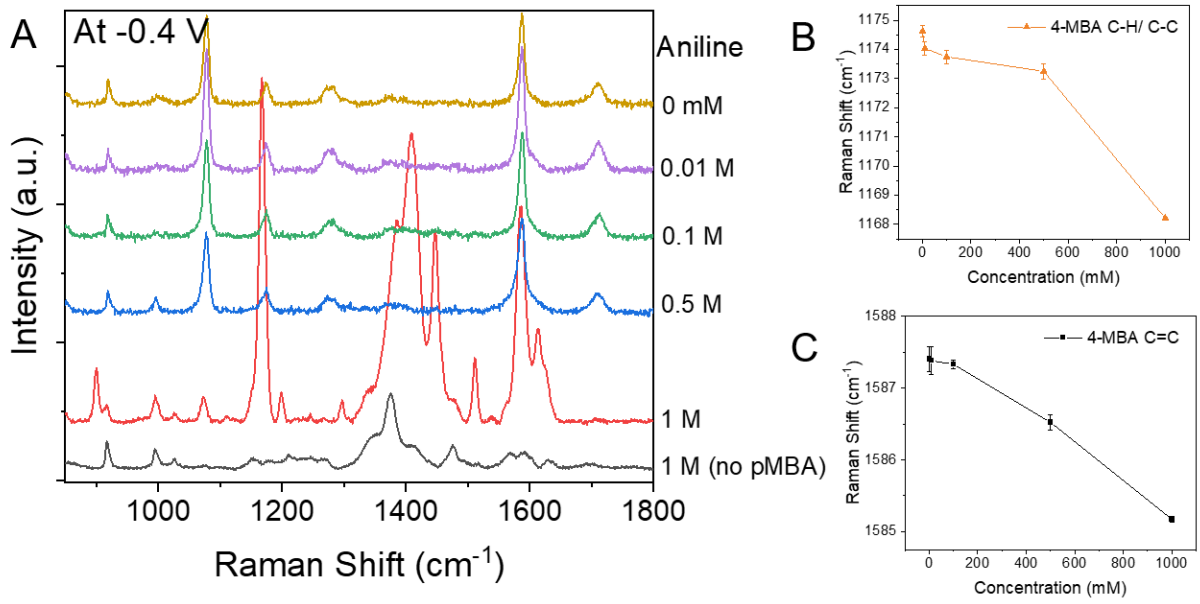

Figure 6.3. Control results of aniline-concentration dependence.
(A) SERS spectra of aniline concentration dependence at -0.4 V. Different colors of the spectrum represents the results in different concentration, the black line represents the result with only 4-MBA and without aniline. (B) the concentration-dependent frequency shift of 4-MBA ~1170 cm^{-1} peak. (C) the concentration-dependent frequency shift of 4-MBA 1587 cm^{-1} peak.

All the peak assignments are summarized in *Table 1*, and to confirm the assignments, we conduct additional electrochemical control at different potentials with 1 M aniline in the solution on bare Au without 4-MBA (*Figure 6.3*) and electrochemical measurement of 4-MBA on Au without aniline (seen in *Figure 6.5*). These additional controls confirm that peaks at ~1168 cm^{-1} and ~1585 cm^{-1} belong to the 4-MBA, and the peaks from 1340 to 1450 cm^{-1} belong to the aniline.

Table 3. Summary of measured and computed Raman peaks of key species

Raman shifts (cm^{-1})	**Species**	**Vibrational modes**
996	Aniline	δ(C-C, ring)[34,36]
1029	Aniline	Wagging ($-NH_2$) [36]

1077	pMBA	ν(C-S)[22,23,26,27]
1167-1173	pMBA/Aniline	δ(C-H)[25]
1375	Aniline	ν(C-C)[28,29] / ν(C-N)[30–33]
1447	Aniline	δ(C-H)[34] / ν(C-C) [35]
1586	pMBA	ν (C-C, ring) [22,23,26,27]
1606	Aniline	ν (C-C, ring) [34,36]
1628	Aniline	Scissoring ((-NH_2) [36]

6.2.2. Reversible hydrogen bonding formation/dissociation at an electrochemical interface

With the spectral confirmation of the hydrogen bonding, we then proceed with the *in situ* electrochemical SERS measurements to track the hydrogen bonding formation and dissociation. As shown in Figure 3A, the potential is applied from 0.2 V to -0.6 V and 0.2 V, and according to the assignments of 4-MBA and aniline-related modes in the previous section, we label the 4-MBA mode as orange and aniline mode as blue, the potential dependent frequency shifts of the modes are also tracked and plotted in Figure 3B, the relative intensity of the peaks as a function of potential can be seen in the *Figure 6.5*B. In a full scan of the potential from 0.2 V to -0.6 V to 0.2 V, we separate the overall surface interchange into 3 stages. Stage I, which is from 0.2 V to -0.2 V, can be seen as a “silent region”, in which the spectra features are mainly occupied by a large portion of the non-hydrogen bonded aniline features (consistent with what is shown in pure aniline control in *Figure 6.6*B), and a small portion of the surface 4-MBA (mostly base form), a detailed fitting of the spectra by the linear combination with the spectra of each portion well proved this in *Figure 6.7*. In Stage II from -0.2 V to -0.6 V and the reverse scan to -0.2 V, a larger

population of hydrogen bonding between the 4-MBA and aniline is observed evidenced by the distinct arising peak intensities and frequency shifts of 4-MBA peak (orange) and aniline peaks (blue). The simultaneous peak shifts in *Figure 6.4*B of the two species validate the hydrogen bonding that occurs between these two species. Another observation within Stage II is that the intensities of the hydrogen-bonded peaks for both 4-MBA and aniline slightly decrease from -0.4 to -0.6 V, showing that the most favorable potential for the hydrogen bonding is at -0.4 V. This observation results from the mechanism of the electrochemical potential controlled hydrogen bonding, which is discussed in depth in later sections. Stage III from -0.4 V to 0.2 V in a reverse scan, is a reversible process of Stage I, duplicates the state of no hydrogen bonded between aniline and 4-MBA, and reflects the process of the surface with a larger hydrogen bonded population gradually turning into a surface with small to no hydrogen bonded population. It should be noted that the spectral frequency shifts on 4-MBA and aniline we observed from -0.2 V to -0.6 V are due to hydrogen bonding rather than the potential dependent frequency shift or the interactions with other electrolyte components.

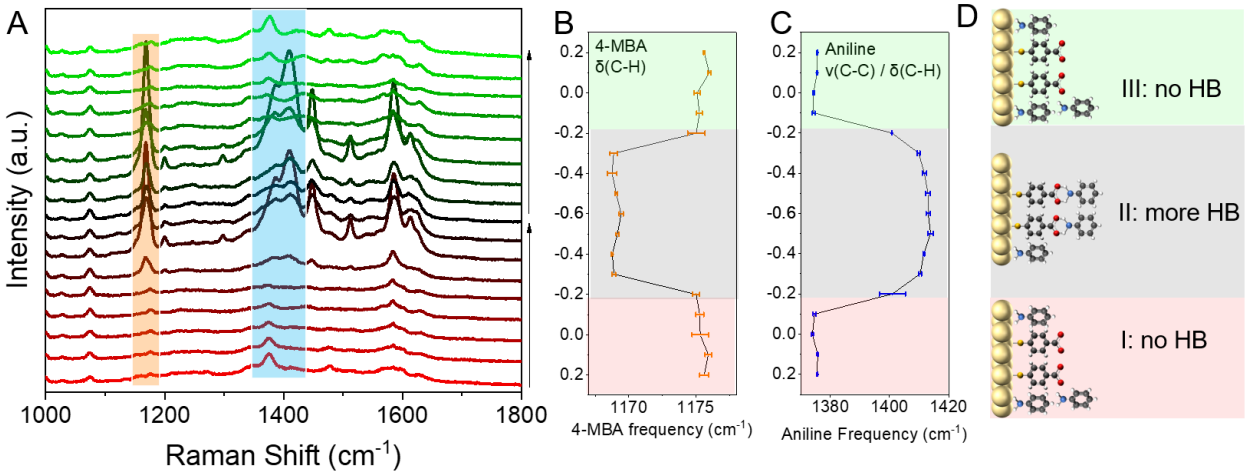

Figure 6.4. *In-situ* Electrochemical SERS measurement of reversible hydrogen bonding. 4-MBA SAM and aniline (1 M) in the electrolyte (0.1 M $TBAPF_6$ in ACN). (A) Potential dependent SERS spectra scanned from 0.2 V to -0.6 V to 0.2 V, interval at 0.1 V. The Representative 4-MBA peak is labeled as orange, representative aniline peak is labeled as blue. (B) the potential dependent frequency shift of orange labeled 4-MBA peak. (C) the potential dependent frequency shift of blue labeled aniline peak. (D) corresponding surface phenomena on hydrogen bonding (HB) at different potential regions, different stages are labeled as different

colors (colors correspond to the spectra line colors and the shaded area colors in frequency shifts).

To confirm the potential-dependent intensity change is due to the H-bonding formation and not to the potential dependent behavior of aniline or 4-MBA, the control measurements of the potential dependent measurements of individual 4-MBA or aniline on Au are shown in *Figure 6.5* and *Figure 6.6*, which presents completely different frequency/intensity changes as a function of potential.

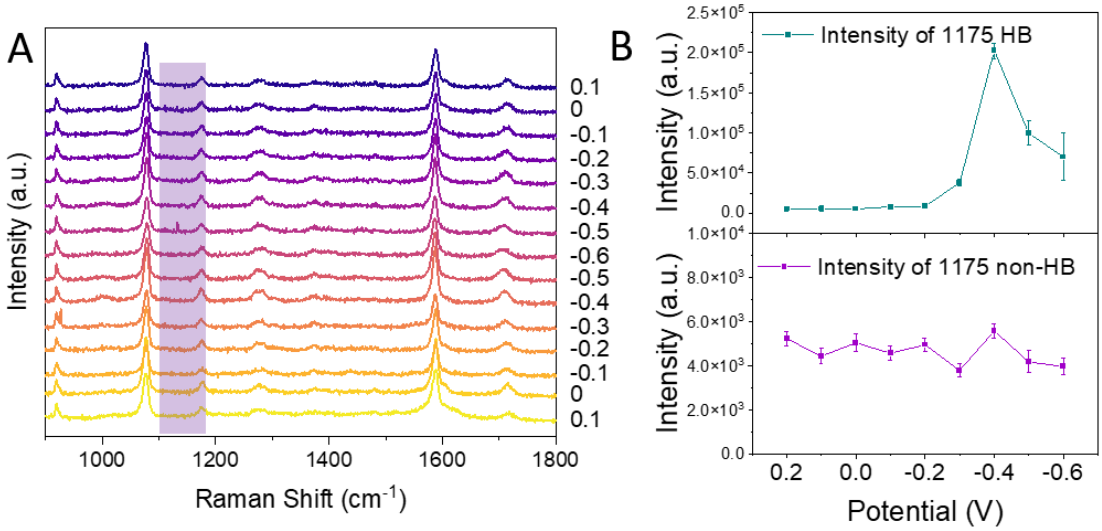

Figure 6.5. Control results of potential dependent 4-MBA.
(A) SERS spectra of potential dependent 4-MBA blank without aniline. (B) potential dependent intensity changes of 1175 cm^{-1} peak (down panel) without aniline, and the comparison of that with aniline (up panel).

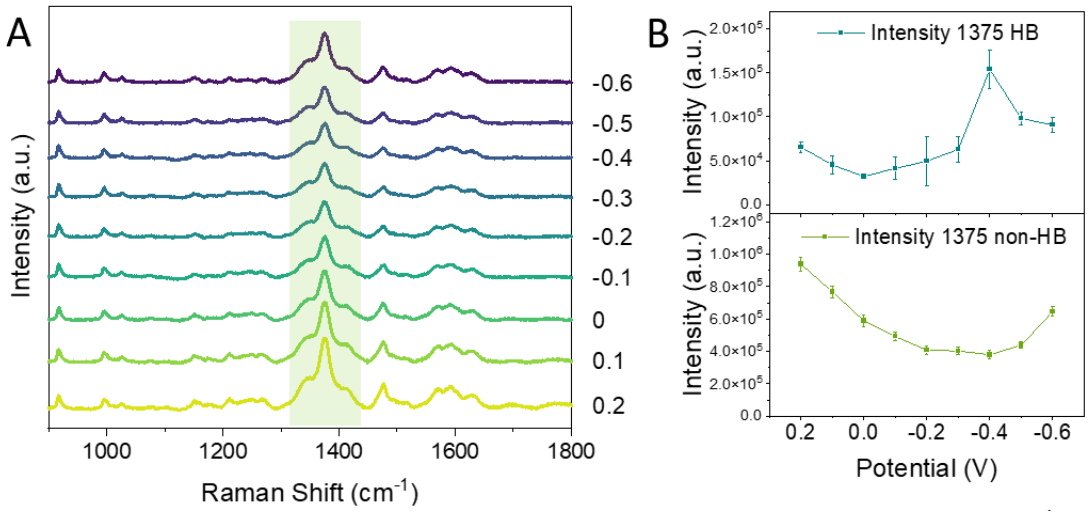

Figure 6.6. Control results of potential dependent aniline.
(A) SERS spectra of potential dependent aniline without 4-MBA. (B) potential dependent intensity changes of 1375 cm^{-1} peak (down panel) without 4-MBA, and the comparison of that with 4-MBA (up panel).

6.2.3. Quantitative analysis of potential dependence on hydrogen bonding

To quantitatively understand the potential dependent population of the hydrogen-bonded (HB) complex at the interface, we conduct the spectra component fitting and analysis. We aim to evaluate the relative intensity ratio of HB complex out of non-HB complex under different potentials, and since the HB-induced spectral features of 4-MBA and aniline are different, therefore, two different methods are applied to fit aniline and 4-MBA related HB complex respectively.

Analysis on HB aniline. HB-induced aniline changes mainly involve large frequency shifts (shifted over 30 cm^{-1} after hydrogen bonding), so the fitting of HB aniline and non-HB aniline is achieved by a component combination simulation. It simulates a combination spectra to fit the experimental spectra by linear combing normalized individual component spectra (4-MBA, HB aniline, non-HB aniline) with different ratios to match with the most distinct features at aniline region from 1200 – 1600 cm^{-1} at Stage II in Figure *6.4*A, besides, we rule out the origins of spectral changes from cations reported previously[22,37] by the pure 4-MBA control in electrolyte with $TBAPF_6$; and the potential dependent HB population is then described by the ratios of HB aniline out of total aniline population obtained by linear combination. We use normalized

spectra of four individual species in this process (shown in Figure *6.7*A), protonated 4-MBA (Figure *6.7*A blue), deprotonated 4-MBA (Figure *6.7*A green), non-HB aniline (Figure *6.7*A purple) and HB aniline (Figure *6.7*A orange). The spectra of pure HB aniline are difficult to obtain experimentally, thus, we manually blue-shifted the non-hydrogen bonded aniline spectra for 33.3 cm^{-1} to simulate its features. With the obtained 4 individual components, experimental spectra from +0.2 V to -0.6 V are fitted into the 4 components in Figure *6.7*B; the degree of hydrogen bonding can be calculated by the ratio of HB aniline and non-HB aniline used in the fitting by the following equation,

$$H\ bonding\ ratio = \frac{Intensity(\ Aniline\ H)}{Intensity(Aniline\ non\ H) + Intensity\ (Aniline\ H)}$$

where the intensity of the HB aniline and that of the non-HB aniline are both obtained in the summarized numerical portions of the simulated fitting results.

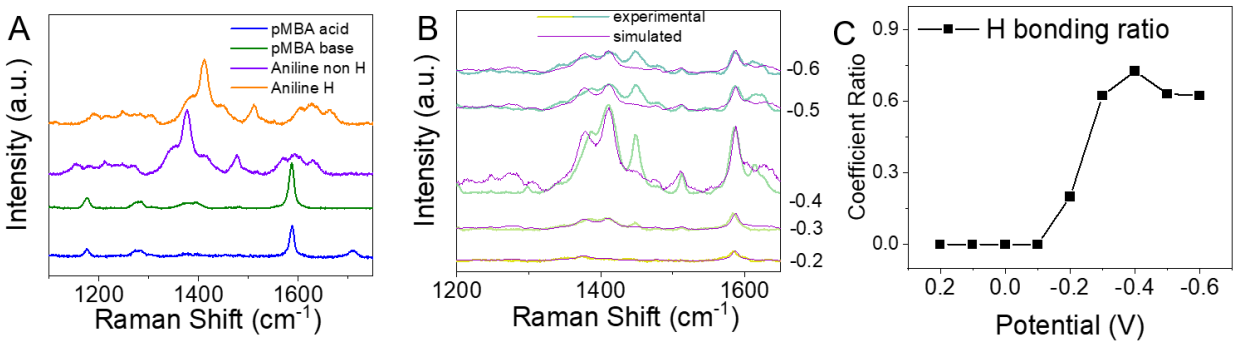

Figure 6.7. Potential dependent 4-component spectra fitting.
(A) SERS spectra of 4 components utilized for spectra fitting: 4-MBA acid form (blue, acquired on Au in 0.1 M $TBAPF_6$ in ACN at -0.4 V), 4-MBA base form (green, acquired on Au 0.09 M $TBAPF_6$ + 0.01 M TBAOH in ACN at -0.4 V), aniline without hydrogen bonding with 4-MBA (purple, acquired in pure 1 M aniline + 0.1 M TBAPF6 ACN on Au at -0.4 V), aniline with hydrogen bonding with 4-MBA (orange, acquired by manually shift 33.5 cm^{-1} of the purple spectrum of non-H-bonded aniline). (B) a linear combination fitting of 4 components to fit the peaks from 1300 to 1600 cm^{-1} region. (C) potential dependent surface hydrogen bonded aniline ratio based on the fitting results.

The results in Figure *6.7*C reveal that hydrogen-bonded aniline starts to increase intensity at -0.2 V and reaches the peak at -0.4 V with a later decrease from -0.4 V to -0.6 V. These findings in the fitted results match well with the observation and the spectra analysis in the previous section,

both indicating the most favorable potential for the hydrogen bonding between surface 4-MBA and the solution aniline is at -0.4 V. With this method, we analyzed more results with aniline concentrations of 10 mM, 100 mM, 500 mM, 800 mM, and 1000 mM from +0.2 V to -0.6 V and obtained the H-B ratio numbers in Figure *6.8*. We find a noticeable amount of hydrogen-bonded complex is only formed over 0.5 M aniline and favorable at -0.4 V. We believe the concentration effect should be mainly due to that the acid form of 4-MBA requires much more anilines as a base to deprotonate them to engage the hydrogen bonding.

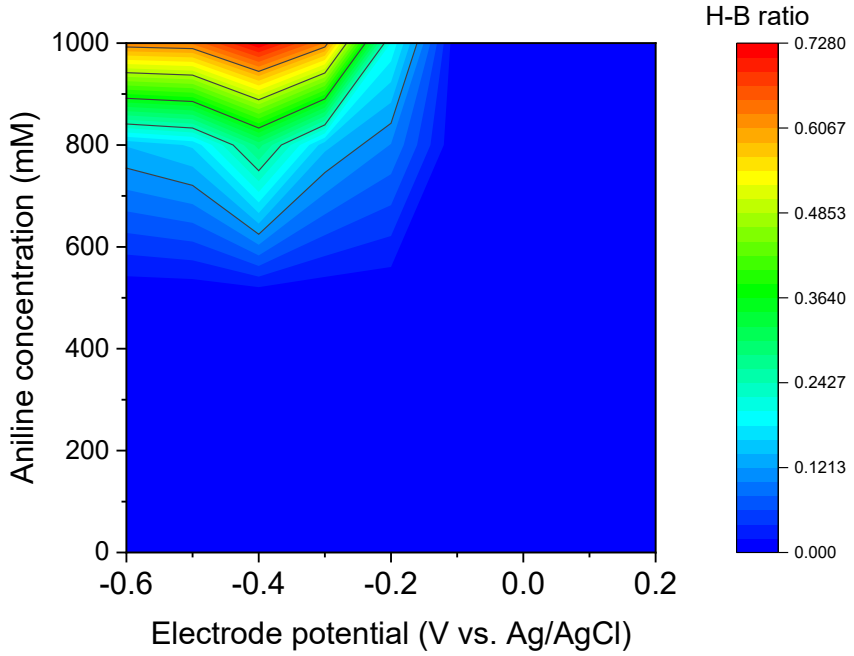

Figure 6.8. Concentration and potential dependent hydrogen-bonded ratios.
The H-B ratios were obtained by the previous spectra fitting and simulation process. The actual experimental data points used in the simulations were collected under 0 mM, 10 mM, 100 mM, 500 mM, 800 mM, and 1000 mM from 0.2 V to -0.6 V with 0.1 V interval. The space between the data points was generated automatically for a smooth connection.

Analysis of HB 4-MBA. The goal of fitting the 4-MBA-related HB species is to find the information on the binding constant of the HB complex and to compare it with our simulation results on the potential dependent thermodynamics. The ideal approach is to distinguish a certain mode of 4-MBA in the spectra from the same mode affected by HB and evaluate their relevant intensities to obtain the "coverage" of HB complex on 4-MBA/Au. However, unlike previous

reports[38,39] with distinguishable A1/B2 C-C stretching mode of 4-MBA before/after HB, most modes of 4-MBA in our system do not produce a "new mode" with HB for the population analysis, they mainly induce a frequency shift, and intensity change of their original modes with HB, as discussed previously in the HB confirmation part. Thus, we use another approach to evaluate the HB-affected 4-MBA modes. As shown in Figure *6.9*, we find that the most distinguishable feature of HB-induced changes on 4-MBA is the intensity increase on the C-H/C-COO- peak at 1167-1173 cm^{-1}, while the C-C stretching ring mode of 4-MBA at 1585 cm^{-1} barely changes. We then take C-C ring mode as the internal standard to do the normalization on the HB-affected (C-H/C-COO-) mode. This approach can be an indirect indicator of the HB "coverage", and we can obtain the relative HB complex population change as a function of aniline concentration under different potentials.

It should be noted that some spectra features of the HB are different from the same system in colloidal aniline/4-MBA/Ag NPs in other report[38]. In the report with a relatively low concentration of aniline, the spectra features of HB are mainly due to the new B2 modes of 4-MBA initiated by the modification in the electronic structures of 4-MBA adsorbed on Ag NPs from charge transfer (CT) SERS mechanism; while in our case, we initiate HB by electrochemical controlling in much more concentrated aniline solutions with quite different energy levels of 4-MBA, thus the relative enhanced modes should differ based on the CT mechanism[40].

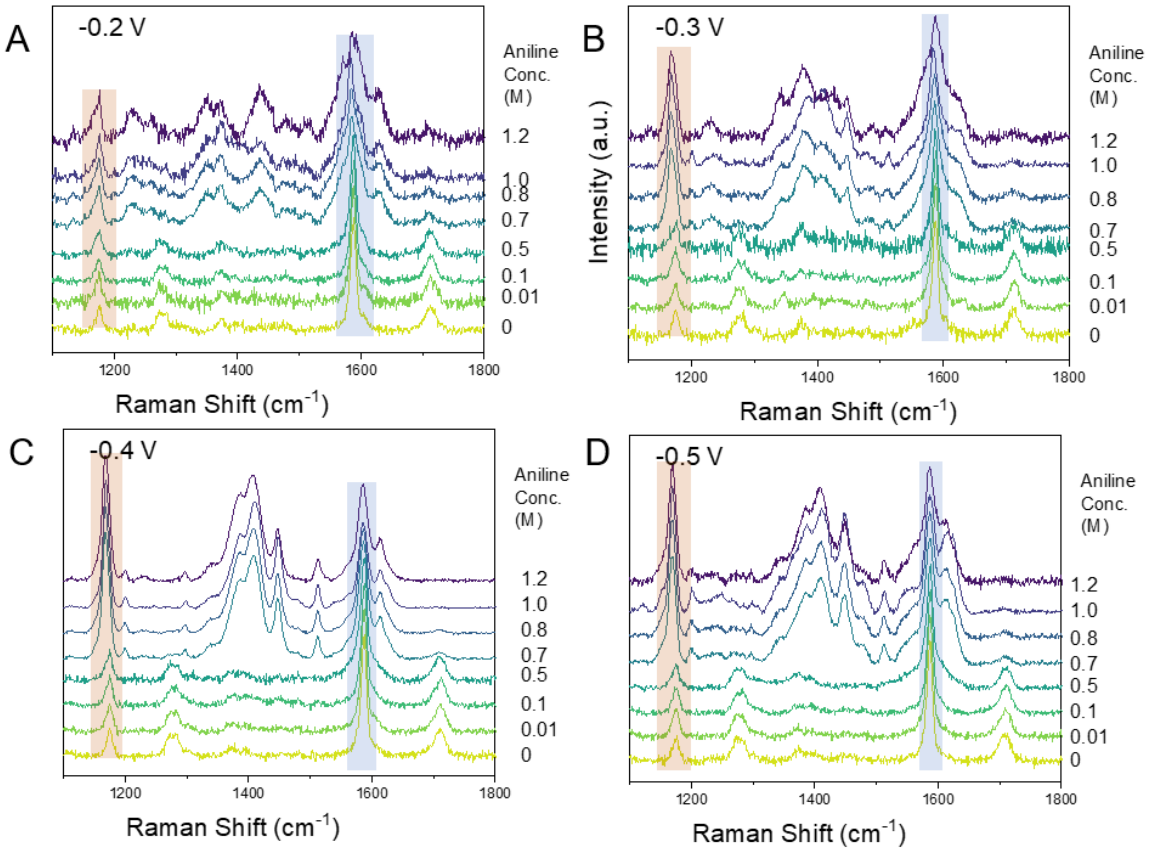

Figure 6.9. Quantitative analysis of 4-MBA-related peaks for HB.
The C-H/C-COO- peak at 1167-1173 cm^{-1}, is labeled orange, and the C-C ring mode of 4-MBA at 1710 cm^{-1} is labeled in blue. Spectra of different potentials are shown in A (-0.2 V), B (-0.3 V), C (-0.4 V), D (-0.5 V).

The aniline concentration-dependent HB degree I(C-H/C-COO-)/I(C-C) by potentials (in ***Figure 6.10***A) show interesting "S-shaped" profiles with 3 stages: a silent region from 0 M to around 0.5 M of aniline, a rapid increasing region from 0.5 M to 1.0 M and a saturation region from 1.0 M to 1.2 M. This indicates the HB complex population experiences a sigmoid increase as a function of aniline concentration. We notice that the spectra with pronounced HB complex peaks (1170, 1360-1500 cm^{-1}) always show no C=O stretching mode from -COOH at 1710 $cm^{-1}$of 4-MBA, so we hypothesize that the sigmoid S-shaped increase of HB complex should be due to the HB complex is only formed with deprotonated 4-MBA and it requires some amount of aniline to deprotonate 4-MBA to make the surface more favorable for HB formation. To validate this hypothesis, we then further analyze the C=O stretching mode in 4-MBA. By plotting the ratio between the intensity of C=O mode and that of the C-C ring mode of 4-MBA, we show the aniline concentration-dependent surface acidity in Figure 6.10B. In all 0 M aniline conditions,

the surface should be mostly covered by protonated 4-MBA, as the solvent ACN is difficult to be pronated by 4-MBA, thus the ratios are quite similar to be around 0.42; with the increasing aniline from 0.5 M to 1.0 M, the surface acidity shows a rapid decrease from 0.42 to around 0, which is an opposite pattern as a function of aniline concentration compared with the HB profile, indicating the 4-MBA deprotonation process is in sync with the HB formation process.

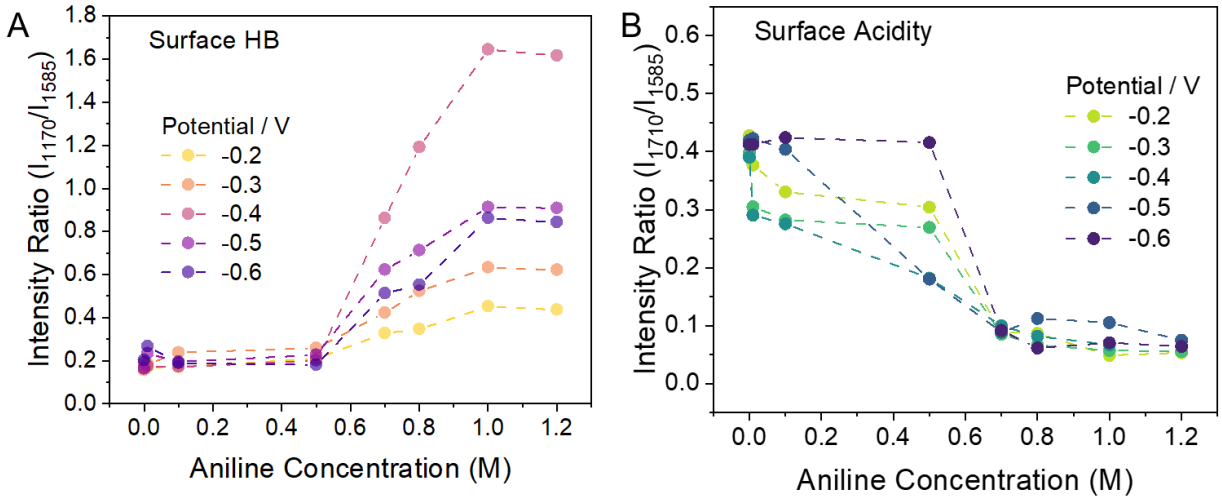

Figure 6.10. Aniline concentration-dependent surface HB and acidity change.
(A) "S-shaped" isotherm-alike aniline concentration-dependent HB changes in different potentials. The ratio of I(C-H/C-COO-)/I(C-C) is plotted as a function of aniline concentration; the dots of different colors represent the experimentally measured ratios under different potentials.
(B) Surface acidity as a function of aniline concentration. The ratio of I(C=O)/I(C-C) is plotted as a function of aniline concentration; the dots of different colors represent the experimentally measured ratios under different potentials.

The potential dependent binding constant for HB complex. With the previous validation on the speciation of HB complex, we then conduct a detailed analysis to obtain the binding constant for HB complex. Firstly, we define θ as the fraction of the surface 4-MBA that is hydrogen bounded by the aniline,

$$\theta(\text{HB complex coverage}) = \frac{HB\ complex\ population\ on\ Au\ surface}{Total\ 4{-}MBA\ on\ Au\ surface} \quad (1)$$

Then a normalization to obtain θ using the degree of HB data in ***Figure 6.10*** A. As the 1170 peak also exists in pure 4-MBA without aniline, the peak ratio of 1170 and 1585 in 0 M aniline is normalized as θ =0, where the surface is fully covered by non-HB 4-MBA (protonated 4-MBA); in all data points, we find the highest HB peak ratio in 1.2 M aniline at -0.4 V, is then normalized as θ =1, where the amount non-HB surface 4-MBA can be neglected. Then all the data in ***Figure 6.10*** A can be converted into HB θ numbers as a function of aniline concentration and potentials shown in ***Figure 6.11***C. In experimental data, we observe the maximum values of the HB complex at different potentials reached different θ, suggesting a different maximum capacity of the surface from the HB complex. From the previous validation of the acid form of 4-MBA, we think it is due to the limitation of available "sites" on the surface for HB formation, which is the deprotonated 4-MBA population on the surface.

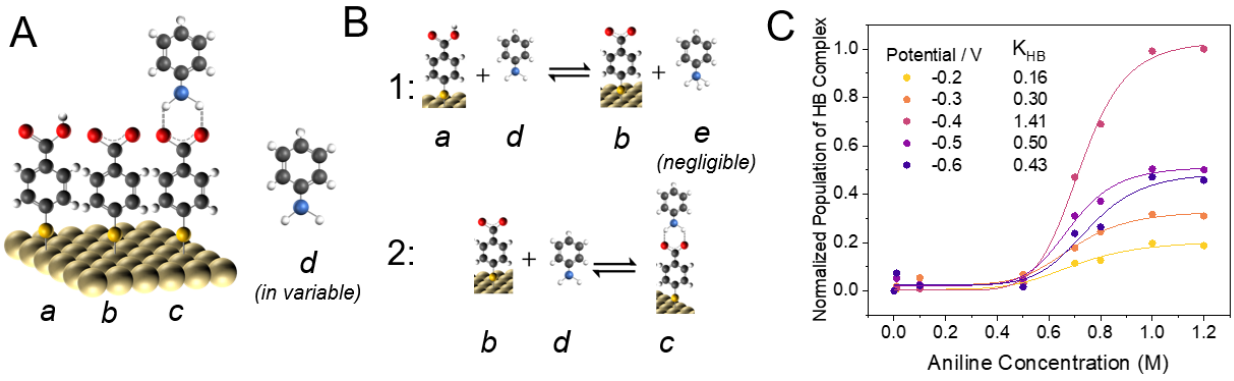

Figure 6.11. The model for fitting the equilibrium constant.
(A) Define 4-MBA (acid) as A, 4-MBA (base) as B, HB complex as C, and aniline in bulk as D; the total number of binding sites (sum of A, B, and C) is constant and normalized to 1.
(B) Two reactions happen at the interface, reaction 1 is a 4-MBA (acid) deprotonation reaction to 4-MBA (base) by an excess amount of aniline in bulk, and reaction 2 is 4-MBA (base) HB reaction with aniline in bulk. (C) Aniline concentration dependent θ of HB complex. θ is defined as normalized HB complex coverage.

The model to fit the experimental data of θ can be seen in ***Figure 6.11***. We assume 3 types of 4-MBA related species exist on the surface, 4-MBA (protonated) as species A, 4-MBA (deprotonated) as species B, HB complex as species C, the total population of the 3 species is a fixed number, and Theta reflects the relative population portion of HB complex among the three species. The model involves two reactions, the deprotonation of 4-MBA by aniline, and the HB formation with deprotonated 4-MBA and aniline. The first reaction can be seen as a surface

"phase" transition for HB formation, which converts the surface from unfavorable HB (protonated 4-MBA covered) to favorable HB (deprotonated 4-MBA covered); with the HB favorable deprotonated 4-MBA on the surface, the HB formation reaction occurs. From the aspect of a 1:2 reactants ratio (4-MBA: aniline) in the whole process, this 2-step process is similar to the cooperative binding behavior in biochemistry. The binding of ligands involves two steps, and the first ligand binding promotes the second one. The logistic function is widely used in fitting these binding systems in biochemical systems[41], so we also try to adapt this model to fit our results.

The equation used in this model is:

$$\theta([D]) = \frac{L}{1+e^{-K(D-x_0)}} \quad (2)$$

where θ([D]) is the fitted relative portion of HB complex at a given concentration of aniline ([D]), L is the maximum value of the θ, K is the slope of the curve which indicates the steepness of the transition, x_0 is the value of the aniline concentration ([D]) at the midpoint of the curve.

The fitting curves are seen in ***Figure 6.11***C. The binding constant K_{HB} thus can be obtained from the approximating of the fitting parameters. At the midpoint of the fitting curve, when aniline concentration [D]=x_0, Theta=L/2, assuming [B]=1-[C], then K_{HB} can be calculated as the equation,

$$K_{HB} = \frac{[C]}{[B][D]} \approx \frac{L/2}{(1-\frac{L}{2})x_0} \quad (3)$$

The relative K_{HB} is then calculated as follows, 0.16 (-0.2 V), 0.30 (-0.3 V), 1.41 (-0.4 V), 0.50 (-0.5 V), 0.43 (-0.6 V) shown in ***Figure 6.11***C.

The results reveal that different electrochemical potentials can affect the free energy of the HB formation reaction, altering the binding affinity. The mechanism of this electrochemical effect can be due to the changes of the electronic states of 4-MBA through bond polarization (through-bond effect), intermolecular interactions, or electrolyte ions through the electric field by the applied potential (through-space effect), which is discussed in the following content.

Additionally, if the measurements are conducted in a 4-MBA deprotonated surface, we can also expect that the aniline concentration dependent Theta will behave like a Langmuir-isotherm

profile reported in similar systems[42,43], however, the deprotonation control measurements with base addition (KOH, NaOH, TBAOH) in ACN cannot be achieved due to their extremely low solubility in ACN, replacing solvent controls (such as ethanol or water) fail to exclude the HB interferences of solvent to 4-MBA, thus are also not shown.

6.2.4. Mechanistic understanding of the electrochemical hydrogen bonding at the interface

To understand why the negative potential is more favorable for hydrogen bonding formation and why -0.4 V is the most favorable condition, we carry out additional experiments to investigate the underlying mechanisms of the forming and dissociation of the potential-dependent hydrogen bonding.

Hydrogen bonding is initiated by the unique ability of hydrogen atoms to form directional bonds with electron-rich atoms. Due to its nature as an electrostatic attraction in forming and dissociation, one may consider two common effects in terms of forming hydrogen bonding at the electrochemical interface: the static electric field effect leads by changing potential to attract hydrogen (electric field, EF effect) to the electrode, and the intramolecular inductive effect to increase the electron density of the hydrogen bond acceptor lead by the electrode (electrode induction effect). When a negative potential is applied, the two effects may both contribute to forming a hydrogen bond. There are some cases with similar interactions, on the one hand, it is well-discussed that the external electric field can affect the hydrogen bonding strength in proteins and further manipulate the structures of the protein folding[37]; on the other hand, electro-induction effects are also widely applied in organic synthesis at the electrode surfaces[21] and to discuss the mechanisms of Lewis adduct formation[20] at the electrode surfaces. Thus, in our case, it is essential to elucidate whether it is due to the static EF taking part in interacting and stabilizing the H of $-NH_2$ for engagement of hydrogen bonding, or the electrode-induced electron density change of the carboxylate group ($-COO^-$) to form hydrogen bonding.

To rule out the contribution from EF, we designed the system with molecular 4-MPAA (4-mercaptophenylacetic acid) with non-conjugation and reproduced the measurements with conjugated acid 4-MBA shown in the previous sections. The results are shown in *Figure 6.9*A, compared by the 4-MBA with noticeable spectral feature change on hydrogen bonding at -0.2 V,

the non-conjugated 4-MPAA shows no noticeable changes at -0.4 V under the same condition and electrolytes. This control illustrates that in our case (seen in *Figure 6.9*B), the electric field effect should not be the major contribution of the hydrogen bonding, the conjugation of the molecules is the key to changing the electron density of the whole acid molecules, and increase the hydrogen bonding donor (carboxylate groups) affinity on H atoms in aniline, further influence the stability of the hydrogen bonding. This induction-induced mechanism helps to explain when we apply a negative potential from +0.2 V to -0.4 V, the increase of the hydrogen bonding. Notably, the charge transfer signs in these steps do not involve any actual redox reaction, they only represent the degree of the charge transfer interactions between the electrode and SAM.

As for the observation of the decrease in the hydrogen bonding from -0.4 V to -0.6 V, we think it is likely to originate from the interactions between the 4-MBA (carboxylate groups) and the cations in the system when the potential negative than -0.4 V is applied, insertion of the cations may weaken the hydrogen bonding, we have no spectral evidence on the noticeable cation peaks to support this claim, but the similar interaction is discussed and supported in the Lewis adduct dissociation[20].

Notably, this electro-induction effect (on 4-MBA) along with the electric field effect (on solution phase aniline and electrolyte ions) are usually discussed together to contribute to the interfacial phenomenon and reactions[20]. In our case, if only 4-MBA and aniline, both effects may pose a positive influence on the stability of the hydrogen bonding at a negative potential and should be similarly dependent on the potential energies; however, the electric field effect also can manipulate the behaviors of electrolyte ions (cations) at a negative potential, where it shows the opposite contribution to hydrogen bonding compared with that of the electro-induction. In summary, our observation can be explained by a gradual competing process including an electro-induction-initiated hydrogen bonding from -0.2 V to -0.4 V on the surface, and an outcompeted electric field effects on cations to destabilize hydrogen bonding from -0.4 V to -0.6 V.

With these understandings of the mechanisms, we also find the following factors are crucial in hydrogen bonding formation: the acid/base form of 4-MBA, the solvent types (with different dielectric constants), and the concentration of the aniline. First, for the form of 4-MBA, all our results indicate that the deprotonated (base) form of the 4-MBA comprises the majority

population of the hydrogen bonding complex. It can be evidenced by the control experiments with strong acid added (seen in *Figure 6.8*, we notice the hydrogen bonding complex is formed with carboxylate when 1710 cm^{-1} (-C=O stretching of -COOH) is missing, so we purposely conduct the acid test and obtain the results in *Figure 6.8* middle line by adding strong acid (1 mM H_2SO_4), which presents obvious 1710 cm^{-1} peak and much weaker hydrogen bonding complex peaks (1168 cm^{-1}, 1340 -1450 cm^{-1}). Secondly, the solvent type also affects the formation of hydrogen bonding, in our control measurement of exchanging solvent from ACN to DCM (Dichloromethane, CH_2Cl_2) in the same 1 M aniline + 0.1 M $TBAPF_6$ electrolyte (*Figure 6.8* lower line), we find that no hydrogen bonding complex is formed from +0.2 V to -0.5 V, and most of 4-MBA stay in acid form (with 1710 cm^{-1} peak) in DCM. We understand this difference in the solvent effect by the dielectric constant (DC) difference, ACN exhibits a higher DC around 35.95[38] while DCM only has a DC around 9.0-9.2[39], and the solvent with higher DC tends to stabilize the ion form rather than the natural form of the species, which is supported by the report on solution phase organic acid/base reactions[40]. This solvent effect also serves as side evidence to support that the base form of 4-MBA leads to most of the hydrogen bonding.

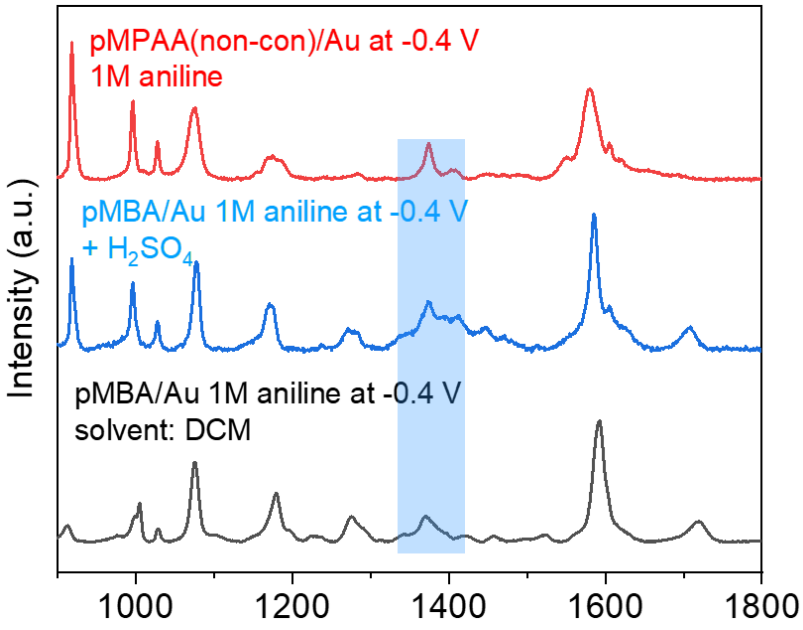

Figure 6.12. Additional control measurements on H bonding formation.

The red line represents the result under the 1M aniline in ACN; the blue line represents the result under 1 M aniline in ACN with 1 mM H_2SO_4 added; the black line represents the result under 1 M aniline in DCM as solvent.

For a spectroscopic aspect, we also comment on the abrupt intensified 1168 cm^{-1} peak of 4-MBA at -0.4 V, we believe it originated from a hydrogen-bonding-induced charge transfer Raman enhancement (CT, from Au SERS substrate to 4-MBA and following selective-enhancement on the B2 mode, non-totally symmetric mode), similar CT-induced spectral mechanisms have been utilized in other systems[41,42]. The reason is that in Figures 3 and 4, we observed that the 1168 cm^{-1} peak at -0.4 V is much more intense than the original 1168 cm^{-1} peak in the plausible fitting model of the 4-MBA component, which means that if we try to fit the intensity of the 1168 cm^{-1} peak by the intrinsic spectra of component 4-MBA, intensity of other modes (such as 1585 cm^{-1}) will be out-fitted; at the same time, there is no aniline related peaks at this region to contribute to the intensity. Thus, this unmatched 1168 cm^{-1} peak should be explained by a "super intensified" 4-MBA peak. By consulting the previous studies, we find a plausible explanation for the enhanced peak. The charge transfer (between SERS substrate and the adsorbate) enhancement (CT or chemical enhancement) of the SERS is usually considered one of the two major enhancement mechanisms, theoretical and experimental results[43] have revealed that CT enhancement can selectively pick up non-totally symmetric normal modes for additional enhancement, while symmetric modes are more pronounced in non-CT cases. In a 4-MBA case, specifically, the symmetric modes, labeled as A1, such as the 1585 cm^{-1} peak, are shown in most spectra with no or less CT occurring, but the non-totally symmetric modes, including the 1168 cm^{-1} peak, labeled as B2[44], will be selectively enhanced when more CT enhancement take place[42]. Under a hydrogen bonding at -0.4 V, due to the more charge of the 4-MBA taking part in the engagement of the bond formation, the CT takes place from the Au SERS substate to the 4-MBA molecules, then the B2 mode is selectively enhanced. A previous study utilized another B2 mode at 1572 cm^{-1} to correlate with the degree of hydrogen bonding. We also observed the related enhancement of the mode in Figure 3.

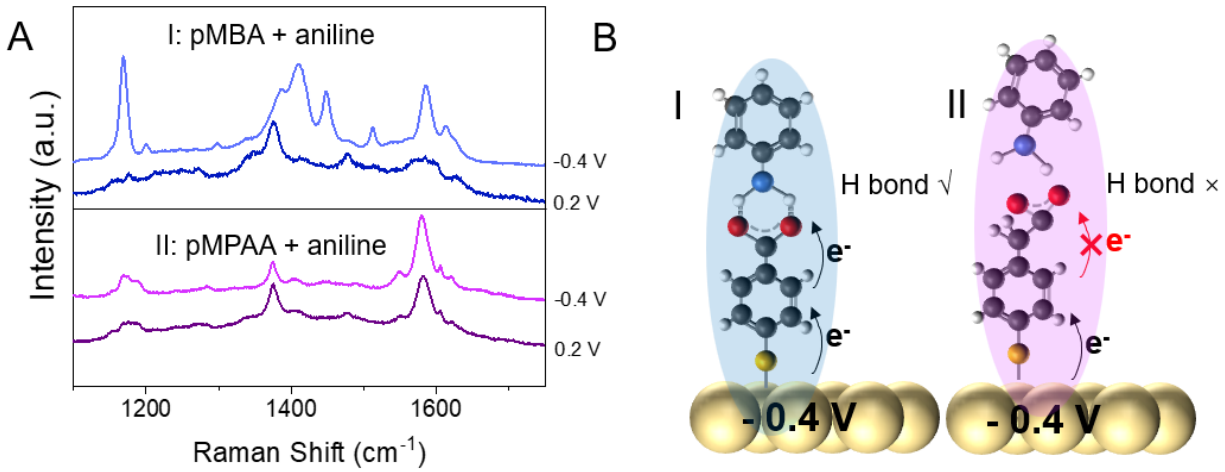

Figure 6.13. Mechanistic control on molecular conjugation (electrode induction). (A) Comparison of SERS spectra of hydrogen bonding in conjugated acid (pMBA at -0.4 V with noticeable shifts for peaks at 1168, 1340 cm^{-1}) and non-hydrogen bonding in non-conjugated acid pMPAA at -0.4 V with no spectral shifts). (B) the scheme to illustrate the results in A of electrochemical induction effect on hydrogen bonding. The electron transfer signs in B do not involve redox reactions, only representing the non-redox movement of charge between the electrode and the SAMs.

Finally, we followed a potential-jump approach to acquire kinetic SERS spectra (in *Figure 6.10*A). The potential was applied at 0.2 V for the first 10 s and jumped to -0.4 V for over 30 s to initiate hydrogen bonding formation, the kinetic *in-situ* SERS measurement (spectrum acquisition time for 1 s) proceeded along the whole time to observe the growth of the key spectra features. As shown in Figure 6A, when the potential is applied at +0.2 V, several spectral features belonging to aniline around 1360-1380 cm^{-1} can be distinguished as most distinct peaks, after the potential at -0.4 V is applied at the 10^{th} second, the intense peaks from 1360-1380 cm^{-1} can be seen to experience a gradual blue-shift to 1400-1430 cm^{-1} region to the equilibrium state within 5-10 s and stay relatively stable, at the same time, the intensified peak at 1168-1178 cm^{-1} is also increasing its intensity and reach the stable and saturated point. As the analysis of the 1360-1450 cm^{-1} region is complicated when multiple modes are involved, we choose to analyze the time-dependent peak intensity of the 1168-1178 cm^{-1} peak and have the kinetic information in Figure 6B. Under the assumption that the hydrogen bonding is a pseudo-first-order kinetic (as the activity of aniline is much larger than the surface activity of 4-MBA), we can obtain the kinetic rate constant around 3.4 ± 0.6 s^{-1}. This approximation process neglects the direct current charging response so it may not be the direct accurate measurement of the rate constant, but it to

a reasonable extent reflects the rough reaction rate of the electrochemical potential induced hydrogen bonding at the interface.

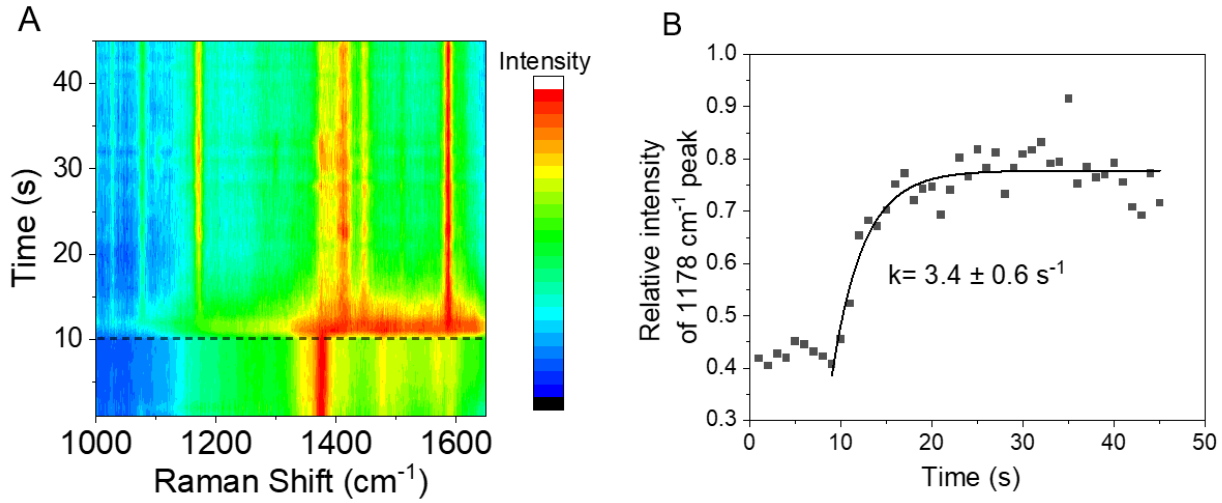

Figure 6.14. Kinetic SERS measurement of hydrogen bond formation.
(A) kinetic time-dependent normalized SERS spectra of the 4-MBA on Au in 1 M aniline (0.1 M in 0.1 M $TBAPF_6$ in CAN), potential jumped at 10 s from +0.2 V to -0.4 V. (B) kinetic reaction rate constant fitting based on the normalized intensity of 1178 cm^{-1} peak.

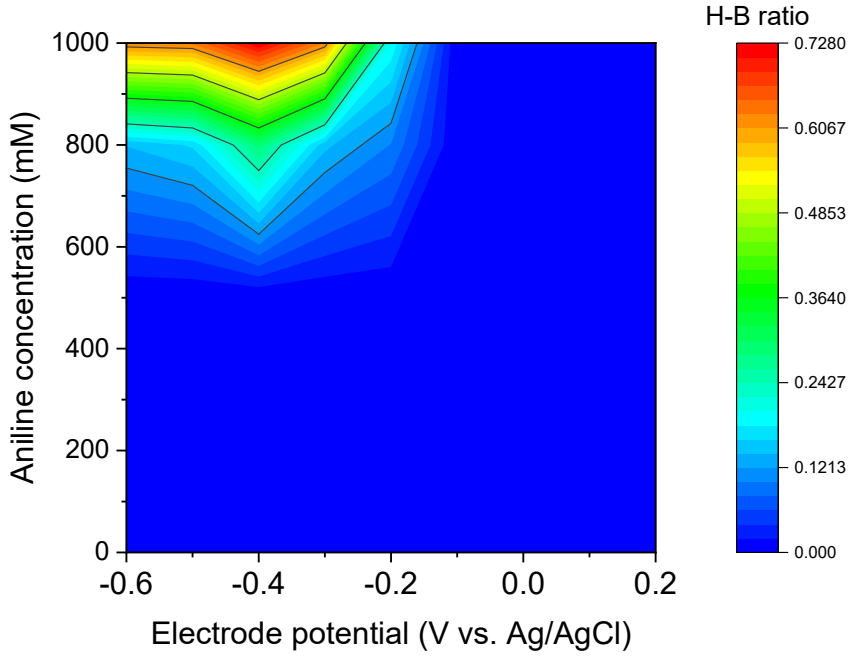

Figure 6.15. Concentration and potential dependent hydrogen-bonded ratios.

The H-B ratios were obtained by the previous spectra fitting and simulation process. The actual experimental data points used in the simulations were collected under 0 mM, 10 mM, 100 mM, 500 mM, 800 mM, and 1000 mM from 0.2 V to -0.6 V with 0.1 V interval. The space between the data points was generated automatically for a smooth connection.

Finally in terms of the concentration of aniline, to analyze the aniline concentration effect on forming hydrogen-bonded complex, we conducted the control measurements with aniline concentrations of 10 mM, 100 mM, 500 mM, 800 mM, and 1000 mM from +0.2 V to -0.4 V. With the experimental results, we obtained the H-B ratio numbers based on the previous fitting and simulation process and plotted them seen in *Figure 6.11*. We find a noticeable amount of hydrogen-bonded complex is only formed in 1000 mM aniline electrolyte and a small number of the complex in 800 mM. We believe the concentration effect should be due to two possible reasons: 1) the hydrogen bonding is relatively weak and requires a lot more aniline to participate, and 2) the acid form of 4-MBA requires much more anilines as a base to deprotonate them to make base form 4-MBA as the hydrogen bonding acceptor.

6.3. Conclusions

In conclusion, we reported a new method of controlling hydrogen bonding between 4-MBA and aniline by electrochemistry at the interface, with a comprehensive investigation into the mechanism of the formation and ruling factors for this H-bonding at the electrochemical interface. By applying the *in-situ* SERS measurements, we identified the spectral features from the hydrogen-bonded complex and confirmed its existence between 4-MBA and aniline with 1 M aniline in ACN. Our observation and further quantitative analysis showed the potential dependent of hydrogen bonding is most favorable at -0.4 V with maximum population. To answer why -0.4 V is the most favorable condition, additional control measurements revealed the molecular formation mechanism of the H-bonding: the electrochemical H-bonding is mainly initiated by the intramolecular induction, the conjugation of the SAM 4-MBA acid to the electrode leads the major role in forming hydrogen bonding, while it can be also destabilized by a competing factor originated from the interaction with electrolyte ions under the electric field.

Besides, throughout additional experiments, we also unraveled the speciation (acid/base form) of SAM species in H-bonding and investigated other ruling factors to form H-bonding such as aniline concentration, and solvent types (dielectric constants).

From these results, our study reported a novel observation of H-bonding at an electrochemical interface, we gained insights into the formation, stabilization, and fine-tuning factors of the electrochemical interfacial H-bonding. For broader impacts, our findings can provide a new method of harnessing and designing surface interactions for surface assembly, electro-catalysis, and surface analytical chemistry.

6.4. References

(1) Herschlag, D.; Pinney, M. M. Hydrogen Bonds: Simple after All? *Biochemistry* **2018**, *57* (24), 3338–3352. https://doi.org/10.1021/acs.biochem.8b00217.
(2) Pimentel, G. C.; McClellan, A. L. Hydrogen Bonding.
(3) Hunt, P. A.; Ashworth, C. R.; Matthews, R. P. Hydrogen Bonding in Ionic Liquids. *Chem. Soc. Rev.* **2015**, *44* (5), 1257–1288. https://doi.org/10.1039/C4CS00278D.
(4) Emsley, J. Very Strong Hydrogen Bonding. *Chem. Soc. Rev.* **1980**, *9* (1), 91. https://doi.org/10.1039/cs9800900091.
(5) Hobza, P.; Havlas, Z. Blue-Shifting Hydrogen Bonds. *Chem. Rev.* **2000**, *100* (11), 4253–4264. https://doi.org/10.1021/cr990050q.
(6) Xi, W.; Shrestha, B. K.; Haes, A. J. Promoting Intra- and Intermolecular Interactions in Surface-Enhanced Raman Scattering. *Anal. Chem.* **2018**, *90* (1), 128–143. https://doi.org/10.1021/acs.analchem.7b04225.
(7) Alkorta, I.; Rozas, I.; Elguero, J. Non-Conventional Hydrogen Bonds. *Chem. Soc. Rev.* **1998**, *27* (2), 163. https://doi.org/10.1039/a827163z.
(8) Xu, Q.; Han, B.; Yan, H. Equilibrium Constant and Enthalpy for the Hydrogen Bonding of Acetic Acid with Tetrahydrofuran in Supercritical CO $_2$. *J. Phys. Chem. A* **1999**, *103* (27), 5240–5245. https://doi.org/10.1021/jp9900739.
(9) Simonvi, M. Determination of the Equilibrium Constant of Hydrogen Bonding between Substituted H-[d]-Phenols and Vinyl Acetate in CCI4 by i.r. Measurements.
(10) Sovago, M.; Campen, R. K.; Wurpel, G. W. H.; Müller, M.; Bakker, H. J.; Bonn, M. Vibrational Response of Hydrogen-Bonded Interfacial Water Is Dominated by Intramolecular Coupling. *Phys. Rev. Lett.* **2008**, *100* (17), 173901. https://doi.org/10.1103/PhysRevLett.100.173901.
(11) Sovago, M.; Kramer Campen, R.; Bakker, H. J.; Bonn, M. Hydrogen Bonding Strength of Interfacial Water Determined with Surface Sum-Frequency Generation. *Chem. Phys. Lett.* **2009**, *470* (1–3), 7–12. https://doi.org/10.1016/j.cplett.2009.01.009.
(12) Scatena, L. F.; Brown, M. G.; Richmond, G. L. Water at Hydrophobic Surfaces: Weak Hydrogen Bonding and Strong Orientation Effects. *Science* **2001**, *292* (5518), 908–912. https://doi.org/10.1126/science.1059514.
(13) Kreibig, U.; Vollmer, M. *Optical Properties of Metal Clusters*; Toennies, J. P., Gonser, U., Osgood, R. M., Panish, M. B., Sakaki, H., Lotsch, H. K. V., Series Eds.; Springer Series in Materials Science; Springer: Berlin, Heidelberg, 1995; Vol. 25. https://doi.org/10.1007/978-3-662-09109-8.
(14) Sarkar, S.; Tseng, C.; Maitra, A.; Voegtle, M. J.; Dawlaty, J. M. Advances in Vibrational Stark Shift Spectroscopy for Measuring Interfacial Electric Fields. In *ACS Symposium Series*; Berman, M. R., Young, L., Dai, H.-L., Eds.; American Chemical Society: Washington, DC, 2021; Vol. 1398, pp 199–224. https://doi.org/10.1021/bk-2021-1398.ch010.
(15) Zhao, K.; Chang, X.; Su, H.; Nie, Y.; Lu, Q.; Xu, B. Enhancing Hydrogen Oxidation and Evolution Kinetics by Tuning the Interfacial Hydrogen-Bonding Environment on Functionalized Platinum Surfaces. *Angew. Chem.* **2022**, *134* (39), e202207197. https://doi.org/10.1002/ange.202207197.

(16) Wang, T.; Zhang, Y.; Huang, B.; Cai, B.; Rao, R. R.; Giordano, L.; Sun, S.-G.; Shao-Horn, Y. Enhancing Oxygen Reduction Electrocatalysis by Tuning Interfacial Hydrogen Bonds. *Nat. Catal.* **2021**, *4* (9), 753–762. https://doi.org/10.1038/s41929-021-00668-0.
(17) Li, J.; Li, X.; Gunathunge, C. M.; Waegele, M. M. Hydrogen Bonding Steers the Product Selectivity of Electrocatalytic CO Reduction. *Proc. Natl. Acad. Sci.* **2019**, *116* (19), 9220–9229. https://doi.org/10.1073/pnas.1900761116.
(18) Zheng, Q.; Huang, X.; Liu, Y.; Fang, X.; Zhang, J.; Shao, H. Electrochemical Quantification of Intermolecular Hydrogen Bonding between Ferrocenemethanol and 3-Mercaptopropanoic Acid on Gold. *J. Phys. Chem. C* **2017**, *121* (40), 22123–22129. https://doi.org/10.1021/acs.jpcc.7b06497.
(19) Li, C.-Y.; Chen, M.; Liu, S.; Lu, X.; Meng, J.; Yan, J.; Abruña, H. D.; Feng, G.; Lian, T. Unconventional Interfacial Water Structure of Highly Concentrated Aqueous Electrolytes at Negative Electrode Polarizations. *Nat. Commun.* **2022**, *13* (1), 5330. https://doi.org/10.1038/s41467-022-33129-8.
(20) Menachekanian, S.; Voegtle, M. J.; Warburton, R. E.; Hammes-Schiffer, S.; Dawlaty, J. M. Inductive Effect Alone Cannot Explain Lewis Adduct Formation and Dissociation at Electrode Interfaces. *J. Am. Chem. Soc.* **2023**, *145* (10), 5759–5768. https://doi.org/10.1021/jacs.2c12370.
(21) Heo, J.; Ahn, H.; Won, J.; Son, J. G.; Shon, H. K.; Lee, T. G.; Han, S. W.; Baik, M.-H. Electro-Inductive Effect: Electrodes as Functional Groups with Tunable Electronic Properties. *Science* **2020**, *370* (6513), 214–219. https://doi.org/10.1126/science.abb6375.
(22) Delley, M. F.; Nichols, E. M.; Mayer, J. M. Electrolyte Cation Effects on Interfacial Acidity and Electric Fields. *J. Phys. Chem. C* **2022**, *126* (19), 8477–8488. https://doi.org/10.1021/acs.jpcc.2c01134.
(23) Delley, M. F.; Nichols, E. M.; Mayer, J. M. Interfacial Acid–Base Equilibria and Electric Fields Concurrently Probed by *In Situ* Surface-Enhanced Infrared Spectroscopy. *J. Am. Chem. Soc.* **2021**, *143* (28), 10778–10792. https://doi.org/10.1021/jacs.1c05419.
(24) Ge, A.; Kastlunger, G.; Meng, J.; Lindgren, P.; Song, J.; Liu, Q.; Zaslavsky, A.; Lian, T.; Peterson, A. A. On the Coupling of Electron Transfer to Proton Transfer at Electrified Interfaces. *J. Am. Chem. Soc.* **2020**, *142* (27), 11829–11834. https://doi.org/10.1021/jacs.0c03472.
(25) Liu, Y.; Yuan, H.; Fales, A. M.; Vo-Dinh, T. pH-Sensing Nanostar Probe Using Surface-Enhanced Raman Scattering (SERS): Theoretical and Experimental Studies: pH-Sensing Nanostar Probe Using SERS. *J. Raman Spectrosc.* **2013**, *44* (7), 980–986. https://doi.org/10.1002/jrs.4302.
(26) Marques, F. C.; Alves, R. S.; dos Santos, D. P.; Andrade, G. F. S. Surface-Enhanced Raman Spectroscopy of One and a Few Molecules of Acid 4-Mercaptobenzoic in AgNP Enabled by Hot Spots Generated by Hydrogen Bonding. *Phys. Chem. Chem. Phys.* **2022**, *24* (44), 27449–27458. https://doi.org/10.1039/D2CP03375E.
(27) Zhou, L.; Zhou, J.; Lai, W.; Yang, X.; Meng, J.; Su, L.; Gu, C.; Jiang, T.; Pun, E. Y. B.; Shao, L.; Petti, L.; Sun, X. W.; Jia, Z.; Li, Q.; Han, J.; Mormile, P. Irreversible Accumulated SERS Behavior of the Molecule-Linked Silver and Silver-Doped Titanium Dioxide Hybrid System. *Nat. Commun.* **2020**, *11* (1), 1785. https://doi.org/10.1038/s41467-020-15484-6.
(28) Qi, Y.; Hu, Y.; Xie, M.; Xing, D.; Gu, H. Adsorption of Aniline on Silver Mirror Studied by Surface-Enhanced Raman Scattering Spectroscopy and Density Functional Theory Calculations: SERS of Aniline Adsorbed on Silver Mirror. *J. Raman Spectrosc.* **2011**, *42* (6), 1287–1293. https://doi.org/10.1002/jrs.2864.

(29) Chiş, V.; Venter, M. M.; Leopold, N.; Cozar, O. Raman, Surface-Enhanced Raman Scattering and DFT Study of Para-Nitro-Aniline. *Vib. Spectrosc.* **2008**, *48* (2), 210–214. https://doi.org/10.1016/j.vibspec.2008.01.001.
(30) Morávková, Z.; Dmitrieva, E. The First Products of Aniline Oxidation – SERS Spectroelectrochemistry. *ChemistrySelect* **2019**, *4* (30), 8847–8854. https://doi.org/10.1002/slct.201802878.
(31) Morávková, Z.; Šeděnková, I.; Bober, P. The First Stages of Chemical and Electrochemical Aniline Oxidation—Spectroscopic Comparative Study. *Appl. Sci.* **2020**, *10* (6), 2091. https://doi.org/10.3390/app10062091.
(32) Holze, R. The Adsorption of P-Nitroaniline on Silver and Gold Electrodes as Studied with Surface Enhanced Raman Spectroscopy (SERS). *Electrochimica Acta* **1990**, *35* (6), 1037–1044. https://doi.org/10.1016/0013-4686(90)90039-3.
(33) Ping, Z.; Nauer, B. G. E.; Neugebauer, H.; Theiner, J.; Neckel, A. Protonation and Electrochemical Redox Doping Processes of Polyaniline in Aqueous Solutions: Investigations Using in Situ FTIR-ATR Spectroscopy and a New Doping System. *J. Chem. Soc. Faraday Trans.* **1997**, *93* (1), 121–129. https://doi.org/10.1039/a604620g.
(34) Holze, R. The Adsorption of Aniline on Gold: A SERS Study. *J. Electroanal. Chem. Interfacial Electrochem.* **1988**, *250* (1), 143–157. https://doi.org/10.1016/0022-0728(88)80199-2.
(35) Łuczak, T.; Bełtowska-Brzezinska, M.; Bron, M.; Holze, R. The Adsorption of Benzylamine on a Polycrystalline Gold Electrode: A Combined Spectroelectrochemical Study. *Vib. Spectrosc.* **1997**, *15* (1), 17–25. https://doi.org/10.1016/S0924-2031(97)00015-5.
(36) Zhao, L.-B.; Huang, R.; Bai, M.-X.; Wu, D.-Y.; Tian, Z.-Q. Effect of Aromatic Amine−Metal Interaction on Surface Vibrational Raman Spectroscopy of Adsorbed Molecules Investigated by Density Functional Theory. *J. Phys. Chem. C* **2011**, *115* (10), 4174–4183. https://doi.org/10.1021/jp1117135.
(37) Tong, L.; Yu, Z.; Gao, Y.-J.; Li, X.-C.; Zheng, J.-F.; Shao, Y.; Wang, Y.-H.; Zhou, X.-S. Local Cation-Tuned Reversible Single-Molecule Switch in Electric Double Layer. *Nat. Commun.* **2023**, *14* (1), 3397. https://doi.org/10.1038/s41467-023-39206-w.
(38) Wang, Y.; Ji, W.; Sui, H.; Kitahama, Y.; Ruan, W.; Ozaki, Y.; Zhao, B. Exploring the Effect of Intermolecular H-Bonding: A Study on Charge-Transfer Contribution to Surface-Enhanced Raman Scattering of *p* -Mercaptobenzoic Acid. *J. Phys. Chem. C* **2014**, *118* (19), 10191–10197. https://doi.org/10.1021/jp5025284.
(39) Zhang, X.; Yu, Z.; Ji, W.; Sui, H.; Cong, Q.; Wang, X.; Zhao, B. Charge-Transfer Effect on Surface-Enhanced Raman Scattering (SERS) in an Ordered Ag NPs/4-Mercaptobenzoic Acid/TiO_2 System. *J. Phys. Chem. C* **2015**, *119* (39), 22439–22444. https://doi.org/10.1021/acs.jpcc.5b06001.
(40) Lombardi, J. R.; Birke, R. L. A Unified Approach to Surface-Enhanced Raman Spectroscopy. *J. Phys. Chem. C* **2008**, *112* (14), 5605–5617. https://doi.org/10.1021/jp800167v.
(41) Prinz, H. Hill Coefficients, Dose–Response Curves and Allosteric Mechanisms. *J. Chem. Biol.* **2010**, *3* (1), 37–44. https://doi.org/10.1007/s12154-009-0029-3.
(42) Jagadeesh, R. V.; Lakshminarayanan, V. Adsorption Kinetics of Phosphonic Acids and Proteins on Functionalized Indium Tin Oxide Surfaces Using Electrochemical Impedance Spectroscopy. *Electrochimica Acta* **2016**, *197*, 1–9. https://doi.org/10.1016/j.electacta.2016.03.008.

(43) Latour, R. A. The Langmuir Isotherm: A Commonly Applied but Misleading Approach for the Analysis of Protein Adsorption Behavior. *J. Biomed. Mater. Res. A* **2015**, *103* (3), 949–958. https://doi.org/10.1002/jbm.a.35235.
(44) Wu, H.; Ghaani, M. R.; Futera, Z.; English, N. J. Effects of Externally Applied Electric Fields on the Manipulation of Solvated-Chignolin Folding: Static- versus Alternating-Field Dichotomy at Play. *J. Phys. Chem. B* **2022**, *126* (2), 376–386. https://doi.org/10.1021/acs.jpcb.1c06857.
(45) Cunningham, G. P.; Vidulich, G. A.; Kay, R. L. Several Properties of Acetonitrile-Water, Acetonitrile-Methanol, and Ethylene Carbonate-Water Systems. *J. Chem. Eng. Data* **1967**, *12* (3), 336–337. https://doi.org/10.1021/je60034a013.
(46) Gestblom, B.; Songstad, J.; Mattinen, J.; Bernáth, G.; Eberson, L. Solvent Properties of Dichloromethane. VI. Dielectric Properties of Electrolytes in Dichloromethane. *Acta Chem. Scand.* **1987**, *41b*, 396–409. https://doi.org/10.3891/acta.chem.scand.41b-0396.
(47) Fu, X.; Liao, Y.; Glein, C. R.; Jamison, M.; Hayes, K.; Zaporski, J.; Yang, Z. Direct Synthesis of Amides from Amines and Carboxylic Acids under Hydrothermal Conditions. *ACS Earth Space Chem.* **2020**, *4* (5), 722–729. https://doi.org/10.1021/acsearthspacechem.0c00009.
(48) Li, R.; Lv, H.; Zhang, X.; Liu, P.; Chen, L.; Cheng, J.; Zhao, B. Vibrational Spectroscopy and Density Functional Theory Study of 4-Mercaptobenzoic Acid. *Spectrochim. Acta. A. Mol. Biomol. Spectrosc.* **2015**, *148*, 369–374. https://doi.org/10.1016/j.saa.2015.03.132.

7. Chapter 7 *In situ* spectroscopic studies of electrochemical catalysis in CO2RR

7.1. Introduction

The electrocatalytic CO_2 reduction reaction (CO_2RR) has emerged as a promising solution for addressing the global challenge of greenhouse gas emissions, providing a way to store renewable electrical energy in the form of chemical bonds.[1,2] Copper is a particularly advantageous material for CO_2 reduction due to its cost-effectiveness and its ability to generate energy-dense and economically valuable C_{2+} products (compounds with more than two carbons) with minimal overpotentials.[3–5] For C_{2+} product-oriented pathways on Cu, *CO (* indicating adsorption to the electrode) is a crucial precursor for the C-C coupling reaction to make C_{2+} products. To better understand fuel-forming reactions following the conversion of CO_2 to CO conversion, a variety of theoretical, electro-kinetic, and spectroscopic studies have been conducted on the C-C coupling process.[6–16] While these studies have been invaluable in advancing our understanding of the reaction, a greater focus must now be devoted to the initial stage of CO_2 reduction on Cu, namely generating CO via CO_2 activation.[6,17–19].

Reducing CO_2 to CO is a complex, multi-step process that involves multiple intermediates and competing pathways[1,20] the most accepted mechanism is shown in Scheme 1. The very first step is the initial activation of CO_2 which also includes many intermediates/possible pathways. Previous research has identified the reductive chemisorption of CO_2 to a carboxylate group coordinated through carbon and oxygen to the metal surface, η^2(C,O)-COO^- (B in Scheme 1), following Eq. (1), to be the activation intermediate for CO_2 reduction on Cu(poly).[18] It undergoes further reactions to produce either CO (D) or formate (CHO_2). However, the precise mechanism behind this reaction remains a subject of debate.[5] Hori et al. proposed that a strongly bound carboxylate (B) can undergo protonation, i.e. Eq (2), to form a carboxyl group (*COOH, C in Scheme 1), which can then be further reduced to make CO via proton-coupled electron transfer (PCET), following Eq (3).[3,5] Alternatively, Chernyshova et al. proposed that a weakly bonded carboxylate can have its carbon protonated to form formyloxyl (*OCHO), following Eq (4), which is further reduced to produce formate[18].

$$CO_2 + e^- \rightleftharpoons * COO^- \quad (1)$$

$$*COO^- + H^+ \rightleftharpoons *COOH \quad (2)$$

$$*COOH + e^- + H^+ \rightleftharpoons CO + H_2O \quad (3)$$

$$*COO^- + H^+ \rightleftharpoons *OCHO \quad (4)$$

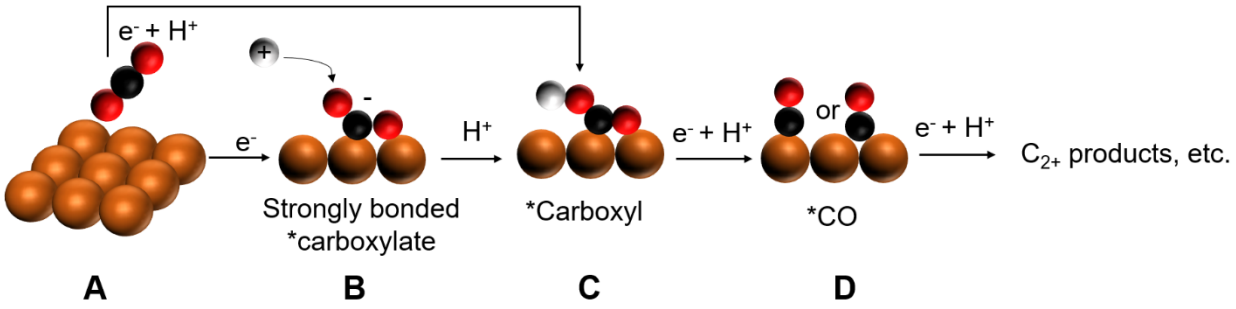

Scheme 7.1. Electrochemical reduction of CO_2 to CO pathway on polycrystal Cu. Different color spheres represent different atoms: black-carbon, red-oxygen, white-hydrogen, brown-copper.

However, the above reaction mechanism model from CO_2 to CO or formate[17,21,22] may not accurately describe the reactions at a polarized Cu interface with other surface binding species that can affect activities. In a commonly-used $NaHCO_3$ aqueous solution at a polarized Cu interface, surface bonded species such as carbonate,[23] bicarbonate,[24,25] Cu(I) oxide/Cu[6,17] and *OH on Cu[15,19] have been reported to alter the reaction and affect the product distribution. The conventional model fails to consider the interaction, rearrangement, and displacement between the CO2-reduced intermediates and the electrolyte ions which may alter the reaction pathway. Besides, though the importance of these interactions has been realized by many studies, the mechanistic understanding is still impeded due to the unclear assignments for the key CO2-reduced intermediates. For example, A controversial aspect concerns the assignment of the Raman peaks at ~360 cm^{-1} and ~1540 cm^{-1}, which have been assigned to bidentate adsorbed carbonate,[24,26–29] a CO_2 activated intermediate (cations stabilized adsorbed carboxylate, $*COO^-M^+$),[18,30] and a copper-carbonate-hydroxide intermediate (malachite).[31]

In this study, we aim to address the drawback of the conventional CO_2 to CO reduction model by the additive consideration of competitive binding of electrolyte anions and the development of a detailed spectroscopic assignment of the key intermediates during the

electrochemical CO_2 reduction process. We firstly combine *in situ* Shell-Isolated Nanoparticle Enhanced Raman Spectroscopy (SHINERS) and density functional theory (DFT) calculations in the species assignment: through experimental spectra involving isotope labeling and modification of the electrolyte, we resolve the assignments of the distinct spectral features to surface species, reactants, products, and reactive intermediates at low overpotentials. We assign these spectra based on our results of DFT calculations with the information on potential-dependent frequency shifts, isotope shifts, and binding energies under various reaction conditions. Then by comparing the results of electrolyte solutions with differently decreasing amounts of bicarbonate (the source of carbonate on the surface), we analyze the potential dependent intensity change of the surface species during CO_2 reduction to CO affected by competitive surface carbonate. To evaluate the physical implications of our observations on the carbonate binding affected CO_2 reduction, we perform Monte Carlo simulations of a simple lattice model of surface adsorption involving different species: comparing MC simulation to experimental results under the three conditions with only carbonate, only CO and carbonate competing CO allows us to validate the conclusions on the competing binding role of the carbonate anion in the electrolyte at this stage of CO_2 reduction.

7.2. Anion competitive binding effects in CO_2 reduction on Cu electrodes

We firstly combine *in situ* Shell-Isolated Nanoparticle Enhanced Raman Spectroscopy (SHINERS) and density functional theory (DFT) calculations in the species assignment: through experimental spectra involving isotope labeling and modification of the electrolyte, we resolve the assignments of the distinct spectral features to surface species, reactants, products, and reactive intermediates at low overpotentials. We assign these spectra based on our results of DFT calculations with the information on potential-dependent frequency shifts, isotope shifts, and binding energies under various reaction conditions. Then by comparing the results of electrolyte solutions with differently decreasing amounts of bicarbonate (the source of carbonate on the surface), we analyze the potential dependent intensity change of the surface species during CO_2 reduction to CO affected by competitive surface carbonate. To evaluate the physical implications of our observations on the carbonate binding affected CO_2 reduction, we perform Monte Carlo

simulations of a simple lattice model of surface adsorption involving different species: comparing MC simulation to experimental results under the three conditions with only carbonate, only CO and carbonate competing CO allows us to validate the conclusions on the competing binding role of the carbonate anion in the electrolyte at this stage of CO_2 reduction.

7.2.1. Raman measurements of CO2 reduction on Cu

Figure 7.1 shows schematically the *in situ* SHINERS measurement for electrocatalysis on Cu electrodes in a three-electrode setup. In this study, we use shell-insolated nanoparticles (SHINs) comprised of a 55±5 nm diameter Au core and a 2-3 nm SiO_2 shell, synthesized by a literature procedure.[32] For *operando* SHINERS measurement, SHINS were deposited on the Cu electrode to form gap plasmonic modes that amplify Raman intensity by about 6 orders of magnitude (**Figure 7.1**A)[32]. The method has been successfully used for probing surface intermediates involved in CO/CO_2 reduction to C_{2+} products on Cu(*hkl*)/Cu(poly) electrodes[10,33,34].

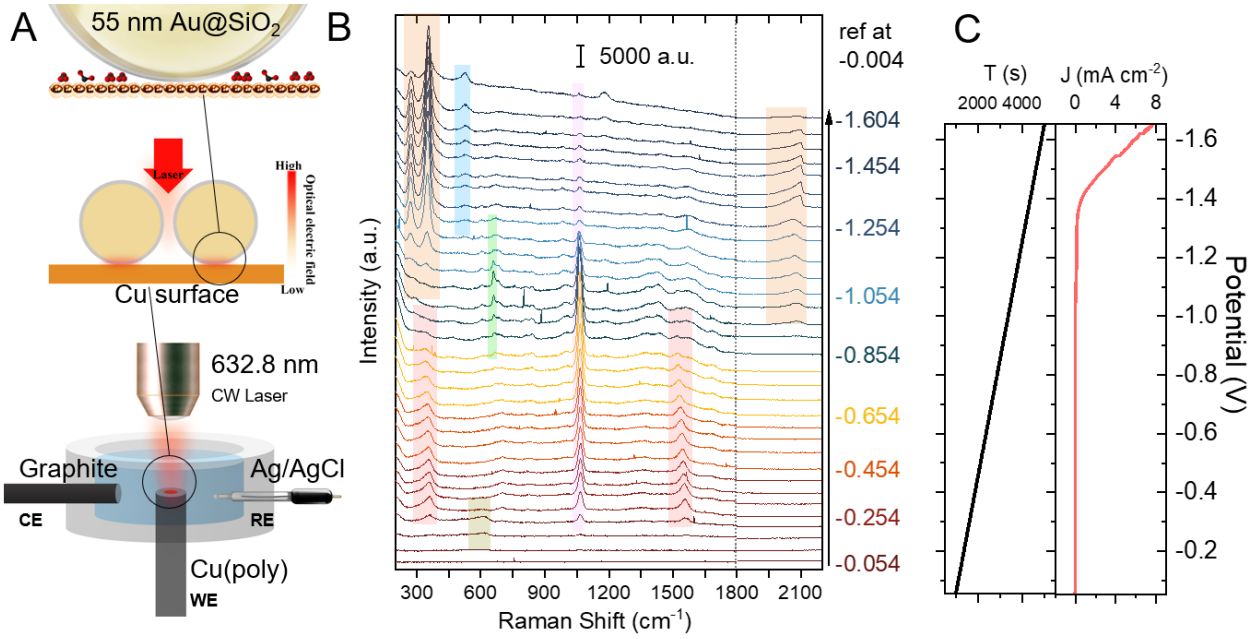

Figure 7.1. *in situ* electrochemical SHINERS measurement
(A) Scheme of *in situ* electrochemical SHINERS measurement. (B) *in situ* Raman spectra of CO_2 reduction to CO in 0.5 M $NaDCO_3/D_2O$ on Cu (poly) at indicated potentials (vs Ag/AgCl). Each potential indicates a range of +/ 25 mV. The same color-coded Raman peaks represent different modes of the same species. (C) Linear sweep voltammetry during spectra scan (potential applied as a function of time shown as left black curve, obtained current density as a function of applied potential shown by the right red curve, scan rate 0.4 mV/s).

Figure 7.1 B shows the representative potential-dependent *in situ* SHINERS difference spectra measured on polycrystalline Cu in 0.5 M $NaDCO_3$ D_2O solution saturated with CO_2. Spectra were obtained every 125 seconds during the linear sweep voltammetry (LSV) measurement from 0.346 V (vs. Ag/AgCl) to -1.654 V at a 0.4 mV/s scan rate. Each spectrum is the average of 50 mV potential range and only the average potential is indicated in **Figure 7.1** B. The spectral windows from 100 to 1800 cm^{-1} and 1800 to 2200 cm^{-1} were measured separately and then combined to generate the full spectrum. The represented linear sweep voltammograms (LSV) of these measurements are shown in **Figure 7.1** C. The spectra contain contributions of species within the double layer and in bulk solution, whose Raman spectra are dependent and independent of the applied potentials, respectively. To isolate the contribution of the former, all raw Raman spectra are subtracted by the reference spectrum at -0.004 V to produce the corresponding difference in Raman spectra, as shown in Figure S3. This reference spectrum is chosen at -0.004 V, a potential at which no CO_2 reduction-related reactions have occurred, as shown in Figure S3 and S4. Figure S4 compares the raw and subtracted spectra in both H_2O and D_2O at selected potentials. Similar SHINERS spectra were also measured in H_2O to help the assignment of OH/OD-related Raman peaks. The potential-dependent Raman peaks in **Figure 7.1** B and **Figure 7.2** have been color-coded, with the modes of the same species in the same color. We attribute these spectral features to surface-adsorbed species that are affected by the potential-dependent electric field (through the vibrational Stark effect), populations, orientations, and other interactions.

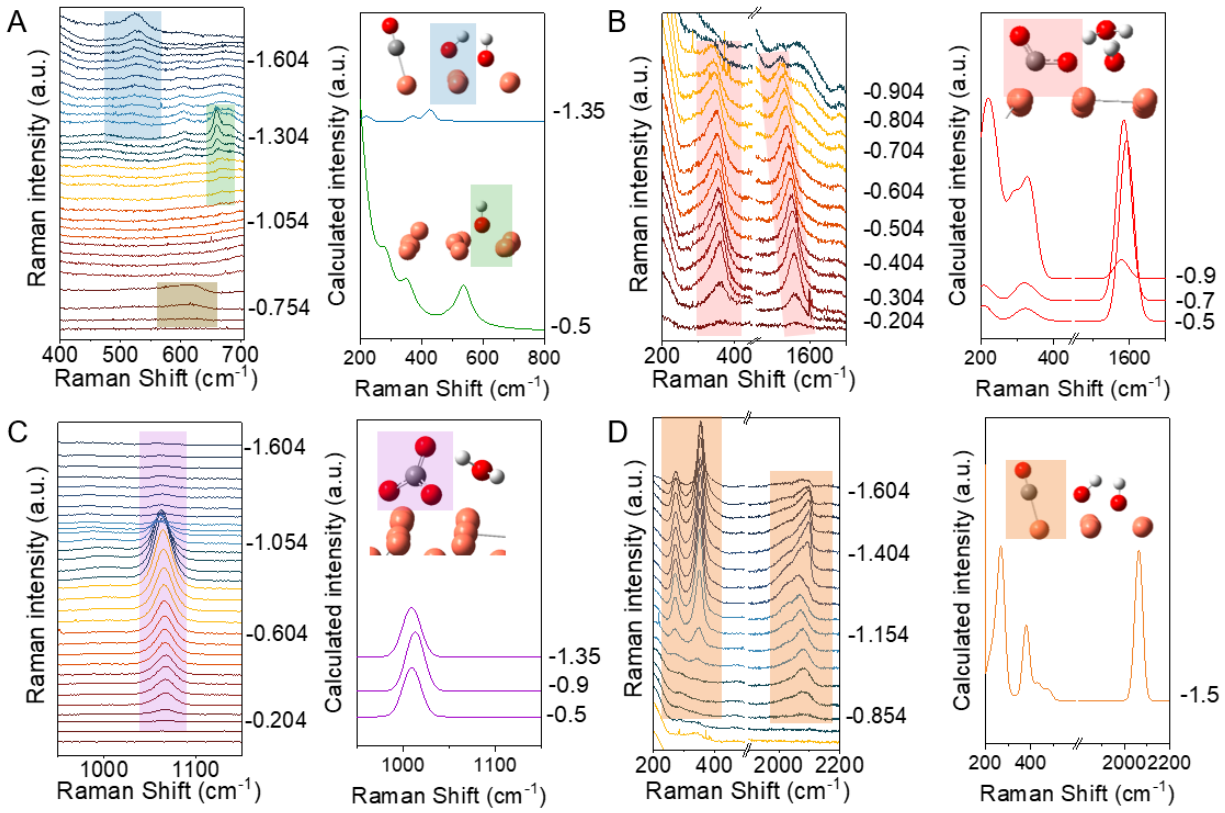

Figure 7.2. Assignments of key species
Comparison of measured potential dependent Raman spectra (left) and computed Raman spectra (right) of proposed adsorbed species. Color codes for atoms: C (grey), O (red), and D(H) (white). (A) Cu_2O at 623 cm^{-1} (dark yellow shaded), Cu-OD at ~670 cm^{-1} (green shaded) and $CuO_x(OD)_y$ at ~525 cm^{-1} (blue shaded), (B) $*COO^-$ M^+ at ~1540 and ~340 cm^{-1} (red shaded), (C) $*CO_3^{2-}$ at ~ 1070 cm^{-1} (purple shaded), (D) *CO at ~280 cm^{-1}, ~360 cm^{-1} and 2080 cm^{-1} (orange shaded).

7.2.2. Key species assignments

To assign the observed Raman spectral peaks, we conducted DFT calculations and compared the computed Raman spectra to the experimental observations in D_2O. **Figure 7.2** A to D shows the comparison of the measured and computed Raman spectra of key surface adsorbed species and their computed structures and additional computed spectra are provided in Figure S5-9. We used three key observations to facilitate the assignment: Raman frequencies, the direction of potential-dependent vibrational frequency shifts (Stark shifts), and H/D isotopic effects (Table S1 and Figure S9-15), and the detailed assignment and discussion are provided in Section SI2.3-

2.5. The observed surface species can be classified into two distinct categories: carbon-containing species (*CO, *COO^-, and (*CO_3^{2-}) and non-carbon-containing (Cu oxygen-related) species. The ~1540 cm^{-1} and the ~360 cm^{-1} peaks from -0.2 V to -0.85 V (red shaded in **Figure 7.2**B) are assigned to surface cation stabilized carboxylate (*COO^- M^+). This assignment is consistent with a recent report[18], although different assignments have also been reported[24,26–29,31]. A detailed discussion of this assignment is provided in SI 2.4. The Raman peak at ~1055 cm^{-1} from -0.2 V to -1.3 V (purple shaded in Figure 2C) is assigned to surface adsorbed carbonate anions (*CO_3^{2-}), following literature reports and the carbonate peak in solution[35,36]. The Raman peaks at ~2080 cm^{-1}, ~290 cm^{-1}, and ~350 cm^{-1} from -0.904 V to -1.604 V (orange shaded in **Figure 7.2**B) are assigned to the surface adsorbed carbon monoxide (*CO), consistent with literature reports. The Raman peak at~623 cm^{-1} from -0.054 to -0.204 V (dark yellow shaded in **Figure 7.2**A) can be assigned to Cu_2O following literature reports[10,37]. The ~660 cm^{-1} peak and ~523 cm^{-1} peak (green and blue shaded in **Figure 7.2**A) are tentatively assigned to Cu-O-D(H) species, as discussed in SI 2.5. Both their spectral assignment and role in the CO_2 reduction reaction remain unclear and will not be further discussed in this work. Table 1 summarizes the assignments of the key species, along with their corresponding vibrational modes.

7.2.3. Potential dependent adsorbate coverage during CO_2 reduction

Using the surface species assignments in the previous section, **Figure 7.3**A plots each adsorbate's normalized Raman intensity as a function of applied potential during a cathodic scan of a Cu electrode in CO2-saturated 0.5 M $NaHCO_3$ solution (the plot including more species under the same condition can be found in Figure S16). This figure illustrates an interchange between electrolyte anions and the CO_2 reduction intermediates on the surface. We divide the overall interchange into a sequence of four stages in the cathodic scan. In Stage 1 (Cu_2O reduction), from ~ 0.0 to 0.3 V, Cu_2O is reduced to Cu, following Eq. (1), which initiates surface co-adsorption of $*COO^-$ and $*CO_3^{2-}$, following Eq (2a) and (2b), respectively. These processes lead to the onset of a small Faradaic current shown in **Figure 7.3**A lower panel. This result suggests that poly-Cu reduction (a Cu-rich surface) is required before CO_2 reduction can proceed, consistent with previous reports[10,13,37,38]. In Stage 2 (Competitive binding), from ~ -0.3 - 0.85 V, the surface coverage of $*CO_3^{2-}$ continues to increase, while that of $*COO^-$ reaches a peak value and then decreases. At around -0.85 V, the Cu surface is primarily covered by $*CO_3^{2-}$. As discussed in the next section, this is attributed to the strong binding of carbonate on Cu, which inhibits the formation of more $*COO^-$. In stage 3 (Carbonate desorption), from -0.85 V to – 1.4 V, the increasingly negative surface charges caused by applied potential leads to desorption of $*CO_3^{2-}$, Eq (2b), which coincides with the formation of *CO, a product of CO_2 reduction, following Eq. (3). At this potential range *CO, instead of $*COO^-$ is a stable intermediate. This observation is also consistent with the competitive binding of *CO and $*CO_3^{2-}$ reported previously[28,29,39,40] In stage 4 (CO reduction), from -1.4 to -1.6V, the population of *CO decreases while the Faradic current increases, indicating the increasing rate of *CO reduction.

$$Cu_2O + 2e^- + 2H^+ \rightleftharpoons Cu + H_2O \quad (1)$$

$$* + CO_2 + e^- \rightleftharpoons *COO^- \quad (2a)$$

$$* + CO_3^{2-} \rightleftharpoons *CO_3^{2-} \quad (2b)$$

$$*COO^- + e^- + H^+ \rightleftharpoons *CO \text{ (statically stable)} + OH^- \quad (3)$$

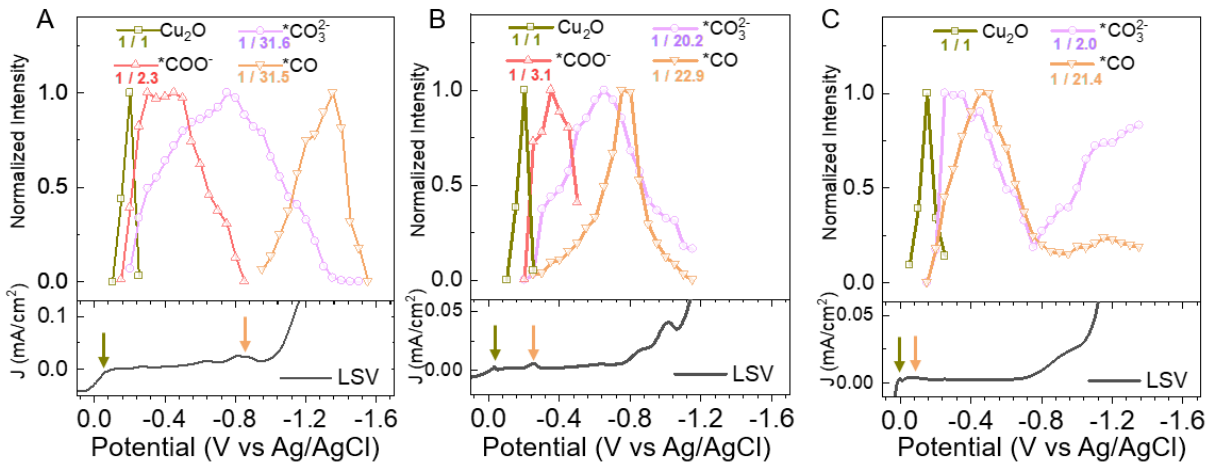

Figure 7.3. Potential dependent surface species during CO_2 reduction and linear sweep voltammetry current density (black line, bottom panel).
In electrolyte (A) E1 (0.5 M NaHCO3, saturated with CO_2, pH=7.2), (B) E2 (0.1 M NaHCO3 + 0.4 M NaClO4, saturated with CO_2, pH=6.8) and (C) E3 (0.5 M $NaClO_4$, saturated with CO_2, pH=4.6). Scan rate 0.4 mV/s. Raman frequency of key species: 623 cm^{-1} (Cu_2O, grey line with square points), 1540 cm^{-1} (*COO^-, red line with triangle points), 1065 cm^{-1} (*CO_3^{2-}, purple line with round points), ~2000 to 2100 cm^{-1} (*CO, orange line with inverted triangle points). The intensity was normalized to the maximum intensity of Cu_2O and is scaled down by the factor mentioned in the numbers within the figures (labeled as the same colors as the intensity data points of species, i.e., 1 / 2.3 represents the original intensity values is scaled down by 2.3 times to be plotted in this figure). The arrow markers with colors in LSV panels represent the onset potentials for the species plotted in the same color in intensity panels. Relevant Raman spectra for B and C can be found in SI 2.8 (Figure S17 to S 18).

To test this hypothesis of carbonate competitive binding with *COO^- and *CO, we carried out a study of the effect of carbonate concentration on CO_2 reduction. This is done by comparing three electrolyte solutions: (E1) CO_2-saturated 0.5 M $NaHCO_3$ (pH=7.2), (E2) CO_2-saturated 0.1 M $NaHCO_3$ + 0.4 M $NaClO_4$ solution (pH = 6.8), and (E3) CO_2-saturated 0.5 M $NaClO_4$ solution (pH = 4.6). The result of E1 has been shown in Figures 7.1, 2, and 3A and discussed above. These solutions have different ratios of $NaHCO_3$ and $NaClO_4$, but the total ion concentrations are kept the same to maintain the same ionic strength. Perchlorate is chosen for this experiment because perchlorate anions are reported to be non-adsorbing species on Cu electrodes[28,39]. Because carbonate is in equilibrium with bicarbonate in solution, its concentration is controlled by the concentration of initially added bicarbonate (specified above). The equilibrium also dictates that changing carbonate concentration is necessarily accompanied by a change in solution pH. Thus, both the effects of pH and carbonate concentration changes on CO_2 reduction should be considered.

The potential dependent Raman spectra during the cathodic scan in electrolyte solutions E2 and E3 are shown in Figures S17 and S18, respectively. **Figure 7.3** A-C compare the normalized intensity of key species as a function of potential for the three systems of various bicarbonate concentration. SHINER intensity depends on the population, Raman cross-section, and field enhancement factor, and because the field enhancement factor varies from one measurement to another, this variation should be accounted for to compare relative populations from different measurements. To do that, the highest intensity of Cu_2O is set to one and all other species are normalized relative to Cu_2O for each measurement in Figure 3A-C, and the normalization factors, which set the peak relative intensity to 1, are indicated in the legend. If we assume that the Cu_2O signal is proportional to electrode surface area, the normalization factor indicates the relative peak population of these species in different electrolyte solutions per unit surface area. As shown in Figure 3A-C, the relative peak $*CO_3^{2-}$ coverage is 31.6, 20.2, and 2.0 in electrolytes E1, E2, and E3, decreasing at lower initial bicarbonate concentration in the electrolyte. Although in electrolyte E3, no carbonate or bicarbonate was added to the solution, a small amount of carbonate can be expected due to conversion between dissolved CO_2, carbonic acid, bicarbonate, and carbonate in a CO2-saturated solution[41]. Furthermore, the potential of peak $*CO_3^{2-}$ coverage shifts from ~ -0.8V in E1 to ~-0.6 V in E2 and ~ -0.2 V in E3. As shown in Figure S21, the estimated potential of zero charge (PZC) of Cu electrodes is at ~ -0.85 V, ~-0.4 V, and ~-0.15 V in electrolytes E1, E2, and E3, respectively, which correlates with potentials of peak $*CO_3^{2-}$ coverage. *CO onset occurs at ~-0.85 in electrolyte E1 (Figure 3A), ~ -0.25 V in E2 (**Figure 7.3**B), and ~-0.15 V in E3 (**Figure 7.3**C), shifting to more anodic potentials in electrolytes with lower bicarbonate concentration. We also plot the *CO intensity under the RHE scale in Figure S20, which also shows a similar trend in the *CO onset potentials in these electrolytes. The LSV responses in these electrolyte solutions, shown in the lower panel of **Figure 7.3** and detailed in Figure S19B, show peaks at -0.3 V in E2 and -0.1 V in E3, in accordance with the increasingly more anode onset potentials of *CO peak in the Raman spectra. We also conducted DEMS measurements to support the observation of earlier CO formation (seen in SI 2.11), but bulk phase CO was below the instrument detection limit to be detected. It should be noted that similar potential dependent intensity peak changes on *CO, $*CO_3^{2-}$ have been reported previously and were discussed according to a different mechanism,[31,42] which is discussed in SI 2.10.

The change in *CO formation onset potential in electrolytes E1, E2, and E3 may be caused by different pH and/or different $*CO_3^{2-}$ coverage (competitive binding). Previous experimental studies[43–45] have shown that for CO_2 to CO reaction, neither the onset potential of CO detected by DEMS nor the experimental current due to CO_2RR to CO exhibit significant pH dependence, and a zero reaction order was found in all possible proton sources (HA[43], bicarbonate[46], water[47]) in the electrolytes. The independence of the CO onset on the pH was rationalized by a model with the formation of $*COO^-$ being the rate-determining step (RDS) in the overall CO_2RR. Thus, we attribute the earlier formation *CO in E2 and E3 to an anodic shift of the $*CO_3^{2-}$ competitive binding (or "poisoning") on the surface, which frees up active sites for CO_2 reduction. According to the $*CO_3^{2-}$ competitive binding model, under low carbonate binding conditions (both in E2 and E3), the onset of *CO formation begins when Cu_2O reduction occurs (~-0.15V); but under high carbonate binding conditions (E1 and E2), *CO formation is delayed due to the much stronger adsorption of $*CO_3^{2-}$ that block surface reaction sites.

7.2.4. Competitive binding model for CO_2 reduction on Cu

During the CO_2 reduction study described above, the potential dependent competitive binding of $*CO_3^{2-}$ with $*COO^-$ and *CO is convoluted with the potential dependent CO_2 reduction reaction itself, which hinders quantitative modeling. To better understand the competitive binding process, we carried out a study of competitive binding between $*CO_3^{2-}$ and *CO in CO-saturated carbonate solution using both *in situ* Raman spectroscopy and Monte Carlos (MC) modeling. This study involves Raman measurement in three electrolytes: 1) the first experiment probes the potential dependent adsorption behavior of $*CO_3^{2-}$ in the absence of CO in C1 electrolyte (0.25 M Na_2CO_3 aqueous solution saturated with Ar, pH=11.95); 2) the second experiment investigates the potential dependent adsorption of *CO on Cu in the absence of carbonate in C2 electrolyte (0.5 M $NaClO_4$ aqueous solution saturated with CO, pH=7.62); and the third control experiment examines the competitive binding of $*CO_3^{2-}$ and *CO in C3 electrolyte (0.5 M $NaHCO_3$ aqueous solution saturated with CO, pH=8.44).

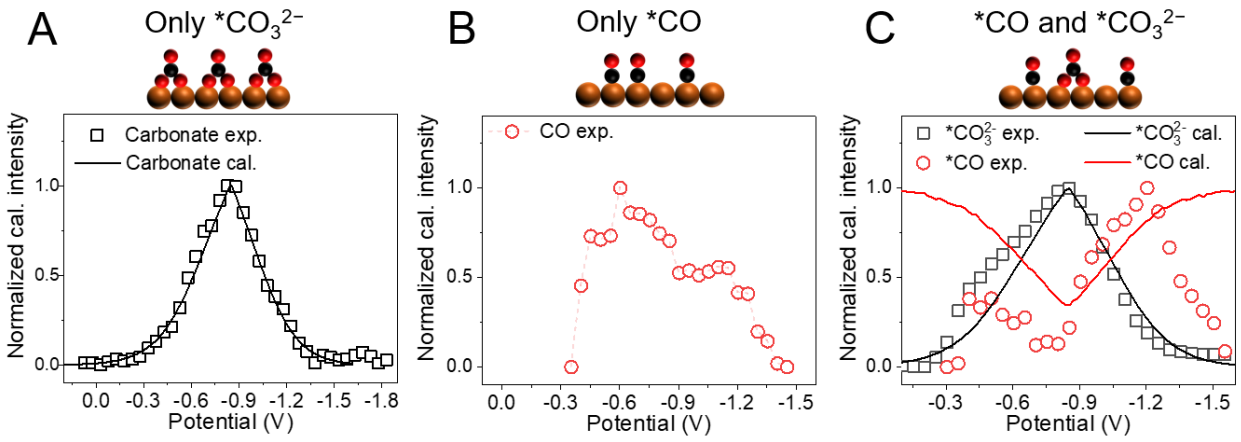

Figure 7.4. Experimental and Monte Carlo modeling of competitive binding between $*CO_3^{2-}$, *CO, and H_2O on Cu electrodes.
(A) Comparison of potential dependent coverage of $*CO_3^{2-}$ in the absence of *CO measured by SHINER in C1 electrolyte (0.25 M Na_2CO_3 aqueous solution saturated with Ar, pH=11.95) (hollow square) and calculated by MC simulation (solid black line). (B) Potential dependent coverage of *CO in the absence $*CO_3^{2-}$ measured by SHINER in C2 electrolyte (0.5 M $NaClO_4$ aqueous solution saturated with CO, pH=7.62). (C) Comparison of potential dependent coverage of $*CO_3^{2-}$ and *CO measured by SHINER in C3 electrolyte (0.5 M $NaHCO_3$ aqueous solution saturated with CO, pH=8.44) and simulated by MC modeling. Black square and red round (with transparent dash line) represent the $*CO_3^{2-}$ and *CO data points measured by experimental Raman spectra

respectively, and black solid line and red solid line represent the MC simulated $*CO_3^{2-}$ and *CO data points respectively. Relevant Raman spectra can be found in SI 2.12 (Figure S24 to S27).

To examine the potential dependent $*CO_3^{2-}$ in the absence of CO or CO_2 reduction intermediates (*CO, $*COO^-$), we carried out *in situ* SHINER measurement in C1 electrolyte (Ar-saturated 0.25 M Na_2CO_3, pH=11.95). The Raman spectra (shown in Figure S24) during a cathodic scan from +0.1 V to -1.8 V show a clear peak of $*CO_3^{2-}$. The spectra show negligible signatures associated with $*COO^-$ and *CO (~360 cm^{-1}, ~1540 cm^{-1}, and ~2080 cm^{-1}), which is consistent with the negligible amount of dissolved CO_2 and associated CO_2 reduction intermediates under the alkaline pH conditions in an Ar saturated solution. Therefore, under this condition, the potential dependent $*CO_3^{2-}$ intensity reflects the direct competitive binding between carbonate anions and water on Cu surfaces (without the participation of other carbon-containing species). The normalized intensity of $*CO_3^{2-}$ and MC simulated population of $*CO_3^{2-}$ as a function of potential is plotted in **Figure 7.4**A, both of which show a peak at around -0.8 V and decrease at more positive or negative potentials. This potential dependent $*CO_3^{2-}$ intensity profile in Ar (pH~12.0, **Figure 7.4**A) resembles that in CO_2 saturated 0.5M $NaHCO_3$ solution (pH~7.2, Figure 3). The similarity suggests that CO_2 and CO_2 reduction intermediates ($*COO^-$ and *CO) have negligible effects on the surface population of $*CO_3^{2-}$, which is likely determined by its competitive binding with water. In addition, because of the large pH difference in these solutions, this similarity also suggests that the potential dependent $*CO_3^{2-}$ Raman intensity profile is not caused by potential dependent local pH change near the Cu electrode surface.

To investigate how *CO population on Cu changes with potential in the absence of $*CO_3^{2-}$, we measured the SHINER spectra of *CO on Cu in C2 electrolyte (CO-saturated 0.5 M $NaClO_4$, pH = 7.62). Perchlorate solution is chosen as a control since it is a weak binder to Cu among other anions[28,39]. The raw Raman spectra during the cathodic scan from +0.046 to -1.504V (Figures S24) show a peak of ClO_4^- ions (~ 946 cm^{-1}) and *CO (~ 2080 cm^{-1}). The ClO_4^- peak shows negligible potential dependent frequency and intensity (Figure S25 to S26), suggesting the signal is dominated by ClO_4^- ions in the bulk solution with negligible interaction with the electrode. The *CO peak frequency and intensity show a pronounced potential dependence. *CO peak appears at -0.3V, near the potential of Cu_2O reduction; increases its intensity at a more negative potential

to reach a maximum at ~ -0.7 V (**Figure 7.4**B); decreases in intensity at further cathodic scan due to the reduction of CO (see SI 2.10 Figure S19 and SI 2.12 Figure S25 for details).

To examine how *CO adsorption competes with $*CO_3^{2-}$, we carried out a Raman measurement in C3 electrolyte (CO saturated 0.5 M $NaHCO_3$ aqueous solution, pH=8.44**Figure 7.4**C plots the corresponding experimental Raman intensities and calculated populations for $*CO_3^{2-}$ and *CO. **Figure 7.4**C reveals a similar symmetric profile for adsorbed carbonate's intensity that shows a peak at around -0.83 V. This feature is the same as those in the absence of CO or CO_2 (**Figure 7.4**A) and under CO_2 reduction conditions (**Figure 7.3**A), which indicates that the characteristic potential-dependent surface coverage of carbonate is not altered by the presence of carbon-containing species (*CO, $*COO^-$, $*CO_2$). Moreover, *CO's intensity exhibits a bimodal curve with the local minimum coincides with the potential at which carbonate's intensity maximizes. This is clear evidence of competitive adsorption between $*CO_3^{2-}$ and *CO. During the cathodic scan, *CO's intensity shows the first maximum at -0.35 V, suggesting that at low surface coverage (before -0.35V), both $*CO_3^{2-}$ and *CO coverage increases at a more negative potential, until $*CO_3^{2-}$ out-competes and displaces *CO at -0.35V - ~-0.8V. At more negative potential, $*CO_3^{2-}$ desorption occurs and *CO coverage increases until reaching the second peak coverage at -1.2V, after which *CO coverage decreases, likely due to the reduction of CO, similar to that observed in the absence of carbonate (**Figure 7.4**B) and under CO_2 reduction conditions (**Figure 7.3**A).

To understand the competitive binding of $*CO_3^{2-}$ with carbon-containing species observed above, we carried out Monte Carlo simulations. The details of the simulation are provided in SI 2.14, and only the key findings are summarized here. The potential dependent $*CO_3^{2-}$ surface coverage in the absence of carbon-containing species, as shown in **Figure 7.4**A can be modeled by the competitive binding of $*CO_3^{2-}$ and $*H_2O$. At potential more negative of the PZC, one expects that Coulombic repulsion between the anion and a more negatively charged electrode to drive $*CO_3^{2-}$ desorption. This effect is captured in our Monte Carlo model where at negative potentials, water gradually replaces $*CO_3^{2-}$ on the lattice (**Figure 7.4**A). The potential dependent $*CO_3^{2-}$ coverage at a potential more positive of PZC is more complicated. If only Coulombic interactions are considered, one expects that at more positive potentials, $*CO_3^{2-}$ will be increasingly attracted to the surface until it saturates the available binding sites and its intensity

plateaus. Since during a cathodic scan, the $*CO_3^{2-}$ Raman intensity turns on after Cu_2O reduction and increases gradually as the surface becomes less positively charged (towards PZC), it may indicate a slow potential-dependent surface rearrangement that weakens carbonate binding at positive potentials. This hypothesis is supported by a rapid intensity decrease of carbonate at -0.15 V, the potential of Cu oxidation, in an anodic scan (Figure S28), and the large hysteresis of $*CO_3^{2-}$ in the cathodic and anodic scan. In our Monte Carlo model, we represent this effect on $*CO_3^{2-}$ by giving the adsorbate a V-shaped binding energy (Figure S29), where it is most stable at the experimental maximum Raman intensity. This V-shaped binding energy in our Monte Carlo model becomes essential to replicating the results of the next section.

In the presence of CO, as shown in **Figure 7.4**C, the Monte Carlo model includes the competitive binding of $*CO_3^{2-}$, *CO, and $*H_2O$. The simulation shows that *CO coverage minimizes at the potential with maximal $*CO_3^{2-}$ coverage, and recovers its population on either side of the $*CO_3^{2-}$ peak (**Figure 7.4**C). Our modeling results are qualitatively a good match with experimental results, and the assumption that carbonate dominates adsorption competition over other CO-related species at potentials around -0.7 V. Unlike the experiment, however, our model does not include Cu oxidation/reduction events. Consequently, the simulated *CO population does not decrease from -0.3 to -0.5 V like it does in experiments. Most importantly, the *CO intensity in this system displays a bimodal profile, which is quite alike the summation profile of $*COO^-$ and *CO under CO_2 reduction (-0.9 V, **Figure 7.3**A), This suggests that strongly adsorbed carbonate outcompetes other carbon-containing adsorbates.

These three control cases provide the following key conclusions. Firstly, the potential dependent intensity change of carbonate on Cu is mainly due to the surface binding rather than a result of surface pH change. Secondly, carbonate exhibits preferential binding from -0.2 V to -0.8 V on Cu and it can outcompete $*COO^-$ or *CO at the potential region. Thirdly, removing carbonate from the solution allows *CO adsorption at the carbonate dominant adsorption region (from -0.2 V to -0.8 V). Fourthly, some phenomenon other than another competitive binder is selectively decreasing species adsorption from 0.2 V to -0.7 V. This phenomenon might be a slow surface rearrangement as Cu_2O reduces to Cu in the cathodic scan that somehow prevents carbonate's coordination to the surface.

7.2.5. A new competitive binding model for CO_2 reduction on Cu

Our results show that $*CO_3^{2-}$ out-competes $*COO^-$ and *CO over the potential range of -0.3 to -1.0V (vs Ag/AgCl). A similar competitive binding of $*CO_3^{2-}$ and *CO has been observed previously in CO-saturated bicarbonate solution in the range of -0.56V to 1.05 V vs. SHE (-0.783 to 0.827 V vs. Ag/AgCl)[29]. Thus, we propose that $*CO_3^{2-}$ competes with many carbon-containing intermediates on the Cu surface, including $*CO_2$, $*COO^-$, *COOH, *CO, and this competitive binding delays the onset of CO_2 reduction by blocking the surface reaction sites. CO_2 reduction can only occur when $*CO_3^{2-}$ desorbs from the surface at negative potential. The conventional CO_2 reduction pathway shown in Scheme 1 does not fully capture the reaction mechanism. We propose a revised reaction mechanism in Scheme 2, in which the competitive binding step is explicitly considered. Scheme 2 depicts three key species involved in three representative potentials for a CO_2 reduction process on Cu electrodes in a CO2-saturated 0.5 M $NaHCO_3$ electrolyte. At -0.15 V, where most Cu_2O is reduced to Cu, CO_2 and CO_3^{2-} co-adsorb on the surface to form $*COO^-$ and $*CO_3^{2-}$; at -0.7 V, $*CO_3^{2-}$ outcompetes $*COO^-$ in binding and dominates the surface, decreasing the available surface sites for CO_2 activation; at -1.2 V, the surface coverage of $*CO_3^{2-}$ decreases, which open up surface sites for CO_2 to CO conversion (with *CO on the surface as a product).

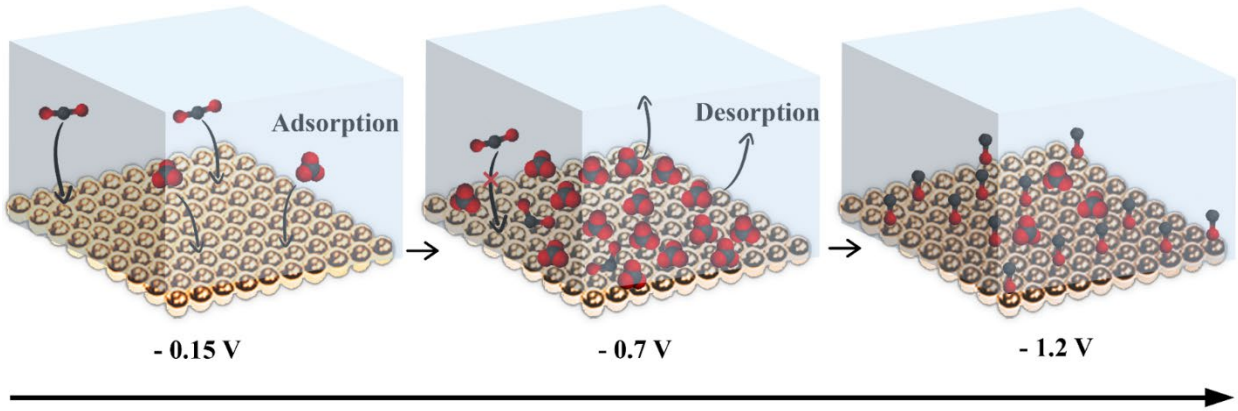

Scheme 2. Competitive binding model for CO_2 reduction. Schematic representation of potential-dependent surface species surface during CO_2 activation at featured potentials along a cathodic scan in the low overpotentials region for a Cu(pc) electrode in a CO_2 saturated 0.5 M $NaHCO_3$ electrolyte. Only major species are shown: CO_2, CO_3^{2-}, CO. Color code for atoms: Cu

atoms (metallic brown color balls), C atoms (black), O atoms (red), aqueous electrolyte (the blue cube on top of the surface).

To support this model, we have provided strong evidence to show that at low overpotential regions on Cu polycrystal surfaces, the adsorbed carbonate anions play a role in hindering the adsorption of other species and intermediates. This effect is partially based on carbonate's electrostatic interaction with the charged Cu surface under different PZC of the surfaces, and it largely affects and out-competes the binding of $*COO^-$ and *CO species until really negative potential where it starts to fall off from the surfaces.

Thus, we believe at least three key factors are essential to the onset of *CO generation from CO_2 reduction. First, a relatively Cu-rich surface (from Cu_2O reduction) to enable the stable adsorption of carbon-containing species; second, a favorable local environment with enough proton sources and sufficient electrochemical potential to enable CO_2 reduction (CO pathway); third, enough available surface sites without adsorbate "poisoning", such as carbonate in our case. It is also reasonable to infer that the diminished carbonate binding in a more acidic medium may be one of the reasons to explain the different CO_2 reduction selectivity in acidic electrolytes[43,48]. Especially on Cu, lowering pH not only affects the possible pathways and energy parameters[49] but also depletes the surface adsorbed carbonate. Therefore, the selection of less-surface-binding electrolytes can also be a parameter in improving CO_2 reduction reactions. Another note is that the electrolyte binding preferences vary for different metals. For example, on Au electrodes, no competitive binding between $*CO_3^{2-}$ and *CO is observed[29], and when pH is tuned from 7.4 to 5.7 with the same ionic strength, the onset potential for the detection of bulk CO production also does not change[50].

7.3. Conclusions

In summary, we conducted a spectroscopic experimental and theoretical study to analyze the competitive binding of carbonate anions on a polycrystalline copper surface during the early steps of CO_2 activation and reduction at low overpotentials. Our results can be summarized in two parts. Firstly, we used *in situ* Raman spectroscopy and bias-dependent DFT computation to identify surface-adsorbed species on Cu generated by CO_2 reduction, including $*CO_3^{2-}$, $*COO^-M^+$, and hydroxyls.

Specifically, to verify the previous controversial assignments on Raman peaks at 1540 cm^{-1} and 360 cm^{-1} to be $*CO_3^{2-}$, carboxylate$*COO^-$, or malachite, evidence was provided to support the assignment of the $*COO^-(Na^+)$ species, while H/D isotope studies were used to distinguish adsorbed hydroxyls from overlapped peaks in H_2O. Secondly, to explain the gap between the disappearance of the $*COO^-$ peak and the onset of the *CO peak during the potential scan, we introduced a hypothesis with a carbonate anion competitive binding model. Supplemental measurements and MC calculations were conducted to test the hypothesis and the results confirm that carbonate anions remain strongly adsorbed from the potential of Cu_2O/Cu conversion to the CO onset potential, leading to the suppressed adsorption of $*COO^-$ and *CO. Furthermore, carbonate concentration dependence control measurements show that CO production and the adsorption of *CO can be delayed due to the high coverage of carbonate. This suggests that high coverage of carbonate anions on Cu(pc) at low overpotentials inhibits the electrocatalytic CO_2RR by preventing the adsorption of key intermediates, $*COO^-$ and *CO. Lowering the concentration of carbonate can improve the delayed onset of *CO from the binding competition but at the cost of lowering pH. Additionally, our results suggest that the step-wise observed “halfway” intermediates at low overpotentials may not be the actual short-time scale intermediates at high overpotentials due to the different local surface environments. Therefore, step-wise potential dependent measurements may not be the most suitable ones to provide accurate information on time scale intermediates at different catalytic conditions.

Our findings elucidate the negative influence of carbonate anions on CO_2 reduction, even though it is seldom discussed due to its limited presence at low overpotentials. This furthers our understanding of anions' contributions to modulating reaction pathways and can inform future

efforts to optimize electrolyte solution concentration, anion choice, and pH conditions to achieve efficient CO_2 reduction.

7.4. Supporting Information

7.4.1. Extended description of experimental methods

Preparation of nanoparticles

Au and Au@SiO_2 nanoparticles were prepared based on the methods developed by Li, et al[54]. The obtained shell-isolated nanoparticles were characterized by TEM and electrochemical methods to verify the SiO_2 shell fully covered the Au core.

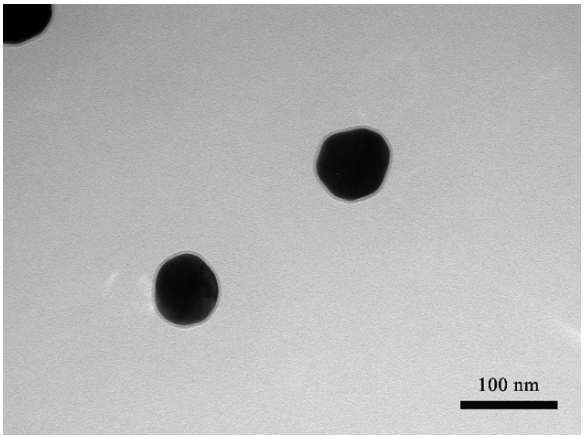

Figure S1. TEM image of synthesized Au@SiO_2 nanoparticles.
(With diameter ~55 nm, thickness of Si_2O shell ~ 2-3 nm)

Preparation of Cu working electrodes

The polycrystalline Cu disk electrodes (OD 6 mm, ALS, Co., Ltd) were firstly polished with 0.05 μm Al_2O_3 with polishing pads, then rinsed with ultrapure water and electrochemically cleaned in 85% H_3PO_4 at 1.5 V vs. Ag/AgCl (1 M KCl) for 30 seconds until showing mirror-like surfaces.

7.4.2. Extended results analysis and discussion

7.4.2.1 Discussion on the background subtraction of Raman spectra

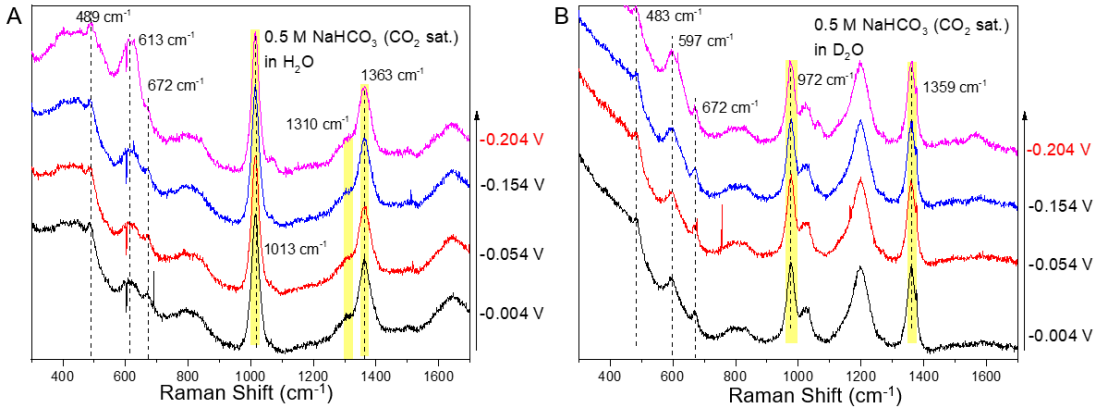

Figure S2. Background Raman spectra selection.
(A) Raw (un-subtracted) potential dependent SHINERS spectra in H_2O. (B) Raw (un-subtracted) potential dependent SHINERS spectra in D_2O. The Raman peak of bicarbonates is highlighted in yellow.

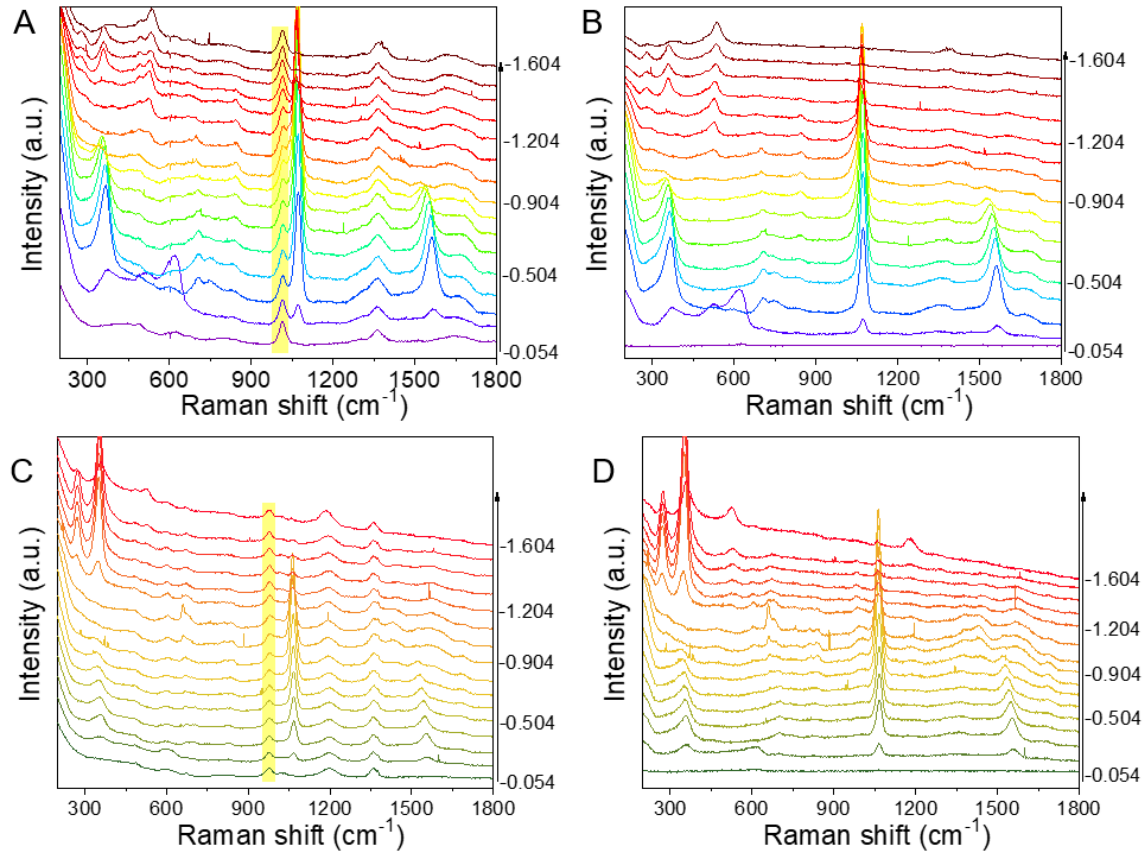

Figure S3. Spectra before and after Background subtraction.
Comparison of (A) unsubtracted and (B) subtracted Raman spectra in H_2O; and (C) unsubtracted and (D) subtracted Raman spectra in D_2O. Raman peaks of bicarbonates are heightened in yellow in A and C.

To facilitate the analysis of potential-dependent spectral features, a background subtraction was conducted. As shown in **Figure S3**, at potentials more positive of -0.204V, the Rama spectra show negligible potential dependence, and as shown in Figure S4, at potentials more negative of -0.204 V, significant potential-dependent features appear. Therefore, the spectrum at -0.004 V is taken as a reference and the raw (un-subtracted) spectra are subtracted by this reference spectrum to remove potential independent spectral components. For example, the main peaks of bicarbonate, ~1020 cm^{-1}, ~1370 cm^{-1} in H_2O and ~980 cm^{-1}, ~1360 cm^{-1} in D_2O, highlighted as yellow color in **Figure S2** and **Figure S3**(A and C), can be nearly completely removed in the subtracted (difference) spectra. This indicates that in our system of 0.5 M $NaHCO_3$ solution, most observed bicarbonate Raman peaks are caused by species in the bulk solution, and there is negligible signal due to adsorbed bicarbonate. The assignment of these peaks agrees well with bicarbonate peaks in bulk solution (**Figure S4**).

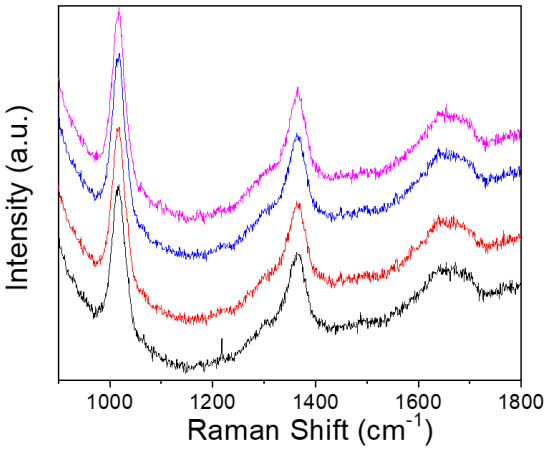

Figure S4. Raman spectra of solution (bulk) phase in 0.5 M $NaHCO_3$ (CO_2 sat.) water solution. Different spectra of different colors represent the different sample spots.

7.4.2.2 Additional DFT calculated Raman spectra of key species

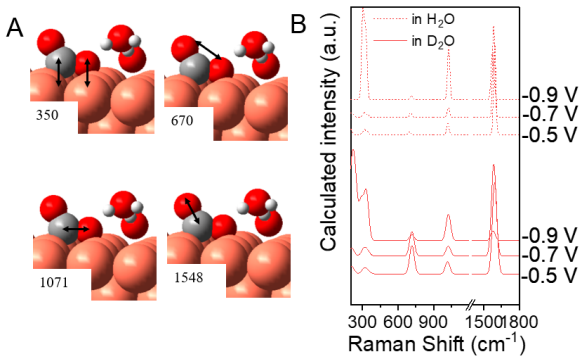

Figure S5. DFT calculation of *COO^- with explicit water. (A) DFT calculated the structure of *COO^- with explicit water. (B) corresponding calculated Raman spectra of *COO^- in H_2O/D_2O.

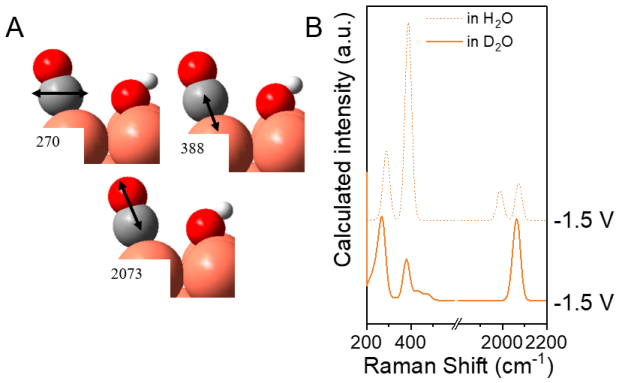

Figure S6. DFT calculation of *CO with nearby *OH.
(A) DFT calculated structure of *CO with nearby *OH. (B) corresponding calculated Raman spectra of *CO in H_2O/D_2O.

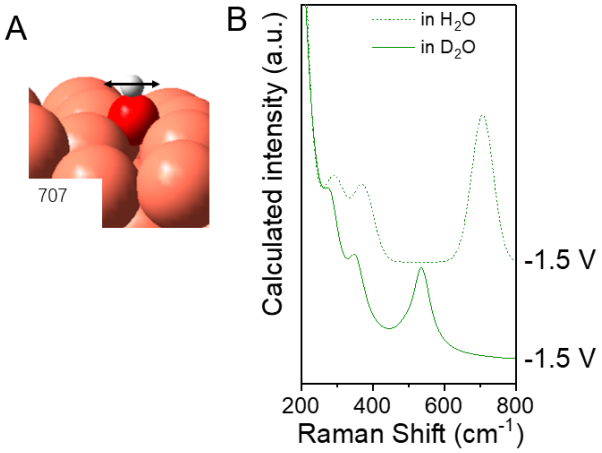

Figure S7. DFT calculation of *OH.
(A) DFT calculated structure of *OH. (B) corresponding calculated Raman spectra of *OH(*OD) in H_2O/D_2O.

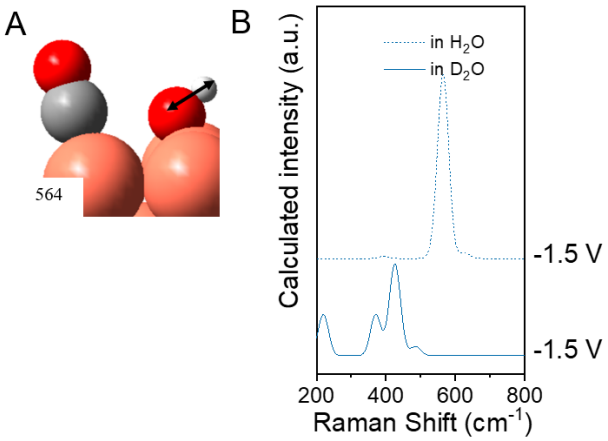

Figure S8. DFT calculation of *OH with nearby *CO.
(A) DFT calculated structure of *OH with nearby *CO. (B) corresponding calculated Raman spectra of *OH(*OD) in H_2O/D_2O.

7.4.2.3 Summary of the Raman peaks assignment

Table S1. Summary of measured and computed Raman peaks of key species on Cu(pc)

Species	Vibrational modes	Solvents	Measured Frequency (cm^{-1})	Computed Frequency (cm^{-1})	Measured frequency shift (cm^{-1}/V)
$*CO_3^{2-}$	ν (a1')[34,36]	H_2O	~ 1076 (-0.4 V)	1022 (-0.9 V)	8.0 ± 0.4 (-0.4 to -1.2 V)
		D_2O	~ 1071 (-0.4 V)	1022 (-0.9 V)	8.6 ± 0.3 (-0.4 to -1.2 V)
$*COO^- Na^+$	ν (Cu-C)	H_2O	~ 360 (-0.4 V)	315 (-0.5 V)	34.8 ± 2.1 (-0.2 to -0.8 V)
		D_2O	~ 350 (-0.4 V)	322 (-0.5 V)	29.7 ± 1.0 (-0.2 to -0.8 V)
$*COO^- Na^+$	ν_a (C=O)	H_2O	~ 1555 (-0.4 V)	1592 (-0.5 V)	62.6 ± 2.1 (-0.2 to -0.8 V)
		D_2O	~ 1548 (-0.4 V)	1592 (-0.5 V)	64.3 ± 1.4 (-0.2 to -0.8 V)
Cu-OH (non-hydrogen bonded)	δ (Cu-O-H)	H_2O	~ 700 (-0.5 V)	707 (-0.5 V)	Unobtained due to overlapping
		D_2O	~ 670 (-0.5 V)	536 (-0.5 V)	19.7 ± 2.1 (-0.5 to -1.15 V)
Cu-OH in $CuO_x(OH)_y$	ν (Cu-O)	H_2O	~ 527 (-1.1 V)	565 (-0.5 V)	-26.1 ± 0.8 (-1.0 to -1.5 V)
		D_2O	~ 523 (-1.1 V)	485 (-0.5 V)	-7.5 ± 1.6 (-1.0 to -1.5 V)
*CO	ν (Cu-C)	H_2O	~272 (-1.25 V)	289 (-1.5 V)	-8.6 ± 2.8 (-1.25 to -1.6 V)
		D_2O	~280 (-1.25 V)	268 (-1.5 V)	-3.8 ± 0.4 (-1.25 to -1.6 V)
*CO	ρ (Cu-C-O)	H_2O	~358 (-1.25 V)	389 (-1.5 V)	-12.0 ± 4.0 (-1.25 to -1.6 V)
		D_2O	~350 (-1.25 V)	380 (-1.5 V)	-11.3 ± 0.2 (-1.25 to -1.6 V)
*CO	ν (C-O)	H_2O	~2020 to 2100	~2020 to 2100	Multiple modes (Seen in SI 2.4)
		D_2O	~2020 to 2100	~2020 to 2100	

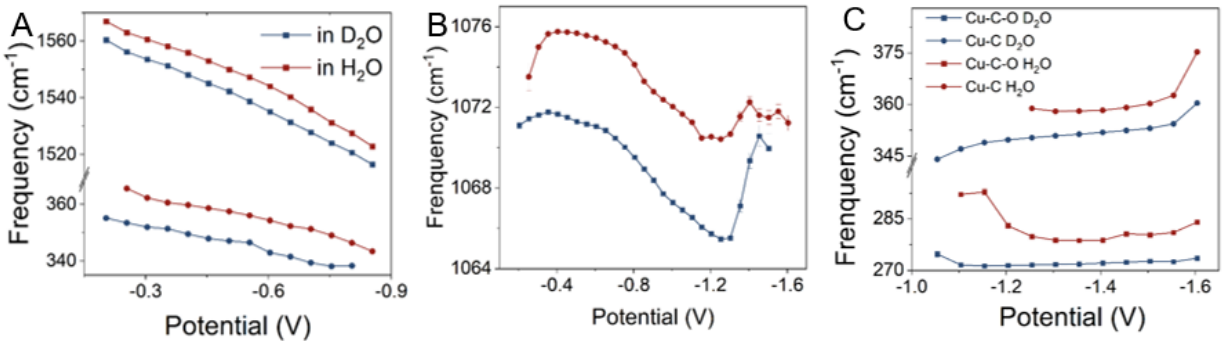

Figure S9. Potential dependent frequency shifts of carbon-containing species in H_2O and D_2O. (A)COO^-(1540 and 360 cm^{-1}), (B)carbonate (1071 cm^{-1}), (C)Cu-CO (280 and 370 cm^{-1}).

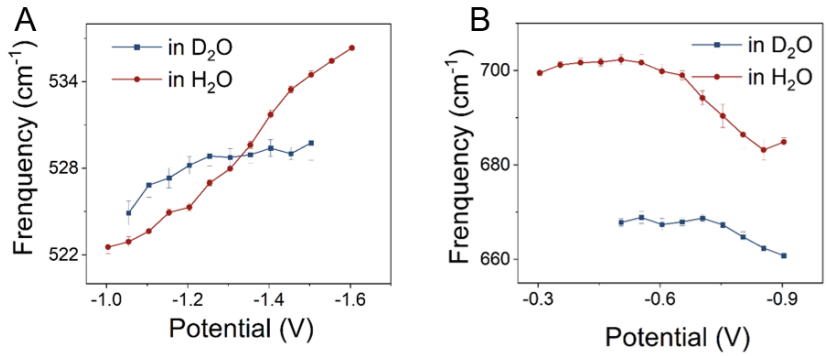

Figure S10. Potential dependent frequency shifts of OH-containing species in H_2O and D_2O. (A) hydrogen bonding Cu-OH(OD) bending (520 cm^{-1}) and (B) free Cu-OH(OD) (670 cm^{-1}).

The potential dependent frequency shifts of observed species indicate that they are surface adsorbed as they have to be close enough to the electrode surface to experience the electric field changes. **Table S1** also shows the H/D isotope effect of these species. The experimentally observed higher and lower frequency modes of COO^- both show 5-10 cm^{-1} frequency differences in H_2O and D_2O, which indicate this species interacts with proton or water molecules. Similar isotope effects are also observed for adsorbed carbonate and CO. Therefore, in our DFT models, to account for the adsorbate-water interaction, we include explicit water molecules into the system in addition to an implicit solvent. Zero, two, three, and seven glasses of water are included around COO^- in a test to determine how the additional water molecules impact spectra. For the higher and lower frequency peaks, small changes of <5 cm^{-1} can be seen with the inclusion of hydrogen bonding for any number of explicit water molecules.

$*CO_3^{2-}$ Peaks. We assign the Raman peak at ~1071 cm^{-1} in the potential range of -0.2 V to -1.3 V to the symmetric stretching mode of bidentate adsorbed $*CO_3^{2-}$(Figure 2B), based on its agreement with the reported Raman spectra of carbonate in the solution phase[35]. This peak shows a ~5 cm^{-1} frequency shift over the potential range, indicating that the absorbed carbonate can sense changes in the electric field of the double layer. Specifically, it shows a red shift from -0.2 to -1.2 V and a blue shift from -1.2 to -1.6 V (**Figure S9**B); this potential dependent frequency shift is also corroborated by our DFT calculations (Figure 2B). Furthermore, this peak also shows a ~5 cm^{-1} red shift from H_2O to D_2O (**Figure S9**B), suggesting that its frequency is affected by interactions with nearby water molecules. This effect has not been reproduced by the DFT calculation, which may be due to insufficient water molecules near the carbonate in the computation model. Our calculation indicates that $*CO_3^{2-}$ can be either bidentate or monodentate when adsorbed on Cu surfaces, consistent with a previous literature report.[33]

HCO_3^- Peaks. In the raw Raman spectra before subtraction, shown in **Figure S9**A and C, we observe an intense peak at ~980 cm^{-1} in D_2O and ~1018 cm^{-1} in H_2O, which can be attributed to the in-plane C-O stretching mode of uncoordinated bicarbonate in the bulk solution (**Figure S4**) [36]. This is consistent with the observation that this peak shows negligible dependence on the applied bias and has a negligible intensity in the subtracted spectra shown in Figure 2B. As shown in **Figure S4**, in the bulk solution phase, Raman spectra are dominated by bicarbonate (1018 cm^{-1}) with negligible carbonate contribution (1055 cm^{-1}), consistent with the expected concentration ratio ($[H_2CO_3]$ /$[HCO_3^-]$ /$[CO_3^{2-}]$≈2:8:0.01 at pH=7.2[41]). However, our raw Raman spectra at the interface (**Figure S3**) show a much lower HCO_3^-/ CO_3^{2-} intensity ratio compared to the bulk solution, and the subtracted Raman spectra show negligible HCO_3^- intensity. These results suggest that there is a preferential accumulation of CO_3^{2-} on the surface, consistent with literature reports[53,55,56].

$*COO^-$ Peaks. Our experimental and computational results suggest that the ~1540 cm^{-1} and the ~360 cm^{-1} peaks should be assigned to $*COO^-M^+$, a cation M^+ stabilized adsorbed $*COO^-$, rather than other literature assignments such as carbonate [24,26,27], malachite [31], or *COOH [57]. A detailed discussion of the reasons for supporting the $*COO^-M^+$ assignment and ruling out other possibilities can be found in SI 2.4.

CO Peaks. We assign the broad Raman peak at ~2080 cm^{-1} from -0.904 V to -1.604 V to the C-O stretching mode of *CO. This broad Raman band consists of three overlapping *CO species: ~2030 cm^{-1}, ~2060 cm^{-1} and ~2090 cm^{-1}. These species show different potential dependent frequency tuning rates (shown in SI 2.6.), indicating they are *CO adsorbates in different chemical environments[15,58]. In previous studies, vibrational peaks in the 2000 to 2100 cm^{-1} region are assigned to atop *CO, but multiple reasons have been suggested for the wide distribution of vibrational frequencies[15,58], including a distribution of the coordination number of the Cu sites[58] and the extent of interaction of surrounding *OH group[15]. In our analysis, we fit these CO modes and obtain the total intensity of all atop *CO bands. Our DFT calculations and experiments also identify lower frequency modes at 270 cm^{-1} and 350 cm^{-1} (Figure 2C). We assign these to the Cu-C-O bending (Cu-CO restricted rotation) and the Cu-C stretching modes of Cu-CO respectively, consistent with previous literature reports[15,16,58].

Cu_2O and Cu-OH/OH^- Peaks. The ~623 cm^{-1} peak (brown) appears between -0.054 V and -0.204 V (Figure 1B) and shows negligible frequency change in H_2O. This peak is assigned to Cu_2O and its disappearance at more negative potential has been attributed to the reduction of Cu_2O to Cu[37,38]. Immediately following the decline of the ~623 cm^{-1} peak intensity, a rise of $*COO^-$ and $*CO_3^{2-}$ peaks are observed (Figure 3). This suggests that the reduction of the electrode surface from Cu_2O to Cu initiates CO_2RR and the adsorption of carbon-containing species.

In addition, the ~660 cm^{-1} peak (green shaded peak in Figure 1B and 2D) is assigned with the bending mode of Cu-O-H(D) that is minimally engaged in hydrogen bonding, and the ~523 cm^{-1} peak (blue shaded peak in Figure 1B and 2D) is assigned with the OH stretching mode of $CuO_x(OH)_y$. The ~660 cm^{-1} peak shows a relatively consistent isotopic H/D effect, while the ~523 cm^{-1} peak position and its H/D shifts can be greatly affected by the environment (e.g. the population of adsorbed CO); therefore, we believe the 523 cm^{-1} peak should be a special mode that possibly hydrogen bonds with surface *CO such that its spectral feature has the property of adsorbing *O with diminished H/D isotopic shifts. Further reasoning and discussion for the assignments can be found in SI 2.5.

7.4.2.4 Additional discussion on *COO− peaks assignments

We assign the Raman peaks at ~1540 cm^{-1} and ~360 cm^{-1} to $*COO^{-}M^{+}$, agreeing with a recent SERS study by Chernyshova et al.[18]

The ~1540 cm^{-1} peak, which we argue based on frequency matching to DFT calculation is from an asymmetric C=O stretching mode of $*COO^{-}$. The ~360 cm^{-1} peak, in accordance, should be assigned with the Cu-C stretching mode. The cation M^{+} is to stabilize the total structure on the surface. This Raman peak presents itself over a broad potential region (-0.204 to -0.854 V), and since it manifests before the appearance of *CO, it is largely believed to be a possible precursor and the rate-limiting step in the CO_2RR mechanism to make *CO.

We also assign the ~360 cm^{-1} Raman peak to the Cu-C stretching mode of $*COO^{-}M^{+}$ with DFT calculations as evidence. In the experiment, this Raman peak exists within the same potential region as the ~1540 cm^{-1} peak, and both the ~1540 cm^{-1} and the ~360 cm^{-1} peaks exhibit a similar change in intensity as a function of potential as well as a similar shift in frequency direction due to Stark effect and possible coverage dependence effects[59] (Figure 2-A). In detail, in CO_2-saturated 0.5 M $NaDCO_3$, the ~1540 cm^{-1} and the ~360 cm^{-1} peaks both grow in intensity from -0.15 and -0.5 V and maximize around -0.5 V. In addition, their potential dependent frequency tuning rates are 64.3 ± 1.4 and 29.7 ± 1.0 cm^{-1}/V respectively (**Table S1**). These results suggest that the ~1540 cm^{-1} and the ~360 cm^{-1} peaks belong to the same adsorbed species.

Nevertheless, many studies present inconsistent assignments on the chemical identity attributed to the ~1540 cm^{-1} and ~360 cm^{-1} peaks, with the literature reports assigning them to carbonate [24,26,27], malachite [31], $*COO^{-}$ [18,60], and *COOH [57]. The challenge is because the peak's frequency range of 1500-1600 cm^{-1} can belong to the C=O bond stretch in many different species, and the corresponding Cu-C or Cu-O mode is also at 300-400 cm^{-1} region.

Ruling out carbonate or bicarbonate.

We exclude the possibility of assigning the ~1540 cm^{-1} peak carbonate or bicarbonate based on the following 3 reasons. Firstly, the ~1540 cm^{-1} peak cannot be solution phase species,

as it was not observed in our bulk spectra(**Figure S4**) or any previous studies on bulk carbonate/bicarbonate[36,61].Secondly, under CO_2 reduction conditions, its intensity potential dependency doesn't change accordingly with known carbonate/bicarbonate peaks. While it increases in intensity from -0.204 to -0.3 V, plateaus from -0.3 to -0.5 V, and then decreases in intensity until -0.854 V (Figure 2A), the profile of the ~1055 cm^{-1} peak belonging to $*CO_3^{2-}$ whose intensity increases at -0.6 V, and that of the ~1018 cm^{-1} peak belonging to HCO_3^- whose intensity shows no potential-dependence. Thirdly, in our pure carbonate solution binding control shown in **Figure S21**, Ar-saturated 0.25 M Na_2CO_3 solution (pH = 11.95), there is no 1540 cm^{-1} peak. This result replicates those of the Chernyshova et al. SERS study[18]. It should be noted that on other metals with different ion-affinity, such as Au[62] or Pt[56], the 1500-1600 cm^{-1} assignments can be different because many C=O containing species such as carbonate/bicarbonate do have similar stretching modes in the similar frequency region.

At the same time, We excluded the assignment of ~360 cm^{-1} Raman peak to be carbonate reported by other paper[27], this is mainly due to the inconsistency on the potential dependent intensity compared to ~1055 cm^{-1} peak (Figure 1 B and Figure 2), i.e., from -0.85 V to -1.15 V where the ~1071 cm^{-1} peak shows a large intensity, the ~360 cm^{-1} peak disappears, thus it should not be assigned to carbonate species.

Ruling out *COOH.

Moreover, we disagree with assigning the ~1540 cm^{-1} peak to anti-symmetric stretching of *COOH. Shown in **Figure S11**B, our DFT calculations of *COOH give prominent vibrational modes at ~302, ~369, ~523, and ~1696 cm^{-1}. The calculation predicts that the peaks ~523 and ~800 cm^{-1} show similar intensities and Stark tuning rates as the observed peak at ~369 cm^{-1}; these peaks are not observed in **Figure S11**A. The calculated ~1696 cm^{-1} peak also shows a small frequency shift towards higher frequency in the cathodic scan, while the experimental ~1540 cm^{-1} peak shows a frequency shift in the opposite direction. Thus, we excluded the possibility of *COOH assignment.

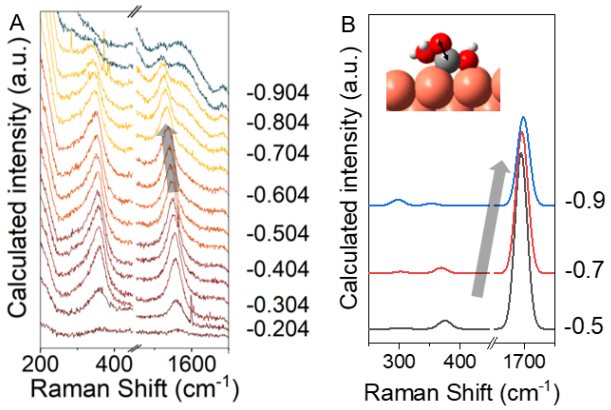

Figure S11. Ruling out the assignment of *COOH.
(A) Zoom-in potential dependent spectra at ~1540 cm^{-1} and ~340 cm^{-1} (left, red square coded) (B) calculated spectra of *COOH with simulated structure (right, red square coded). The different atoms are shown in different colors: C atom-grey, O atom-red, and H atom-white. From positive to negative potentials, the experimental results showed a red shift while DFT results showed a blue shift, indicating the mismatched assignment of *COOH.

Ruling out malachite.

The previous work by Jiang et al.[31] reported the assignment of ~ 1070 cm^{-1} and 1540 cm^{-1} to be the malachite, a type of Cu hydroxide carbonate species, not the adsorbed carbonate. Other previous work[51,52] has predicted and shown that malachite is an important precursor of Cu surface chemical conversion in altering CO_2 reduction activity. Especially for purposely prepared malachite according to the work[52], it shows clear different vibrational spectral features compared with Cu or Cu_2O and exhibits featured selectivity difference by product analysis method. In light of this information, the assignment of ~ 1070 cm^{-1} and 1540 cm^{-1} to be malachite is reasonable in some ways. i.e., the featured peaks in malachite Raman spectra are by the reported ~ 1070 cm^{-1} and 1540 cm^{-1} peaks, as well as ~360 cm^{-1} and ~700 cm^{-1} peaks. We appreciate the detailed work on the malachite tuning reaction activities, and we also believe the malachite formation may not be ruled out,

We disagree with the conclusion on the Raman peak assignments during CO_2RR on Cu based on the following reasons. In terms of assigning ~1540 cm^{-1} peak, we disagree with assigning the ~1540 cm^{-1} peak to the anti-symmetric stretching of carbonate in malachite based on these reasons: (1) under CO_2 reduction condition, the potential dependent relative intensity changes of "malachite-related" vibrational modes are not in sync, i.e. from -0.3 V to -0.8 V, ~1070 cm^{-1} peak stops increasing while ~1540 cm^{-1} and ~360 cm^{-1} continues to grow; (2) the

missing ~1540 cm^{-1} peak in malachite-enriched sample control under CO_2 reduction condition[31], even though the purposely malachite-enriched sample shows same spectra features of malachite, but the potential dependent spectra showed no peaks at ~1540 cm^{-1}; (3) the missing ~1540 cm^{-1} peak in 0.25 M Ar saturated Na_2CO_3 carbonate control (**Figure S21**) or their carbonate reported control[31].

In terms of assigning ~360 cm^{-1} peak, we disagree with the possible assignment on O-Cu-O bending modes of carbonate-induced malachite[31] due to: (1) the different direction of ~360 cm^{-1} peak potential dependent frequency shift: while a noticeable red shift (from -0.2 V to -0.8 V) of around ~30 cm^{-1}/V is observed for the ~360 cm^{-1} Raman peak, the O-Cu-O bending mode of malachite bulk species should not see any frequency shifts; (2) in our H/D labeling experiment of CO_2-saturated 0.5 M $NaH(D)CO_3$, the ~360 cm^{-1} peak in H_2O exhibits an isotope shift to ~350 cm^{-1} in D_2O, indicating stronger interaction of surface species and explicit solvents. This 10 cm^{-1} isotope shift disagrees with a previous report that suggests that the bulk malachite system does not have a significant H/D shift[31].

For the listed reasons, we tend to support the assignments of surface carbonate (~1070 cm^{-1}) and $*COO^-$ (~360 cm^{-1} ~1540 cm^{-1}) rather than malachite. There are some additional discussions on the mechanism of potential dependent intensity change for the related peaks, which will be provided in a later section SI 2.9.

7.4.2.5 Supplement discussion on Cu-OH-related species assignments

We assign the ~660 cm^{-1} peak (green) to be the bending mode of Cu-O-H(D) that is minimally engaged in hydrogen bonding, which is also consistent with the assignments by Bodappa et al.[37] In our experiments, we find the ~660 cm^{-1} peak in D_2O shifts to around 700 cm^{-1} in H_2O. However, in H_2O, the precise peak analysis is difficult as this ~700 cm^{-1} peak may overlap with other modes associated with carbonate or $*COO^-$ [18,30]. Our DFT calculations find that Cu-O-H bending mode with hydrogen bonding (with H_2O or CO) exhibits a 678 or 568 cm^{-1} peak that shifts to ~707 cm^{-1} for that without hydrogen bonding. Thus, we tend to assign it with the Cu-O-H(D) bending mode of minimal hydrogen-bonding engaged Cu-OH(D).

We assign the ~523 cm^{-1} (blue) peak to be the bending mode of a Cu-O-H in an OH against an O-containing species, $CuO_x(OH)_y$, due to its smaller isotope shift and more negative onset potential when more CO is added to the system.

In the Ar-saturated 0.01 M KOH/KOD solution (**Figure S12**), the blue peak and green peak have similar onset potentials. In addition, the blue peak exhibits a H/D isotopic shift as large as 30 cm^{-1} (~520 cm^{-1} with H, ~490 cm^{-1} with D), which is consistent with the previous report of Cu-OH species in the Cu electrooxidation system. In calculations, this H/D shift is exaggerated, likely due to a lack of explicit solvent. In comparison, in CO_2-saturated 0.5 M $NaHCO_3$ solution, the blue peak appears at a more negative potential than the green peak (-1.154 V vs. -0.704 V for the green peak), and it shows a significantly smaller 6-7 cm^{-1} isotopic shift (~527 cm^{-1} with H, ~523 cm^{-1} with D, **Figure S13**). In comparison, in CO_2-saturated 0.5 M $NaHCO_3$ solution, the blue peak appears at a more negative potential than the green peak (-1.154 V vs. -0.704 V for the green peak), and it shows a significantly smaller 6-7 cm^{-1} isotopic shift (~527 cm^{-1} with H, ~523 cm^{-1} with D, **Figure S13**). When even more CO is in the system, in CO-saturated 0.01 M KOH solution, the blue peak has an even smaller isotopic shift of 2-3 cm^{-1} (~532 cm^{-1} with H, ~530 cm^{-1} with D, **Figure S14**).

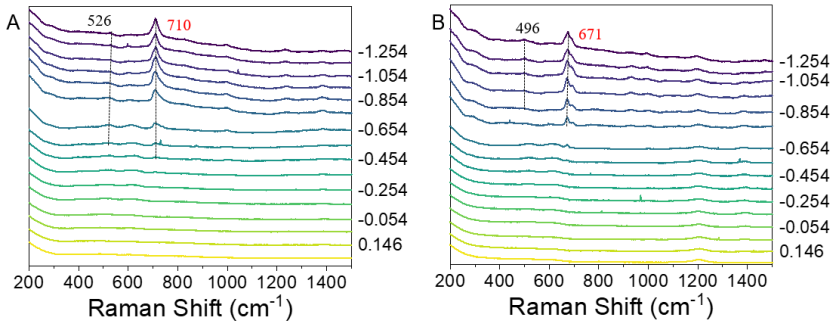

Figure S12. H/D Raman spectra of OH without CO.
(A) Raman spectra in Ar saturated 0.01 M KOH. (B) Raman spectra in Ar saturated 0.01 M KOD, O-H stretching mode is labeled by the black, Cu-O-H bending mode is labeled by the red color. O-H stretching presents 526 cm^{-1} in H_2O, 496 cm^{-1} in D_2O at -1.254 V, Cu-O-H bending presents 710 cm^{-1} in H_2O, 671 cm^{-1} in D_2O at -1.254 V.

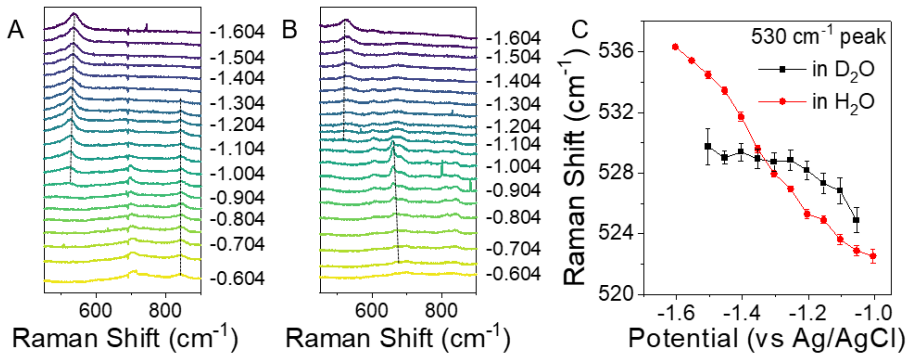

Figure S13. H/D Raman spectra of OH with a medium level of CO.
(A) in CO_2 saturated 0.5 M $NaHCO_3$. (B) in CO_2 saturated 0.5 M $NaDCO_3$. (C) Comparison of the potential dependent frequencies of the O-H stretching mode in H/D solutions.

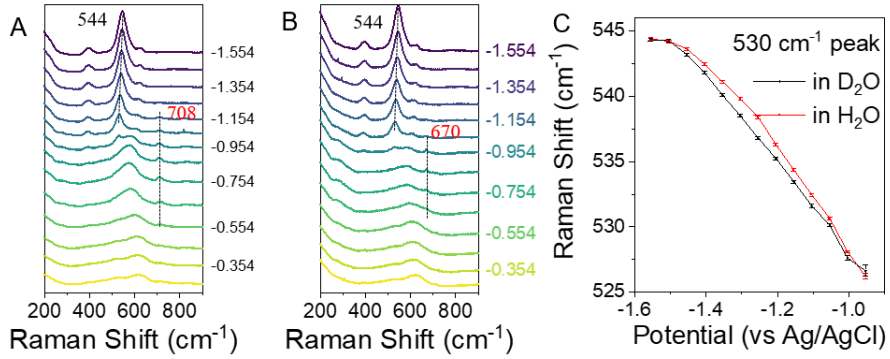

Figure S14. H/D Raman spectra of OH with a high level of CO.
(A) in CO saturated 0.01 M KOH. (B) in CO saturated 0.01 M KOD. (C) Comparison of the potential dependent frequencies of the O-H stretching mode in H/D solutions.

Given the correlation between the green and blue peaks in the CO-purged system, we believe the blue peak in this environment behaves more like a Cu-OH group engaged in hydrogen bonding. When more CO is added to the system, the blue peak behaves more like a Cu-O group, due to its smaller isotope effect. One explanation for this is that the introduction of *CO results in more *CO—*OH hydrogen bonding/interation[15,63], and disrupts the hydrogen-bonding network among *OH and explicit waters or other *OH near the electrochemical interface such that there is less hydrogen coordination to affect Cu-O stretching from Cu-OH. Another explanation is that *CO reduction involves the deprotonation of Cu-OH to form another product, such as $Cu\text{-}O_{ad}$ species reported on the Cu(111) surface[37]. Hence, we argue that this blue peak belongs more to a $CuO_x(OH)_y$ species.

This assignment aligns with those found in other studies[10,13]. In the scope of our CO_2RR experiments, the appearance of the green peak between -0.504 V and -1.154 V and then the subsequent appearance of the blue peak between -1.104 V and -1.604 V suggests that the

electrode surface is changing from Cu_2O to Cu-OH to $CuO_x(OH)_y$. Moreover, given how the rise of the blue peak coincides with *CO onset and $*CO_3^{2-}$ desorption, these changes in the surface are correlated with CO_2 reduction processes.

7.4.2.6 Supplement electrochemical Raman spectra on *CO

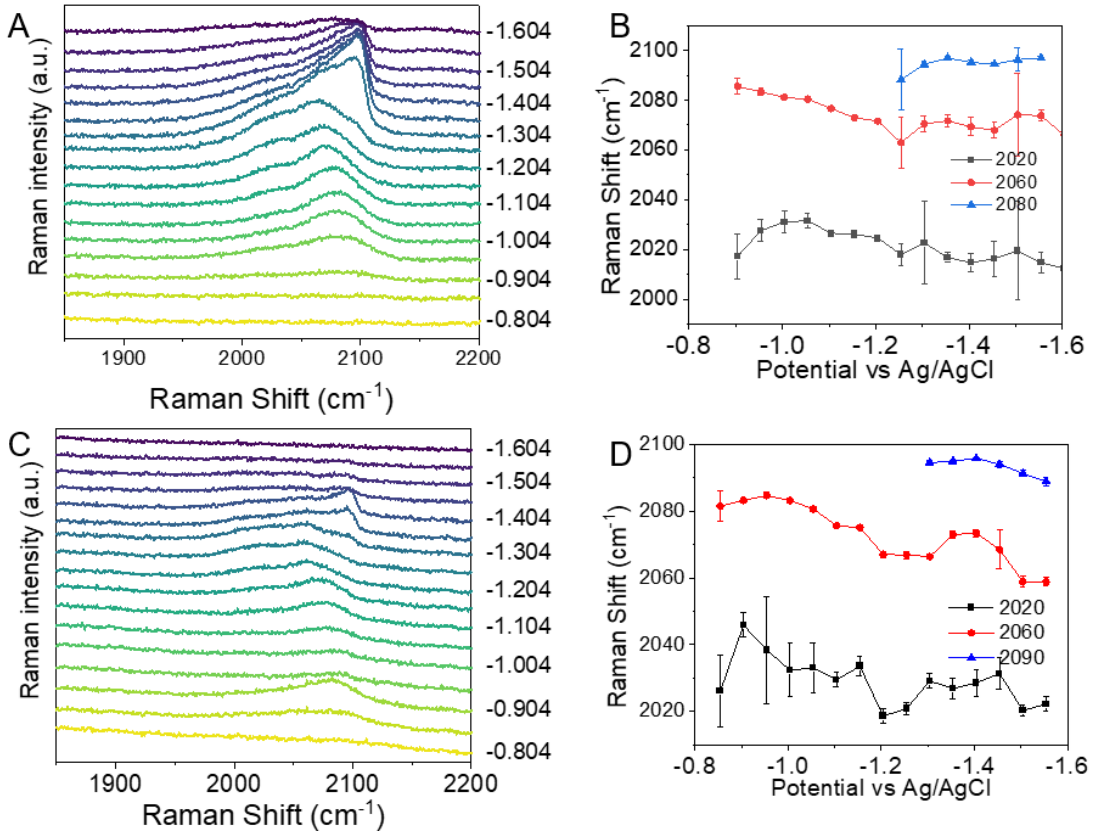

Figure S15. Raman spectra of CO_2 reduced *CO on Cu.
(A) potential dependent Raman spectra in 0.5 M $NaDCO_3$ D_2O (CO_2 saturated). (B) Fitted Raman peaks of 3 modes at different frequencies of *CO in 0.5 M $NaDCO_3$ D_2O (CO_2 saturated). (C) potential dependent Raman spectra in 0.5 M $NaHCO_3$ H_2O (CO_2 saturated). (D) The tuning rates of the three modes are difficult to identify as the peak width and frequency both show potential dependency.

7.4.2.7 Additional plot of potential dependent intensity

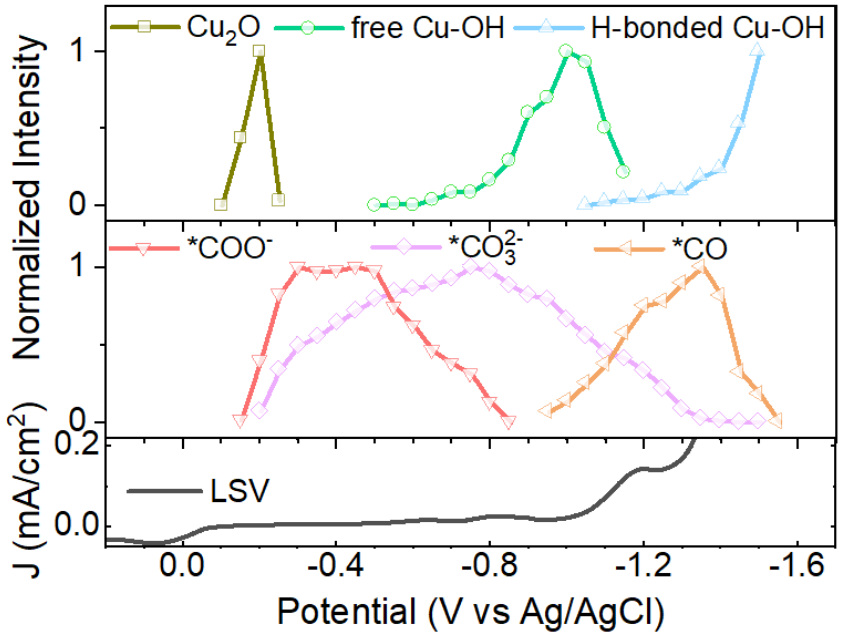

Figure S16. Potential-dependent Raman peak intensity of all Cu-O (top panel) and Cu-C (middle panel) containing species in D_2O.
Raman frequency of key species: 623 cm^{-1} (Cu_2O), 520 cm^{-1} (hydrogen bonding Cu-OH bending) and (B) 670 cm^{-1} (free Cu-OH), 1540 cm^{-1} ($*COO^-$), 1070 cm^{-1} ($*CO_3^{2-}$), ~2000 to 2100 cm^{-1} (*CO).

7.4.2.8 Additional results on $*CO_3^{2-}$ population dependence

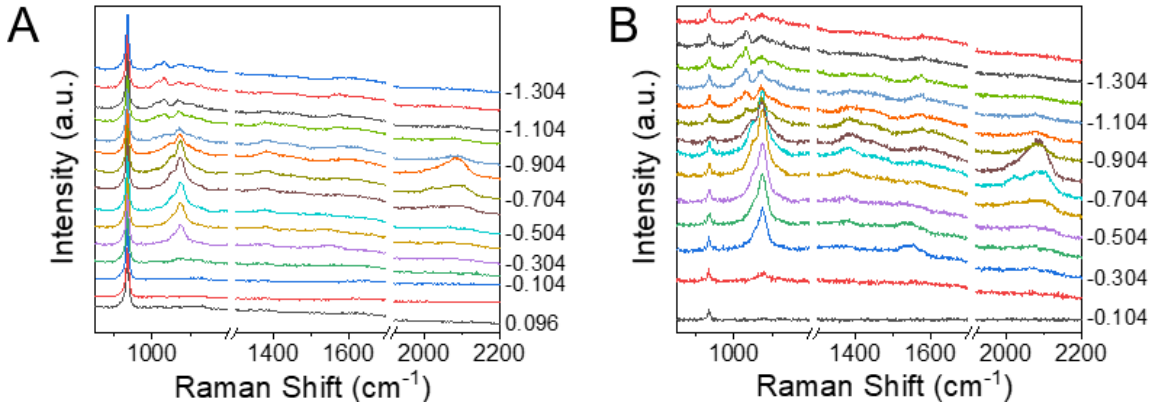

Figure S17. *CO onset potentials using electrolytes with different carbonate concentrations. Comparison of (A) unsubtracted and (B) subtracted Raman spectra (background at -0.004 V) of intermediate carbonate concentration in 0.1 M $NaClO_4$ + 0.4 M $NaHCO_3$ (CO_2 sat. pH=6.8) solution.

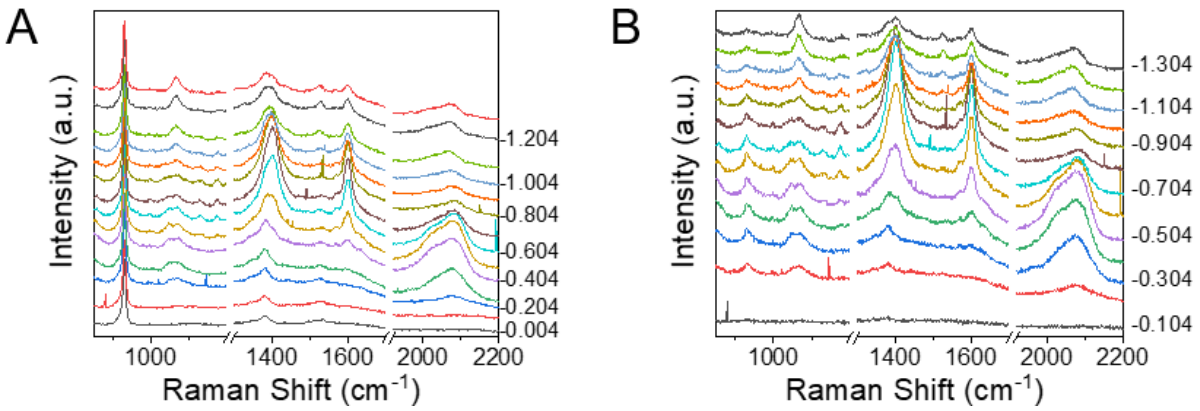

Figure S18. *CO onset potentials using electrolytes with different carbonate concentrations. Comparison of (A) unsubtracted and (B) subtracted **(**background at -0.004 V**)** Raman spectra of low carbonate concentration in 0.5 M $NaClO_4$ (CO_2 sat. pH=4.6) solution.

Notably, in **Figure S18**, the peaks at 1389 cm^{-1} and 1601 cm^{-1} should be related to the CO reduction products, such as HOCCOH at 1397 cm^{-1} and OCCOH at 1576 cm^{-1}, based on previous literature[7,8,64].

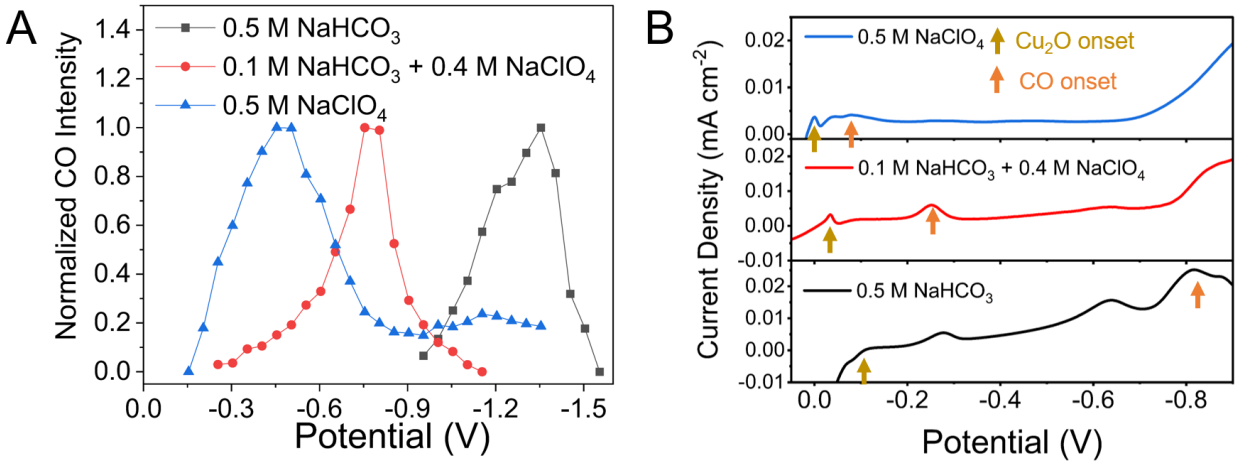

Figure S19. Comparison of CO onset under different amounts of carbonate. (A) Potential dependent *CO intensity in different solutions: 0.5 M $NaHCO_3$ (CO_2 sat. pH=7.2) in black; 0.1 M $NaClO_4$ + 0.4 M $NaHCO_3$ (CO_2 sat. pH=6.8) in red; 0.5 M $NaClO_4$ (CO_2 sat. pH=4.6) in blue. (B) Comparison of linear sweep voltammograms (scan rate 0.4 mV/s) of Cu (poly) in 0.5 M $NaHCO_3$ (CO_2 sat. pH=7.2) in black; 0.1 M $NaClO_4$ + 0.4 M $NaHCO_3$ (CO_2 sat. pH=6.8) in red; 0.5 M $NaClO_4$ (CO_2 sat. pH=4.6) in blue. The onset potentials of Cu2O reduction are marked as dark yellow arrows, and those of CO production are marked as orange arrows.

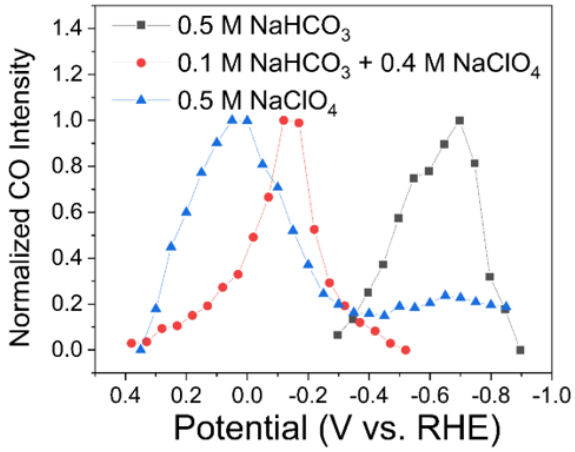

Figure S20. Comparison of normalized intensity of CO in different solutions under RHE scale. 0.5 M $NaHCO_3$ (CO_2 sat. Ph=7.2) in black; 0.1 M $NaClO_4$ + 0.4 M $NaHCO_3$ (CO_2 sat. Ph=6.8) in red; 0.5 M $NaClO_4$ (CO_2 sat. Ph=4.6) in blue.

7.4.2.9 Estimation of potentials of zero charge for systems

In our competitive binding model, we think that the strong preferential binding of carbonate on Cu is also controlled by the potential of zero charge (PZC) of the system, to verify this hypothesis, we conducted the potential dependent capacitance measurements of different systems, the PZC can be found at the minimum of the capacitance. The potential dependent differential capacitance was obtained by the potential dependent impedance measurements and followed by the previous report[65]. However, this method can only provide an estimation of the PZC due to the complexity of the system (involving multiple Faradaic reactions), the exact determination may require other methods[52].

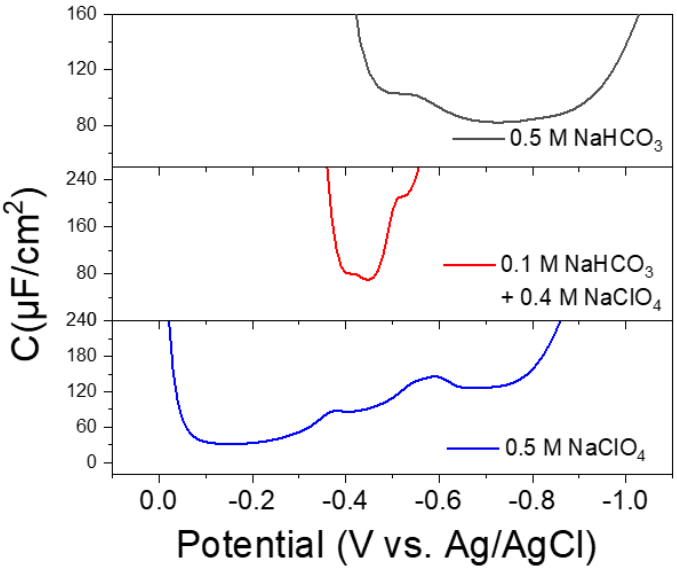

Figure S 21. The differential capacitance for Cu(pc) in different solutions.
Potential dependent capacitance at 25 Hz in different solutions: 0.5 M $NaHCO_3$ sat. with CO_2 (pH=7.2, black line); 0.1 M $NaHCO_3$ + 0.4 M $NaClO_4$ sat. with CO_2 (pH=6.7, red line); 0.5 M $NaClO_4$ sat. with CO_2 (pH=4.6, blue line).

By estimation, the PZC for Cu(pc) in 0.5 M $NaHCO_3$ sat. with CO_2 is roughly around -0.8 to -0.9 V vs. Ag/AgCl, in 0.1 M $NaHCO_3$ + 0.4 M $NaClO_4$ sat. with CO_2 is around -0.4 V, in 0.5 M $NaClO_4$ sat. with CO_2 is around -0.1 to -0.2 V. We observed a pH/carbonate population dependent PZC change, as the carbonate population or the pH becomes smaller, the PZC also decreases. In each case, the PZC values are also roughly in sync with the potentials for carbonate starting to decrease intensity, thus we believe this carbonate and *CO competitive binding should be directly related to the PZC change of the system. Moreover, the pH-dependent PZC change was also reported by previous work in alkaline solutions[52] (from -0.51 V vs. Ag/AgCl at pH=13 to -

0.25 V at pH=10 in $NaClO_4$ solutions). In our case, we observed how PZC changes from medium pH (pH=7.2) with more carbonate binding to relatively acidic condition (pH=4.6) and less carbonate binding, thus the variation among our reported values and others' should be mainly induced by different amounts of the adsorbates (*carbonate and reaction intermediates) binding.

7.4.2.10 DEMS Results Analysis

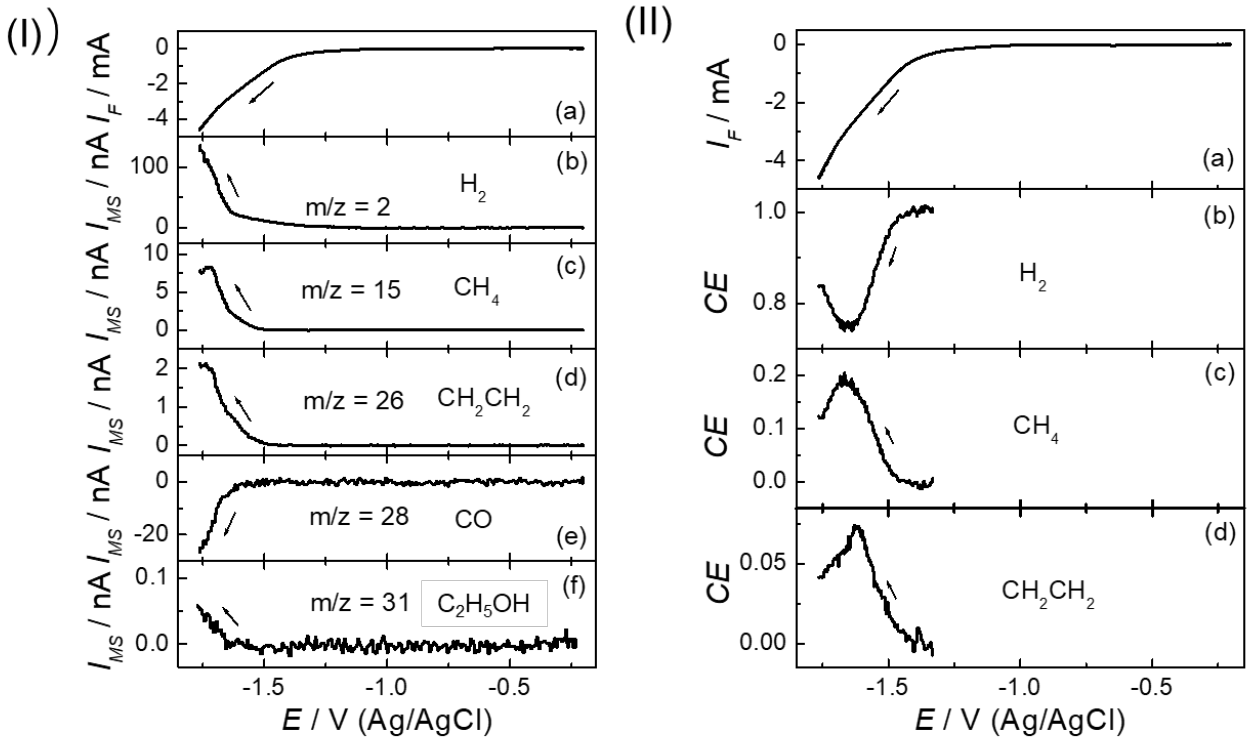

Figure S22. DEMS results analysis.

(I) Linear scan voltammetric (LSV) profile for CO_2 reduction on a bulk Cu electrode in CO_2 saturated 0.1 M $KHCO_3$ (a) and corresponding mass spectrometric currents at m/z = 2 (b), m/z = 15 (c), m/z = 26 (d), m/z = 28 (e) and m/z = 31(f). Scan rate: 50 mV/s. (II) LSV profile (a) and current efficiencies of H_2 (b), CH_4 (c), and CH_2CH_2 (d) plotted vs. potential.

The DEMS results (seen in **Figure S28**) showed that the CO_2 reduction on Cu generated large amounts of methane and ethylene, and also small amounts of ethanol as solution volatile products. Formate/formic acid was also formed during CO_2 reduction; however, it is not volatile enough to be detected. The amount of CO formed in the solution was too small to be detected with DEMS. It should be noted that the decrease of the mass spectrometric signal of CO at m/z =

28 at potentials below -1.6 V was due to the decrease in CO_2 concentration near the Cu surface (Figure S22-Ie) rather than the decrease in CO concentration, since CO_2 also had a fragment of CO^+. The formation of adsorbed CO (*CO) onset at around -0.20 to -0.25 V vs. RHE, as observed by SHINERS, while most product analysis measurements[66,67] found the onset of bulk CO at a more negative potential than -0.2 V vs. RHE. We think the inconsistency among the bulk and surface measurements may result from 1) the sensitivity in measuring bulk CO with DEMS in our measurement was not ideal; (2) when the lower overpotentials were applied, there was one adlayer of *CO resulting in an extra energy barrier for continuous CO formation; 3) there is only limited amount of CO at low overpotentials, with no efficient mass transport of *CO to the bulk phase; 4) before it reaches the more negative potential for CO desorption, *CO takes part into *CO reduction, so only sub-monolayer of *CO can be seen. We find some evidence for the fourth reason with peaks of possible CO reduction intermediates (1178 cm^{-1} OCCO, 1401 cm^{-1} OCCOH, and 1599 cm^{-1} HOCCOH [7,8]) observed in from -0.3 to -1.0 V vs. Ag/AgCl (**Figure S18**). It is also evidenced by the DEMS data that methane, ethylene, and ethanol were formed as soluble products. And to test other possibilities, a more sensitive fast-stirring spectroscopic study with a more sensitive product analysis method may be more helpful in answering this question.

7.4.2.11 Additional results on competitive binding control

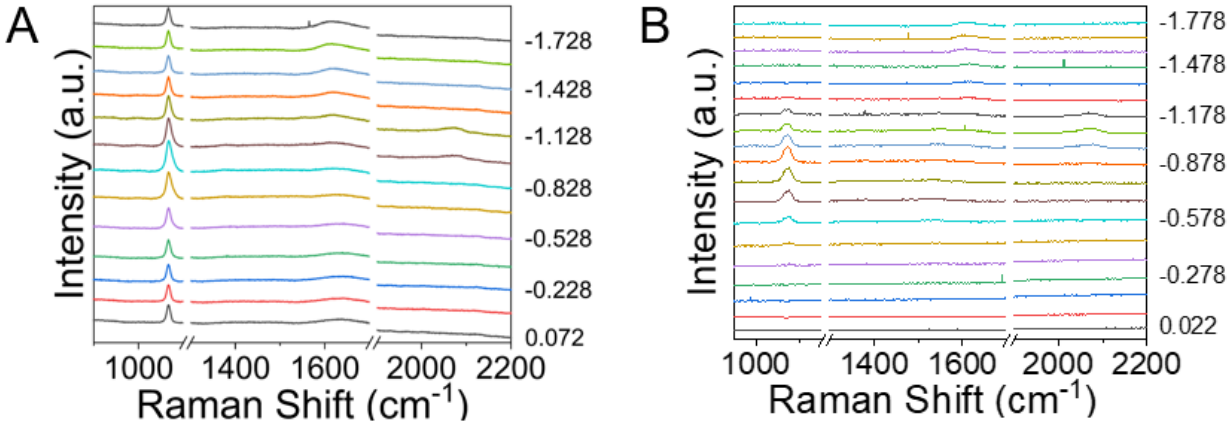

Figure S23. Raman spectra of potential dependent coverage of $*CO_3^{2-}$ in the absence of *CO. (A) unsubtracted and (B) subtracted Raman spectra Raman spectra in 0.25 M Na_2CO_3 sat. with Ar (pH=11.95).

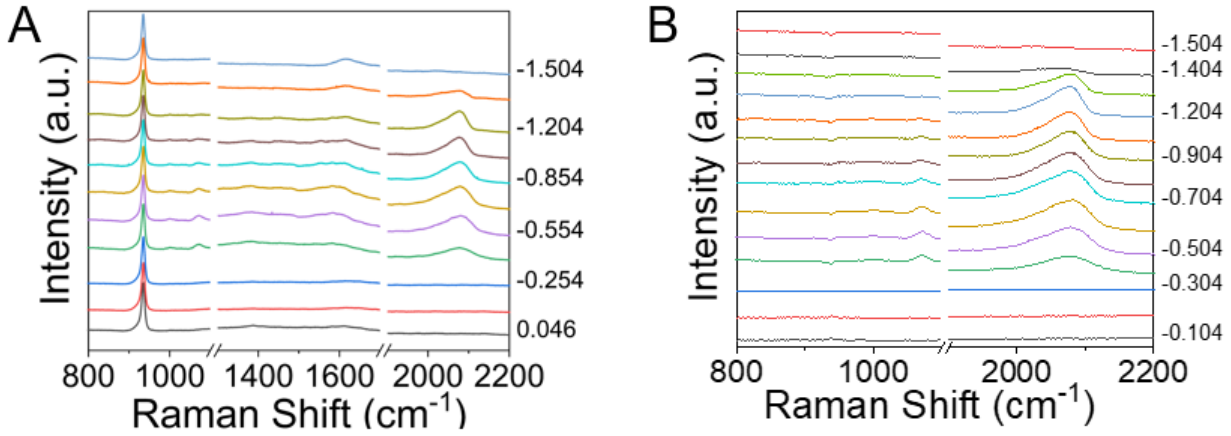

Figure S24. Raman spectra of potential dependent coverage of *CO in the absence $*CO_3^{2-}$. (A) unsubtracted and (B) subtracted Raman spectra in 0.5 M $NaClO_4$ sat. with CO (pH=7.62).

In **Figure S25**, there are also some small peaks at 1389 cm^{-1} and 1601 cm^{-1} from -0.554 V to -1.204 V, similar to the above cases in **Figure S18**, they should be related to the CO reduction products[7,8,64] (HOCCOH at 1397 cm^{-1} OCCOH at 1576 cm^{-1}).

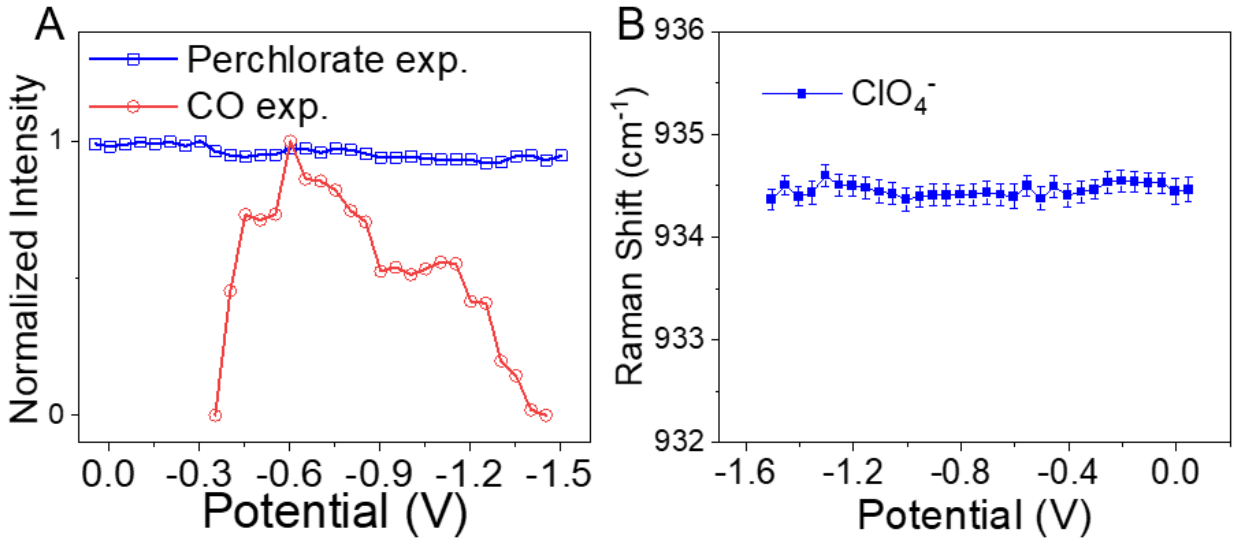

Figure S25. Analysis of the Raman spectra in 0.5 M $NaClO_4$ sat. with CO (pH=7.62). (A) potential dependent intensity of perchlorate and CO intensity. (B) potential dependent frequency of perchlorate anions.

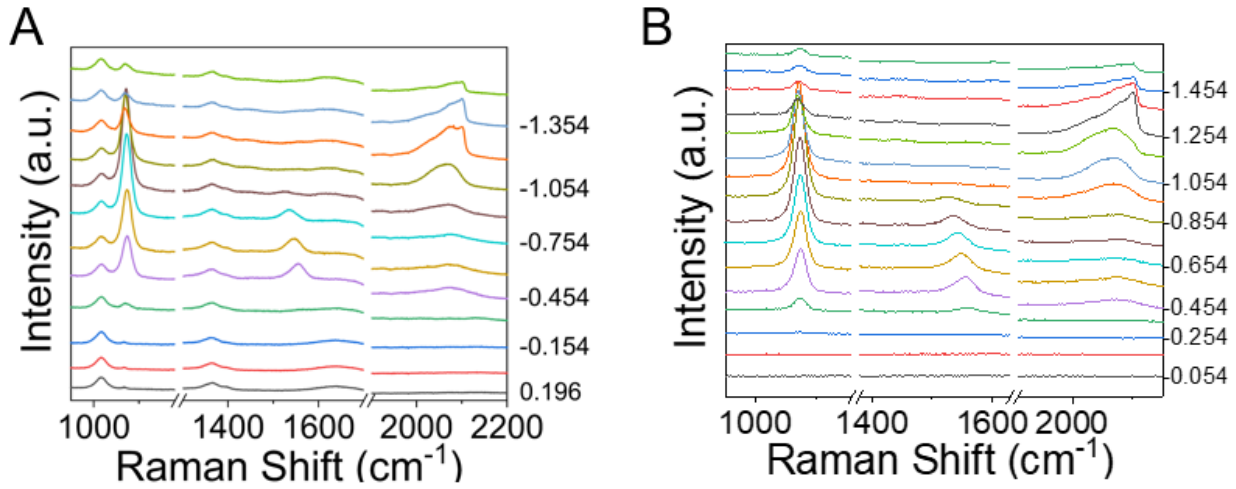

Figure S26. Raman spectra of potential dependent coverage of $*CO_3^{2-}$ and *CO. (A) unsubtracted and (B) subtracted Raman spectra Raman spectra in 0.5 M $NaHCO_3$ sat. with CO (pH=8.44).

7.4.2.12 Discussion on Cu_2O reduction induced carbonate intensity change

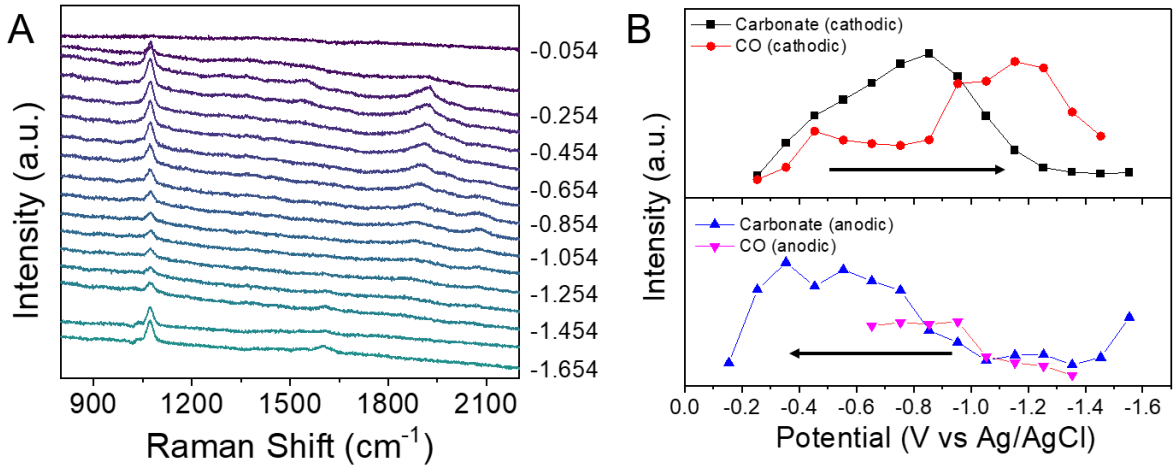

Figure S27. Anodic/cathodic potential dependent coverage of $*CO_3^{2-}$ and *CO
(A) Raman spectra in CO-saturated 0.5 M $NaHCO_3$ during an anodic scan. (B) comparison of the analyzed intensity of carbonate and CO. The cathodic scan intensity is obtained from **Figure S24**.

The potential dependent carbonate intensity changes in an anodic scan shown in **Figure S25** present a different scheme compared with that in a cathodic scan, while the former shows a rapid change from -0.3 V to -0.1 V, the latter shows a gradual increase from -0.1 V to -0.6 V. By this comparison, we believe the main reason is that the Cu_2O reduction process is a slower one resulting in slow arrangement of surface adsorbates, the reversible Cu to Cu_2O oxidation process is a faster process that quickly finishes.

7.4.2.13 Additional discussions of other possible interpretations of the mechanism

In the main text Figure 3 and SI **Figure S16**, we plot the potential dependent intensity changes of different species and proposed the carbonate competitive binding mechanism to explain these interchanges of the different species. In this section, we would like to share our insights into similar observations by other previous reports[31,42] with different mechanisms during CO_2 reduction and re-state the evidence and discussions to support our arguments.

Malachite-precursor mechanism. The first mechanism to explain the similar potential dependent intensity changes is based on the malachite-precursor mechanism,[31] where *CO is a direct product of 1540 cm^{-1} peak (assigned with malachite), these two processes would be expected to coincide along the potential scan, where one converts to the other during the scan. This seems correct under the conditions with 0.1 M $NaHCO_3$ (CO_2 saturated, pH=6.7)[18] or 0.1 M $KHCO_3$ (CO_2 saturated, pH=6.8)[31], where the interchange of disappearing of 1540 cm^{-1} peak and onset of *CO can overlap from 0.1 V to -0.1 V (vs. RHE); however, our measurement of 0.5 M $NaHCO_3$ (CO_2 saturated, pH=7.2), has a later *CO onset at around -0.2 V to -0.25 V vs. RHE, where the peak of ~1540 cm^{-1} starts to decreases at ~ 0.1 V and is no longer observed at -0.1 V. Under the malachite mechanism, it cannot explain what other products malachite (1540 cm^{-1} peak) converts to from 0.1 V to -0.2 V when it decreases its intensity. Thus, this observed large potential gap between the diminishment of the 1540 cm^{-1} peak and the appearance of *CO in our measurements (**Figure S16** or Figure 3 A) can also serve as one more evidence to support the assignment on $*COO^-$ instead of malachite.

Malachite-formation induced local pH change mechanism. Another interpretation of the potential dependent carbonate Raman peak intensity change was reported by Henckel et al.[42]. In their work, the relative potential dependent carbonate peak intensity change at the same potential region was also observed but regarded as an indicator of surface pH change, so that the potential dependent pH change profile on Cu during CO_2 reduction can be obtained by the ratio

of intensity ratio of carbonate and bicarbonate, followed by the mechanism to explain the pH decreases including the malachite formation. We believe the surface pH changes as the potential is swept cathodically, especially the Cu oxide reduction and other side reactions must occur and change the local pH; however, we disagree with attributing the potential-dependent intensity change of carbonate to the pH change, at least not in a significant amount. The reason is mainly due to the adsorption of carbonate. First, it has been shown in a SEIRAS study[23] that, on the Au surface, the vibrational modes for carbonate and bicarbonate at ~1363 to ~1400 cm^{-1} can be utilized to quantify the surface pH changes, this is well accepted, as the bicarbonate or carbonate is not a specific strong adsorbate on Au, showing no competition with adsorbed *CO [29]; however, it is also proven that[28,29], carbonate on Cu shows specific adsorption and greatly affects other adsorbates. Therefore, in the case of Cu, the increased intensity of carbonate cannot be solely seen as a pH change. Second, in our specific case, we observed at least around 8~9 cm^{-1}/V Stark shift for carbonate in any control experiments, so we believe the carbonate in our system can be seen as an adsorbate so that it can feel and respond to the electric field change. Third, as **Figure 5-A, B** shows, in our Ar saturated 0.25 M Na_2CO_3 control with a different pH = 11.95 compared with the ones around 6~7, we observed a similar potential-dependent intensity change of carbonate, which is unlikely to be a case with pH probe. Therefore, for these three reasons, we believe the carbonate in our system exhibits more features of adsorbates rather than a local pH probe. At the same time, we also think that more studies similar to the gradient vibrational detection study[53] are needed to disentangle the contribution from the gradient pH change and that of adsorption.

Stepwise intermediates during electrochemical measurements. Lastly in terms of "intermediates", it is commonly seen that potential-dependent spectroscopic methods are used in measuring halfway "intermediates" for a reaction, as it provides an easy way to control the thermodynamics input of the reaction and stop at the halfway to measure. However, our measurements again indicate that, for many cases, these step-wise measurements only reflect and measure the species steadily at the "halfway" condition. In other words, they cannot fully represent the exact mechanistic intermediates at a different potential (thermodynamic condition) where the final product is produced, as the surface environment can be greatly different between

the two cases. Taking our measurements as an example, in the CO_2 saturated 0.5 M $NaHCO_3$ case, from -0.2 V to -0.85 V, only *COO^- but no *CO was observed due to the required energy input for reducing *COO^- being higher than provided. And from -0.9 V to -1.3 V, similarly, *CO becomes the more stable species, but the surface environment (binding ions, pH, etc.) is quite different from the previous case; therefore, the exact pathway and intermediates at this potential may also change as the environment changes. In the second case, perhaps a fixed potential but faster time-resolved or time-dependent measurement can be introduced to detect actual intermediates. Our results suggest that it is not accurate to ascribe the probed species at low overpotentials to Faradaic intermediates. Specifically, the cations stabilized -C,O down carboxylate, *COO^- have yet to be attributed to either specific CO or formate pathways, even though we have detected and assigned the *COO^- species. This is because it was detected at a specific low overpotential where carbonate still binds on the surface, and no other significant amount of products (CO or formate) were detected. This may account for previous reports with no other products except for only traces amount of formate detected at the potential of *COO^- observed.[18] When the potential is increased to a more cathodic level where the Faradaic current increases, the surface local environment including binding ions, pH, etc. changes significantly. This highlights the importance of applying a step-wise potential to the electrocatalysis surface, as it not only affects the energy parameters but also the local environment; the ideal case is for the step-wise applied potentials to only affect the energy input.

7.5. References

(1) Birdja, Y. Y.; Pérez-Gallent, E.; Figueiredo, M. C.; Göttle, A. J.; Calle-Vallejo, F.; Koper, M. T. M. Advances and Challenges in Understanding the Electrocatalytic Conversion of Carbon Dioxide to Fuels. *Nat. Energy* **2019**, *4* (9), 732–745. https://doi.org/10.1038/s41560-019-0450-y.
(2) Nitopi, S.; Bertheussen, E.; Scott, S. B.; Liu, X.; Engstfeld, A. K.; Horch, S.; Seger, B.; Stephens, I. E. L.; Chan, K.; Hahn, C.; Nørskov, J. K.; Jaramillo, T. F.; Chorkendorff, I. Progress and Perspectives of Electrochemical CO_2 Reduction on Copper in Aqueous Electrolyte. *Chem. Rev.* **2019**, *119* (12), 7610–7672. https://doi.org/10.1021/acs.chemrev.8b00705.
(3) Hori, Y.; Kikuchi, K.; Suzuki, S. PRODUCTION OF CO AND CH_4 IN ELECTROCHEMICAL REDUCTION OF CO_2 AT METAL ELECTRODES IN AQUEOUS HYDROGENCARBONATE SOLUTION. *Chem. Lett.* **1985**, *14* (11), 1695–1698. https://doi.org/10.1246/cl.1985.1695.
(4) Hori, Y.; Wakebe, H.; Tsukamoto, T.; Koga, O. Electrocatalytic Process of CO Selectivity in Electrochemical Reduction of CO2 at Metal Electrodes in Aqueous Media. *Electrochimica Acta* **1994**, *39* (11–12), 1833–1839. https://doi.org/10.1016/0013-4686(94)85172-7.
(5) Hori, Y. Electrochemical CO2 Reduction on Metal Electrodes. In *Modern Aspects of Electrochemistry*; Vayenas, C. G., White, R. E., Gamboa-Aldeco, M. E., Eds.; Modern Aspects of Electrochemistry; Springer New York: New York, NY, 2008; Vol. 42, pp 89–189. https://doi.org/10.1007/978-0-387-49489-0_3.
(6) Xiao, H.; Goddard, W. A.; Cheng, T.; Liu, Y. Cu Metal Embedded in Oxidized Matrix Catalyst to Promote CO_2 Activation and CO Dimerization for Electrochemical Reduction of CO_2. *Proc. Natl. Acad. Sci.* **2017**, 201702405. https://doi.org/10.1073/pnas.1702405114.
(7) Pérez-Gallent, E.; Figueiredo, M. C.; Calle-Vallejo, F.; Koper, M. T. M. Spectroscopic Observation of a Hydrogenated CO Dimer Intermediate During CO Reduction on Cu(100) Electrodes. *Angew. Chem.* **2017**, *129* (13), 3675–3678. https://doi.org/10.1002/ange.201700580.
(8) Pérez-Gallent, E.; Marcandalli, G.; Figueiredo, M. C.; Calle-Vallejo, F.; Koper, M. T. M. Structure- and Potential-Dependent Cation Effects on CO Reduction at Copper Single-Crystal Electrodes. *J. Am. Chem. Soc.* **2017**, *139* (45), 16412–16419. https://doi.org/10.1021/jacs.7b10142.
(9) Li, J.; Chang, X.; Zhang, H.; Malkani, A. S.; Cheng, M.; Xu, B.; Lu, Q. Electrokinetic and in Situ Spectroscopic Investigations of CO Electrochemical Reduction on Copper. *Nat. Commun.* **2021**, *12* (1), 3264. https://doi.org/10.1038/s41467-021-23582-2.
(10) Zhao, Y.; Chang, X.; Malkani, A. S.; Yang, X.; Thompson, L.; Jiao, F.; Xu, B. Speciation of Cu Surfaces During the Electrochemical CO Reduction Reaction. *J. Am. Chem. Soc.* **2020**. https://doi.org/10.1021/jacs.0c02354.
(11) Li, J.; Li, X.; Gunathunge, C. M.; Waegele, M. M. Hydrogen Bonding Steers the Product Selectivity of Electrocatalytic CO Reduction. *Proc. Natl. Acad. Sci.* **2019**, *116* (19), 9220–9229. https://doi.org/10.1073/pnas.1900761116.
(12) Malkani, A. S.; Li, J.; Oliveira, N. J.; He, M.; Chang, X.; Xu, B.; Lu, Q. Understanding the Electric and Nonelectric Field Components of the Cation Effect on the Electrochemical CO Reduction Reaction. *Sci. Adv.* **2020**, *6* (45), eabd2569. https://doi.org/10.1126/sciadv.abd2569.
(13) Chang, X.; Zhao, Y.; Xu, B. pH Dependence of Cu Surface Speciation in the Electrochemical CO Reduction Reaction. *ACS Catal.* **2020**, *10* (23), 13737–13747. https://doi.org/10.1021/acscatal.0c03108.

(14) Gunathunge, C. M.; Ovalle, V. J.; li, yawei; Janik, M. J.; Waegele, M. M. Existence of an Electrochemically Inert CO Population on Cu Electrodes in Alkaline pH. *ACS Catal.* **2018**. https://doi.org/10.1021/acscatal.8b01552.
(15) Iijima, G.; Inomata, T.; Yamaguchi, H.; Ito, M.; Masuda, H. Role of a Hydroxide Layer on Cu Electrodes in Electrochemical CO $_2$ Reduction. *ACS Catal.* **2019**, *9* (7), 6305–6319. https://doi.org/10.1021/acscatal.9b00896.
(16) Zhan, C.; Dattila, F.; Rettenmaier, C.; Bergmann, A.; Kühl, S.; García-Muelas, R.; López, N.; Cuenya, B. R. Revealing the CO Coverage-Driven C–C Coupling Mechanism for Electrochemical CO $_2$ Reduction on Cu $_2$ O Nanocubes *via Operando* Raman Spectroscopy. *ACS Catal.* **2021**, *11* (13), 7694–7701. https://doi.org/10.1021/acscatal.1c01478.
(17) Favaro, M.; Xiao, H.; Cheng, T.; Goddard, W. A.; Yano, J.; Crumlin, E. J. Subsurface Oxide Plays a Critical Role in CO $_2$ Activation by Cu(111) Surfaces to Form Chemisorbed CO $_2$, the First Step in Reduction of CO $_2$. *Proc. Natl. Acad. Sci.* **2017**, 201701405. https://doi.org/10.1073/pnas.1701405114.
(18) Chernyshova, I. V.; Somasundaran, P.; Ponnurangam, S. On the Origin of the Elusive First Intermediate of CO $_2$ Electroreduction. *Proc. Natl. Acad. Sci.* **2018**, 201802256. https://doi.org/10.1073/pnas.1802256115.
(19) He, M.; Li, C.; Zhang, H.; Chang, X.; Chen, J. G.; Goddard, W. A.; Cheng, M.; Xu, B.; Lu, Q. Oxygen Induced Promotion of Electrochemical Reduction of CO2 via Co-Electrolysis. *Nat. Commun.* **2020**, *11* (1). https://doi.org/10.1038/s41467-020-17690-8.
(20) Dattila, F.; Seemakurthi, R. R.; Zhou, Y.; López, N. Modeling Operando Electrochemical CO $_2$ Reduction. *Chem. Rev.* **2022**, *122* (12), 11085–11130. https://doi.org/10.1021/acs.chemrev.1c00690.
(21) Feaster, J. T.; Shi, C.; Cave, E. R.; Hatsukade, T.; Abram, D. N.; Kuhl, K. P.; Hahn, C.; Nørskov, J. K.; Jaramillo, T. F. Understanding Selectivity for the Electrochemical Reduction of Carbon Dioxide to Formic Acid and Carbon Monoxide on Metal Electrodes. *ACS Catal.* **2017**, *7* (7), 4822–4827. https://doi.org/10.1021/acscatal.7b00687.
(22) Cheng, T.; Xiao, H.; Goddard, W. A. Reaction Mechanisms for the Electrochemical Reduction of CO $_2$ to CO and Formate on the Cu(100) Surface at 298 K from Quantum Mechanics Free Energy Calculations with Explicit Water. *J. Am. Chem. Soc.* **2016**, *138* (42), 13802–13805. https://doi.org/10.1021/jacs.6b08534.
(23) Dunwell, M.; Yang, X.; Setzler, B. P.; Anibal, J.; Yan, Y.; Xu, B. Examination of Near-Electrode Concentration Gradients and Kinetic Impacts on the Electrochemical Reduction of CO $_2$ Using Surface-Enhanced Infrared Spectroscopy. *ACS Catal.* **2018**, 3999–4008. https://doi.org/10.1021/acscatal.8b01032.
(24) Zhu, S.; Jiang, B.; Cai, W.-B.; Shao, M. Direct Observation on Reaction Intermediates and the Role of Bicarbonate Anions in CO $_2$ Electrochemical Reduction Reaction on Cu Surfaces. *J. Am. Chem. Soc.* **2017**, *139* (44), 15664–15667. https://doi.org/10.1021/jacs.7b10462.
(25) Dunwell, M.; Lu, Q.; Heyes, J. M.; Rosen, J.; Chen, J. G.; Yan, Y.; Jiao, F.; Xu, B. The Central Role of Bicarbonate in the Electrochemical Reduction of Carbon Dioxide on Gold. *J. Am. Chem. Soc.* **2017**, *139* (10), 3774–3783. https://doi.org/10.1021/jacs.6b13287.
(26) Heyes, J.; Dunwell, M.; Xu, B. CO $_2$ Reduction on Cu at Low Overpotentials with Surface-Enhanced in Situ Spectroscopy. *J. Phys. Chem. C* **2016**, *120* (31), 17334–17341. https://doi.org/10.1021/acs.jpcc.6b03065.
(27) Moradzaman, M.; Mul, G. In Situ Raman Study of Potential-Dependent Surface Adsorbed Carbonate, CO, OH, and C Species on Cu Electrodes During Electrochemical

Reduction of CO2. *ChemElectroChem* **2021**, *8* (8), 1478–1485. https://doi.org/10.1002/celc.202001598.
(28) Hori, Y.; Koga, O.; Watanabe, Y.; Matsuo, T. FTIR Measurements of Charge Displacement Adsorption of CO on Poly- and Single Crystal (100) of Cu Electrodes. *Electrochimica Acta* **1998**, *44* (8–9), 1389–1395. https://doi.org/10.1016/S0013-4686(98)00261-8.
(29) Wuttig, A.; Ryu, J.; Surendranath, Y. Electrolyte Competition Controls Surface Binding of CO Intermediates to CO_2 Reduction Catalysts. *J. Phys. Chem. C* **2021**, *125* (31), 17042–17050. https://doi.org/10.1021/acs.jpcc.1c04337.
(30) de Ruiter, J.; An, H.; Wu, L.; Gijsberg, Z.; Yang, S.; Hartman, T.; Weckhuysen, B. M.; van der Stam, W. Probing the Dynamics of Low-Overpotential CO_2 -to-CO Activation on Copper Electrodes with Time-Resolved Raman Spectroscopy. *J. Am. Chem. Soc.* **2022**, jacs.2c03172. https://doi.org/10.1021/jacs.2c03172.
(31) Jiang, S.; D'Amario, L.; Dau, H. Copper Carbonate Hydroxide as Precursor of Interfacial CO in CO_2 Electroreduction. *ChemSusChem* **2022**, *15* (8). https://doi.org/10.1002/cssc.202102506.
(32) Li, J. F.; Huang, Y. F.; Ding, Y.; Yang, Z. L.; Li, S. B.; Zhou, X. S.; Fan, F. R.; Zhang, W.; Zhou, Z. Y.; Wu, D. Y.; Ren, B.; Wang, Z. L.; Tian, Z. Q. Shell-Isolated Nanoparticle-Enhanced Raman Spectroscopy. *Nature* **2010**, *464* (7287), 392–395. https://doi.org/10.1038/nature08907.
(33) Shao, F.; Wong, J. K.; Low, Q. H.; Iannuzzi, M.; Li, J.; Lan, J. In Situ Spectroelectrochemical Probing of CO Redox Landscape on Copper Single-Crystal Surfaces. *Proc. Natl. Acad. Sci.* **2022**, *119* (29), e2118166119. https://doi.org/10.1073/pnas.2118166119.
(34) Zhao, Y.; Zhang, X.-G.; Bodappa, N.; Yang, W.-M.; Liang, Q.; Radjenovica, P. M.; Wang, Y.-H.; Zhang, Y.-J.; Dong, J.-C.; Tian, Z.-Q.; Li, J.-F. Elucidating Electrochemical CO_2 Reduction Reaction Processes on Cu(*Hkl*) Single-Crystal Surfaces by *in Situ* Raman Spectroscopy. *Energy Environ. Sci.* **2022**, *15* (9), 3968–3977. https://doi.org/10.1039/D2EE01334G.
(35) Rudolph, W. W.; Irmer, G.; Königsberger, E. Speciation Studies in Aqueous HCO_3^-–CO_3^{2-} Solutions. A Combined Raman Spectroscopic and Thermodynamic Study. *Dalton Trans* **2008**, No. 7, 900–908. https://doi.org/10.1039/B713254A.
(36) Rudolph, W. W.; Fischer, D.; Irmer, G. Vibrational Spectroscopic Studies and Density Functional Theory Calculations of Speciation in the CO_2 —Water System. *Appl. Spectrosc.* **2006**, *60* (2), 130–144. https://doi.org/10.1366/000370206776023421.
(37) Bodappa, N.; Su, M.; Zhao, Y.; Le, J.-B.; Yang, W.-M.; Radjenovic, P.; Dong, J.-C.; Cheng, J.; Tian, Z.-Q.; Li, J.-F. Early Stages of Electrochemical Oxidation of Cu(111) and Polycrystalline Cu Surfaces Revealed by *in Situ* Raman Spectroscopy. *J. Am. Chem. Soc.* **2019**, *141* (31), 12192–12196. https://doi.org/10.1021/jacs.9b04638.
(38) Niaura, G. Surface-Enhanced Raman Spectroscopic Observation of Two Kinds of Adsorbed OH− Ions at Copper Electrode. *Electrochimica Acta* **2000**, *45* (21), 3507–3519. https://doi.org/10.1016/S0013-4686(00)00434-5.
(39) Koga, O.; Matsuo, T.; Hoshi, N.; Hori, Y. Charge Displacement Adsorption of Carbon Monoxide on [110] Zone Copper Single Crystal Electrodes in Relation with PZC. *Electrochimica Acta* **1998**, *44* (6–7), 903–907. https://doi.org/10.1016/S0013-4686(98)00193-5.
(40) Hori, Y.; Wakebe, H.; Tsukamoto, T.; Koga, O. Adsorption of CO Accompanied with Simultaneous Charge Transfer on Copper Single Crystal Electrodes Related with

Electrochemical Reduction of CO2 to Hydrocarbons. *Surf. Sci.* **1995**, *335*, 258–263. https://doi.org/10.1016/0039-6028(95)00441-6.
(41) Zosel, J.; Oelßner, W.; Decker, M.; Gerlach, G.; Guth, U. The Measurement of Dissolved and Gaseous Carbon Dioxide Concentration. *Meas. Sci. Technol.* **2011**, *22* (7), 072001. https://doi.org/10.1088/0957-0233/22/7/072001.
(42) Henckel, D. A.; Counihan, M. J.; Holmes, H. E.; Chen, X.; Nwabara, U. O.; Verma, S.; Rodríguez-López, J.; Kenis, P. J. A.; Gewirth, A. A. Potential Dependence of the Local pH in a CO_2 Reduction Electrolyzer. *ACS Catal.* **2021**, *11* (1), 255–263. https://doi.org/10.1021/acscatal.0c04297.
(43) Marcandalli, G.; Monteiro, M. C. O.; Goyal, A.; Koper, M. T. M. Electrolyte Effects on CO_2 Electrochemical Reduction to CO. *Acc. Chem. Res.* **2022**, *55* (14), 1900–1911. https://doi.org/10.1021/acs.accounts.2c00080.
(44) Ringe, S.; Morales-Guio, C. G.; Chen, L. D.; Fields, M.; Jaramillo, T. F.; Hahn, C.; Chan, K. Double Layer Charging Driven Carbon Dioxide Adsorption Limits the Rate of Electrochemical Carbon Dioxide Reduction on Gold. *Nat. Commun.* **2020**, *11* (1), 33. https://doi.org/10.1038/s41467-019-13777-z.
(45) Bondue, C. J.; Graf, M.; Goyal, A.; Koper, M. T. M. Suppression of Hydrogen Evolution in Acidic Electrolytes by Electrochemical CO_2 Reduction. *J. Am. Chem. Soc.* **2021**, *143* (1), 279–285. https://doi.org/10.1021/jacs.0c10397.
(46) Wuttig, A.; Yoon, Y.; Ryu, J.; Surendranath, Y. Bicarbonate Is Not a General Acid in Au-Catalyzed CO_2 Electroreduction. *J. Am. Chem. Soc.* **2017**, *139* (47), 17109–17113. https://doi.org/10.1021/jacs.7b08345.
(47) Dong, Q.; Zhang, X.; He, D.; Lang, C.; Wang, D. Role of H_2O in CO_2 Electrochemical Reduction As Studied in a Water-in-Salt System. *ACS Cent. Sci.* **2019**, *5* (8), 1461–1467. https://doi.org/10.1021/acscentsci.9b00519.
(48) Monteiro, M. C. O.; Dattila, F.; Hagedoorn, B.; García-Muelas, R.; López, N.; Koper, M. T. M. Absence of CO2 Electroreduction on Copper, Gold and Silver Electrodes without Metal Cations in Solution. *Nat. Catal.* **2021**, *4* (8), 654–662. https://doi.org/10.1038/s41929-021-00655-5.
(49) Xiao, H.; Cheng, T.; Goddard, W. A.; Sundararaman, R. Mechanistic Explanation of the pH Dependence and Onset Potentials for Hydrocarbon Products from Electrochemical Reduction of CO on Cu (111). *J. Am. Chem. Soc.* **2016**, *138* (2), 483–486. https://doi.org/10.1021/jacs.5b11390.
(50) Marcandalli, G.; Goyal, A.; Koper, M. T. M. Electrolyte Effects on the Faradaic Efficiency of CO_2 Reduction to CO on a Gold Electrode. *ACS Catal.* **2021**, *11* (9), 4936–4945. https://doi.org/10.1021/acscatal.1c00272.
(51) Eilert, A.; Roberts, F. S.; Friebel, D.; Nilsson, A. Formation of Copper Catalysts for CO_2 Reduction with High Ethylene/Methane Product Ratio Investigated with In Situ X-Ray Absorption Spectroscopy. *J. Phys. Chem. Lett.* **2016**, *7* (8), 1466–1470. https://doi.org/10.1021/acs.jpclett.6b00367.
(52) Spodaryk, M.; Zhao, K.; Zhang, J.; Oveisi, E.; Züttel, A. The Role of Malachite Nanorods for the Electrochemical Reduction of CO2 to C2 Hydrocarbons. *Electrochimica Acta* **2019**, *297*, 55–60. https://doi.org/10.1016/j.electacta.2018.11.124.
(53) Lu, X.; Zhu, C.; Wu, Z.; Xuan, J.; Francisco, J. S.; Wang, H. In Situ Observation of the pH Gradient near the Gas Diffusion Electrode of CO_2 Reduction in Alkaline Electrolyte. *J. Am. Chem. Soc.* **2020**, *142* (36), 15438–15444. https://doi.org/10.1021/jacs.0c06779.

(54) Li, J. F.; Huang, Y. F.; Ding, Y.; Yang, Z. L.; Li, S. B.; Zhou, X. S.; Fan, F. R.; Zhang, W.; Zhou, Z. Y.; Wu, D. Y.; Ren, B.; Wang, Z. L.; Tian, Z. Q. Shell-Isolated Nanoparticle-Enhanced Raman Spectroscopy. *Nature* **2010**, *464* (7287), 392–395. https://doi.org/10.1038/nature08907.
(55) Chernyshova, I. V.; Ponnurangam, S.; Somasundaran, P. Linking Interfacial Chemistry of CO2 to Surface Structures of Hydrated Metal Oxide Nanoparticles: Hematite. *Phys. Chem. Chem. Phys.* **2013**, *15* (18), 6953. https://doi.org/10.1039/c3cp44264k.
(56) Iwasita, T.; Rodes, A.; Pastor, E. Vibrational Spectroscopy of Carbonate Adsorbed on Pt(111) and Pt(110) Single-Crystal Electrodes. *J. Electroanal. Chem.* **1995**, *383* (1–2), 181–189. https://doi.org/10.1016/0022-0728(94)03708-B.
(57) Firet, N. J.; Smith, W. A. Probing the Reaction Mechanism of CO_2 Electroreduction over Ag Films via Operando Infrared Spectroscopy. *ACS Catal.* **2017**, *7* (1), 606–612. https://doi.org/10.1021/acscatal.6b02382.
(58) Gunathunge, C. M.; Li, X.; Li, J.; Hicks, R. P.; Ovalle, V. J.; Waegele, M. M. Spectroscopic Observation of Reversible Surface Reconstruction of Copper Electrodes under CO_2 Reduction. *J. Phys. Chem. C* **2017**, *121* (22), 12337–12344. https://doi.org/10.1021/acs.jpcc.7b03910.
(59) Pfisterer, J. H. K.; Zhumaev, U. E.; Cheuquepan, W.; Feliu, J. M.; Domke, K. F. Stark Effect or Coverage Dependence? Disentangling the EC-SEIRAS Vibrational Shift of Sulfate on Au(111). *J. Chem. Phys.* **2019**, *150* (4), 041709. https://doi.org/10.1063/1.5047941.
(60) Jiang, S.; Klingan, K.; Pasquini, C.; Dau, H. New Aspects of Operando Raman Spectroscopy Applied to Electrochemical CO_2 Reduction on Cu Foams. *J. Chem. Phys.* **2019**, *150* (4), 041718. https://doi.org/10.1063/1.5054109.
(61) Kloprogge, J. T.; Wharton, D.; Hickey, L.; Frost, R. L. Infrared and Raman Study of Interlayer Anions CO_3^{2-}, NO_3^-, SO_4^{2-} and ClO_4^- in Mg/Al-Hydrotalcite. *Am. Mineral.* **2002**, *87* (5–6), 623–629. https://doi.org/10.2138/am-2002-5-604.
(62) Arihara, K.; Kitamura, F.; Ohsaka, T.; Tokuda, K. Characterization of the Adsorption State of Carbonate Ions at the Au(111) Electrode Surface Using in Situ IRAS. *J. Electroanal. Chem.* **2001**, *510* (1–2), 128–135. https://doi.org/10.1016/S0022-0728(01)00498-3.
(63) Kimura, K. W.; Casebolt, R.; Cimada DaSilva, J.; Kauffman, E.; Kim, J.; Dunbar, T. A.; Pollock, C. J.; Suntivich, J.; Hanrath, T. Selective Electrochemical CO_2 Reduction during Pulsed Potential Stems from Dynamic Interface. *ACS Catal.* **2020**, *10* (15), 8632–8639. https://doi.org/10.1021/acscatal.0c02630.
(64) Kim, Y.; Park, S.; Shin, S.-J.; Choi, W.; Min, B. K.; Kim, H.; Kim, W.; Hwang, Y. J. Time-Resolved Observation of C–C Coupling Intermediates on Cu Electrodes for Selective Electrochemical CO_2 Reduction. *Energy Environ. Sci.* **2020**, *13* (11), 4301–4311. https://doi.org/10.1039/D0EE01690J.
(65) Łukomska, A.; Sobkowski, J. Potential of Zero Charge of Monocrystalline Copper Electrodes in Perchlorate Solutions. *J. Electroanal. Chem.* **2004**, *567* (1), 95–102. https://doi.org/10.1016/j.jelechem.2003.11.063.
(66) Hori, Y.; Murata, A.; Takahashi, R. Formation of Hydrocarbons in the Electrochemical Reduction of Carbon Dioxide at a Copper Electrode in Aqueous Solution. *J. Chem. Soc. Faraday Trans. 1 Phys. Chem. Condens. Phases* **1989**, *85* (8), 2309. https://doi.org/10.1039/f19898502309.
(67) Kuhl, K. P.; Cave, E. R.; Abram, D. N.; Jaramillo, T. F. New Insights into the Electrochemical Reduction of Carbon Dioxide on Metallic Copper Surfaces. *Energy Environ. Sci.* **2012**, *5* (5), 7050. https://doi.org/10.1039/c2ee21234j.

8. Chapter 8 Photo-enhanced Electrochemical CO_2 reduction on Au electrodes

8.1. Introduction

Among catalytic metals, Au has been recognized for its unique capability to reduce CO_2 into carbon monoxide (CO), which is an important raw material for many synthetic processes. To enhance the efficiency and energy utilization for CO_2 reduction on Au in aqueous solution, one promising strategy has been developed to couple the photo/light into the electrochemical catalysis. Recent studies[1–4] have shown that light can modulate the interfacial electrochemical reaction pathways and greatly enhance CO_2 reduction efficiency through light irradiation at the Au/aqueous interface. However, such light-induced effects on CO production and their correlation with other surface properties (e.g., roughness) have not been well understood and the relevant molecular mechanism remains unclear. Herein, we present a report on utilizing laser light to enhance the CO_2 reduction to CO on the Au surface and the investigations into the enhancement mechanism.

In this section, by using VSFGS with 800 nm and ~5000 nm pulsed probed light, we first studied the CO_{ad} on Au during CO_2 reduction. We found a high onset potential at 1.1 V for CO production on Au under this condition, surprisingly above the predicted value at around 0.2 V. This observation led us to propose a mechanism involving photo-assisted CO_2 reduction on Au, in which the probe light in the SFG setup also takes part. To further validate the photo-assisted mechanism, we did two types of measurements: 1) we conducted a series of photocurrent measurements by different light sources and revealed that the photo-illumination from 532 nm to 800 nm on the Au electrode under the electrochemical conditions can initiate noticeable photocurrents for CO_2 reduction; 2) we prepared samples including small 3-6 nm Au, Cu NPs in aqueous solutions and on Indium Tin Oxide (ITO) electrodes, then by the identification of the characteristic signal of solvated electrons by the Transient Absorption (TA) Spectroscopy, were able to confirm the generation of solvated electrons and measure their lifetime, partially supporting the mechanism of possible triggered by solvated electrons generated from the metal surface.

However, this photo-enhanced electrochemical CO_2 (PEEC) reduction is a complicated

system that may involve many different contributions, i.e. hot electron generation from the Au surface, laser heating effect, and direct laser-induced reduction in the liquid phase. With these possible mechanisms coexisting, there is no direct way to rule out each possible contribution, thus the whole picture for this interesting observation of PEEC is still not well understood. At the current stage, we only presented one possible mechanism and the part of validation. To make a better understanding, we propose more follow-up experiments to fully elucidate the mechanisms of PEEC on the Au surfaces.

8.2. Results and analysis

8.2.1. SFG observation of the photo-enhanced and photo-induced *CO on Au

Au has emerged as an effective material for electrochemical CO_2 reduction to CO, as it shows high selectivity for CO instead of other products in aqueous solutions. To find out the molecular mechanisms, many studies have been focusing on utilizing *in situ* spectroscopic techniques to study the CO_2 reduction to CO on Au. Dunwell et al. have used the ATR-SEIRAS[5] to successfully observe the onset of CO_2 reduction of CO on Au at around 0.2 V vs. RHE. To investigate the molecular interfacial mechanisms of the electrochemical CO_2 reduction in the Au system, we also conduct a similar potential-dependent measurement with SFG.

We consider the electrochemical interface with probe light as the environment where the electromagnetic fields from light beams (pulse lasers in SFG) and the static electrical fields from electrochemical potential coexist. The most ideal case in our original prediction is that the light pulses only serve as a probe which poses as minor as possible impacts on the electrochemical interfaces, while the bias mainly triggers and influences the CO_2 reduction reaction. In this case, we should observe a similar electrochemical onset potential with different optical techniques.

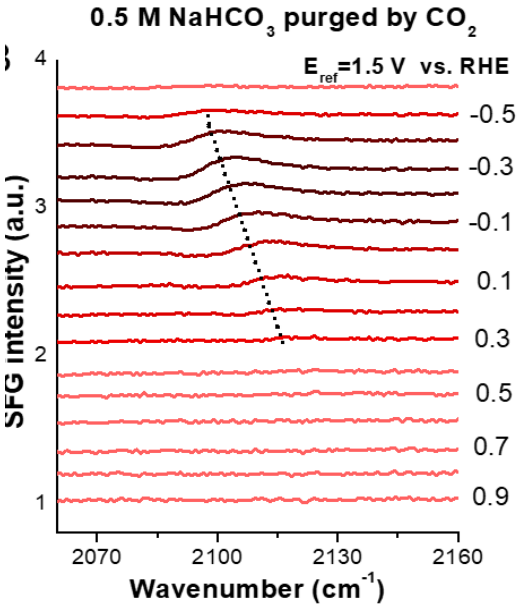

Figure 7.1. Potential-dependent SFG spectra for **smoother Au** surface
The potential dependent SFG results on Au (0.05 μm Al_2O_3 polished)

Thus, we first studied how electrochemical SFG results behave differently than those by non-invasive SEIRAS technique. In **Figure 7.17**, we showed the results of electrochemical CO_2 reduction on Au studied by SFG. According to the previous study with ATR-SEIRS by Dunwell et al[5], the onset potential of CO2-reduced CO should be around + 0.2 V vs RHE. In our potential dependent SFG spectra on a smoother Au surface, a similar result was also observed. The basic understanding of the onset potential is that, from the potential positive than +0.2 V, CO_2 molecules or other activated CO_2 reduced precursors can be adsorbed or stay near the Au surfaces, where the CO_2 reduction has not happened; form potential +0.2 V to -0.5 V, *CO starts to be observed, as the reduction reaction happens and the +0.2 V can be regarded as the onset potential; and when the potential is negative than -0.5 V, it is assumed that the stronger absorption of cations leads to the desorption of CO, thus a decrease of *CO can be seen. The related scheme can be seen in **Figure 7.18**.

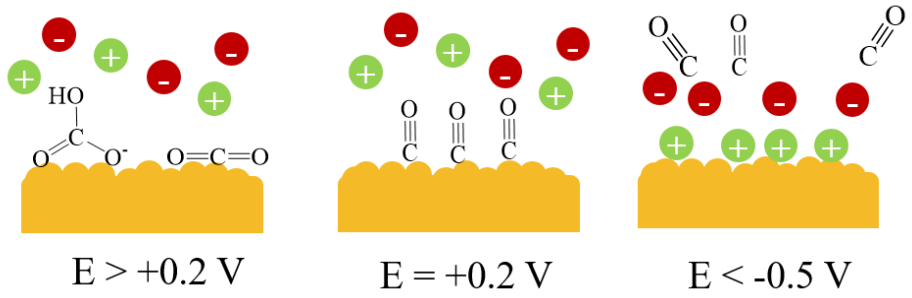

Figure 7.2. Proposed scheme of surface phenomenon on CO_2 reduction on Au

However, when we replace the Au electrode to be a more roughened one (from 0.05 μm Al_2O_3 polished to 0.3 μm Al_2O_3 polished), more contribution from the photo/lasers shows up and the previous assumption no longer predicts the observation accurately. As shown in **Figure 7.19** A, the onset potential of CO from CO_2 reduction changed from +0.2 V vs. RHE to around +1.2 V. In previous studies, the potential positive than +0.6 V is often regarded as the CO desorption and oxidation potential, thus, the observation of *CO at +0.6 V to +1.2 V can be seen as quite unlikely to happen. Besides, at the same potential region from 1.2 to 0.1 V, more CO signal was also observed in the roughened Au case. A direct comparison of the roughened and the smooth surface at 0.1 V can more clearly show the difference, shown in **Figure 7.19** B, where the roughened Au shows a more intense *CO peak.

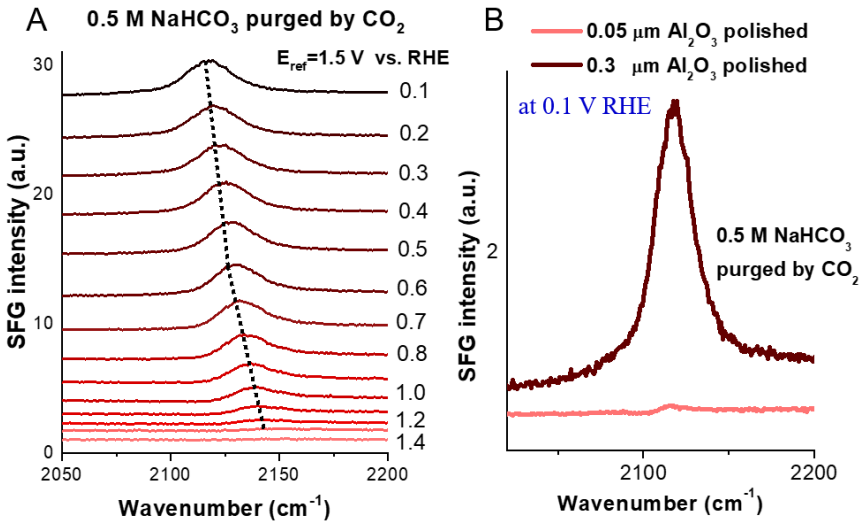

Figure 7.3. Potential-dependent SFG spectra for **roughened Au** surface
(A) Potential dependent SFG spectra on Au (0.3 μm Al_2O_3 polished). (B) SFG spectra with different roughness comparison at +0.1 V vs. RHE.

The increase of the surface roughness not only results in a stronger *CO signal, but also results in a positive onset potential, which means the pure electrochemical CO_2 reduction may be altered into a mixed photo-enhanced electrochemical CO_2 reduction, and a stronger CO signal or the positive onset can be attributed to a roughness dependent photo-induced effect. To verify the light-induced or the photo-enhanced effect, we conduct another control measurement with only the pulses in the system without any bias applied. **Figure 7.20** shows the results of the differently roughened Au surfaces with only light (800 nm and mid-IR pulses from SFG generation) and without bias. Under this condition, all the original energy levels of Au surfaces should be the same and equal to the fermi level of Au at open circuit potentials, and the lasers in the system not only work as a reaction trigger but also as a probe to generate SFG pulses. With 10 min exposure to the two laser pulses, *CO signal can be observed on all three samples of raw SFG spectra, and the most roughened Au surface showed the most intense CO signal. In the actual measurement, the laser beams required for the CO generation are confirmed by the observation of gradually increasing *CO signal from zero during the moving of the probed area to different spots. These measurements further validate that there is a surface morphology-dependent photo-induced effect that can initiate the reaction and lead to the CO_2 being reduced to CO.

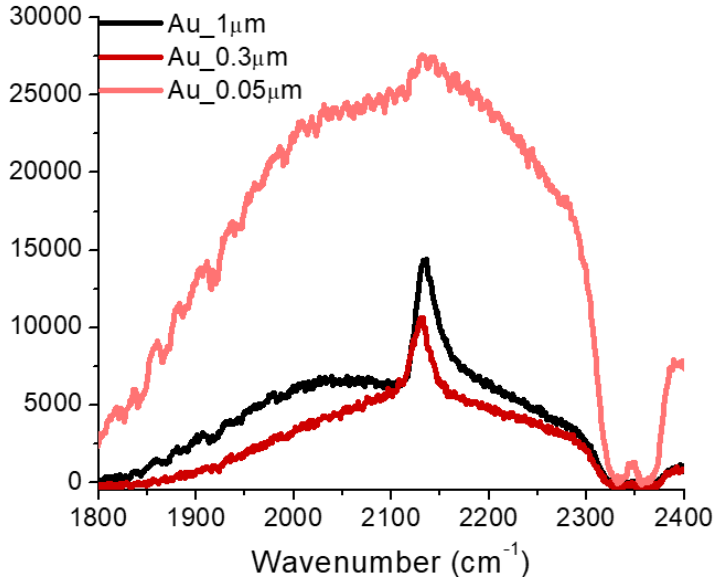

Figure 7.4. Raw SFG spectra of light-induced *CO generation measurement
Different numbers of μm in the labels represent the different sizes of the Al_2O_3 used in polishing the Au surface. The larger the Al_2O_3 is, the more roughened the surfaces are. The spectra are obtained by the 10-minute-long time exposure of the collection signal. The big Gaussian peaks in

three spectra are due to the non-resonant signal of the Au surface, the 2 major peaks at 2336 and 2362 cm^{-1} are due to the CO_2 absorption in the IR beam path, the wavy line-shape is due to the water vapor absorption in the IR beam path.

In summary, the observation with potential dependent SFG spectra on roughened Au and the spectra without bias both indicate that the probe light of SFG can greatly influence the reaction of reduction CO_2 to CO at the interfaces. Under the SFG probe light, the pure electrochemical reaction has been tuned to a photo-enhanced/assisted electrochemical reaction where light plays an important role in initiating the reactions; besides, this photo-enhanced / assisted phenomenon is surface morphology dependent: a more roughened surface should induce more photo effects. However, the mechanism of how the photo/lasers take part in the reaction remains unclear, whether the application of SFG laser light can be broadened to more universal lights also and requires more investigation. Therefore, we did the more control measurements shown as follows to possibly elucidate the mechanism.

8.2.2. Photocurrent measurements of PEEC CO_2 reduction

We first conducted the photocurrent measurements to estimate the internal photo-current efficiency (IPCE), to have an estimation of the efficiency of the system converts the energy from photons to contribute to the electrochemical reaction. The previous SFG measurements indicate that surface roughness can be a key factor in making a high yield of CO from CO_2 reduction. Following this concept, we purposely prepared the Au film samples with a high surface area that can be utilized for the photocurrent measurements. As **Figure 7.21**-A shows, we can directly shine the light on the working electrode, and with the given surface area and the corresponding photocurrent information, the IPCE can be calculated. The electrodes we used are shown in **Figure 7.21**-B, which are the electrochemical deposited Au on the ITO electrodes with a high surface roughness area. In **Figure 7.21**-C, the Au nanostructures are estimated to have around 150 to 250 nm diameter, and in **Figure 7.21**-4, we observed a higher absorptance from 500 to 540 nm on the samples.

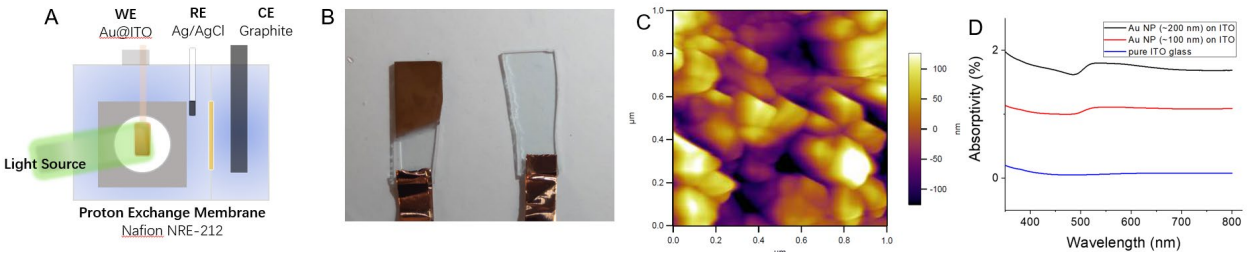

Figure 7.5. Electrochemical photocurrent measurements
(A) The scheme of the electrochemical cell used in the photocurrent measurement. (B) The electrochemical deposited Au on the ITO electrode. (C) AFM image of the microscopic structural information of the Au/ITO electrode. (D) Photo absorptivity test of different samples.

To have a quantitative analysis of the surface roughness, an electrochemical area factor determination is also conducted on these differently roughened surfaces. The idea of the measurement is to utilize the reduction peak of the monolayer Au oxide to Au at around 0.8 V vs Ag/AgCl during the electrochemical voltammogram scan to estimate the electrochemical active monolayer surface area, as the quantity of the charge that this monolayer reduction is a constant in most cases, in our measurements, we utilized the number from the literature[6], 482 mC/cm^2 for one monolayer. The electrochemical active area factor can be calculated with ***Equation 3***.

$$\text{th F} = \frac{\text{electroactive area}}{\text{geometric area}}$$

Equation 2. Electrochemical active area factor calculation

According to the results shown in **Figure 7.22**. The electrochemical active area factor for different samples is: 0.05 μm polished—**1.24**, 0.3 μm polished—**1.86**, and EAF for **NP** electrode —**1.41.**

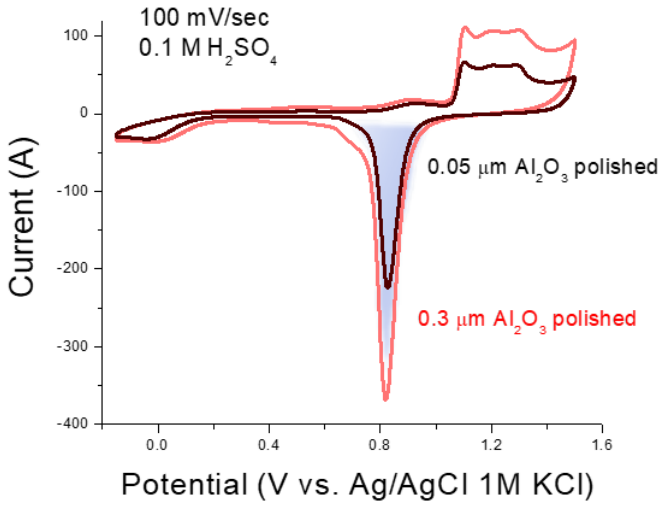

Figure 7.6. Electrochemical area factor determination measurement
The peak at 0.8 V is used to calculate the active surface area of the Au electrode.

In the photocurrent measurements, 532 nm light is selected to make a higher absorption on the Au films, according to the adsorption measurement in **Figure 7.21**D. Three potential points were chosen shown in **Figure 7.23**A, one point at +0.12 V, which has only a few overpotential for electrochemical CO_2 reduction and only a small constant current can be seen, one point at -0.08 V, and the other point at -0.28 V, which are both relatively more reductive potentials with larger reductive currents. For data analysis of the photocurrent measurements in **Figure 7.23**B, we used the Cottrell equation (current-time response) to simulate the light-off current values at a certain time (with the assumption that diffusion is a good approximation), and to get the photo-induced current difference values is the deduction from the simulated light-off current and the measured light-on current. Different power intensities of light are chosen to give a detailed profile of how the light intensity affects the phot current.

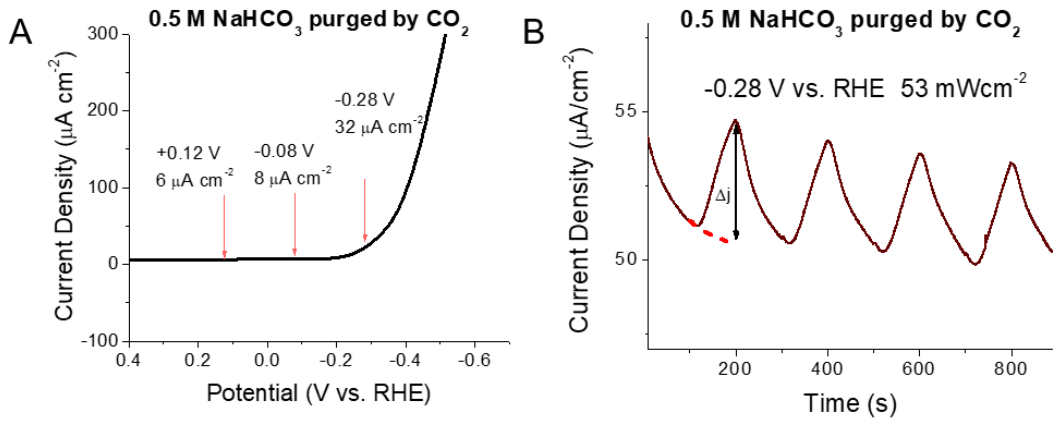

Figure 7.7. Electrochemical area factor determination measurement
(A) Potential data points selection and (B) the photocurrent contribution calculation.

The power intensity-dependent photocurrent measurements are shown in **Figure 7.24**A-C, and the results from light-induced contribution are shown in **Figure 7.24**D. At each potential, the 532 nm light shows a noticeable enhancement in the photocurrent and apparent photo-current efficiency (APCE, shown in **Figure 7.25**) with a light-on period, and we find a super linear relationship in all potential results, because the current density increase can be directly related with a reaction rate increase, and the super linearity between the reaction rate and the light intensity is also regarded as a signature of electron-driven chemical reactions on metals[7] rather than a pure thermal heating effect[8]. The IPCE and corresponding APCE can be obtained from ***Equation 4***. To further validate this assumption and exclude the contributions from charging/discharging currents and the photo-assisted hydrogen evolution reactions, the measurements in CO_2 saturated solutions and those in the inert gas solutions (with only HER and charging/discharging) are also compared, shown in **Figure 7.25**, the results of photo enhanced effects towards the hydrogen evolution reaction shows no intensity dependence thus exclude the possibility of charging/discharging and HER contribution. In our system, the IPCE for CO_2 reduction is around ~0.05%, though it is not as high as some systems with Ag nanostructures[2,3] (~0.3 to 0.6 %), it is still quite compatible with other Au nanostructure systems with 10^-4 % [1].

Equation 3. Electrochemical APCE calculation

$$APCE\% = \frac{IPCE\%}{Absorptivity} = \frac{J_{photocurrent\ density}(amp/cm^2)}{P_{light\ intensity}(Watt/cm^2) \times Absorptivity} \times \frac{1240}{\lambda_{excitation}(nm)} \times 100\%$$

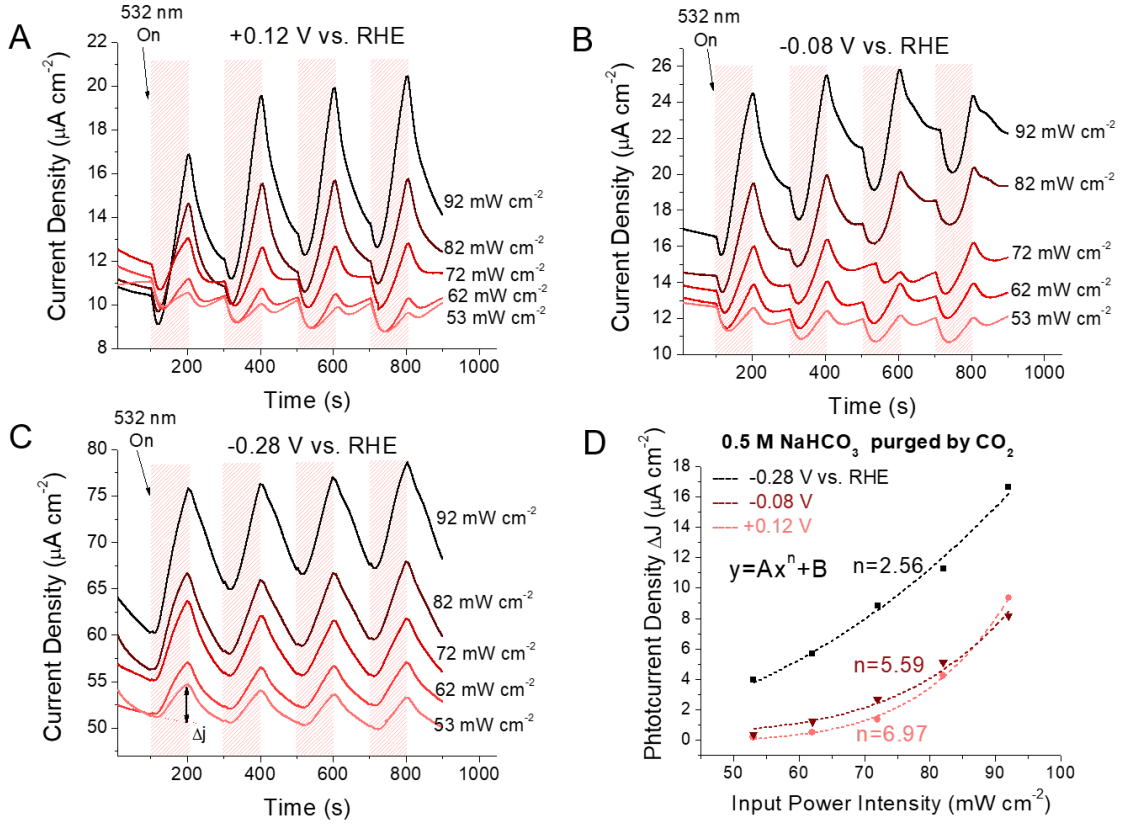

Figure 7.8. Electrochemical photocurrent measurement results
(A) Photocurrent measurement results at +0.12 V (B) at -0.08 V and (C) at -0.28 V. (D) Photocurrent density change as a function of the input power intensity.

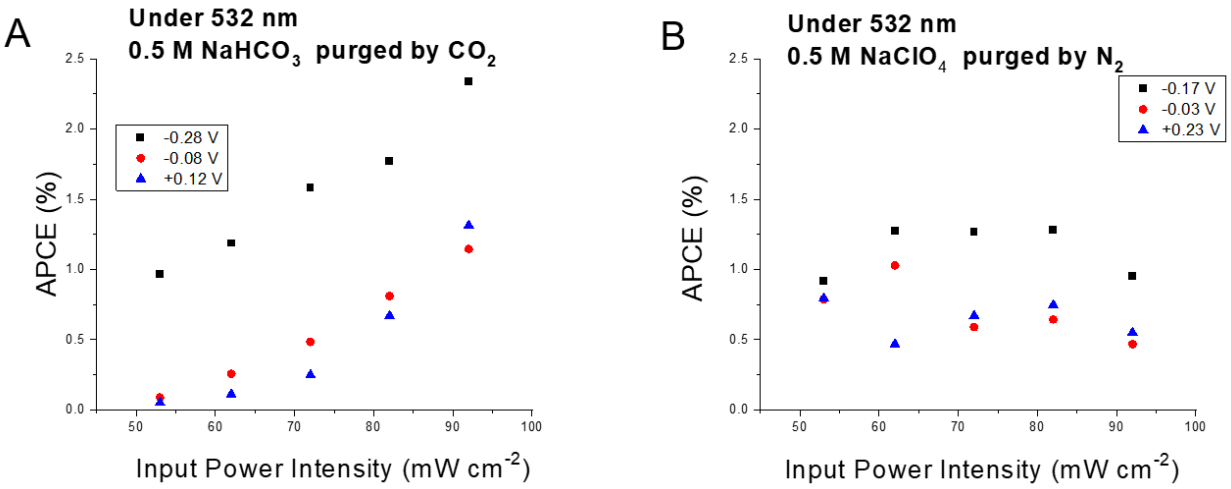

Figure 7.9. Electrochemical area factor determination measurement
(A) Potential data points selection and (B) the photocurrent contribution calculation.

8.2.3. Evidence of solvated electrons species

The previous results provide some evidence to support photo-enhanced CO_2 reduction may be partially due to the Au generated electron driven chemical reaction, but it cannot fully answer the questions on why the positive onset of *CO can be observed in SFG and why more roughened Au surface can induce a larger *CO signal. Thus, to find out the possibility of other hidden mechanisms of the previous observation, we conducted more experiments with different techniques. Previous results[9,10] in colloidal Cu and Au plasmonic nanoparticles inspired us that the smaller NPs can generate a large number of solvated electrons, even in the aqueous solutions. Further studies based on other materials to generate solvated electrons for nitrogen fixation and CO_2 reduction prove its applicability in reducing reactions[11–13]. Thus we tried to conduct measurements to validate the possibility of a mechanism on solvated electrons.

We proceed with two types of time-resolved spectroscopic measurements on two types of samples to observe the existence of the solvated electrons. The first one is the transient reflectance measurement on a gold film working electrode (the same Au film used in IPCE measurements), and the second one is the transient absorption measurement of Cu colloidal nanoparticles in an aqueous solution. The first measurement is to test whether, under the same conditions of IPCE or SFG measurements, the solvated electrons can be detected. The second measurement is to test in general whether the solvated electrons can be generated.

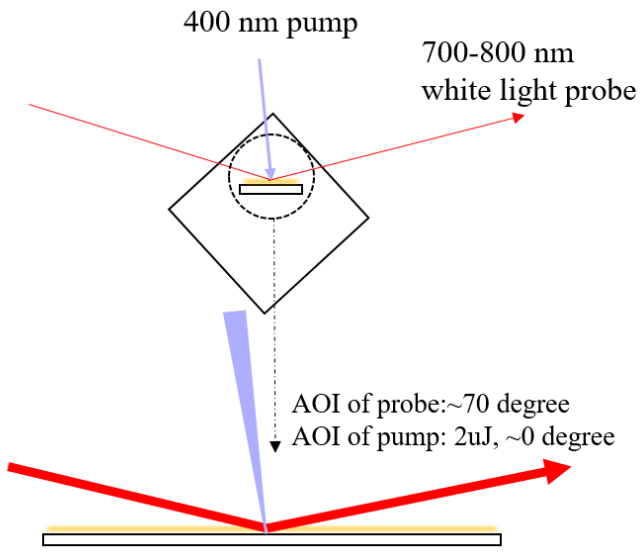

Figure 7.10. Scheme of transient reflectance measurement
The beam size is focused smaller (tens of microns) for an easier time zero response location in measurements.

We proceed with a wide-angle probe (shown in **Figure 7.26**) in the transient reflectance measurement to maximize the interaction between the probed beam and the solvated electrons. According to reports[9,10,13], the solvated electron in an aqueous solution should present a broad peak feature at around 700-800 nm absorption with quite low absorptivity. Thus, we specifically locate the region to obtain the time-resolved response of the signal (shown in **Figure 7.27**).

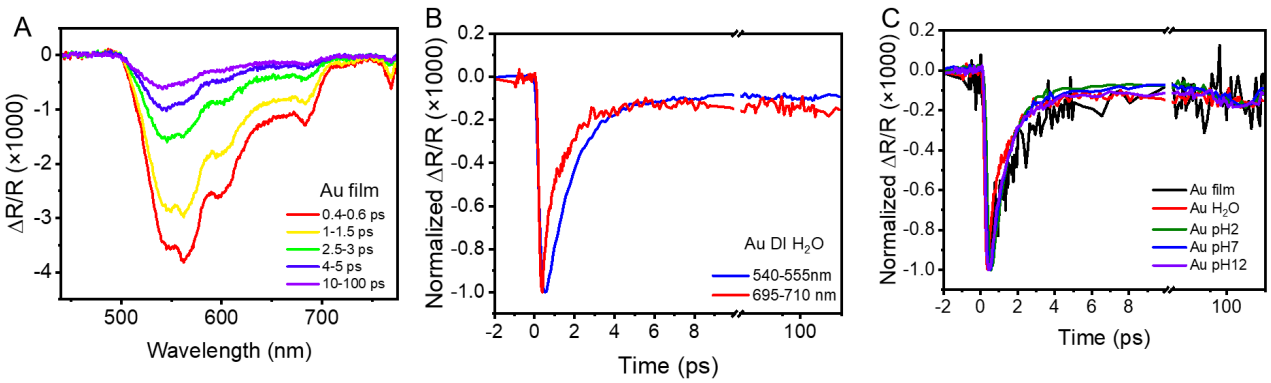

Figure 7.11. Transient reflectance results of Au film
(A) Different time scale responses of the Au film sample from 400 to 800 nm. (B) Normalized kinetic signal change at 700 nm and 540-550 nm decay as a function of time. (C) Kinetics of 700 nm signal change in different pH solutions.

The results in in **Figure 7.27**, show that the kinetics (decay) of the signal changes at 700 nm is quite similar to that at 540-550 nm. As the signal at 540-550 nm is usually directly related to the plasmon band of Au, this similarity means that in the Au film electrode case, the time-resolved signal change should be regarded as a residual signal of the plasmon band of Au at this region rather than the signal from solvated electrons. Additionally, another control measurement in **Figure 7.27**C also proves that the signal is irrelevant with the solvated electrons, as the signal lifetime should be directly pH-dependent (protons can consume electrons quickly). Therefore, these results indicate that it is quite difficult to directly detect solvated electrons signal from the Au film electrode, the possible reasons may be due to the insufficient probe light path interaction with the electrode surface depth and area (as the solvated electrons can be quickly and easily quenched in solutions), or the insufficient population of solvated electrons generated in the system (too large Au NPs).

We have reached the detection limit on the increasing limit on the first factor, thus we tried to increase the population of generated solvated electrons. We followed the report[65] and synthesized similar 2-3 nm Cu NPs, as the smaller NPs exhibit a bigger possibility to generate higher energy hot electrons to make more solvated electrons.

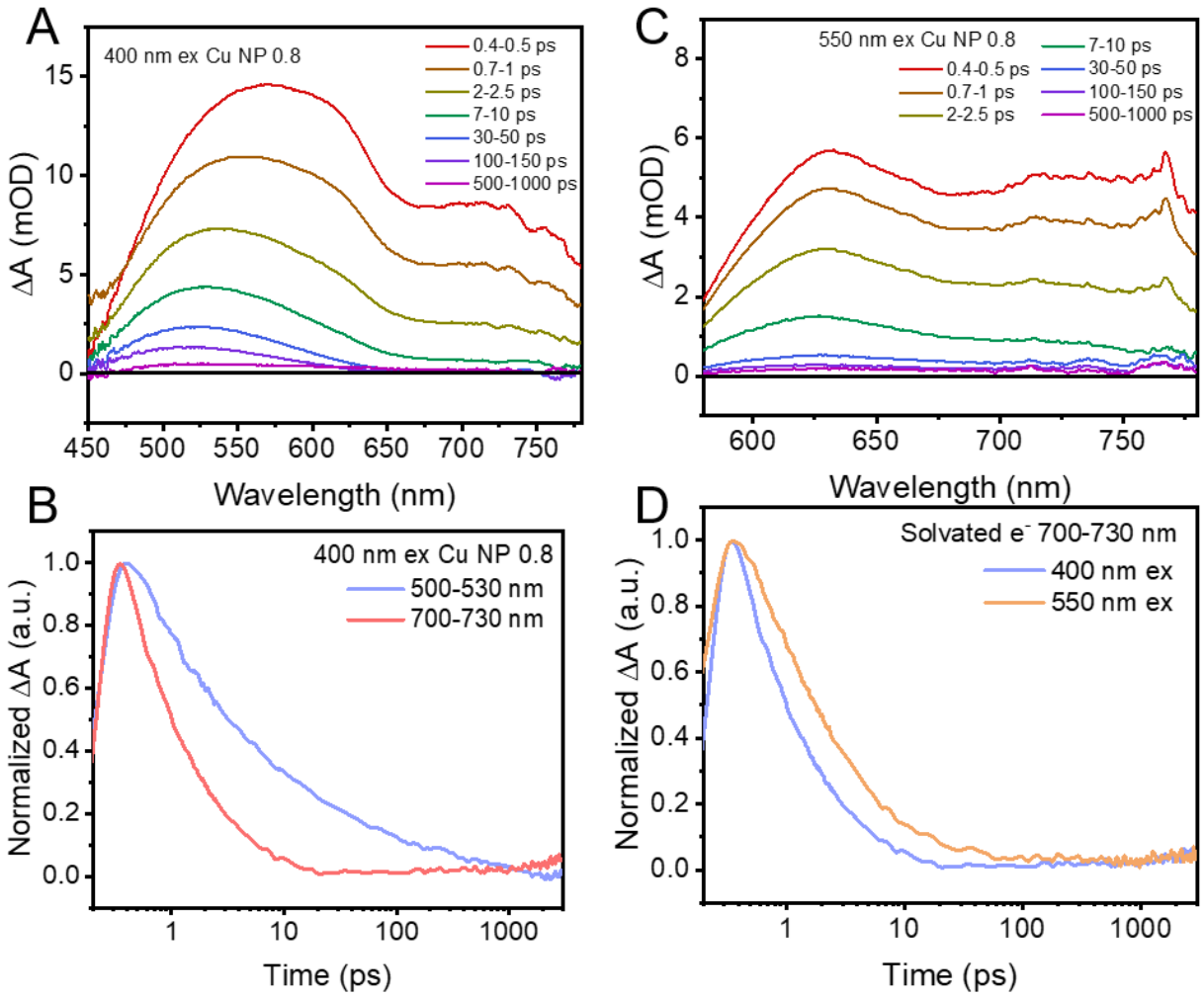

Figure 7.12. Transient absorption results of Cu NPs
(A) Different time scale responses of the Au film sample from 450 to 800 nm under 400 nm excitation. (B) Normalized kinetic signal change at 700 nm and 540-550 nm decay as a function of time. (C) Different time scale responses of the Au film sample from 450 to 800 nm under 550 nm excitation. (D) Normalized kinetic signal change at 700 nm and 540-550 nm decay as a function of time.

The results in in **Figure 7.28**, show that under 400 nm and 550 nm excitation, we observe a time-resolved signal change at 700 nm in both cases, and it has a faster decay kinetics compared to that of the signal at 530 nm. Thus, we believe this is clear evidence that the solvated electrons can be generated and probed in aqueous solution. However, it cannot help to answer whether similar solvated electrons can be generated in the Au film case for the CO_2 reduction reaction.

8.2.4. Discussion on the mechanisms in PEEC CO_2

The observation of light-enhanced *CO production on Au surfaces by SFG drives us to investigate deeper into the underlying mechanisms that could account for this phenomenon. But based on our experimental results and existing literature, we cannot fully resolve which possible mechanism may lead the major role in making *CO on the Au surface, we thus propose a possible mechanism with a mixture of three key contributions: the direct hot electron transfer from the Au electrodes to the adsorbates (such as weakly bonded *CO_2), the generation of solvated electrons through Au plasmon excitation, and direct laser-induced reduction. The first mechanism is supported by the photocurrent measurements and involves the hot electron generation from the excitation of the plasmons on the Au surface and following electron-hole separation; the second mechanism involves a different followed-up step with the production of solvated electrons after the excitation of plasmons on the Au surface. The excitation of surface plasmons on Au has been previously demonstrated to induce hot electron transfer, which can result in the generation of solvated electrons in the surrounding solution[14]. These solvated electrons can serve as powerful reducing agents, capable of triggering the reduction of CO_2 to CO[10]. In our study, the presence of solvated electrons was confirmed through transient absorption spectroscopy, which serves as evidence for its generation and decay dynamics. This evidence supports the solvated electron mechanism as a possible pathway for light-enhanced CO_2 reduction on Au. The third proposed mechanism involves direct laser-induced reduction in the liquid phase[15]. This mechanism suggests that high-intensity laser light can directly excite CO_2 molecules in the solution, causing them to transition to high-energy states conducive to

reduction. A recent study[15] provided solid evidence for this mechanism, demonstrating that laser light can directly reduce CO_2 in the liquid phase under certain conditions. It is plausible that similar processes could be taking place in our system, given the use of high-intensity laser light in our SFG setup. However, further experimental investigations are required to verify the occurrence and significance of this mechanism in our system. Thus, while all the direct electron transfer reduction, solvated electron, and direct laser-induced reduction mechanisms can potentially account for the observed light-enhanced CO_2 reduction on Au, more detailed studies are needed to fully understand their respective roles and contributions. We can provide evidence to prove the existence of one of them (the generation of the solvated electrons) but cannot rule out the possibilities of other mechanisms. We believe more measurements are needed to fully disentangle these mechanisms so that we can gain a deeper understanding of the roles of light in electrochemical reactions at the Au/aqueous interface.

8.3. Conclusions

In conclusion, in this section, we showed the study on photo-enhanced electrochemical CO_2 reduction and the mechanism of the interaction between light irradiation and electrochemical processes at the Au surface. The utilization of VSFGS enabled us to observe the unusual phenomenon occurring at the Au/electrolyte interface—a positive onset potential for CO production on Au surfaces during CO_2 reduction. By more photochemical experimental measurements without bias, we believe this unexpected observation should involve several possible mechanisms to achieve photo-assisted/photo-enhanced electrochemical CO_2 reduction, where the pulsed laser excitation from the SFG setup plays a vital role. Through systematic photo-current measurements employing various light wavelengths and pulses, we found noticeable photocurrents produced by different wavelengths of light, which further proves the light-enhancement effect within the CO_2 reduction system. With the experimental evidence, we introduced two possible pathways to explain this PEEC phenomenon—the generation of solvated electrons from the Au surface and direct laser-induced reduction in the liquid phase. While our detailed investigation utilizing TA spectroscopy provided evidence for the former mechanism, confirming the generation of solvated electrons on Au NPs in aqueous solutions, we still think another mechanism may occur as we cannot fully rule out the other possibilities on a roughened Au disk electrode. In summary, the insights from our observation possibly provide a better understanding of photo-enhanced CO_2 electroreduction on Au, but due to the complexities of the system and other possible mechanisms, We propose that further investigations should be designed to elucidate alternative mechanisms on Au surfaces. Nevertheless, this study enriches our understanding of the interaction between light irradiation and electrochemical interfaces on metals.

8.4. References

(1) DuChene, J. S.; Tagliabue, G.; Welch, A. J.; Cheng, W.-H.; Atwater, H. A. Hot Hole Collection and Photoelectrochemical CO_2 Reduction with Plasmonic Au/p-GaN Photocathodes. *Nano Lett.* **2018**, *18* (4), 2545–2550. https://doi.org/10.1021/acs.nanolett.8b00241.

(2) Kim, Y.; Creel, E. B.; Corson, E. R.; McCloskey, B. D.; Urban, J. J.; Kostecki, R. Surface-Plasmon-Assisted Photoelectrochemical Reduction of CO2 and NO3− on Nanostructured Silver Electrodes. *Adv. Energy Mater.* **2018**, *8* (22), 1800363. https://doi.org/10.1002/aenm.201800363.

(3) Creel, E. B.; Corson, E. R.; Eichhorn, J.; Kostecki, R.; Urban, J. J.; McCloskey, B. D. Directing Selectivity of Electrochemical Carbon Dioxide Reduction Using Plasmonics. *ACS Energy Lett.* **2019**, 1098–1105. https://doi.org/10.1021/acsenergylett.9b00515.

(4) Corson, E. R.; Kas, R.; Kostecki, R.; Urban, J. J.; Smith, W. A.; McCloskey, B. D.; Kortlever, R. In Situ ATR–SEIRAS of Carbon Dioxide Reduction at a Plasmonic Silver Cathode. *J. Am. Chem. Soc.* **2020**, *142* (27), 11750–11762. https://doi.org/10.1021/jacs.0c01953.

(5) Dunwell, M.; Lu, Q.; Heyes, J. M.; Rosen, J.; Chen, J. G.; Yan, Y.; Jiao, F.; Xu, B. The Central Role of Bicarbonate in the Electrochemical Reduction of Carbon Dioxide on Gold. *J. Am. Chem. Soc.* **2017**, *139* (10), 3774–3783. https://doi.org/10.1021/jacs.6b13287.

(6) Tian, Y.; Liu, H.; Zhao, G.; Tatsuma, T. Shape-Controlled Electrodeposition of Gold Nanostructures. *J. Phys. Chem. B* **2006**, *110* (46), 23478–23481. https://doi.org/10.1021/jp065292q.

(7) Christopher, P.; Xin, H.; Marimuthu, A.; Linic, S. Singular Characteristics and Unique Chemical Bond Activation Mechanisms of Photocatalytic Reactions on Plasmonic Nanostructures. *Nat. Mater.* **2012**, *11* (12), 1044–1050. https://doi.org/10.1038/nmat3454.

(8) Maley, M.; Hill, J. W.; Saha, P.; Walmsley, J. D.; Hill, C. M. The Role of Heating in the Electrochemical Response of Plasmonic Nanostructures under Illumination. *J. Phys. Chem. C* **2019**. https://doi.org/10.1021/acs.jpcc.9b01479.

(9) Pavliuk, M. V.; Gutiérrez Álvarez, S.; Hattori, Y.; Messing, M. E.; Czapla-Masztafiak, J.; Szlachetko, J.; Silva, J. L.; Araujo, C. M.; A. Fernandes, D. L.; Lu, L.; Kiely, C. J.; Abdellah, M.; Nordlander, P.; Sá, J. Hydrated Electron Generation by Excitation of Copper Localized Surface Plasmon Resonance. *J. Phys. Chem. Lett.* **2019**, *10* (8), 1743–1749. https://doi.org/10.1021/acs.jpclett.9b00792.

(10) Al-Zubeidi, A.; Ostovar, B.; Carlin, C. C.; Li, B. C.; Lee, S. A.; Chiang, W.-Y.; Gross, N.; Dutta, S.; Misiura, A.; Searles, E. K.; Chakraborty, A.; Roberts, S. T.; Dionne, J. A.; Rossky, P. J.; Landes, C. F.; Link, S. Mechanism for Plasmon-Generated Solvated Electrons. *Proc. Natl. Acad. Sci.* **2023**, *120* (3), e2217035120. https://doi.org/10.1073/pnas.2217035120.

(11) Zhang, L.; Zhu, D.; Nathanson, G. M.; Hamers, R. J. Selective Photoelectrochemical Reduction of Aqueous CO_2 to CO by Solvated Electrons. *Angew. Chem. Int. Ed.* **2014**, *53* (37), 9746–9750. https://doi.org/10.1002/anie.201404328.

(12) Zhu, D.; Zhang, L.; Ruther, R. E.; Hamers, R. J. Photo-Illuminated Diamond as a Solid-State Source of Solvated Electrons in Water for Nitrogen Reduction. *Nat. Mater.* **2013**, *12* (9), 836–841. https://doi.org/10.1038/nmat3696.

(13) Bachman, B. F.; Zhu, D.; Bandy, J.; Zhang, L.; Hamers, R. J. Detection of Aqueous Solvated Electrons Produced by Photoemission from Solids Using Transient Absorption

Measurements. *ACS Meas. Sci. Au* **2022**, *2* (1), 46–56. https://doi.org/10.1021/acsmeasuresciau.1c00025.
(14) Qi, J.; Resasco, J.; Robatjazi, H.; Alvarez, I. B.; Abdelrahman, O.; Dauenhauer, P.; Christopher, P. Dynamic Control of Elementary Step Energetics via Pulsed Illumination Enhances Photocatalysis on Metal Nanoparticles. *ACS Energy Lett.* **2020**, *5* (11), 3518–3525. https://doi.org/10.1021/acsenergylett.0c01978.
(15) Yan, B.; Li, Y.; Cao, W.; Zeng, Z.; Liu, P.; Ke, Z.; Yang, G. Highly Efficient and Highly Selective CO2 Reduction to CO Driven by Laser. *Joule* **2022**, *6* (12), 2735–2744. https://doi.org/10.1016/j.joule.2022.11.005.